Hydrodynamics of Supercooled Drops Encountering Solidification at Various Moments of Impact

TECHNISCHE
UNIVERSITÄT
DARMSTADT

Mechanical Engineering
Department

SLA

Hydrodynamics of Supercooled Drops Encountering Solidification at Various Moments of Impact

For my family and my love

Erklärungen laut Promotionsordnung

§8 Abs. 1 lit. c PromO

Ich versichere hiermit, dass die elektronische Version meiner Dissertation mit der schriftlichen Version übereinstimmt.

§8 Abs. 1 lit. d PromO

Ich versichere hiermit, dass zu einem vorherigen Zeitpunkt noch keine Promotion versucht wurde. In diesem Fall sind nähere Angaben über Zeitpunkt, Hochschule, Dissertationsthema und Ergebnis dieses Versuchs mitzuteilen.

§9 Abs. 1 PromO

Ich versichere hiermit, dass die vorliegende Dissertation selbstständig und nur unter Verwendung der angegebenen Quellen verfasst wurde.

§9 Abs. 2 PromO

Die Arbeit hat bisher noch nicht zu Prüfungszwecken gedient.

Darmstadt, 08.08.2022

M.G. Gloerfeld

Abstract

Icing of surfaces is a hazard to numerous technical applications like aircraft, wind turbines, ships and power lines exposed to cold environments. Ice accretion on crucial parts can lead to significant decrease in efficiency, unpredictable limitation of function or complete failure. Particularly threatening icing scenarios often involve the impact of supercooled large water drops. Being in an initially meta-stable liquid state, their solidification exhibits a dynamic stage involving fast propagation of dendrites in their bulk. The interaction of dendrites with the fluid flow of a drop impact represents a complex problem which is to date not fully understood.

This dissertation is devoted to gaining insight into the underlying physics of the impact of a supercooled large drop onto a cold solid surface superimposed by an impinging cold air flow. Focus lies on the onset of solidification at various times of the impact which relates to different stages of an ice layer growing on a surface. For experimental investigations, an icing wind tunnel was designed, built and commissioned in the course of this thesis. It facilitates experiments of single supercooled large drops of different sizes impacting onto solid surfaces with controlled variation of drop temperature, impact velocity and speed of the superimposing air flow.

Investigations involve the impact of supercooled liquid drops which develop a corona splash upon impact. The splash extent and remaining fluid on the surface is connected to an existing theoretical model considering the onset of splashing. A superimposed air flow entails a deformation of the drops before impact which is incorporated in the splashing model and also in a semi-empirical approach, aiming for estimation of the maximum spreading diameter. Moreover, the impact of drops on a flat ice surface is investigated, which is characterized by an early onset of freezing. A vital influence of the fluid supercooling, i.e. the dendrite propagation velocity, is quantified and a modified model for estimation of the spreading diameter of the frozen drop is introduced. Furthermore, the impact of drops experiencing nucleation before impact is investigated. The impact behaviour of such partially frozen drops has never been investigated before and the adaption of a plasticity flow model enabled the quantification of rheological properties of this mixed phase.

   The findings of this work contribute to a deeper understanding of the physics involved in the fluid flow and its interaction with the dynamic solidification arising upon impact of single supercooled drops. The adapted models, empirical approaches and quantified properties can ultimately be employed to improve numerical models aimed at the prediction of ice accretion on technical surfaces.

Zusammenfassung

Vereisung von Oberflächen stellt eine Gefahr dar für zahlreiche technische Anwendungen, wie Luftfahrzeuge, Windturbinen, Schiffe und Oberleitungen, die kalten Umgebungsbedingungen ausgesetzt sind. Eisansammlungen auf wesentlichen Komponenten einzelner Anwendungen können zu erheblicher Reduzierung der Effizienz, unvorhersehbaren Einschränkungen von Funktionen bis hin zu totalem Betriebsausfall führen. Besonders kritische Vereisungsszenarien sind oft geprägt vom Aufprall unterkühlter großer Wassertropfen. Diese befinden sich zunächst in einem meta-stabilen Zustand, den sie unter Ausbreitung von schnell voranschreitenden Eisdendriten in der Flüssigphase verlassen. Das Zusammenspiel der Flüssigkeitsströmung mit der dynamischen Erstarrung in Form von Dendriten ist bis heute nicht vollständig verstanden.

Diese Dissertation ist neuen Erkenntnissen bezüglich den zugrundeliegenden physikalischen Mechanismen des Aufpralls eines unterkühlten großen Tropfens auf eine kalte feste Oberfläche überlagert mit Auftreffen einer kalten Luftströmung gewidmet. Der Fokus liegt auf Phänomenen, bei denen die Erstarrung zu verschiedenen Zeitpunkten des Aufpralls einsetzt, wie es in unterschiedlichen Phasen des Anwachsens einer Eisschicht auf einer Oberfläche der Fall ist. Für die entsprechenden Untersuchungen wurde im Rahmen dieser Arbeit ein Vereisungswindkanal ausgelegt, aufgebaut und in Betrieb genommen. Dieser ermöglicht Experimente zum Aufprall einzelner unterkühlter Tropfen verschiedener Größe unter kontrollierter Variation von Tropfentemperatur, Aufprallgeschwindigkeit und Strömungsgeschwindigkeit des überlagerten Luftstroms.

Die Untersuchungen umfassen den Aufprall von unterkühlten flüssigen Tropfen, die bei Aufprall einen sogenannten Corona-Splash ausbilden. Das Ausmaß des Splashes und die zurückbleibende Tropfenmasse werden mit einem existierenden Modell bezüglich des Einsetzens des Splashing in Zusammenhang gesetzt. Bei Überlagerung mit einem auftreffenden Luftstrom verformen die Tropfen sich vor dem Aufprall merklich. Die Auswirkungen der Verformung werden sowohl im Splashing-Modell, als auch in einem semiempirischen Modell zur Abschätzung des maximalen Ausbreitungsdurchmessers der Tropfen eingebunden. Zudem wird der Aufprall unterkühlter Tropfen auf eine planare Eisoberfläche betrachtet, welcher gekennzeichnet ist durch ein frühes Einsetzen der Erstarrung. Es wird gezeigt, dass die Unterkühlung der Tropfen vor Aufprall, d.h. Ausbreitungsgeschwindigkeit der Dendriten, einen wesentlichen Einfluss auf die maximale Ausbreitung hat und ein Modell zur Abschätzung dieser wird vorgestellt. Des Weiteren wird der Aufprall

von Tropfen, die ihre Erstarrung bereits vor dem Aufprall beginnen, betrachtet. Das Verhalten solcher partiell gefrorener Tropfen während des Aufpralls wurde bisher noch nie untersucht und mithilfe eines angepassten Models einer plastischen Strömung wird eine entscheidende rheologische Eigenschaft der gemischten Phase quantifiziert.

Die Ergebnisse dieser Arbeit tragen zu einem tieferen Verständnis der Physik der Flüssigkeitsströmung des Aufpralls unterkühlter Tropfen und dessen Interaktion mit der auftretenden dynamischen Erstarrung bei. Die angepassten Modelle, empirischen Korrelationen und quantifizierte Eigenschaften können schließlich verwendet werden, um numerische Modelle zur Vorhersage von Vereisung auf technischen Oberflächen zu verbessern.

Journal publications

Gloerfeld, M.; Schremb, M.; Roisman, I. V.; Hussong, J.; Tropea, C.: Wall impact of mushy frozen water drops. Cold Regions Science and Technology 206, (2023), https://doi.org/10.1016/j.coldregions.2022.103732

Gloerfeld, M.; Roisman, I.V.; Hussong, J.; Tropea, C.: Measurements and modelling of the residual mass upon impact of supercooled liquid drops. Experiments in Fluids 62, 204 (2021), https://doi.org/10.1007/s00348-021-03292-7

Seiler, P.M.; Gloerfeld, M.; Roisman, I.V. and Tropea, C.: Aerodynamically driven motion of a wall-bounded drop on a smooth solid substrate. In: Physical Review Fluids, 4.2 (2019), https://doi.org/10.1103/PhysRevFluids.4.024001

Conference proceedings

Gloerfeld, M.; Schremb, M.; Roisman, I.V.; Tropea, C. ; Hussong, J: Impact of mushy frozen water particles onto a cold surface. Proc. of 15th Triennial International Conference on Liquid Atomization and Spray Systems – ICLASS 2021, Edinburgh, UK, August (2021), https://doi.org/10.2218/iclass.2021.5994

Gloerfeld, M.; Schremb, M.; Tropea, C.: A Slingshot Device for the Experimental Investigation of High-Speed Drop Impact. 10th International Conference on Multiphase Flow - ICMF 2019, Rio de Janeiro, Brazil, May (2019)

Acknowledgements

First of all, I would like to thank Prof. Cameron Tropea for the opportunity to start working at the Institute for Fluid Mechanics and Aerodynamics at the Technical University of Darmstadt, and for the advice and supervision regarding my doctoral work. Second, I want to thank Prof. Jeanette Hussong for enabling a continuation of my work at the institute, helpful discussions and for acting as second reviewer of this dissertation. Additionally, I like to thank Prof. Dimos Poulikakos for also acting as an external reviewer of this thesis.

I further want to express my gratitude to apl.-Prof. Ilia Roisman for his expertise, which was crucial to the models developed in this work. I would also like to thank all my colleagues from the Institute of Fluid Mechanics and Aerodynamics who always showed great interest in fruitful exchange during work, lunch breaks and occasional breakfasts. In particular, I want to thank Louis Reitter and Dr. Markus Schremb for countless valuable discussions and a helping hand in the lab whenever necessary, Sebastian Wegt for accompanying me almost the entire time at the institute and aiding with the numerical work of this study, Benedikt Schmidt for the joint endeavour in the SFB-TRR 75, apl.-Prof. Suad Jakirlic, who also enabled my work on this project, Bastian Stumpf, Sebastian Blahout and Maximilian Lausch for their input and proofreading of this work along with further helpful discussions and Mingyue Ding for her help in experiments. Moreover, I thank Birgit Neuthe and Corinna Neumann for helping with all administrative matters. Furthermore, I would like to thank Ilona Kaufhold, Timm Geelhaar and the rest of the workshop team for the manufacturing of the wind tunnel and countless other parts without which the experiments in this work would not have been possible. I thank Julian Preußler, Julian Solzer, Kevin Antonowicz and Marcel Hübner for their contributing work in the scope of their theses and as assistants. I also want to acknowledge the financial support by DFG in the scope of the SFB-TRR 75.

My innermost gratitude belongs to my friends and my family, in particular my parents, without whom I could have never accomplished everything I achieved so far. Last but foremost, I am incredibly grateful to my girlfriend Alke for her endless support, patience and love not only during preparation of this work but, above all, the entire way she already stands by me.

Nomenclature

Dimensionless Groups

Ca	Capillary number, Eq. (2.4)
Oh	Ohnesorge number, Eq. (2.3)
Re	Reynolds number, Eq. (2.1)
St	Stephan number, Eq. (2.39)
We	Weber number, Eq. (2.2)

Greek letters

β	Splashing parameter after Riboux and Gordillo (2014), Eq. (2.24)	
$\dot{\gamma}$	Equivalent strain rate	1/s
γ_{BL}	Boundary layer constant	
Δ	Difference	
δ_{BL}	Boundary layer thickness	m
ϵ	Similarity variable	
ε	Empirical constant	s
ζ	Dimensionless particle dislodging	
η	Dynamic viscosity	N s/m^2
θ	Contact angle	°
ϑ	Dimensionless temperature	
I	Thermal conductivity	Wm^{-1}K^{-1}
κ	Front curvature of drop	1/m
Λ	Speed/Position function of freezing front	

λ	Mean free path of gas	m
μ	Boundary layer thickness constant	
ν	Kinematic viscosity	m^2/s
ξ	Volume fraction	$\%_{vol}$
ρ	Density	kg/m^3
σ	Surface tension	N/m
σ'	Deviatoric stress	N/m
σ_{ii}	Internal stress component	N/m
τ	Constant in lamella flow remote asymptotic solution	
ϕ	Potential function	m^2/s
φ	Azimuthal coordinate	rad
χ	Empirical constant	
Ψ	Number of active nucleation sites	
ψ	Elliptic coordinate	rad
ω	Elliptic coordinate	m

<u>Indices</u>

0	Value of the equivalent undisturbed spherical drop before impact
∞	Far field
κ	Value accounts for front curvature of drop
2nd	Secondary drops
air	Air
amb	Ambient
BL	Boundary layer
bnd	Boundary
bulk	Bulk
BU	Break-up

cor	Corona
cr	Critical
diag	Along s_{diag}
diss	Dissipated
ecc	Eccentricity
el	Elongation
exp	Value obtained from experiment
frz	Considering superposition of freezing
het	Heterogeneous
hom	Homogeneous
hyd	Hydraulic
ice	Ice
imp	Impact
kin	Kinetic
lam	Lamella
lay	Initial ice layer
liq	Liquid
loc	Local
max	Maximum
mn	Mean
mod	Value obtained from model
nl	Nucleus/liquid interface
rel	Relative
res	Residual
rim	Rim
R	Scaled with the drop radius R_0

splat	Splat (frozen drop)	
sprd	Spreading	
st	Instantaneous	
tot	Total	
TPS	Two phase Stefan problem	
trg	Target	
TS	Test section	
upper	Upper bound	
wl	Wall/liquid interface	
wn	Wall/nucleus interface	
wt	Wetted	
σ	Interfacial	
θ	Considering wettability effects	
c	Contact	
d	Dendrite tip	
e	Moment of lamella lift off	
f	Dendrite cloud front	
g	Gaseous	
h	Horizontal	
m	At the melting point of water	
n	Nucleus	
v	Vertical	
w	Wall	
z	in z-direction	

Latin letters

A	Area	m^2

a	Radius of force transition area	m
$\mathcal{A}$	Dimensionless function	
$\overline{a}$	Dimensionless radius of force transition area	
b	Proportionality constant of kinematic spreading	
$\mathcal{B}$	Dimensionless function	
b_0	Proportionality constant of spherical drop	
$\mathcal{C}$	Dimensionless function	
C_i	Empiric constants	
c_p	Isobaric heat capacity	$\mathrm{J\,kg^{-1}\,K^{-1}}$
c_v	Isochoric heat capacity	$\mathrm{J\,kg^{-1}\,K^{-1}}$
D	Diameter	m
$\boldsymbol{E}$	Rate-of-strain tensor	1/s
F	Force	N
$\mathcal{F}$	Shape factor	
G	Gibbs free energy	J
ΔG_V	Energy of fusion per unit volume	$\mathrm{J/m^3}$
h	Thickness/height	m
$\overline{h}$	Dimensionless thickness/height	
H_e	Lamella front thickness in moment of lift-off	m
J	Rate of nucleation per unit area	$\mathrm{m^{-2}s^{-1}}$
K	Scaled axial momentum	
K_{ls}	Loss coefficient	
K_l	Lubrication coefficient	
K_u	Suction coefficient	
l	Length	m
L_f	Latent heat of fusion per unit mass	J/kg

M	Total axial momentum	Ns
N	Number of drops	
o	Intersection height of particle and surface	m
p	Local pressure	Pa
ΔP	Pressure difference	Pa
$\mathcal{P}_{\mathrm{nll}}$	Probability of zero nucleation sites	
$\dot{Q}$	Heat flux	W
R	Radius	m
r	Radial coordinate	m
$\bar{r}$	Dimensionless radial coordinate	
R_n^*	Critical nucleus radius	m
S	Dimensionless spreading coefficient	
$\tilde{S}_{\mathrm{max}}$	Adapted prediction of dimensionless maximum spreading	
$s(t)$	Boundary layer evolution function in dendritic freezing of lamella	m
s_{diag}	Coordinate diagonally through the test section	m
T	Temperature	$^\circ$C
t	Time	s
ΔT	Temperature difference/ supercooling $(T_m - T)$	K
Tu	Turbulence Intensity	%
$\bar{t}$	Dimensionless time	
U	Impact velocity	m/s
u	Local velocity	m/s
$\boldsymbol{u}$	Velocity field	m/s
$\bar{u}$	Dimensionless local velocity	
u_i'	Turbulent velocity fluctuation	m/s
U_e	Lamella front velocity in moment of lift-off	m/s

V	Volume	m^3
$\dot{V}$	Volume flow	m^3/s
v_d	Dendrite tip velocity	m/s
v_f	Dendrite cloud front velocity	m/s
W	Width	m
x	x-coordinate	m
Y	Yield strength	Pa
y	y-coordinate	m
$\overline{Y}$	Dimensionless yield strength	
$y(\dot{\gamma})$	Dimensionless strain rate scaling function	
Y_0	Static yield strength	Pa
Z	Impact parameter (Schremb et al., 2017c), Eq. (2.47)	
z	z-coordinate	m

Contents

List of Figures

List of Tables

1 Introduction

Nature and our everyday life are constantly marked by the presence of water in manifold constitution. Whereas it remains volatile in most of its forms, it attains more tangible shapes in its solid phase as ice. Upon solidification, water possibly develops countless patterns of crystals and agglomeration whose characteristics greatly depend on their surroundings (Libbrecht, 2017). These unique shapes can exhibit several length scales from single tiny snowflakes to composite structures covering entire trees or buildings. However, as fascinating as these different formations are, they often pose a hazard to nature and technical applications exposed to them. The risks some of these icing phenomena represent and how they motivated this thesis is illuminated in the following.

1.1 Motivation and Background

The ubiquity of water entails icing phenomena in almost every natural cold environment which affects living organisms as well as technical surfaces sojourning in it as seen in Fig. 1.1. While organisms which are not able to escape this environment, e.g. plants, evolved mechanisms to withstand the ice (Scholander et al., 1953), manifold technical applications are possibly constricted in their function or experience failure. Hence, in a cold environment icing is a potential threat to aircraft (Cebeci and Kafyeke, 2003; Cao et al., 2018; Yamazaki et al., 2021), wind turbines (Jasinski et al., 1998; Dalili et al., 2009; Parent and Ilinca, 2011), ships (Makkonen, 1987; Samuelsen, 2018) and power lines (Makkonen, 1998; Szilder et al., 2002).

  The process of ice accumulating on surfaces can be versatile, yet one mechanism arises as particularly interesting in studies regarding ice accretion, namely the icing due to supercooled water drops (Roisman and Tropea, 2021). When water experiences temperatures below its melting temperature, it may remain in a liquid phase as long as the environment is calm and low in contaminants. This meta-stable state is referred to as supercooled and it persists until contamination or a sudden impulse triggers nucleation of the fluid. The subsequent solidification is characterized by two stages. First, the propagation of dendrites into the bulk which leaves a mixture of ice and water in equilibrium at melting temperature (Shibkov et al., 2003). Second, the solidification of the remaining liquid in between the dendrites. On the way to complete solidification of the liquid, the dispersion of

(a) Used with permission by Aviation Safety. (www.aviationsafetymagazine.com)

(b) Reprinted by permission from Springer Nature Customer Service Centre GmbH: Nature, Greer (2010), Copyright (2010).

Figure 1.1: Examples of severe icing on the propeller of a small aircraft (a) and rime ice accumulating on a tree (b).

dendrites is significantly faster than the progression of a freezing front at melting temperature (Schremb and Tropea, 2016). The rapid development of a framework of ice dendrites in the bulk favors the stabilization of the current shape of the liquid phase and the attachment of the fluid to the surface. Subsequently, the bulk is bound by complete solidification of the mixed phase leaving an adherent ice agglomeration.

The adhesive characteristics of water to numerous materials paired with its fast freezing dynamics in the supercooled state entail a rapid growth of conjoined ice layers on any affected surface. It is most severe if supercooled water is continuously supplied, e.g. in form of drops from precipitation or levitating in clouds. The ice accruing from supercooled drops can exhibit different forms depending on the prevailing conditions and the drop characteristics. The different types of icing are generally referred to as rime ice, glaze ice and mixed ice (Cao et al., 2018).

Rime ice develops from small supercooled drops ($\lesssim 100\,\mu\text{m}$) exhibiting low temperatures ($\lesssim -20\,°\text{C}$) which impact with low speed at a low rate. This way, the drops maintain a hemispherical shape upon impact and during solidification. The resulting ice layer is comparable to a packing of spheres with air in between which results in a soft texture. This kind of icing is often observed after mist loaded with supercooled drops passes over landscapes covering plants and buildings as for instance shown in Fig. 1.1b. Moreover, it occurs on aircraft, when they pass through clouds containing supercooled drops. The rime ice usually accumulates

(a) Rime ice

(b) Glace Ice

(c) Mixed ice

(d) Severe supercooled large drop ice
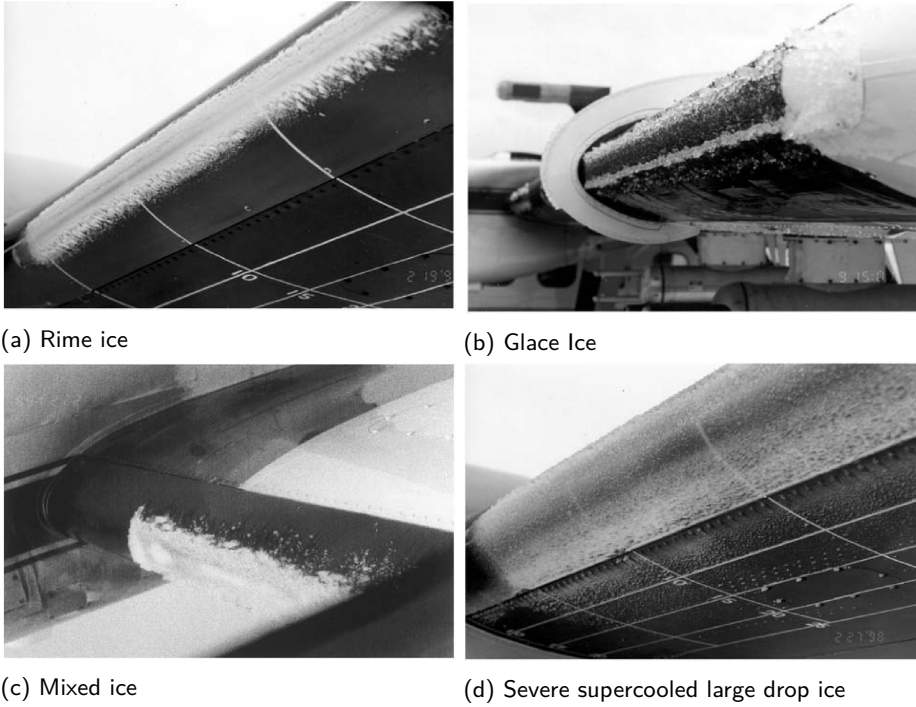
Figure 1.2: Different types of ice from supercooled drop impact on airfoils of a research aircraft of the NASA Glenn Research center. Reprinted from Politovich (2015), with permission from Elsevier.

at the leading edge of the wings as seen in Fig. 1.2a and for continuing growth it builds a spear like shape on the airfoil. For a change in impact speed, the drops no longer retain their spherical form and spread on the surface. Moreover, a higher temperature ($\gtrsim -10\,^\circ\mathrm{C}$) or higher impact frequency of drops further favor coalescence of the drops before solidification which results in a dense ice layer referred to as glace ice. This layer exhibits a smooth surface and is generally harder, adheres better to the affected surface and is more difficult to remove than rime ice. Typical shapes on airfoils feature two so called horns above and/or below the leading edge as seen in Fig. 1.2b. For severe loads of water, the ice accumulation possibly covers large parts of the airfoil even aft of the leading edge and significantly alter the apparent airfoil shape as shown in Fig. 1.2d. In mixed conditions, the differentiation of these two icing phenomena is not always selective and the accruing ice may exhibit aspects of both other types which is referred to as mixed ice (cf. Fig. 1.2c).

Accretion of ice on aircraft wings occurs when they pass through clouds in heights

between ca. 1200 m and 6700 m where they may be loaded with supercooled drops (Cao et al., 2018). The accumulating ice is a serious problem, since a change in airfoil shape possibly affects the lift and drag generated by the wing. In severe cases of icing, it can decrease the stall angle of attack as well as the lift and increase drag so drastically that the aircraft is no longer able to maintain its altitude (Cao et al., 2018). Ice accretion of this extent is usually formed by glaze ice since it forms more resistant geometries. However, even in less dangerous scenarios, icing of the wings may affect lift and drag significantly entailing an increase in fuel consumption which is aggravated by the additional weight of the ice. Furthermore, the maneuverability of the aircraft might be affected, for instance when ice covers slats and flaps of the wing. Moreover, ice accretion can cause problems on several other parts of the aircraft by further increasing drag or affecting the function of vital components like propeller (see Fig. 1.1a). If ice also covers the front window of a plane, the pilot has to completely rely on its instruments. However, in this case, it is likely that sensors like Pitot tubes and stall warning systems are also affected by icing which may entail falsified signals; with potentially severe consequences. Furthermore, ice accretion on various components possibly causes analog problems for different aircraft, e.g. the rotor blades of helicopters (Cao et al., 2018).
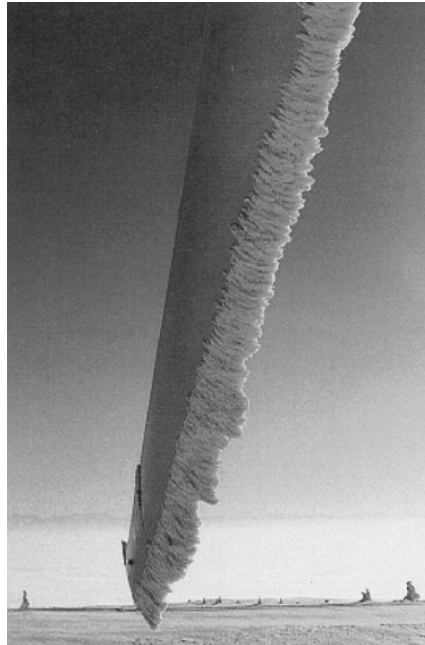
Figure 1.3: Wind turbine with ice accumulation on the leading edge of the turbine blades. Reprinted from Dalili et al. (2009), with permission from Elsevier.

Next to aircraft, icing is a hazard to wind turbines operated in cold environments when clouds or mist are passing. Similar to icing of airfoils, ice can accumulate on the leading edges of the turbine blade as seen in Fig. 1.3. While the corresponding alteration of the blade profile is usually not a severe safety issue for turbines, it can greatly reduce the efficiency of the turbine. Estimation of power losses exhibit a broad range from 0.005 to 50 % of the annual production depending on the frequency and severity of icing but also on the evaluation method of losses. Mechanical failures due to the additional weight of the ice are also possible which are sometimes only preventable by shutting down the wind turbines. The operation is then adjourned until the ice is removed resulting in long downtime. Moreover, sensors like wind speed anemometers affected by icing can send false signals which aggravate the wind turbine control (Parent and Ilinca, 2011). Other applications prone to icing in cold environments are overhead power lines (cf. Fig. 1.4). The additional weight of the ice can cause the lines to collapse and lead to power outages in the concerned region (Laforte et al., 1998). Besides the environmental conditions governing the growth of ice layers, the high electric fields have an influence on the nucleation probability of supercooled drops in contact with conductors which motivated scientific interest in this topic (Löwe et al., 2021). Whereas icing

Figure 1.4: Transmission line at Ålvikfjellet, Norway collapsed due to icing. Photo reprinted from Engdahl et al. (2020).

scenarios introduced so far arise due to clouds or precipitation in cold environments, icing may also occur independent from atmospheric phenomena. Ships travelling through the sea in cold climate experience icing from supercooled drops originating from sea spray. Usually the water load and drop sizes in this spray is significantly higher than from atmospheric droplets, yet considerable supercooling of the drops is less likely due to their salinity (Rashid et al., 2016). Nevertheless, icing from sea spray may entail severe icing of superstructures of ships as seen in Fig. 1.5. Such

a thick layer of ice on deck represents a threat to the crew members safety and prohibits undisturbed execution of numerous tasks as long as it remains on the ship.

Figure 1.5: Severe icing of cargo vessel superstructure from sea spray in the port of Quebec. Reprinted from Dehghani-Sanij et al. (2017), with permission from Elsevier.

In order to regain and maintain function of affected technical applications numerous approaches to remove the ice and prohibit new ice accretion were already developed. For aircraft, a treatment with chemicals melting any accumulated ice on the wings and other parts prior to lift-off is nowadays standard procedure at airports in regions with the risk of icing. However, the infrastructure associated with this method is costly and it only applies for aircraft already back on the ground. In order to reduce the risks of in-flight icing, large commercial aircraft usually have a heating system installed in the wings and other parts prone to icing. In case the aircraft experiences conditions with the risk of icing, the heating is turned on to prevent the freezing of adherent drops and melt ice already build up on the surface. Smaller airplanes sometimes possess so called de-icing boots on their wings which consist of an inflatable envelope. In case ice accumulates on the wing, it is chipped off by expansion of the boots. However, these solutions are not always able to completely prevent icing or remove the entire ice load and they increase the weight of the airplane which entails an increased fuel consumption (Cao et al., 2018). Approaches to passive ways of icing prevention usually involve coatings with icephobic properties but adequate solutions are still subject of current research (Eberle et al., 2014; Grizen et al., 2020).

Concepts of wind turbine de-icing are mostly based on the methods developed for aircraft, i.e. heating of blades or application of chemicals (Parent and Ilinca, 2011). While the heating entails the same weight issues as in aircraft, the application of chemicals represents a more challenging task due to the high altitudes of the turbine blades. While the conventional procedure requires the operation of a helicopter, newer approaches consider the service of a drone to reduce costs (Villeneuve et al., 2022). On power lines, de-icing is complicated due to the long range of affected

conductors. Approaches reach from thermal methods by temporarily increasing the current in the cables to icephobic coatings on the conductors exterior. However, most of these methods are either expensive, inefficient or not yet realizable (Laforte et al., 1998). De-icing of ship superstructures is mainly performed with chemicals, since thermal methods only qualify for local application. In the worst case, the removal of ice is achieved manually with handheld tools (Rashid et al., 2016).

All the approaches to remove and prevent icing would profit from a reliable prediction of the ice accretion occurring in conditions the corresponding applications are exposed to. Detailed knowledge of ice accretion patterns could enable adaptions of de-icing system components (e.g. locally focused heating) or appropriate placement of sensitive instruments (Pitot tubes, etc.), to locations less prone to icing. However, the examination of real icing scenarios is complicated since affected surfaces on aircraft and wind turbines are not easily reached and icing is usually avoided for safety reasons. Moreover, the lack of control over the prevailing conditions make reproducible scenarios unlikely. Large scale experiments imitating realistic icing conditions may offer better control of the surroundings but usually entail high costs of setup and operation. Hence, reliable numerical simulation of icing scenarios would help to predict icing patterns and develop adaptions to the corresponding application. Numerous approaches to simulate ice accretion, e.g. on aircraft wings, have been conducted so far, yet verification of the obtained icing geometries is often only possible in qualitative manner and in a narrow range of impact parameters (Cao et al., 2012). Moreover, the possibility to confirm validity of the models is limited since experimental data is still rare (C. Zhang et al., 2018). From the knowledge obtained about ice accretion so far, consensus has already been reached on the importance of the impact process of single supercooled drops and the related physics (Cao and Xin, 2020). However, the physical mechanisms governing this impact and the significant influences are not fully understood by now and uncertainties in its description scale to inaccuracy in large scale simulations.

Whereas it is evident that in most icing scenarios high impact velocities lead to a splashing of the drops, the influences on the extent of the splash and the entailed ejection of fluid remain unclear. The fluid mass deposited at the impact location (also sticking efficiency) is already identified as a crucial parameter (Baumert et al., 2018), yet its dependence on the general impact parameters of a single drop is elusive and numerical models often rely on statistical approaches (Moreira et al., 2010). Moreover, Brakel et al. (2007) point out that the heat transferred by the impact of a single drop is crucial for the development of an ice layer on airfoils. It is known that this heat flux between a drop and an impact surface is greatly dependent on the area wetted by a single drop after impact (Breitenbach et al., 2018). However, the development of drop spreading for an impact with high impact velocities in a surrounding cold air flow and a potential superimposed solidification is still vague. Additionally, the spreading and subsequent freezing particularly on an already existing ice layer is most likely a vital factor in the formation of the ice

layer roughness which influences the further ice layer growth (Steiner and Bansmer, 2016). The surface texture and the overall shape of the growing ice layer are potentially also dependent on the characteristics of a mixed ice-water phase as it arises, for instance, after the first solidification stage of supercooled water. However, the knowledge about this transient phase is scarce since it is eventually displaced by complete solidification. Thus, in order to improve numerical codes predicting ice accretion, the physics of a single supercooled drop impact and the influence of the surrounding environment is imperative. To contribute to a deeper understanding of these physics, generic experiments considering a single drop impacting on a cold surface with variable impact conditions and a superimposing air flow are conducted in the course of this dissertation.

1.2 Objectives and Outline of this Thesis

The current work is dedicated to gaining knowledge about the impact of supercooled drops as it occurs in different stages of an ice layer growing on a surface. With regard to icing scenarios of aircraft and wind turbines, the impact is superimposed by a cold air flow in the corresponding experiments. Focus is placed on three different scenarios in which the nucleation of the drop fluid occurs at different times of the impact.

First, the beginning of ice accretion on a dry cold surface is considered. In this case, the drops impact on a target free from ice in their supercooled liquid state with a considerable delay of nucleation. Upon impact, they develop a corona splash of which the extent and the ejected fluid mass are the central subject of investigations. Moreover, the influence of drop deformation caused by the superimposed air flow is examined. Second, an impact on a flat ice surface is analysed which resembles the impact of supercooled drops impacting on a surface already covered by ice from previous impacts. Focal point of this study is the spreading behaviour of the drop with regard to a fast onset of nucleation after first contact with the surface. Third, the impact of drops experiencing nucleation before impact is investigated. The nucleation during the descend towards the impact target enables the investigation of impact behaviour of a partially frozen drop and the properties of the mixed phase which arises after finalization of the first freezing stage. The major part of experiments is conducted in a custom icing wind tunnel which was designed, built and commissioned in the course of this dissertation. The drops impact in its test section, where a controlled variation of drop temperature, impact velocity and speed of the superimposing air flow is rendered possible for different drop sizes.

Leading to the discussion of these investigations, **Chapter 2** elucidates important knowledge gained so far on the impact of supercooled drops. Being a combination of two basic phenomena, the characteristics of a liquid drop impacting on a dry surface without solidification are depicted first. Subsequently, the general nature of the solidification process of supercooled water is described. Eventually,

insights regarding the interaction of fluid flow of a drop impact and solidification of supercooled drops gained from research so far are introduced. In the following **Chapter 3**, the installations and methods used for the execution of experiments and measurement of different parameters are presented. First, the custom icing wind tunnel and its capabilities are introduced along with a quantification of the prevailing flow profile in the test section. Moreover, additional installations used for further analysis of impact outcomes and supplementary experiments are illustrated. In **Chapter 4**, the results obtained from the experiments are presented and discussed. Starting with the latest occurrence of nucleation, the impact of a liquid drop on a dry cold surface is analysed. Subsequently, the findings obtained from an impact on a planar ice surface with its fast freezing onset are reviewed. At last, the knowledge gained on the impact of drops partially frozen before impact is elucidated. Ultimately, the results are concluded in **Chapter 5** and an outlook on remaining questions and possible experiments tying in with the current findings is given.

2 Theoretical Background and State of the Art

The impact of a single supercooled drop is a highly complex phenomenon combining physics of multiple disciplines. First, the characteristics of the fluid flow of an impacting drop and their dependence on exterior influences still remain an enigma under certain conditions. Second, the solidification of supercooled water with its statistical nature and the subsequent highly dynamic phase change in order to attain thermodynamic equilibrium still lacks a universal description. The combination of both problems is even more elusive, since the ice phase introduces dynamic changes in boundary conditions to the fluid flow of the impacting liquid drop and vice versa. This thesis aims to advance knowledge about different aspects of this phenomenon. In the present chapter, important known features of the fluid flow of a single drop impacting onto a solid surface are outlined. Subsequently, the solidification process is illuminated with focus on its temperature dependence and dynamic behaviour. Finally, an overview of recent findings about the combination of fluid flow and solidification during the impact of a single supercooled drop is given.

2.1 Characteristics of Drop Impact onto a Solid Surface

The well-known impact of a single drop onto a solid surface is a phenomenon encountered in numerous occasions in nature and technology. It has drawn attention to countless scientific investigations starting as early as the late 19th century (Worthington, 1876). Since then research dedicated to the impact of drops has come a long way, particularly favored by the development and widespread availability of high-speed video cameras (Josserand and Thoroddsen, 2016). Extensive reviews of the most important findings of drops impacting solid surfaces are found in Yarin (2006), Moreira et al. (2010), Josserand and Thoroddsen (2016), and Yarin et al. (2017).

Despite the multitude of studies conducted, numerous uncertainties remain in the description of the involved physics since a variety of involved solid, liquid and gaseous phases entail a broad spectrum of influencing parameters. Moreover, the short timescales on which the fluid movement occurs hinders the quantification of the corresponding effects. Hence, an exhaustive summary of all influences is

still missing; however, consensus has been reached about some parameters clearly affecting the behaviour of a drop impacting onto a solid surface. These comprise the drop geometry, represented by the initial drop diameter D_0, the drop impact velocity U_0 and fluid properties of the drop, namely the density ρ, the viscosity η and the surface tension σ (Josserand and Thoroddsen, 2016).

Usually, a combination of these parameters into dimensionless groups has proven useful in order to relate effects of multiple parameters (Yarin et al., 2017). The most common groups which are also used within the scope of this work are the Reynolds number Re defined by

$$\mathrm{Re} = \frac{\rho U_0 D_0}{\eta},\tag{2.1}$$

and the Weber number We as

$$\mathrm{We} = \frac{\rho U_0^2 D_0}{\sigma}.\tag{2.2}$$

The Reynolds and Weber number combine all of the above mentioned parameters and represent a relation of inertial force to either viscous forces or surface tension. However, some effects are independent of inertial forces and an additional group is considered that can also be derived from the Weber and the Reynolds number. The relation of viscous forces to surface tension forces results in an expression independent of the impact velocity U_0, which is known as the Ohnesorge number

$$\mathrm{Oh} = \frac{\sqrt{\mathrm{We}}}{\mathrm{Re}} = \frac{\eta}{\sqrt{D_0 \rho \sigma}}.\tag{2.3}$$

Moreover, for considerations of the flow inside of the drop in the vicinity of the fluid surface (e.g. dynamic wetting), the Capillary number Ca is often used, which is obtained from a balance of viscous drag forces and surface tension as

$$\mathrm{Ca} = \frac{\mathrm{We}}{\mathrm{Re}} = \frac{\eta U_0}{\sigma}.\tag{2.4}$$

Note that in several more recent studies focus is moved towards the flow in the vicinity of the drop boundary. Hence, dimensionless groups and quantities used in modelling approaches are at times obtained with the inverse curvature, i.e. the radius of the drop R_0. Therefore, it replaces the diameter $D_0 = 2R_0$ as a length scale in these approaches (Riboux and Gordillo, 2014). In the scope of the present work, different approaches using both scaling are used. In order to avoid confusion, groups scaled with R_0 are denoted with a subscript R (Re_R,We_R, etc.). Groups without a subscript are scaled with D_0 according to Eqs. (2.1) - (2.3).

Depending on the governing forces of the impact of a drop on a solid surface, the fluid behaviour can change significantly. The outcome of a single drop impact and the conditions under which it occurs has been motivation for diverse studies in

the past. Generally, a distinction is made between the entire bulk fluid remaining in contact with the surface (deposition) and fluid leaving the surface or the bulk during the impact process. The escape of fluid can occur partly at early impact stages (prompt splash), at later times (corona splash, partial rebound, receding breakup) or as a bulk at the end of the impact (complete rebound) (Yarin, 2006). The findings concerning two of these phenomena, namely deposition and splashing, provide valuable knowledge regarding the impact of a supercooled drop on a smooth surface discussed in the study at hand. First, the fluid movements occurring during deposition which represent the general bulk behaviour and can be found in all possible impact outcomes. Hence, insight into the velocity field in the drop upon impact also aids in understanding any other outcome. Second, the development of a splash which is observed in a majority of the investigated drop impacts of this study. A brief description of the theoretical background of the phenomena of deposition and splash, which are essential to discuss the results of this work, are elucidated in the following.

2.1.1 Characteristics of Drop Deposition on a Solid Surface
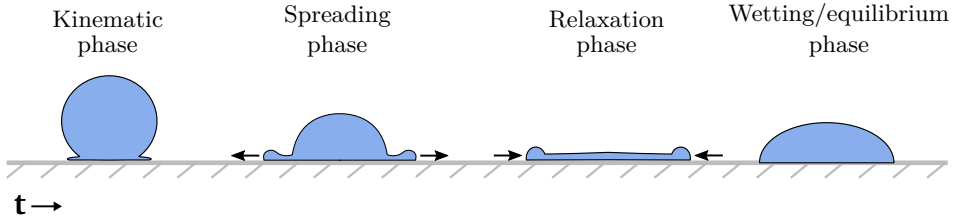
Figure 2.1: Consecutive stages of drop deposition during impact of a drop onto a dry solid substrate.

When a drop impacts on a solid surface with low impact energy, the drop spreads over the surface without developing a splash. In this case, the outcome is divided into four consecutive stages. With regard to a drop deposition which occurs for moderate Reynolds and Weber numbers, these stages are distinctly separable as shown in Fig. 2.1. In the first phase, the fluid at the drop front displaced by the solid surface spreads radially from the impact point. However, the majority of the fluid still maintains its downward velocity due to inertia. Hence, this stage is referred to as the kinematic phase. In the subsequent spreading phase, the fluid continues its radial spreading in a thin film, yet at the outer circumference it agglomerates into a rim. As soon as the decreasing inertial forces are overcome by surface tension and viscous drag, the drop stops spreading and starts receding towards its center in a relaxation phase. This phase continues until the drop fluid reaches an equilibrium shape which is dictated by the wetting characteristics of the fluid/surface combination. The four stages are also visible from an evolution of

the contact area of fluid and surface with continuing time of impact t. The region is approximately circular and represented by its instantaneous diameter $D(t)$. The qualitative progression of the spreading factor $S(\bar{t}) = D(\bar{t})/D_0$ with dimensionless time $\bar{t} = tD_0/U_0$ for arbitrary drop impact events is shown in Fig. 2.2 (Rioboo et al., 2002). The lowest dashed line represents a drop deposition including a receding phase as shown in Fig. 2.1. The other curves correspond to deposition with subsequent wetting (solid line) and no receding (dotted line). While in the last three stages distinct differences of the evolution of spreading factors are noticeable, the spreading factor evolves equally during the kinematic phase for all depicted cases. Thus, the evolution during this phase is crucial for every impact outcome of drops impacting on a solid surface.

The temporal evolution of the spreading during this stage is well approximated
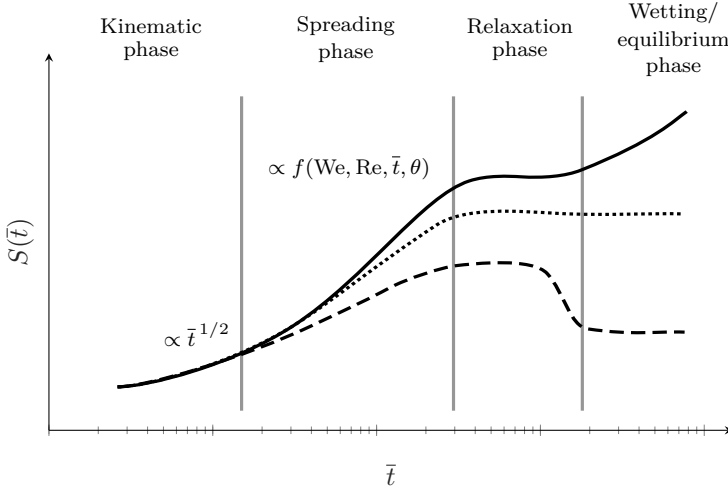
Figure 2.2: Consecutive stage of drop impact onto a solid surface with respect to the qualitative evolution of the spreading factor $D(t)/D_0$. Figure reproduced from Rioboo et al. (2002).

by the intersection of a sphere with a horizontal plane as introduced by Rioboo et al. (2002). Assuming a constant velocity of the sphere, the intersection area evolves proportional to the square root of time ($S(t) \propto \sqrt{t}$ for $t \ll 1$). Considering the spreading as equally axisymmetric, the evolution of the wetted area can also be expressed in terms of the wetting radius r. In this case, the spreading in the kinematic phase is described by

$$\bar{r} = b_0\sqrt{\bar{t}_R}. \tag{2.5}$$

Here, $\bar{r} = r/R_0$ represents the dimensionless spreading radius, $\bar{t}_R$ denotes the dimensionless time scaled with R_0 and b_0 is a proportionality constant. From the parameters incorporated in Eq. (2.5) it is evident that only the initial geometry of the drop represented by R_0 and the impact velocity U_0 affect the spreading in the first moments of impact. The qualitative description of this increase of the radius evolution has been successfully used in several attempts to describe the flow in the kinematic phase (Yarin et al., 2017). For a quantitative prediction of r, a value for the proportionality constant b is necessary. However, different approaches led to diverging values. On the one hand, Rioboo et al. (2002) suggest a constant value of $b_0 = 2.05$ for the impact of spherical drops. – Note that the original value given in their work is obtained with a scaling using D_0, which requires a conversion of the value with the factor $1/\sqrt{2}$ in order to use it with Eq. (2.5).– On the other hand, more recent studies suggest that b_0 is not a constant but depends on the deformation of the drop (Courbin et al., 2009; Q. Liu et al., 2021). Moreover, the effect of drop deformation on b_0 is also part of the findings of this work discussed in 4.1.1.

After the kinematic phase, the fluid continues its expansion in the spreading phase. This phase is governed by viscous forces and surface tension acting against the remaining inertia, which entails a more complex fluid flow. While the flow in the vicinity of the forming rim still eludes an analytical description, the flow in the spreading lamella far from the edge was described by Roisman et al. (2009b). Its description of the lamella flow is used in approaches to interpret the results obtained in Sec. 4.1 and 4.2 and a detailed description is given in the following.

Based on a quasi-two-dimensional approach for thin films of Yarin and Weiss (1995) and the associated self similar solution, an approximate description of the
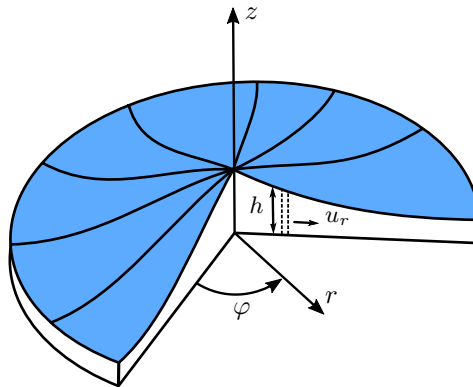
Figure 2.3: Sketch of lamella spreading on a solid surface adapted from Roisman (2009a).

velocity field in the developing lamella was derived. For this purpose, Roisman et al. (2009b) considered the lamella in a cylindrical coordinate system with its origin in the center, as sketched in Fig. 2.3. The motion of the sheet is represented by the radial velocity $u_r(r,t)$ which is averaged over a sheet cross section element of height $h(r,t)$ as illustrated with the dashed line in Fig. 2.3. The mass balance is derived for the volume change of the sheet element due to the flux gradient in radial direction yielding

$$\frac{\partial rh}{\partial t} = -\frac{\partial rhu_r}{\partial r}. \tag{2.6}$$

The momentum balance regarding the sheet element is obtained with consideration of the internal stresses $\sigma_{rr}, \sigma_{\varphi\varphi}$ and the capillary pressure applied to the upper free surface p_σ as

$$\rho\frac{\partial rhu_r}{\partial t} + \rho\frac{\partial rhu_r^2}{\partial r} = \frac{\partial rh\sigma_{rr}}{\partial r} - h\sigma_{\varphi\varphi} + p_\sigma r\frac{\partial h}{\partial r}. \tag{2.7}$$

Here, the internal stresses are given by $\sigma_{rr}(p_\sigma, u_r, r)$ and $\sigma_{\varphi\varphi}(p_\sigma, u_r, r)$ and the capillary pressure is approximated by a long wave approximation of the Young-Laplace equation as $p_\sigma(r,h)$ (Roisman, 2009a). Incorporating these stresses into Eq. (2.7) along with Eq. (2.6) a momentum balance equation in explicit form is obtained. In a dimensionless consideration for high Reynolds and Weber numbers it can be further linearized assuming a small gradient of the film thickness $h^{-1}\partial h/\partial r \ll 1$ which provides

$$\frac{\partial \overline{u}_r}{\partial \overline{t}} + \overline{u}_r\frac{\partial \overline{u}_r}{\partial \overline{r}} \approx \frac{4}{\mathrm{Re}}\frac{\partial}{\partial \overline{r}}\left[\frac{1}{\overline{r}}\frac{\partial \overline{r}\,\overline{u}_r}{\partial \overline{r}}\right], \tag{2.8}$$

where all lengths are scaled according to $\overline{r} = r/D_0$, time is scaled with $\overline{t} = tU_0/D_0$ and velocities are scaled $\overline{u}_r = u_r/U_0$. The dimensionless axial velocity $\overline{u}_z$ is obtained from the continuity equation. For the axisymmetric incompressible lamella flow it reduces to

$$\frac{\partial \overline{r}\,\overline{u}_z}{\partial \overline{z}} + \frac{\partial \overline{r}\,\overline{u}_r}{\partial \overline{r}} = 0. \tag{2.9}$$

Thus, the velocity field of the spreading lamella results from a solution of Eqs. (2.8) and (2.9) as

$$\overline{u}_r = \frac{\overline{r}}{\overline{t}+\tau}, \qquad \overline{u}_z = -\frac{2\overline{z}}{\overline{t}+\tau}, \tag{2.10}$$

where $\tau \approx 0.25$ is a constant determined by Roisman (2009a). From the axial velocity, the remote asymptotic solution of Yarin and Weiss (1995) for the thickness of the lamella can be obtained with $\partial \overline{h}/\partial \overline{t} = \overline{u}_z(\overline{h}) = -2\overline{h}/(\overline{t}+\tau)$ as

$$\overline{h} = \frac{C}{(\overline{t}+\tau)^2}, \tag{2.11}$$

where C is a constant. Note that this solution is only valid far from the rim forming on the outer edge of the spreading drop.

The velocity field given by Eq. (2.10) provides a good description of the flow from times $\bar{t} \approx 0.5$. However, with successive spreading of the lamella a boundary layer develops inside of the fluid from the surface upwards as sketched in Fig. 2.4 (Roisman, 2009a). As the lamella thickness h approaches the boundary layer
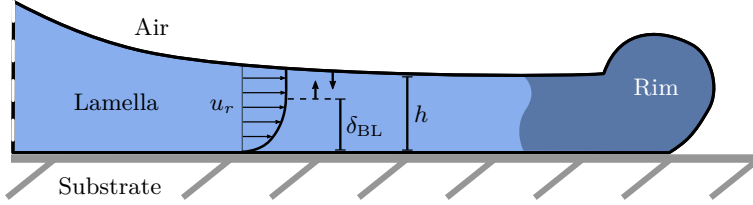
Figure 2.4: Sketch of the viscous boundary layer flow developing during spreading of the lamella after drop impact.

thickness δ_{BL} the velocity field can be described as progressively damped. For distances from the surface distinctly exceeding δ_{BL}, the remote asymptotic solution for the axial velocity can be extended yielding

$$u_{z,\mathrm{BL}} = -\frac{2z}{t} + 2\gamma_{\mathrm{BL}}\sqrt{\frac{\nu}{t}} \quad \text{at} \quad z > \delta_{\mathrm{BL}}, \tag{2.12}$$

where $\nu = \eta/\rho$ is the kinematic viscosity and $\gamma_{\mathrm{BL}} \approx 0.6$ is a constant determined numerically (Roisman, 2009a). Note that this estimation neglects τ from Eq. (2.11) since the flow description considers long times after the flow initiation ($\bar{t} \gg \tau$). From the velocity, a differential equation for the lamella thickness can be directly derived as

$$\dot{h} = -\frac{2h}{t} + 2\gamma_{\mathrm{BL}}\sqrt{\frac{\nu}{t}} \quad \text{at} \quad h > \delta_{\mathrm{BL}}, \tag{2.13}$$

where the dot denotes the derivative with respect to t, i.e. $\dot{h} = \partial h/\partial t$. The solution of Eq. (2.13) consists of an inviscid part h_{inv} which resembles Eq. (2.11) and a viscous thickness increment h_ν (Roisman, 2009a). Thus, the lamella thickness far from the surface evolves according to its dimensionless form

$$\bar{h} = \bar{h}_{\mathrm{inv}} + \bar{h}_\nu, \quad \bar{h}_{\mathrm{inv}} = \frac{\mu}{\bar{t}^2}, \quad \bar{h}_\nu = \frac{4\gamma}{5}\sqrt{\frac{\bar{t}}{\mathrm{Re}}}. \tag{2.14}$$

Here, μ is a constant obtained from numerical simulations and given with $\mu \approx 0.39$ (Roisman, 2009a).

When the boundary layer attains the free surface of the lamella at $t = t_{\mathrm{BL}}$, the flow is mainly governed by viscosity. Hence, for times $t > t_{\mathrm{BL}}$ Eq. (2.14) is no longer valid. A condition providing t_{BL} is obtained from the approximate growth of the boundary layer $\bar{h}_{\mathrm{BL}} = 1.88(\bar{t}/\mathrm{Re})^{1/2}$, i.e. $\bar{h}_{\mathrm{BL}}(\bar{t} = \bar{t}_{\mathrm{BL}}) = \bar{h}$ as suggested by Roisman (2009a). Additionally, he provides an estimation for the height evolution of the lamella after drop impact on a flat surface as

$$\ddot{\bar{h}} - \frac{9}{5}\frac{\dot{\bar{h}}^2}{\bar{h}} + \frac{3}{\mathrm{Re}}\frac{\dot{\bar{h}}}{\bar{h}^2} = 0, \tag{2.15}$$

where the first two terms are associated with inertial forces and the last term accounts for the viscous effects. The solution provided by Eq. (2.15) depends on the Reynolds number, the lamella thickness $\bar{h}_{\mathrm{BL}}$ and axial velocity $\bar{U}_{\mathrm{BL}}$ achieved at $\bar{t} = \bar{t}_{\mathrm{BL}}$. For long times, it strives for a constant value which corresponds to the minimum lamella thickness h_{res}. Approximating the initial conditions with the help of Eq. (2.14), the dimensionless residual lamella thickness is obtained with

$$\bar{h}_{\mathrm{res}} = 0.79\mathrm{Re}^{-2/5}. \tag{2.16}$$

Once the residual lamella height is reached, the spreading will quickly cease, which marks the end of the second impact phase. A particular interesting quantity at this moment is the maximum spreading diameter D_{max} of the fluid on the surface, since it represents a starting point for all fluid movement in the following phases. Empirical correlations using dimensionless numbers were for instance found by Scheller and Bousfield (1995) and Clanet et al. (2004). A short review of different approaches is also found in Breitenbach et al. (2018). A semi-empirical approach was introduced in Roisman (2009a) taking into account the flow of the lamella introduced above.

For high Reynolds and Weber numbers ($\mathrm{Re} \gg 10^2, \mathrm{We} \gg 10$), he roughly approximates the maximum extension, assuming that the fluid exhibits the shape of a thin disc in the moment of maximum spreading. With the residual lamella thickness h_{res} from Eq. (2.16), the maximum spreading is estimated as

$$\frac{D_{\mathrm{max,upper}}}{D_0} \propto \sqrt{\frac{2}{3h_{\mathrm{res}}}} = 0.92\mathrm{Re}^{1/5}. \tag{2.17}$$

However, this approach disregards the formation of the rim on the outer edge of the drop which contains a significant amount of the fluid volume. Hence, Roisman (2009a) took the typical length scale associated with the rim

$$L_{\mathrm{rim}} \propto t_{\mathrm{BL}}\mathrm{We}^{-1/2}h_{\mathrm{res}}^{-1/2} = 0.61\mathrm{Re}^{2/5}\mathrm{We}^{-1/2} \tag{2.18}$$

into account. For larger values of L_{rim}, more fluid is involved in the formation of the rim, which implies a decrease of the maximum spreading S_{max} estimated by Eq. (2.17). Hence, the maximum spreading diameter is obtained by a combination

of Eq. (2.17) and Eq. (2.18), yielding the semi-empirical correlation

$$S_{\max} = \frac{D_{\max}}{D_0} \approx C_1 \mathrm{Re}^{1/5} - C_2 \mathrm{Re}^{2/5} \mathrm{We}^{-1/2}. \qquad (2.19)$$

The constants C_1 and C_2 have to be determined from a fit to experimental data. Roisman (2009a) suggests values of $C_1 = 0.87$ and $C_2 = 0.4$, which exhibit good agreement with experimental data of drop impacts onto partially wetting surfaces. For superhydrophobic surfaces, Butt et al. (2014) suggests to adjust the value linked to the rim length scale as $C_2 = 0.48$, which underlines the significance of the wetting properties in formation of the rim. The wetting behaviour is governed by surface tension of the fluid and represented for instance by the contact angle. It dictates fluid motion and remaining shape in the last two impact stages which will, however, not be further discussed within the scope of the present study.

The flow developing during the deposition of a drop is characteristic for most phenomena observed when a drop impacts a solid surface. Furthermore, it helps in understanding the momentary conditions in which the fluid is exposed to significant additional forces leading to a divergence from the flow of a depositing drop. The earliest possible deviation from deposition involves fluid leaving the surface during a splash. The conditions in which splashing occurs along with approaches to physical models describing the splash onset are elucidated in the following section.

2.1.2 Development and Threshold of Splashing Upon Impact onto a Solid Surface

A drop impacting onto the surface with high impact energy possibly develops a splash. The reduction of fluid remaining on the surface and the ejection of fluid in form of secondary drops as sketched in Fig. 2.5 entail crucial changes in fluid distribution and its deposition on the surface. Hence, the development of splashing
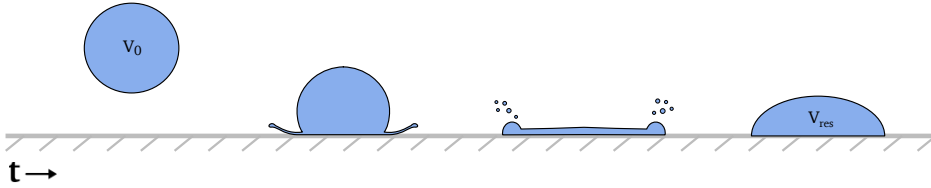
Figure 2.5: Sketch of a drop developing a splash upon impact on a dry solid surface. V_0 represents the initial volume of the drop and V_{res} the reduced remaining volume after the splash.

and the conditions in which it occurs have been extensively studied in the recent past (Moreira et al., 2010; Josserand and Thoroddsen, 2016; Yarin et al., 2017). However, the short time and length scales involved in the development of the splash along with chaotic fluid behaviour during the breakup process complicate a detailed experimental study of the fluid flow and the involved physics. In order to predict the occurrence of splashing, numerous studies primarily focused on the influencing parameters and the corresponding limits for the development of a splash.

Early on, a high impact velocity and drop size representing the inertial forces have been identified as crucial for the development of a splash. Furthermore, the fluid properties play an important role as they incorporate viscous forces and surface tension. Usually these parameters are accounted for by dimensionless groups (Re, We, etc.) that describe thresholds for splashing as already suggested by Stow and Hadfield (1981). The relation of all involved forces has been adapted and incorporated into the well-known K-number of Mundo et al. (1995). However, numerous modifications of this number for different experimental studies have suggested that some influences are still missing. For instance, Stow and Hadfield (1981) already considered a significant effect of the surface roughness. This effect was investigated in more detail by Roisman et al. (2015b) who were able to quantify a threshold for a range of different values of roughness. Moreover, in the scope of this work, Roisman et al. (2015b) was able to gather data of multiple experimental studies on drop impact onto a dry surface and their impact outcomes regardless of

the surface roughness. Next to the differentiation between deposition and splashing, the outcomes are further partitioned into two different types of splashing usually referred to as prompt splash (a) and corona splash (b) as shown in Fig. 2.6.

During a prompt splash, the secondary drops leave the fluid shortly after first contact with the surface. The separation of secondary droplets is most likely attributed to instabilities in the fluid film spreading on the surface and their size scales with Re and D_0 ($D_{2nd} \propto D_0 Re^{-1/2}$). However, their onset and physical cause have not yet been understood reliably. Among others, approaches to an explanation involve air entrapment under the spreading fluid (Rein and Delplanque, 2008) or instabilities in the neck of the spreading drop leading to finger like jets and their breakup (Thoroddsen et al., 2012). In any case, the remaining fluid spreads seemingly undisturbed on the surface similar to deposition as seen in Fig. 2.6a. However, under certain conditions, the spreading lamella stays intact through the first moments of spreading and lifts from the surface in a continuous liquid sheet as shown in Fig. 2.6b. Subsequently, this thin film breaks up into secondary drops the size of which is in the order of the rim forming at the outer edge of the film (Roisman et al., 2007). For the differentiation of deposition, prompt and corona splash Roisman et al. (2015b) derived two empirical thresholds for data they gathered from multiple studies. Fig. 2.7 shows a collated map and the corresponding thresholds. For lower Reynolds numbers, deposition and splash regime are well defined by an implicit threshold using the Capillary number and the Ohnesorge number $Ca_{cr} = 0.0067 + 0.6Oh^{0.15}$. For higher Re, the boundary
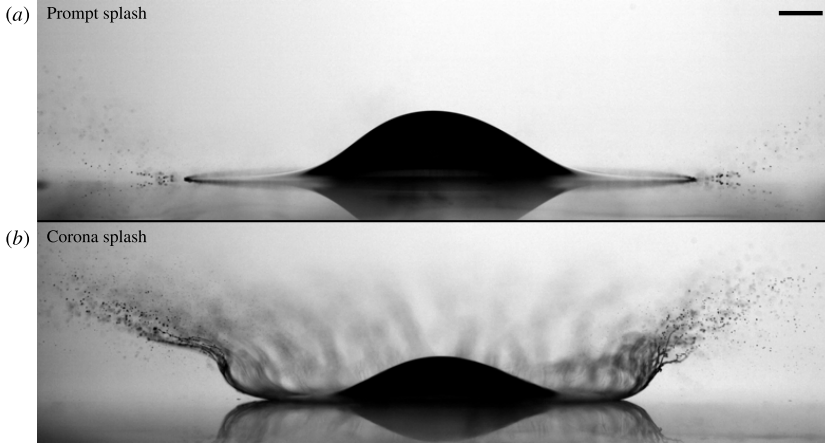
Figure 2.6: Images of prompt splash (a) and corona splash (b) developing upon impact on a dry smooth surface. The scalebar in the top right corner represents $500\mu m$. Figure reprinted from Burzynski et al. (2020).
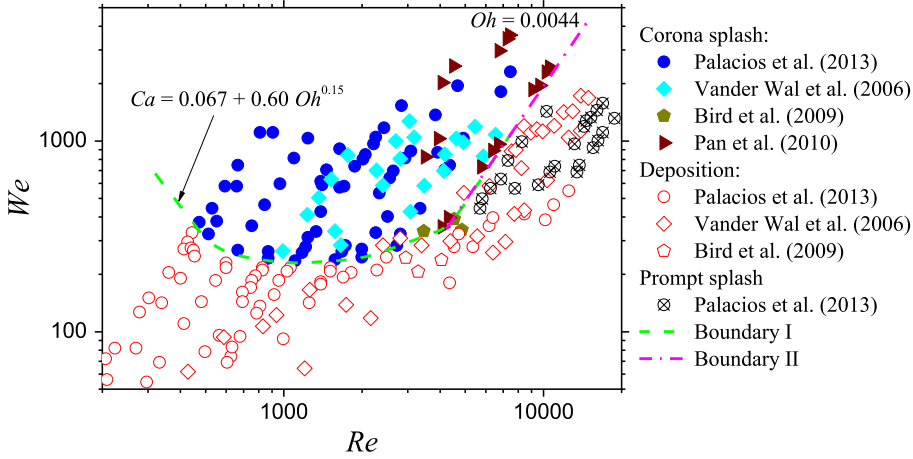
Figure 2.7: Map with splashing thresholds based on multiple experimental studies considering drop impact on dry smooth surfaces at an ambient pressure of $p = 1\text{bar}$. Boundary I confines deposition and corona splash, Boundary II separates corona splash from prompt splash/deposition. Reprinted from Roisman et al. (2015b) with permission from Elsevier.

between splashing and deposition is not distinct. Nevertheless, two regimes are clearly separable when considering the different splashing types. Regardless of the uncertain physical dynamics causing each type, Roisman et al. (2015b) were able to find a simple condition to separate both splashing regimes using a constant critical Ohnesorge number yielding

$$\text{Oh}_{\text{cr}} = 0.0044. \tag{2.20}$$

This boundary is also indicated with a purple dashed line in Fig. 2.7. Hence, for Oh > 0.0044 a corona splash will develop and for lower values either prompt splash or deposition are expected. Note that the experiments considered in the map represent merely drops impacting on a smooth dry surface, e.g. glass, at an ambient pressure of $p = 1\text{bar}$. Hence, Eq. (2.20) is possibly not valid for rougher or more complex surfaces. However, it is worth mentioning that on a smooth surface the development of a prompt or a corona splash is apparently independent of the impact velocity and only determined by the drop size and the fluid properties.

Despite the good agreement of these empirical approaches with experimental data, the primary cause of splashing including their general explanation remain unclear. In search for more physical approaches to predict splashing, the role of the surrounding gas came into focus. Whereas it was often neglected in the empirical correlations using Re, We etc., at the latest with the work of Xu et al. (2005) its significance became evident. In their work, they were able to completely suppress

the splashing phenomenon by decreasing the ambient pressure, suggesting a vital influence of the surrounding air. This effect was confirmed by Stevens et al. (2014) for high and low viscosity fluids. An approach taking into account the surrounding air dynamics and its properties in order to model the uplift of the lamella in a corona splash was derived by Riboux and Gordillo (2014). Due to the relevance of this model to the present work, it will be introduced in detail in the following [1].

The theory of Riboux and Gordillo (2014) considers the corona propagation during drop impact onto a dry smooth substrate as governed mainly by the inertia of the flow in the lamella, surface tension and aerodynamic effects which act on the propagation of the contact line. This propagation is described using the dimensionless parameter β, defined in their work as the ratio of the aerodynamic lift force acting on the spreading lamella to the surface tension force. A critical value $\beta^\star \simeq 0.14$ is given as the splashing threshold. This value represents a scenario in which the front of the spreading lamella spreads faster than the liquid succeeding from the neck of the impacting drop. The arising aerodynamic lift-force initiates the lamella lift-off for a sufficient velocity difference. This scenario occurs if the impact parameters satisfy the condition $\beta > \beta^\star$; thus, a splash develops.
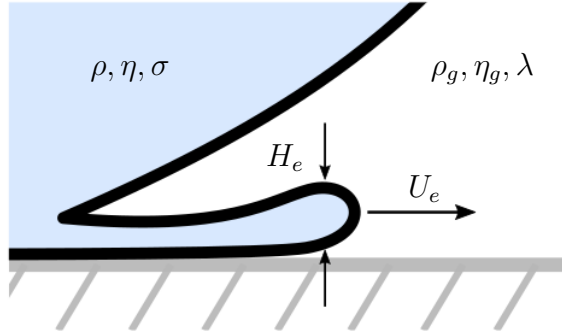
Figure 2.8: Lamella height H_e and velocity U_e in moment of lift-off $t = t_e$ used to determine β (Gloerfeld et al., 2021).

In order to calculate β, the instant t_e at which the lamella starts to lift from the surface is required. The fluid and gas properties and the dimensions of the lamella considered in the model at $t = t_e$ are outlined in Fig. 2.8. To determine the dimensionless value of $\bar{t}_{e,R} = t_e U_0 / R_0$, Riboux and Gordillo (2014) derive a relation of the deceleration from viscous forces and capillary pressure in the lamella front with the acceleration of fluid pushed into the lamella from the neck of the impacting drop. The result is an implicit correlation for $\bar{t}_{e,R}$ with regard to the

---

[1]The following remarks on the model of Riboux and Gordillo (2014) are based on the description given in Gloerfeld et al. (2021) which was published in the course of this dissertation.

impact conditions represented by Re_R and Oh_R according to

$$\frac{\sqrt{3}}{2}\mathrm{Re}_R^{-1}\bar{t}_{e,R}^{-1/2} + \mathrm{Re}_R^{-2}\mathrm{Oh}_R^{-2} = 1.21\bar{t}_{e,R}^{3/2}. \qquad (2.21)$$

Here, Re_R and Oh_R refer to the dimensionless Reynolds and Ohnesorge number, respectively, using R_0 as the characteristic length scale. With knowledge of $\bar{t}_{e,R}$, the lamella thickness H_e and its velocity U_e in the moment of lamella lift-off can be determined. The latter is estimated from the spreading evolution during the kinematic spreading phase similar to the above described estimation of Rioboo et al. (2002). The velocity at the instant of lamella lift-off yields

$$U_e = \frac{\sqrt{3}U_0}{2}\bar{t}_{e,R}^{-1/2}. \qquad (2.22)$$

Considering the momentum flux of fluid from the neck of the drop impact to the front of the lamella, the leading edge thickness is determined as

$$H_e = \frac{\sqrt{12}R_0}{\pi}\,\bar{t}_{e,R}^{\,3/2}. \qquad (2.23)$$

Knowing the geometry and velocity at t_e, the parameter β is obtained from the relation of the lift force and the surface tension acting on the lamella as

$$\beta = \sqrt{\frac{K_l\eta_g U_e + K_u\rho_g U_e^2 H_e}{2\sigma}} \qquad (2.24)$$

with η_g and ρ_g being the surrounding gas dynamic viscosity and density, respectively.

The parameters K_l and K_u are dimensionless coefficients scaling the forces contributing to the vertical force lifting the lamella. According to Riboux and Gordillo (2014), the lift force arising from the air flow around the lamella front is $\propto \rho_g U_e^2 H_e$ but also depends on the shape of the lamella front edge. In a numerical simulation they determined the proportionality factor to be $K_u \simeq 0.3$ over a wide range of Reynolds numbers. Furthermore, the force arising from the air flow between surface and lifted lamella is $\propto \eta_g U_e$ and also depends on the mean free path of the gas molecules λ and H_e which contribute to a factor K_l. It is estimated using the relation

$$K_l \simeq -2[\ln(19.2\lambda/H_e) - \ln(1 + 19.2\lambda/H_e)]. \qquad (2.25)$$

A detailed derivation of both factors is found in Riboux and Gordillo (2014). However, note that Eqs. (2.23) and (2.25) are taken from the erratum published to Riboux and Gordillo (2014).

With the determination of β, Riboux and Gordillo (2014) were able to confirm their splashing threshold value for various experimental data sets. However, the physical dynamics considered in this model suggest that it includes effects which

are not only vital for the onset of splashing but also influence the extent of a splash. A dependence of the deposited mass of a drop developing a splash upon impact was for instance confirmed in Burzynski et al. (2020). A discussion of the correlation of splashing characteristics with β is also found in Sec. 4.1 of this thesis.

As outlined in this chapter, the developing flow upon deposition or splashing of a drop is significantly affected by the fluid properties. The supercooled water in focus of this thesis shows significant divergence in its properties from water at room temperature. In an impact of a supercooled drop, the developing flow possibly overlaps with solidification at any moment of the impact which introduces a complex interaction of the flow with the freezing fluid. In order to illuminate the peculiarities in water properties and the behaviour in case of freezing, the following chapter outlines important characteristics of supercooled water with specific focus on the solidification process.

2.2 Properties and Solidification of Supercooled Water

As widely known, water is capable of showing extraordinary properties in manifold ways. Already under normal conditions water mostly represents the exception rather than the rule in comparison to other fluids (e.g density, heat capacity, etc.). This abnormality becomes even more remarkable when water is brought into conditions below its equilibrium freezing temperature (Debendetti, 2003). In a sub-freezing environment water can enter a meta-stable state in which it remains in a liquid phase.

In this stage, a significant change of fluid properties occurs which strongly depends on the water temperature. Regarding the interaction of this supercooled liquid in any dynamic scenario in which the solidification is pending, e.g. the impact of a supercooled drop on a surface, the effect of this property alteration has to be considered. Hence, the beginning of this chapter will elucidate important fluid properties and their dependence on fluid temperature.

The water possibly leaves its meta-stable state at any time if a trigger event causes sudden solidification of the fluid leading to a phase change (Franks, 1982). The freezing of the water clearly represents an even more vital intervention to any ongoing fluid movement. Since the solidification always begins on a molecular level, its onset is subject to stochastic events. Moreover, once it begins, the freezing process of supercooled water is characterised by two consecutive stages. The first involves a fast propagation of ice dendrites in the bulk liquid which bear the potential to interfere with any current fluid flow. The second stage is comparably slow yet is responsible for solidification of the greater part of the bulk liquid in most scenarios (Schremb and Tropea, 2016; Schremb et al., 2017d). The development of the solidification process in water is greatly dependent on the conditions of the meta-stable state it emerges from. In order to receive an impression of the affecting

parameters and the development of this freezing process, important characteristics of the freezing of supercooled water are presented in this chapter after a brief introduction of important liquid water properties in the sub-freezing environment.

2.2.1 Properties of Liquid Water in the Supercooled State

The thermodynamic properties of water have fascinated scientists for a long time, not only due to the ubiquity of water but also because they stand out in comparison to other fluids (Debendetti, 2003). While the reason for the peculiar behaviour of water is still not comprehensively clarified, the quantification of its properties covers a wide range of conditions with regard to temperature and pressure. Thanks to an increased interest into the meta-stable state of water and newly developed measurement methods, this range now also includes a considerable scope of the subzero conditions for which supercooled water occurs (Holten et al., 2012). Concerning the scope of this work, the dependence of these properties with regard to temperature under atmospheric conditions is particularly relevant.
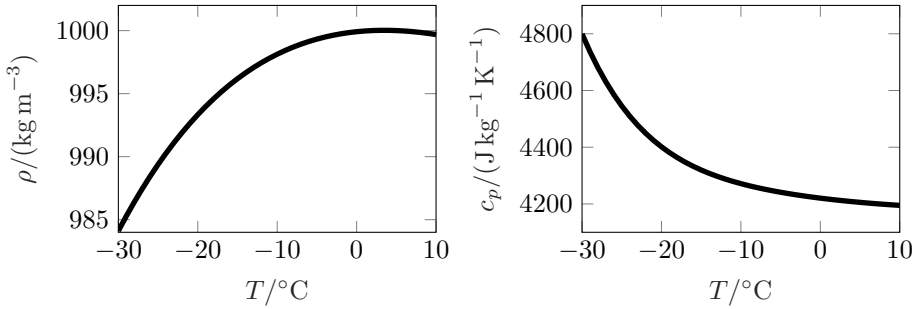
Figure 2.9: Values of density ρ (left) and isobaric heat capacity c_p (right) of supercooled water in atmospheric conditions $p = 1\,\mathrm{bar}$. The displayed curves are based on data obtained from VDI and GVC (2006).

As is widely known, water exhibits its maximum density in atmospheric conditions for a temperature of $T = 4°\,\mathrm{C}$ and exhibits a monotonic decrease for higher and lower temperatures (cf. Fig. 2.9 (left)). For temperatures lower than the melting temperature of water $T_m = 0\,°\mathrm{C}$ (at $p = 1\,\mathrm{bar}$) a decreasing trend is visible as well, although it exhibits a slightly steeper slope than in the region $T > 4°\,\mathrm{C}$. In theory, this trend continues for supercooling $\Delta T = T_m - T$ down to the highest possible supercooling of $\Delta T_{\max} \approx 40K$. However, this point is not easily achieved nor is the measurement of quantities for this temperature (Holten et al., 2012). Hence, in Fig. 2.9 (left) the density is displayed only down to $T = -30°\,\mathrm{C}$ which includes all relevant supercoolings ΔT of this thesis. For the same reason, all following properties are only depicted in the same temperature range. At $T \approx -30°\,\mathrm{C}$ the

liquid water density still exhibits 98.5% of its maximum value; thus, a temperature induced change in density will most likely have no crucial influence on the fluid flow of drop impact in the considered temperature range. In contrast, the isobaric heat capacity c_p experiences a significant rise for increased ΔT. Whereas values near $\Delta T_{\max}$ are yet to be measured, an increase of 13.8% is quantified when decreasing the temperature to $\Delta T = 30\,\mathrm{K}$ which is illustrated in Fig. 2.9 (right) (VDI and GVC, 2006). It is worth mentioning that the isochoric heat capacity c_v does not show a similar increase for the supercooling regime. However, available data regarding c_v for supercooled water is rare and its propagation is mostly based on theoretical models (Holten et al., 2012).

Another property of supercooled water greatly affected by decreasing temperatures
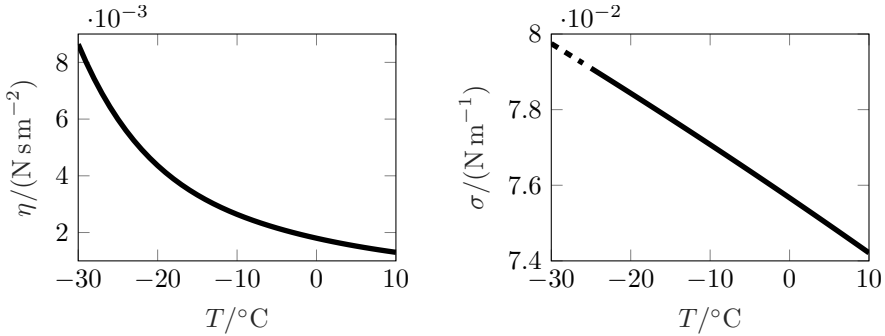
Figure 2.10: Values of dynamic viscosity η (left) and surface tension σ (right) of supercooled water at atmospheric conditions $p = 1\mathrm{bar}$. The displayed curve for η is based on data obtained from VDI and GVC (2006), the propagation of σ is based on measurements of Vinš et al. (2015).

is the dynamic viscosity η. As shown in Fig. 2.10 (left) it increases to 480% of its value at melting temperature for a difference of $\Delta T = 30\,\mathrm{K}$. Considering the relevance of viscosity to the fluid flow of an impacting drop as described in Sec. 2.1, this variation in viscosity represents a crucial influence on the impact of a supercooled drop. Although the growth almost resembles an exponential increase, the variation in viscosity is already significant for small supercooling temperatures, e.g. $\eta(T = -10\,^{\circ}\mathrm{C})/\eta(T = T_m) = 1.47$. A further important property for the fluid flow of drops impacting on a surface is the surface tension σ. As shown in Fig. 2.10, it increases monotonically with decreasing temperatures for water-air interfaces. However, in the considered range of supercooling, it increases only by 4.5%. Hence, a temperature related change in surface tension will most likely have no deciding effect on fluid flows in the supercooling range considered in this thesis. Note that the data for σ obtained by Vinš et al. (2015) covers only temperatures down to $T = -25^{\circ}\,\mathrm{C}$. They suggest that no anomalies for surface tension outside of this range are expected and it can most likely be extrapolated according to

the illustrated trend which is indicated by the dashed line starting at $-25°$ C in Fig. 2.10. The disproportionate change in properties in the supercooling regime in comparison to values above $0\,°\text{C}$ also concern further parameters, for instance the isothermal compressibility, the thermal expansion coefficient, etc. More detailed analysis of these parameters are found for instance in Debendetti (2003) and Holten et al. (2012).

The introduced temperature dependence of parameters is only valid as long as the water remains in a liquid state. However, disturbances may lead to an initiation of freezing in the liquid phase which then exhibits new characteristics of a solid or a mixed solid/liquid phase. The probability of the onset of freezing generally depends on the ambient conditions of the supercooled fluid which are illuminated in the following.

2.2.2 Nucleation of Supercooled Water

The freezing of water requires the emergence of a so called nucleus or seed from which the solidification process commences. The formation of such a nucleus is generally referred to as nucleation. Nuclei tend to form on interfaces of water with a foreign particle or gas bubble. In this case, the nucleation is labeled as heterogeneous. However, even in the absence of foreign matter, supercooled water possibly begins to freeze spontaneously, which is then referred to as homogeneous nucleation. Representing a less complex system, the characteristics of nucleation are first elucidated in the course of the latter.

Homogeneous Nucleation

In the absence of a foreign phase, a nucleus is formed by incidental agglomeration of water molecules into a cluster. If the structure of this cluster resembles the structure of ice, other molecules possibly deposit on it and assemble into a solid ice structure (Franks, 1982). In order to grow, this accretion has to be thermodynamically favourable. One approach to determine whether the cluster growth is advantageous considers the Gibbs free energy of formation of the cluster ΔG_{hom}. Here, the cluster is assumed to represent a spherical solid like agglomeration in the liquid bulk phase. The free energy yields

$$\Delta G_{\text{hom}} = -\frac{4}{3}\pi R_n^3 \Delta G_V + 4\pi R_n^2 \sigma_{\text{nl}}, \tag{2.26}$$

where R_n is the cluster radius, σ_{nl} the interfacial tension between ice and liquid water and ΔG_V represents the volume free energy of water transferring from the liquid bulk phase to the cluster. The latter is a function of temperature and determined according to

$$\Delta G_V = \frac{\Delta T \rho L_f}{T_m}. \tag{2.27}$$

Here, L_f is the latent heat of fusion per unit mass, ρ is the liquid water density and $\Delta T = T_m - T$ denotes the temperature difference to the melting temperature of water (Porter et al., 2009). The first term in Eq. (2.26) is attributed to formation of the spherical solid cluster and the second term originates from the energy required for the generation of an outer solid/liquid interface. In Fig. 2.11, the qualitative
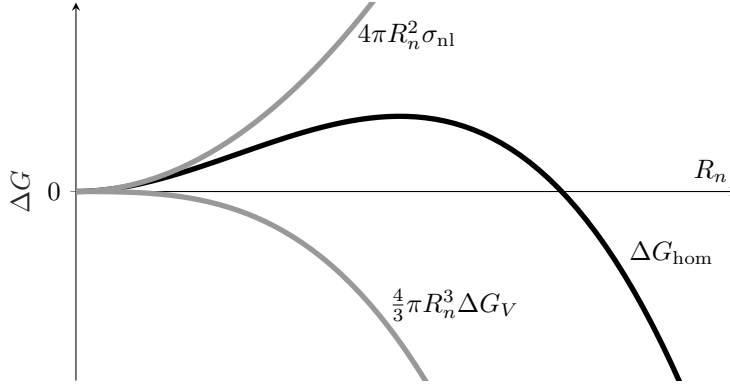
Figure 2.11: Qualitative propagation of G_{hom} depending on cluster radius R_n. Figure adapted from Franks (1982).

propagation of G_{hom} depending on R_n is illustrated. Additionally, the propagation of the two terms in Eq. (2.26) is shown. It is visible that the interfacial energy contribution dominates for smaller radii but is exceeded by the magnitude of latent heat of fusion set free during cluster formation as the radius increases. Since the latter is negative, the free energy G_{hom} of the cluster exhibits a single maximum which is achieved for a critical radius R_n^*. Thus, for $R_n < R_n^*$ it is favorable for the cluster to decay and no nucleus is developed. However, for $R_n > R_n^*$ the Gibbs free energy decreases for bigger clusters which causes the agglomeration to grow continuously and the solidification begins. The value of R_n^* directly follows from Eq. (2.26) subject to the condition $\partial G/\partial R_n = 0$ and with use of Eq. (2.27) as

$$R_n^* = \frac{2\sigma_{\mathrm{nl}}}{\Delta G_V} = \frac{2\sigma_{\mathrm{nl}} T_m}{\rho L_f} \frac{1}{\Delta T}. \tag{2.28}$$

For instance, the critical radius of supercooled water at $T = -40^\circ$ C is in the order of $R_n = \mathcal{O}(1\,\mathrm{nm})$. Since R_n^* is inversely proportional to ΔT, the formation energy exceeds the interfacial energy for smaller radii R_n the higher the temperature difference ΔT is. As described in Sec. 2.2.1 the surface tension change with temperature is minor; therefore, the interfacial energy change is small for a variation in temperatures as well. Thus, the required energy

$$\Delta G_{\mathrm{hom}}(R_n^*) = \frac{16\pi\sigma_{\mathrm{nl}}^3 T_m^2}{3\rho^2 L_f^2} \frac{1}{(\Delta T)^2} \tag{2.29}$$

is achieved for greater R_n at higher temperature, i.e. smaller ΔT and the random agglomeration of a sufficient cluster that promotes solidification is less likely (Porter et al., 2009). The consideration of the free energy with regard to the emergence of a nucleus is based on three vital assumptions: First, the applicability of macroscopic thermodynamic properties on the behaviour of the nucleus. Second, ΔG_V and σ_{nl} are independent of R_n and; third, the nucleus exhibits the continuum mechanic properties of ice which would otherwise especially question the use of σ_{nl}. Non-compliance to any of these assumptions complicate the approach and may reveal uncertainties, especially in determination of absolute values of R_n^* for a given temperature (Franks, 1982). Moreover, this description provides no quantitative information about the probability of the occurrence of a cluster with the critical radius R_n^*. Numerous approaches to predict such a nucleation rate for supercooled water have been derived in the past and some of them are found in Franks (1982), Oxotoby (1992), and Pruppacher and Klett (2010). However, experimental confirmation of the approaches is a difficult task and often error prone.

Heterogeneous Nucleation

In nature, heterogeneous nucleation is mostly responsible for solidification of supercooled water because the emergence of a nucleus is significantly favoured by the presence of foreign matter in the liquid. Similar to the approach of homogeneous nucleation, the size of a sufficient cluster acting as a nucleus is determined by considering its Gibbs free energy. However, if a third phase is involved in formation of a cluster the free energy is affected by two additional interfacial tension forces, as sketched in Fig. 2.12. In this approach, the cluster that potentially evolves into
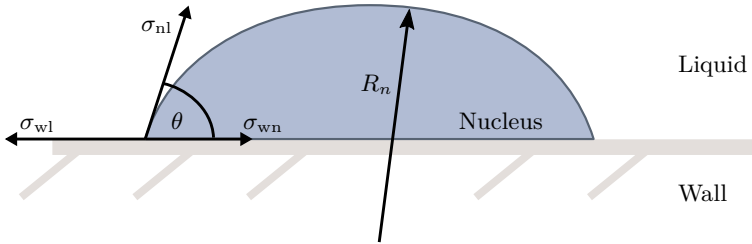
Figure 2.12: Solid nucleus formed on the surface of a foreign particle/wall. Image adapted from Porter et al. (2009).

a nucleus is assumed to exhibit the form of a spherical cap of radius R_n. The interfacial tension forces acting between nucleus/liquid (σ_{nl}), nucleus/wall (σ_{wn}) and wall/liquid (σ_{wl}) determine the contact angle θ subject to the force balance condition $\sigma_{\mathrm{wl}} = \sigma_{\mathrm{wn}} + \sigma_{\mathrm{nl}} \, cos\theta$ (Porter et al., 2009). Additionally, taking the energy

of the cluster formation into account, the free energy of the nucleus yields

$$\Delta G_{\text{het}} = -V_n \Delta G_V + A_{\text{nl}} \sigma_{\text{nl}} + A_{\text{wn}} \sigma_{\text{wn}} - A_{\text{wn}} \sigma_{\text{wl}}. \tag{2.30}$$

Here, V_n denotes the nucleus volume and the two surface areas A_{nl} , A_{wn} represent the upper surface of the nucleus and the contact area with the wall, respectively. Note that the contribution of σ_{wl} is negative since the liquid/wall interface with area A_{wn} is replaced by the nucleus. With respect to the spherical cap geometry and the balance of surface tensions, the free energy of the nucleus is expressed as

$$\Delta G_{\text{het}} = \left(-\frac{4}{3} \pi R_n^3 \Delta G_V + 4\pi R_n^2 \sigma_{\text{nl}} \right) \mathcal{F}(\theta), \tag{2.31}$$

where $\mathcal{F}(\theta)$ is a shape factor defined as

$$\mathcal{F}(\theta) = \frac{(2 + \cos\theta)(1 - \cos\theta)^2}{4}. \tag{2.32}$$

Thus, the free energy of a nucleus forming in heterogeneous nucleation corresponds to the free energy of homogeneous nucleation (Eq. (2.26)) scaled by the form factor $\mathcal{F}(\theta)$ (Porter et al., 2009). Assuming that the interfacial tensions are merely dependent on the involved materials, the free energy exhibits a maximum for a certain radius R_n^* similar to the maximum of ΔG_{hom}. In fact, the required radius R_n^* for the nucleus to grow equals Eq. (2.28), since the shape factor cancels out for $\partial G / \partial R_n = 0$. However, the amount of free energy required for formation of a cluster $\Delta G_{\text{het}}(R_n^*)$ is scaled by $\mathcal{F}(\theta)$. Considering the range of values for the shape factor $0 < \mathcal{F}(\theta) \leq 1$, it is evident that the free energy of a nucleus in homogeneous nucleation $\Delta G_{\text{hom}}(R_n^*)$ is always greater or equal $\Delta G_{\text{het}}(R_n^*)$. The equal amount of energy is achieved for a contact angle of $\theta = 180°$ where the contact area of nucleus and wall reduces to zero. For a contact angle of $\theta = 0°$, $\mathcal{F}(\theta)$ (i.e. also $\Delta G_{\text{het}}(R_n^*)$) approaches zero which is physically impossible, so this approach is only valid for $\theta > 0$.

Furthermore, the reduced value of $\Delta G_{\text{het}}(R_n^*)$ explains the increased likelihood of heterogeneous nucleation compared to homogeneous nucleation in nature. If less energy ΔG is required for formation of a critical heterogeneous nucleus $(\Delta G_{\text{het}}(R_n^*) \leq \Delta G_{\text{hom}}(R_n^*))$, it is already achieved at smaller ΔT (cf. Eq. (2.29)). Thus, as long as any foreign matter is present in the water cooled to subzero temperatures, sufficient nuclei are more likely to arise from heterogeneous formation than from homogeneous clusters in the bulk phase. Additionally, also the probability of heterogeneous nucleation increases, with the contact area of the supercooled liquid with any foreign surface (particles, container wall, etc.) since formation of nuclei is possible all over the interfacial area (Porter et al., 2009).

A general quantification of the probability of both nucleation processes at certain supercooling temperatures is difficult, since the exact conditions for heterogeneous nucleation are hard to define and the ones for homogeneous nucleation are not easy
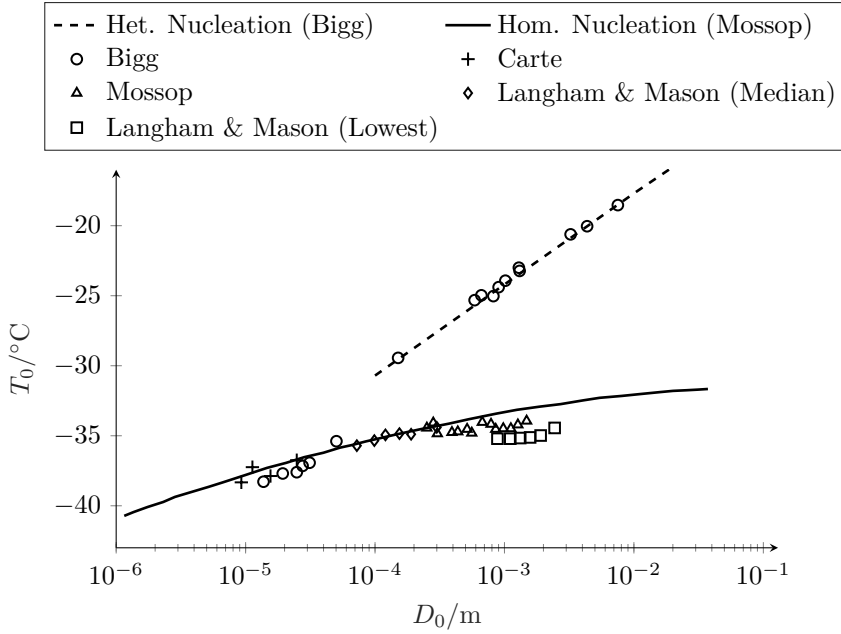
Figure 2.13: Map of freezing of supercooled water drops at various temperatures. The upper line represents freezing due to heterogeneous nucleation and the bottom line summarizes findings regarding homogeneous nucleation. Figure is replicated from Franks (1982).

to accomplish. Hence, experimental investigations often rely on the examination of drops of supercooled water in cloud chambers. In these experiments, foreign matter for heterogeneous nucleation is reduced to particles in the water and the achievable small drop sizes reduce the possibility of contamination to a minimum in order to study homogeneous nucleation. Clearly, the size of a drop influences the chances of nucleation, since in a larger drop more molecules are available to potentially form a nucleus. Therefore, the temperature at which nucleation occurs is examined with respect to the drop size. Fig. 2.13 shows a map including several investigations regarding the onset of nucleation in water drops for various subzero temperatures (Franks, 1982).

The bottom line represents a fit to several studies in which the observed freezing was assumed to commence due to homogeneous nucleation. It is visible that the temperatures at which nucleation occurs decreases slightly with decreasing drop size which accounts for the reduced probability of cluster formation in smaller drops. The lowest temperatures are achieved for smallest drop sizes at $T \approx -40° C$ which is close to the commonly assumed maximum possible supercooling of water.

The line also indicates that homogeneous nucleation is most likely for temperatures $T < -30° C$, although the scatter of different studies still suggest some uncertainties in the exact temperatures. The upper line represents a study in which heterogeneous nucleation due to small particles in the drops was observed (Franks, 1982). Clearly, the temperatures for which heterogeneous nucleation occurs are generally higher, confirming the model regarding the lower free energy of cluster formation. In contrast to the bottom line, no asymptotic behaviour to a threshold temperature is indicated, suggesting that heterogeneous nucleation can occur for the whole supercooling range of water. However, in this case, the probability of nucleation at certain temperatures greatly depend on the size and material of the contamination. Thus, this line rather represents an indicator of the temperature difference to homogeneous nucleation than an exact correlation. A more detailed discussion of the findings of studies considered in this map is found in Franks (1982).

Regardless of the type of nucleation, the solidification of the supercooled water will commence after formation of a sufficient nucleus. The freezing of supercooled water generally involves multiple stages which are described in the following sections along with the basic physics and significant influences.

2.2.3 Solidification of Supercooled Water
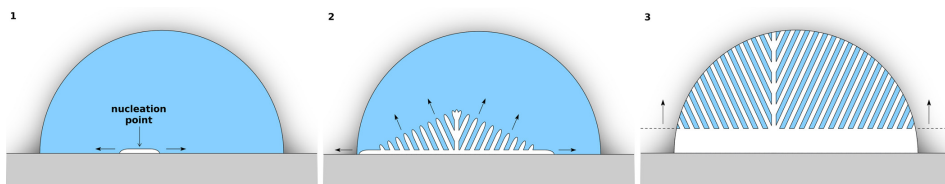
Figure 2.14: Three consecutive freezing stages of a sessile drop on a solid surface: Spreading of an initial ice layer (1), followed by growth of ice dendrites (2) and concluded by solidification of the remaining water (3). Reprinted with permission from Schremb et al. (2017b). Copyright (2017) American Chemical Society.

The solidification of supercooled water involves three consecutive stages. If the water is in contact with a solid continuous surface, a preceding stage occurs in its vicinity before the bulk solidification emerges (Stage I). During this phase an ice layer quickly spreads over the surface in contact with the wall. From multiple points of this layer, ice evolves into the bulk in form of rapidly growing dendrites which mark the second freezing stage (Stage II). In-between these dendrites, some water remains in its liquid form which subsequently freezes in a third stage (Stage III). The three stages are illustrated in Fig. 2.14 for a sessile drop (Schremb et al., 2017b). Stage II and III always occur in a bulk of supercooled water, whereas stage I only arises if the water is in contact with a surface. Since the last two stages

represent general characteristics of the freezing process, they are describe first in the following. Subsequently, stage I is illuminated with respect to the influence of the involved surface.

Dendritic Freezing of Supercooled Water

The dendrites developing in stage II propagate through the supercooled bulk liquid with characteristic shapes and velocity. A theory considering the development of a single dendrite in a bulk of supercooled liquid was suggested by Langer and Müller-Krumbhaar (1978). According to their stability criterion, the propagation velocity v_d of a single dendrite is directly connected to its tip radius r_d as $v_d r_d^2 = \text{const.}$ The shape of single dendrites developing in supercooled water was investigated by Shibkov et al. (2003). They found various shapes of dendrites for different temperatures ranging from dense-branching structures for low $\Delta T = T_m - T$ over fractal structured dendrites to needle like dendrites for higher ΔT. For a further increase of supercooling the needle like dendrites developed in multiple thinner branches. The observed shapes suggested a decrease of r_d with increased supercooling as already proposed in the theory of Langer and Müller-Krumbhaar (1978). Hence, for decreasing r_d with lower supercooling the dendrite tip velocity has to increase $\propto 1/r_d^2$. This dependency was experimentally confirmed by measurements of Shibkov et al. (2003). However, for high ΔT the ice mostly develops in a lattice of dendrites. A similar behaviour is observed when the supercooled water is in contact with a continuous ice phase, as sketched in the second image of Fig. 2.14. In this cloud of dendrites, branches growing close to each other possibly interfere with one another and affect the cloud front velocity v_f. This velocity was measured by Schremb and Tropea (2016) in a sessile supercooled drop. The experimentally determined values for both, v_f and v_d, are shown in Fig. 2.15. The obtained velocity magnitudes are in the order of $\mathcal{O}(0.1\text{m/s})$ and generally obtain similar values for the cloud front velocity and the single dendrite tip velocity. Merely in the range of $10\text{K} < \Delta T < 15\text{K}$, v_f is slightly higher than v_d, suggesting that in this range the dendrites exhibit a small thermal influence from each other in the cloud (Schremb and Tropea, 2016). Generally, the experimental values also agree well with the theory of Langer and Müller-Krumbhaar (1978) for supercooling up to $\Delta T \approx 10\text{K}$. For increasing ΔT, another effect entailing a reduced slope on v_f respectively v_d with temperature arises. At this growth rate, kinetic effects hinder the molecules from the liquid phase from a fast attachment to the solid structure and slow down the propagation of the dendrites. For v_d the influence is noticeable for $\Delta T > 10\text{K}$ (Shibkov et al., 2003), while the dendrite cloud seems to be affected only from $\Delta T > 14\text{K}$ on (Schremb and Tropea, 2016). This effect was already proposed by Langer and Müller-Krumbhaar (1978) and an approach to quantify it is, for instance, found in Shibkov et al. (2005) and Criscione et al. (2015).
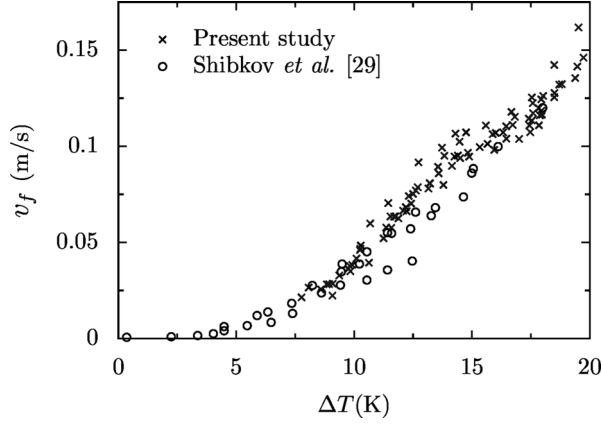
Figure 2.15: Measurements of the tip velocity of single dendrites marked with circles (Shibkov et al., 2003) and cloud front velocity in a sessile drop marked with crosses obtained by Schremb and Tropea (2016) which is referred to as the present study in this plot. Reprinted figure with permission from Schremb and Tropea (2016). Copyright (2016) by the American Physical Society.

During the development of ice dendrites, the supercooled water leaves its meta-stable state, since the dendrites release their latent heat of fusion into the surrounding water. Once the surrounding liquid reaches its melting temperature T_m, the growth ceases and the ice water mixture remains in thermodynamic equilibrium. The amount of ice developed in form of dendrites once T_m is reached depends on the initial supercooling temperature of the water. The composition prevailing after the first freezing stage exhibits both solid and liquid parts, and is also referred to as a mushy (frozen) phase. The fraction of ice in this mushy phase is estimated by the amount of heat absorbed by the liquid water in order to reach T_m. Considering an adiabatic volume of supercooled water, the internal energy changes by $c_p \Delta T$ which is balanced with the latent heat of solidification per unit mass L_f. Adding the change of heat capacity from water (c_p) to ice ($c_{p,\text{ice}}$), the volume fraction of ice ξ_{ice} reached upon thermodynamic equilibrium inside the mushy frozen phase (the freezing fraction) is obtained (Makkonen, 2010; Schremb, 2018):

$$\xi_{\text{ice}} = \frac{\rho c_p \Delta T}{\rho_{\text{ice}} L_f + \Delta T (\rho c_p - \rho_{\text{ice}} c_{p,\text{ice}})}, \tag{2.33}$$

whereby the densities of the supercooled water and ice are denoted with ρ and ρ_{ice}, respectively. In this approach, the energy associated with the viscous dissipation is assumed to be negligibly small. The temperature dependence of fluid properties
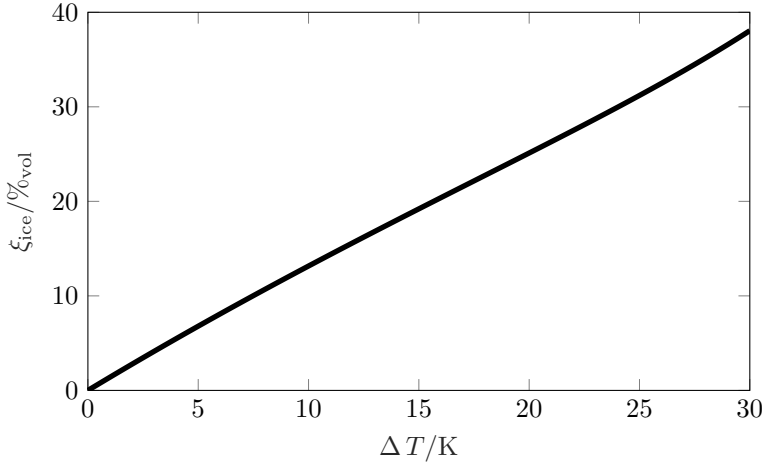
Figure 2.16: Volume ice fraction ξ_{ice} after dendritic freezing of supercooled water for different supercooling temperatures ΔT calculated after Eq. (2.33).

as introduced in Sec. 2.2.1, along with the inevitable achievement of thermal equilibrium after dendritic freezing, leaves the initial supercooling ΔT as the only parameter determining ξ_{ice}. Fig. 2.16 shows ξ_{ice} for supercooled water down to $\Delta T = 30\,\text{K}$.

It is visible that after the dendritic freezing a large amount of water is still liquid at any temperature. However, if the supercooled water is in contact with another material of any kind to which the latent heat of fusion is preferably transferred, the amount of ice increases significantly and Eq. (2.33) is no longer valid to estimate ξ_{ice} in the equilibrium state (Makkonen, 2010; Pasieka et al., 2014). After the dendritic growth has ceased, the remaining liquid water continues to solidify, yet in a less dynamic manner marking the third stage of solidification.

Freezing at Melting Temperature

With the ice-water mixture at melting temperature, a further advancement of solidification requires heat to be released to the surroundings which represents the last freezing stage III. Considering the remaining liquid being trapped in-between dendrites and the liquid in direct contact with the surrounding, the freezing process is described by a one-dimensional one-phase Stefan problem (Davies, 2001). In this approach, the liquid water remains at constant temperature T_m, no fluid movement occurs and both phases are considered as semi-infinite slabs. The solid ice phase is in contact with a boundary colder than the melting temperature, which disturbs the equilibrium condition and entails a growth of the ice phase of thickness $h_{\text{ice}}(t)$. The heat released upon solidification at the water/ice boundary is conducted away

from the advancing front through the solid phase. Within the ice, a temperature gradient arises as sketched in Fig. 2.17. This gradient responds to the boundary
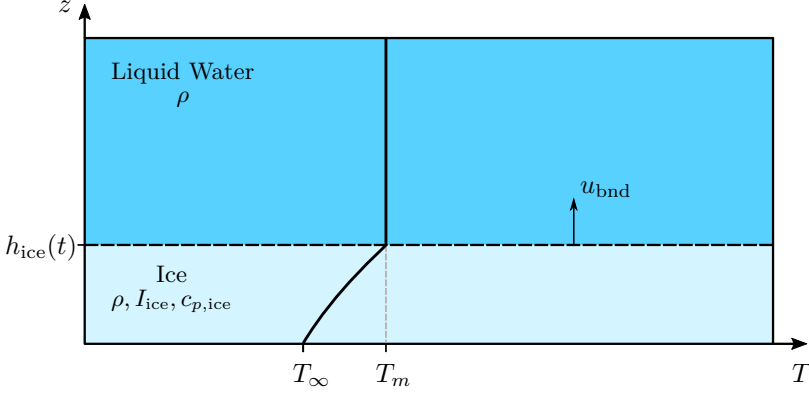
Figure 2.17: One-dimensional one-phase Stefan problem describing the propagation of the solidification front of water at melting temperature T_m. Figure adapted from Schremb (2018).

conditions and the heat conduction in the solid phase. When assuming a constant density for both phases $\rho_{\text{ice}} = \rho$, the velocity of the propagating freezing front can be obtained from an analytical solution (Davies, 2001). Assuming further that the heat conduction in the solid is described by the Fourier law, the heat balance reduces to the standard heat-conduction equation

$$\frac{\partial T_{\text{ice}}}{\partial t} = \frac{I_{\text{ice}}}{\rho \, c_{p,\text{ice}}} \frac{\partial^2 T_{\text{ice}}}{(\partial z)^2}, \tag{2.34}$$

where T_{ice} is the temperature in the ice phase at a given point z and the ice heat capacity $c_{p,\text{ice}}$ and the thermal conductivity I_{ice} are assumed constant. At all times $t > 0$, the ice slab responds to the conditions $T_{\text{ice}}(z = 0) = T_\infty$ and $T_{\text{ice}}(z = h_{\text{ice}}) = T_m$. Additionally, the latent heat released at the ice/water interface equals the heat conducted through the ice phase yielding

$$\rho L_f \frac{\partial h_{\text{ice}}}{\partial t} = I_{\text{ice}} \left. \frac{\partial T_{\text{ice}}}{\partial z} \right|_{z=h_{\text{ice}}(t)}. \tag{2.35}$$

Moreover, T_{ice} is subject to the starting condition $T_{\text{ice}}(t = 0) = T_m$ (Davies, 2001). In order to obtain a solution for the freezing front velocity, the system is transformed using a similarity variable ϵ and a dimensionless temperature ϑ defined as

$$\epsilon = \frac{z}{2} \sqrt{\frac{\rho c_{p,\text{ice}}}{I_{\text{ice}} t}} \quad \text{and} \quad \vartheta(\epsilon) = \frac{T_{\text{ice}}(\epsilon) - T_\infty}{T_m - T_\infty}, \tag{2.36}$$

where $\vartheta(z = 0) = 0$ and $\vartheta(z = h_{\text{ice}}) = 1$. From the definition of ϵ, it is evident that the position of the interface h_{ice} also responds to a function of the form

$$h_{\text{ice}}(t) = 2\Lambda \sqrt{\frac{I_{\text{ice}}}{\rho c_{p,\text{ice}}}\, t}, \tag{2.37}$$

where Λ is an unknown function determining the speed and position of the interface. Transforming Eq. (2.34) and Eq. (2.35) according to Eq. (2.36) yields a dimensionless system of differential equations for ϑ as

$$\vartheta'' + 2\epsilon\vartheta' = 0, \tag{2.38a}$$

$$\vartheta'(\epsilon = \Lambda) = \frac{2\Lambda}{\text{St}}, \tag{2.38b}$$

where the prime denotes derivation with respect to ϵ and St represents the Stefan number

$$\text{St} = \frac{c_{p,\text{ice}}(T_m - T_\infty)}{L_f}. \tag{2.39}$$

A solution is found subject to the conditions $\vartheta(\epsilon = 0) = 0$ and $\vartheta(\epsilon = \Lambda) = 1$ as

$$\sqrt{\pi}\Lambda e^{\Lambda^2} \text{erf}(\Lambda) = \text{St}. \tag{2.40}$$

This implicit solution for Λ shows that the propagation of the freezing front is directly dependent on the difference between the temperature of the lower boundary T_∞ and the melting temperature T_m of the liquid phase. Further, the one-dimensional one-phase Stefan problem can also be applied to the growth of ice in supercooled liquid, where the solid phase exhibits the melting temperature and the heat is conducted through the liquid towards the supercooled bulk. The solution for the propagation of the ice/water boundary in this case is similar to Eq. (2.40) which supports the temperature dependency shown in Fig. 2.15. However, the dynamics and shape of dendrites are generally dictated by instability effects (Langer and Müller-Krumbhaar, 1978). An investigation considering a similar approach in order to implement the freezing dynamics in numerical solvers is found in Berberović et al. (2018) in which they accounted for heat conduction in the liquid as well as in the frozen water, i.e. a two phase Stefan problem.

From the solution of Eq. (2.37) it is evident that the velocity of the freezing front decreases $\propto t^{-1/2}$. By solving Eq. (2.40), the velocity evolution is obtained as $\partial h/\partial t$. For distinct ΔT, it is noticeable that the velocity quickly reduces to significantly lower values than the dendrite tip velocity. For instance, at $\Delta T = 10\,\text{K}$ it is already one order of magnitude lower than the dendritic freezing velocity for $t = 0.001s$ with continuing reduction of its propagation velocity for later times. Considering the description by a Stefan problem, it is perspicuous that the solidification from an equilibrium state always moves opposite to the direction of the heat flux. Hence,

if the initially supercooled liquid is in contact with a surface which enhances heat conduction away from the liquid, the solidification front moves parallel to the surface, as sketched in Fig. 2.14 (3) (Schremb et al., 2017b). Moreover, the presence of a surface affects the freezing even before the dendritic freezing begins, since it leads to the occurrence of a preceding freezing stage.

Initial Ice Layer Spreading along a Solid Surface

As explained in Sec. 2.2.2, nucleation is most likely in the vicinity of a foreign substrate. From the nucleus, ice will spread quickly over the entire contact area of water and surface in the form of an initial ice layer (stage I), as sketched in Fig. 2.14 (1). After this layer covers the surface, dendrites will start to evolve from it into the bulk where the delay of the dendritic freezing decreases with increases supercooling ΔT (Schremb and Tropea, 2016). The initial ice layer was first reported by Kong and H. Liu (2015) and further investigated by Schremb et al. (2017b) for a sessile water drop. The latter study revealed that the ice layer only develops for surfaces with sufficient heat conduction, for instance metals. Moreover, they modelled the ice layer spreading similar to the freezing in stage III as a two-phase Stefan problem. Since the spreading from the nucleation point is approximately axisymmetric, the layer is modelled in a two dimensional approach. Assuming the cross section of the front tip exhibits the shape of a half parabola with radius r_lay, the velocity of the layer u_lay is obtained as

$$u_\text{lay} = \frac{2\Lambda_\text{TPS}^2 \alpha_\text{ice}}{r_\text{lay}}. \tag{2.41}$$

Here, Λ_TPS denotes the solution for the freezing front propagation for a two phase Stefan problem obtained from a solution similar to Eq. (2.40) and α_ice represents the thermal diffusivity of ice. Similar to the velocity of a free dendrite, the solution suggests that the spreading velocity is connected to the tip radius of the ice layer. However, Schremb et al. (2017b) could not measure the tip radius; hence, they estimated it from a fit to the experimental data of the spreading velocity. In contrast to a single dendrite, they suggest that the tip radius r_lay does not depend on the supercooling ΔT and only changes slightly for different materials. Although it is not clear why the tip radius is approximately constant, the experiment and the model agree well for a constant radius $r_\text{lay} = 352\,\text{nm}$ for supercooling temperatures at which kinetic effects are negligible. For the used tip radius, spreading velocities in the order of $\mathcal{O}(1\,\text{m/s})$ were obtained which increased with ΔT according to the solution for Λ_TPS. Thus, on metallic surfaces the ice layer spreads with velocities one order of magnitude higher than the single dendrites in the bulk (cf. Fig. 2.15).

The dynamic freezing of supercooled water in all three stages is particularly important when these effects are superimposed by hydrodynamics of the liquid phase. One example of this interaction is the central theme of this dissertation,

namely the impact of a supercooled liquid drop on a solid surface which has also been subject to multiple scientific studies. Current advances in research on this topic are elucidated in the following chapter.

2.3 Current Knowledge of the Impact and Freezing of Single Supercooled Large Drops

The freezing of supercooled water is greatly dependent on its surroundings with special regard to the temperature and materials in contact with the water. However, even for steady and accurately defined boundary conditions, as they are seldom known in experiments or in nature, nucleation remains a statistical process. Moreover, the three stages of solidification extend over multiple timescales, where each one bears the potential of interaction with any fluid movement occurring on a similar scale which, in turn, potentially alters the probability of solidification by introducing new boundary conditions. As described earlier, the drop impact onto a solid surface also comprises several stages and timescales in which solidification of the fluid would pose a crucial interference to the developing flow. For an interaction of both phenomena influencing the impact outcome, they must involve similar timescales.

Considering the first moments of an undisturbed drop impact until the entire drop fluid is involved in the flow developing on the surface, $t_{\mathrm{imp}} \propto D_0/U_0$ is often used as a typical timescale. Regarding the solidification of supercooled water, the propagation of the dendritic freezing front represents the vital characteristics of the dynamic freezing process of supercooled water. Hence, its velocity v_f (cf. Fig. 2.15) is used for an estimation of a representative time t_{frz}. Similar to t_{imp}, a timescale of freezing would describe the propagation of dendrites from the surface upwards into the drop which yields $t_{\mathrm{frz,imp}} \propto D_0/v_f$. Hence, a relation of both timescales provides $t_{\mathrm{frz,imp}}/t_{\mathrm{imp}} \propto U_0/v_f$. It is clear that an interference of both processes in the first moments of impact requires $t_{\mathrm{frz,imp}}/t_{\mathrm{imp}}$ to obtain values of $\mathcal{O}(1)$ which is only possible for impact velocities in the order of the dendritic freezing front velocity. Considering that $v_f = \mathcal{O}(0.1\,\mathrm{m/s})$, a freezing scenario in which the solidification influences these first moments of impact is unlikely since U_0 usually exceeds v_f by at least one order of magnitude. However, the developing flow of the impact further continues over longer timescales and also exhibits smaller length scales in which freezing may become relevant.

During an impact, the dendrites pervade the fluid spreading on the surface, whereas the smallest length scales are connected to the lamella. As seen from Eq. 2.11 its height evolves approximately with $h_{\mathrm{lam}}/D_0 = 1/\bar{t}^2 = D_0^2/(t^2 U_0^2)$ long after the initial contact with the surface. Considering now, the time the dendritic freezing front needs to travel through the current lamella height ($t_{\mathrm{frz,sprd}} = h_{\mathrm{lam}}(t_{\mathrm{frz,sprd}})/v_f$),

the characteristic timescale of freezing is obtained as $t_{\text{frz,sprd}} \propto D_0 U_0^{-2/3} v_f^{-1/3}$. Regarding the impact of an undisturbed liquid drop, its spreading ceases quickly after the boundary layer attains the free surface of the lamella as described in Sec. 2.1.1. In this moment, the drop reaches its maximum spreading which marks the end of the spreading phase. The time of spreading t_{sprd} is estimated similar to the upper bound for the maximum spreading diameter (Eq. 2.17) as $t_{\text{sprd}} \propto \text{Re}^{1/5} D_0/U_0$ (Roisman and Tropea, 2021). Relating these two timescales yields

$$t_{\text{frz,sprd}}/t_{\text{sprd}} \propto \frac{\nu^{1/5} U_0^{2/15}}{v_f^{1/3} D_0^{1/5}}. \tag{2.42}$$

It obtains values of $t_{\text{frz}}/t_{\text{sprd}} \approx 1$, for instance when a drop with $D_0 = 0.5\,\text{mm}$ and $T_0 = -10\,^{\circ}\text{C}$ impacts a surface with $U_0 = 2\,\text{m/s}$. It also remains in $\mathcal{O}(1)$ for a large range of impact velocities since the influence of U_0 is weak. Thus, the solidification process is able to interfere with the spreading of a drop on a solid surface. Moreover, the drop will usually start to recede on the surface after its maximum spreading is achieved which provides even more time for the solidification to interfere with the continuing fluid flow. Knowing about this potential influence of solidification, a description of the interference with the fluid flow is crucial for the comprehension of icing phenomena involving the impact of supercooled water drops. However, being complex problems each on its own, it is clear that a combination of the fluid flow and the freezing process is even more difficult to understand and predict. It requires a profound knowledge of the involved physical processes which is not sufficiently available so far. Nevertheless, several studies already contributed to a deeper understanding of this topic and a short review of these will be introduced in the following.

Considering the drop impact as the phenomenon determining the boundary conditions of the freezing process, the moment of nucleation is vital for the interaction of both processes. However, the statistical nature of nucleation entails a large variation in the moment of freezing onset. The probability of nucleation with elapsing time after a drop impacts on an aluminium surface was investigated by Schremb et al. (2017d). The number of active nucleation sites Ψ per drop after it has impacted a surface is given as

$$\Psi(t) = \int_0^{A_c(t)} \left(\int_{t_{\text{wt}}(A_c)}^t J_{\text{st}} \right) \mathrm{d}A, \tag{2.43}$$

where $A_c(t)$ denotes the contact area at a given time and t_{wt} is the time at which a certain contact area element is wetted during spreading. The instantaneous rate of nucleation per unit area is taken into account as J_{st}. Considering the relatively short timescale of spreading compared to the following stages (cf. Sec. 2.1), the time of wetting can be neglected and the number of nucleation sites per unit area

Ψ_{st} for $t \gg t_{\text{wt}}$ is obtained as

$$\Psi_{\text{st}}(t) \equiv \int_0^t J_{\text{st}} \mathrm{d}t = \frac{1}{A_c(t)} \ln(\mathcal{P}_{\text{nll}}). \tag{2.44}$$

Here, $\mathcal{P}_{\text{nll}}$ represents the probability of no active nucleation sites being present, which is assumed to follow a Poisson distribution ($\mathcal{P}_{\text{nll}} = e^{-\Psi}$). After conducting numerous experiments, Schremb et al. (2017d) were able to estimate this probability from the number of drops still liquid at a certain time $N_{\text{liq}}(t)$ in comparison to the number of drop experiments performed under the same conditions N_{tot} as $\mathcal{P}_{\text{nll}} = N_{\text{liq}}(t)/N_{\text{tot}}$. From this consideration, it is clear that the probability of nucleation increases with time and contact area of the drop with the surface. Moreover, an increase in nucleation probability was shown for an increase in supercooling ΔT of the fluid before the impact. However, additional factors possibly affecting the nucleation rate are manifold, which makes a general derivation of a nucleation rate virtually impossible. For instance, Schremb et al. (2017d) already pointed out that gas dissolved in the water can influence the nucleation by introducing additional nucleation sites in the form of tiny gas bubbles. Next to contaminants of the liquid, influences can vary from surface effects (Grizen et al. (2020) and Schwarzer et al. (2019)) to superimposing forces, e.g. electric fields (Löwe et al., 2021).

Freezing of a Sessile Drop

The least complex interaction of drop impact and freezing occurs long after the impact, when the fluid movement has already ceased. The sessile drop on the surface will then most likely freeze from bottom to top as illustrated in Fig. 2.14. The freezing front moves upwards, planar to the surface while maintaining the drop shape. Subsequently, when reaching the more curved drop top, the front lifts at the liquid-gas boundary (Schetnikov et al., 2015). The expansion upon freezing of the remaining water leads to the formation of a characteristic "pointy ice-tip" at the drop apex (Snoeijer and Brunet, 2012). This shape is observed regardless of the previous formation of dendrites due to liquid supercooling as shown in Fig. 2.18 (Schremb and Tropea, 2016). In the liquid part of the drop a flow arises during solidification which is mainly attributed to Marangoni convection (Karlsson et al., 2019). However, this flow presumably only arises for low supercooling of the liquid, since a formation of a mesh of dendrites as part of the freezing process would inhibit such a large scale fluid flow.

 In general, the remaining drop shape is significantly dependent on the contour of the equilibrium wetting state of the liquid drop on the surface (H. Zhang et al., 2016; Marín et al., 2014; Jin et al., 2015). Yang et al. (2018) also reported an increased nucleation probability in the curved region of the three phase contact line. However, this increase might be limited to the steady case since contrary
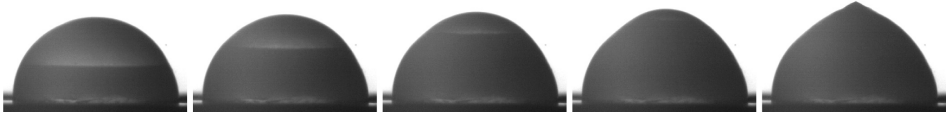
Figure 2.18: Freezing of sessile drop with a tip shaped at the apex as a consequence of volume expansion. Reprinted figure with permission from Schremb and Tropea (2016). Copyright (2016) by the American Physical Society.

observations were made when the liquid was still moving (Schremb et al., 2017d). Considering the shape of the frozen tip, Boulogne and Salonen (2020) suggest that the tip angle is changed by the arising impurities in the water. A numerical model derived by Tembely and Dolatabadi (2019) takes the substrate and surrounding gas influences into account and showed good agreement with the remaining drop shapes of freezing drops. Here, the solidification was considered as a uniform phase, so the formation of dendrites in the supercooling regime was neglected. An approach towards combining all influencing factors into a model that also incorporates the formation of ice in vicinity of the substrate and in the bulk fluid with respect to the point of nucleation was derived by Kong and H. Liu (2018). Hence, their unified icing theory comprises a description of all three stages of solidification of a sessile supercooled water drop on a surface.

However, in most icing scenarios the drops resting on a surface are disturbed by subsequent impacting drops or aerodynamic forces which influence the solidification process decisively. Moreover, the probability for nucleation in the drop is higher for an increased contact area as the drop exhibits it earlier during its impact. Thus, a solidification of the drop during earlier stages of the impact is more probable.

Freezing During Impact

The chances of a long freezing delay after first contact with the surface increase if the drop is not supercooled and reaches the melting temperature only through heat exchange with the surface during spreading. The development of dendrites would require significant supercooling before nucleation arises which is unlikely. In this case, the solidification is characterized by the heat exchange in liquid and solid water and the contacted surface. Thiévenaz et al. (2019) developed a model using heat diffusion in the solid phases coupled with the Stefan condition. It showed good agreement with experiments in which the drops froze into concentric rings with different heights after complete solidification depending on the surface temperature. Crucial for the development of the concentric shapes is a continuous receding of the liquid phase on the solidified water. A model for the solidification in the vicinity of moving contact lines was introduced by Herbaut et al. (2020), who were able to predict freezing induced pinning below a critical contact line

velocity dependent on the fluid temperature. However, the solidification in these studies is assumed to advance in a uniform phase, which deviates from a freezing process involving dendrites. The effect of the more dynamic dendritic freezing was investigated in Herbaut et al. (2019) in which a substrate is moved under a continuously fed drop of hexadecane and pentadecane while dendrites form in the liquid. Pinning occurs as soon as the dendritic solidification front catches up to the contact line. Hence, critical velocities for pinning are in the order of dendrite expansion velocities v_f (cf. Fig. 2.15). Considering the contact line movement during a supercooled drop impact with impact velocities considerably larger than v_f, these velocities are only reached when the spreading of the drop ceases and the contact line velocity approaches zero or in the subsequent receding stage in certain conditions (Roisman et al., 2002).

If nucleation takes place long after the impact, the pinning of a contact line possibly has no effect on the spreading of the drop as observed by Li et al. (2015). However, the heat exchange with the surface already begins during this phase and also greatly depends on the maximum surface area which the drop covers. As explained in Sec. 2.1.1, the latter is, among others, characterized by the fluid viscosity η which exhibits a significant increase in the supercooling regime (cf. Sec. 2.2.1). This effect was also confirmed by Maitra et al. (2014) for the impact of supercooled drops on superhydrophobic surfaces. Further influences on the heat exchange with the surface are the drop diameter, the impact velocity, other fluid properties with respect to the initial temperature and the substrate characteristics. A numerical model combining all these influences in order to determine the heat transfer and connect it with the fluid flow was proposed by Schremb et al. (2017a). Despite the improbability of the contact line pinning due to solidification in its vicinity, the freezing process possibly begins during the spreading phase in arbitrary locations and interferes with the local fluid flow. A first approach to the combination of the hydrodynamics of impact and nucleation theory is introduced by Kant et al. (2020a) for the impact of hexadecane drops onto an undercooled surface. However, the statistical occurrence of nuclei in the fluid make experiments difficult and the available data regarding the local interference with dendrites and their transport in case of fracturing rare.

Freezing Shortly after Contact

An interaction of fluid and dendrites may become particularly relevant if the solidification starts shortly after the impact. One scenario exhibiting a freezing of water without significant delay is to expose it to ice during the impact. With regard to icing scenarios involving drop impact, this process represents an essential mechanism leading to ice accretion after the surface is covered by previously frozen water. For water drops exhibiting a temperature above the melting temperature T_m before impact, the freezing still begins with a delay connected to the heat flux

which is removed in order to cool the fluid down to or below T_m. Subsequently, the freezing process starts and possibly interferes with the arising fluid flow. For sufficiently low temperatures of the ice surface, i.e. high heat flux, the delay is short enough for the drop to freeze in a thin splat close to its maximum expansion as demonstrated by Jin et al. (2017b). For slow heat conduction, the remaining shapes exhibits similar concentric ring profiles as with the impact on a cold surface. A consideration of the heat flux model was successfully used in a study dedicated to this topic by Thiévenaz et al. (2020). This movement depends mainly on the fluid properties and the contact angle of the water on ice which they were able to determine from the remaining ice shapes in the order of $\mathcal{O}(12°)$.

Furthermore, the freezing delay is close to be eliminated, if the liquid water drop exhibits temperatures below T_m before impacting onto the surface. When the drop contacts the ice surface, the solidification will commence from every contact point of fluid and surface. In combination with the dynamic propagation of dendrites into the bulk liquid, the fluid flow is substantially disturbed even shortly after the impact. The possibility for this phenomenon increases with ongoing exposure of a surface to supercooled drop impacts from coincidental collision of a liquid drop with a single frozen drop to impact of drops onto a complete ice layer covering the surface. The former was investigated, for instance, by Jin et al. (2017a) and James et al. (2021). Both studies confirm that a contact between impacting and frozen drop entail fast freezing of the liquid, whereas James et al. (2021) also observed disintegration of the fluid on the surface with subsequent freezing of secondary drops for sufficiently high Weber and Reynolds numbers. However, the frozen drop geometry in combination with arbitrary contact points of the impacting fluid entails a complex fluid flow interacting with developing dendrites. Hence, a detailed description of the governing flow and the interfering solidification is still missing. A less complex situation arises if the ice exhibits an even surface, since the flow of a drop impacting onto a solid planar surface is well-known (cf. Sec. 2.1). The conditions of such an impact resemble the later stages of ice accretion when the ice is already evenly distributed on the surface. The interaction of the developing dendrites with the flow in the lamella of the impacting drop was investigated by Schremb et al. (2017c). In their approach, they assumed the perpendicular propagation of a planar dendrite front in the thinning lamella as depicted in Fig. 2.19. Further, it is assumed that the dendrites in the front stay intact and the water enclosed by dendrites is unaffected by the flow in the lamella. Thus, the fluid in the lamella is assumed to spread on an upwards propagating boundary moving with the velocity of a dendrite cloud v_f (cf. Fig. 2.15). Similar to the description in Sec. 2.1.1, the lamella flow exhibits a viscous boundary layer at the interface of the dendrite cloud as illustrated in Fig. 2.19.
Considering the continuity equation (Eq. 2.9) in a moving coordinate system fixed at the cloud front and assuming a radial velocity similar to Eq. (2.10) for $t \gg \tau$,
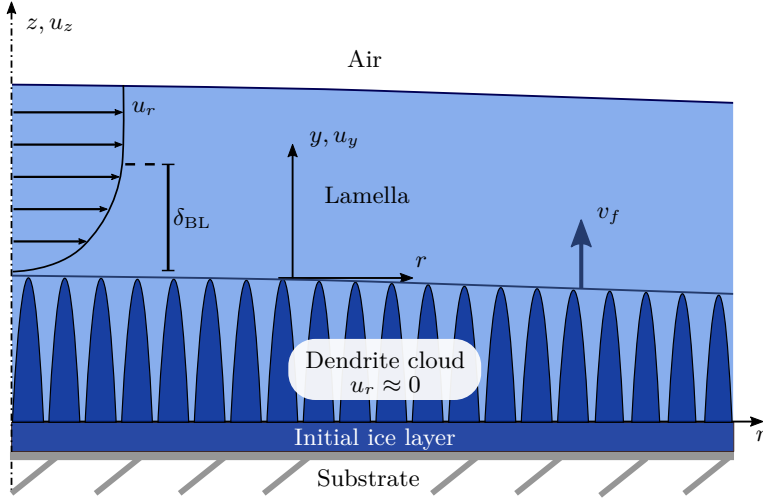
Figure 2.19: Sketch of axisymmetric spreading of the lamella flow on an upwards propagating dendrite cloud arising from a planar ice surface. Figure reproduced from Schremb et al. (2017c).

the velocity field in the lamella is obtained as

$$u_r = \frac{r}{t}\left(1 - e^{-y/s(t)}\right) \qquad u_y = 2\frac{s(t)}{t}\left(1 - \frac{y}{s(t)} - e^{-y/s(t)}\right) - v_f, \qquad (2.45)$$

Here, $s(t)$ is a function associated with the temporal boundary layer evolution. The axial velocity u_y complies with the condition $u_y(y = 0) = v_f$. The function $s(t)$ is determined from a numerical solution of the corresponding momentum equation (cf. Eq. (2.8)). When the dendrite cloud moves towards the upper liquid/air interface, the flow will cease when the remaining distance approaches the thickness of the viscous boundary layer δ_{BL}. The height of the remaining lamella $h_{\mathrm{lam,res}}$ at this moment is obtained from the velocity in the absolute coordinate system using $u_z = u_y - v_f = \mathrm{d}h_{\mathrm{lam}}/\mathrm{d}t$. However, the exact moment when the flow in the lamella ceases completely due to the viscous forces decelerating the fluid in the boundary layer is unknown. Hence, Schremb et al. (2017c) used the instant in which the flow at the lamella surface exhibits 95% of the outer flow to derive an upper bound of residual thickness. They were able to determine the residual lamella thickness, in experiments with drops impacting on an ice target smaller than the supercooled drop diameter. The fluid spreading beyond the target propagated downwards due to its inertia and enabled an unobstructed view of the frozen lamella at the impact axis. The qualitative agreement of the model and the experiment was excellent, yet the predicted thickness was generally overestimated. Schremb et al. (2017c) ascribed this divergence to the unknown moment of flow cessation and used their

findings to derive a semi-empiric correlation for the residual lamella height as

$$h_{\mathrm{lam,res}} = 2.26 \frac{\nu}{v_f} Z^{0.247} \tag{2.46}$$

with

$$Z = \frac{\mu D_0^3 v_f^5}{\nu^3 U_0^2}. \tag{2.47}$$

Here, D_0, U_0 and ν denote the drop diameter, impact velocity and fluid viscosity, respectively. The parameter μ is constant and originates from the inviscid solution for the lamella height evolution as introduced for Eq. (2.14). A numerical simulation of the phenomenon was conducted by Wang et al. (2020) and showed good agreement with the experiment especially for high supercoolings, i.e. higher ice fractions in the dendrite cloud phase.

Freezing Prior to Impact

Whereas the impact of liquid drops on ice exhibits the shortest time to the onset of solidification after impact, the freezing possibly occurs already before the drop contacts the surface. If the nucleation occurs shortly before impact, the drop will impact as a mixture of ice and water. In these mixed phase drops, the dendritic freezing enables an even distribution of ice and water and the drop impacts as a fluid with unfamiliar properties. Little is known about the characteristics of this mushy phase, the composition of which greatly depends on the initial supercooling of the drop (cf. Eq. (2.33)). To the author's knowledge, the impact of a mushy drop has never been investigated and will first be reported on as part of this thesis. Moreover, if the nucleation appears long before the impact, the drop solidifies completely and impacts as an ice particle. The field of ice crystal icing represents a broad new field of research which has drawn interest especially since it turned out to be a crucial factor of icing in aircraft turbines (Yamazaki et al., 2021). A detailed discussion of this topic exceeds the scope of this thesis; however, an approach of Roisman (2022) aiming for the description of the impact of an ice particle is helpful in describing the relevant physics of the developing flow. It is successfully used to model the disintegration of an ice particle upon impact on a solid surface (Reitter et al., 2022) and is also suitable to describe the impact of a mushy frozen drop which are investigated in the scope of this thesis (see Sec. 4.3). A detailed description of the model is given in the following[2].

The deformation of a plastic particle according to Roisman (2022) is described by a kinematically admissible potential flow which satisfies the continuity equation and the impenetrability of the substrate at the impression circle of the radius $a(t)$.

---

[2]The following description of this model is based on the remarks from Gloerfeld et al. (2023).

The momentum balance equation is solved accounting for the inertia of the flow and the plastic stresses. The resulting expressions for the pressure field are then used for the derivation of the total momentum balance of the entire particle and derivation of the equations of the drop deformation.

The flow field inside the impacting particle is approximated by an incompressible potential flow associated with the flow around a thin disc of the radius a. The potential of such a flow is introduced in Batchelor (1967) as

$$\phi = \frac{2aU}{\pi}\cos\psi \; [\sin\omega \; \cot^{-1}(\sinh\omega) - 1] - Uz, \tag{2.48}$$

where U is the unperturbed velocity far from the wall which is located at $z = 0$; ω and ψ are dimensionless elliptic coordinates given as

$$\omega + i\psi = \sinh^{-1}\left(\frac{z + ir}{a}\right). \tag{2.49}$$

Transformation into cylindrical coordinates and linearization of the velocity field $\boldsymbol{u} = \nabla\phi$ near the impact axis (for $r/a \ll 1$) yields

$$u_r = U\left[\frac{2a^3 rU}{\pi(a^2 + z^2)^2} + \mathcal{O}\left(\frac{r^3}{a^3}\right)\right], \tag{2.50a}$$

$$u_z = U\left[\frac{2\cot^{-1}(z/a)}{\pi} - \frac{2az}{\pi(a^2 + z^2)} - 1 - \frac{4a^3 r^2 z}{\pi(a^2 + z^2)^3} + \mathcal{O}\left(\frac{r^3}{a^3}\right)\right]. \tag{2.50b}$$

From this velocity field, a corresponding rate-of-strain tensor $\boldsymbol{E} = [(\nabla\boldsymbol{u}) + (\nabla\boldsymbol{u})^T]/2$ is derived, which is used to obtain an equivalent strain rate ($\dot{\gamma} \equiv \sqrt{2/3}\sqrt{\boldsymbol{E} : \boldsymbol{E}}$) as

$$\dot{\gamma} = \frac{4a^3 U}{\pi(a^2 + z^2)^2}. \tag{2.51}$$

A more detailed derivation of the coordinate transformation, the linearization of the velocity field and the equivalent rate of strain, is found in Roisman (2022). As seen from Eq. (2.48), the flow only depends on the disc radius a and the unperturbed velocity U far from the disc. Considering now the resulting flow field as representative for the flow in an impacting particle, the instantaneous radius of the force transmission area $a(t)$ and the velocity of the rear tip $U(t)$ define the flow at every moment of the impact. These characteristic geometric and kinematic parameters are sketched in Fig. 2.20. Note that the area $a(t)$ over which the impact force is transmitted to the surface does not equal the overall contact area represented by $r(t)$, since fluid particles with a horizontal velocity do not transmit a vertical force to the surface.

In order to describe the instantaneous shape of the impacting mushy drop, the vertical interference of the initially spherical particle with the surface is considered
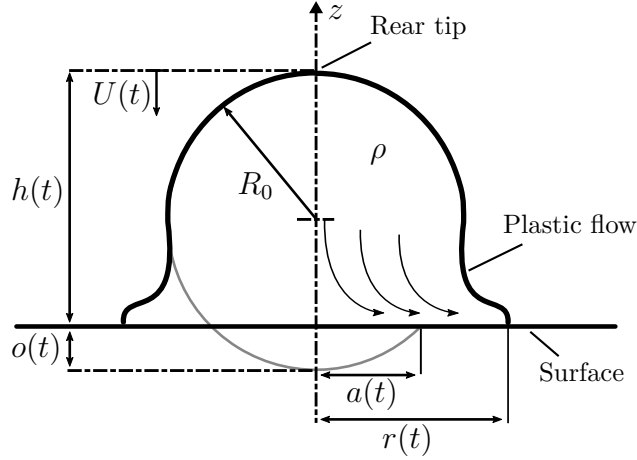
Figure 2.20: Characteristic parameters of the flow inside an impacting mushy frozen particle. Sketch adapted from Roisman (2022).

as $o(t) = 2R_0 - h(t)$, where $R_0 = D_0/2$ is the initial drop radius. For a general analysis, it is considered in terms of a dimensionless particle dislodging $\zeta = o(t)/R_0$, which also corresponds to the rear tip (apex) velocity as

$$\zeta = \frac{1}{R_0} \int_0^t U(t) \, \mathrm{d}t. \tag{2.52}$$

The approximate velocity field in the deforming drop is therefore determined by the instantaneous values of $\zeta(t)$ and $U(t)$.

The momentum balance equation accounts for the stresses associated with the pressure p and the deviatoric stresses $\boldsymbol{\sigma}'$ associated with plasticity

$$\nabla \left(\rho \frac{\partial \phi}{\partial t} + \frac{\rho}{2} \boldsymbol{u} \cdot \boldsymbol{u} + p \right) = \nabla \cdot \boldsymbol{\sigma}', \tag{2.53}$$

where ρ represents the average density of the mushy drop and $\boldsymbol{u}$ is the internal velocity field. The orientation of the plastic stresses coincides with the orientation of the rate-of-strain tensor $\boldsymbol{E}$ but the magnitude is equal to the yield strength Y

$$\sigma' = \sqrt{\frac{2}{3}} \frac{Y}{\sqrt{\boldsymbol{E} : \boldsymbol{E}}} \boldsymbol{E}. \tag{2.54}$$

Ice particles exhibit a hardening behaviour upon impact (Tippmann et al., 2013), which entails a shear rate dependence of the yield strength. This characteristic is incorporated into the model in the manner of

$$Y = Y_0 y(\dot{\gamma}). \tag{2.55}$$

Here, Y_0 corresponds to the static yield strength and $y(\dot{\gamma})$ is a dimensionless function of the equivalent strain rate, determined with Eq. (2.51).

The expression for the pressure field is then obtained as the solution of the Eq. (2.53), subject to the boundary condition at the rear tip $(z = h)$ where the axial stress vanishes. The expression for the axial stress at the wall $z = 0$ and $r = 0$ is then obtained in the form

$$-\sigma_{zz} = \mathcal{A}(\zeta)\rho U\frac{\mathrm{d}U}{\mathrm{d}\zeta} + \mathcal{B}(\zeta)\rho U^2 + \mathcal{C}Y_0, \tag{2.56a}$$

$$\mathcal{A} = \frac{h}{R_0}\left[1 - \frac{2}{\pi}\cot^{-1}\left(\frac{h}{a}\right)\right], \tag{2.56b}$$

$$\mathcal{B} = \frac{2h^2}{\pi R_0\left(a^2 + h^2\right)}\frac{\mathrm{d}a}{\mathrm{d}\zeta}$$

$$+ \frac{1}{2}\left\{\frac{2\cot^{-1}\left(\frac{h}{a}\right)}{\pi} - \frac{2ah}{\pi\left(a^2 + h^2\right)} - 1\right\}^2, \tag{2.56c}$$

$$\mathcal{C} = \frac{2}{3}\int_{\dot{\gamma}(h)}^{\dot{\gamma}(0)}\frac{y(\dot{\gamma})}{\dot{\gamma}}\mathrm{d}\dot{\gamma}, \tag{2.56d}$$

where $\mathcal{A}(\zeta)$ and $\mathcal{B}(\zeta)$ are dimensionless functions of the dimensionless particle dislodging ζ, and $\mathcal{C}$ is a dimensionless function based on the distribution of the strain rates (Roisman, 2022).

In this analysis, the impression radius a is estimated roughly for the initial stages of the drop deformation by approximating the shape of the drop by a truncated sphere, which yields

$$a \approx R_0\sqrt{2\zeta}. \tag{2.57}$$

This approximation resembles the spreading during the first moments of drop impact from Rioboo et al. (2002) as introduced in Sec. 2.1.1. The total axial momentum balance equation of the drop in z direction is estimated in the integral form

$$\frac{\mathrm{d}M}{\mathrm{d}t} \approx \pi a^2 \sigma_{zz}, \tag{2.58}$$

where M is the total axial momentum of the drop

$$M(\zeta) = \pi\rho R_0^3 U(\zeta)K(\zeta). \tag{2.59}$$

The dependence of the scaled axial momentum of the drop K on ζ is determined from computations of Eqs. (2.58) and (2.56) under the condition that $\rho U_0^2 \gg Y_0$. This solution for K entails the elimination of the middle term of Eq. (2.56a) leading to the following system of equations: The variables involved in the problem are written in dimensionless form using

$$a = \bar{a}(\zeta)R_0, \quad h = \bar{h}(\zeta)R_0, \quad t = \bar{t}R_0/U_0, \tag{2.60}$$

$$U = \bar{U}U_0 \quad Y_0 = \rho U_0^2\bar{Y}, \tag{2.61}$$

where dimensionless quantities are marked with a bar. Accordingly, the dimensionless description of the flow near the impact axis of the mushy drop is reduced to the system of ordinary differential equations

$$\overline{U}\frac{\mathrm{d}\overline{U}}{\mathrm{d}\zeta} = -\frac{\overline{a}^2 \mathcal{C}\overline{Y}}{K + \overline{a}^2 \mathcal{A}}, \tag{2.62a}$$

$$\frac{\mathrm{d}\overline{h}}{\mathrm{d}\zeta} = -\frac{2\overline{a}\overline{h}}{\pi(\overline{a}^2 + \overline{h}^2)} - \frac{\mathcal{A}}{\overline{h}}, \tag{2.62b}$$

$$\frac{\mathrm{d}\overline{t}}{\mathrm{d}\zeta} = \frac{1}{\overline{U}}, \tag{2.62c}$$

which have to be solved numerically subject to the initial conditions

$$\zeta = 0, \quad \overline{U} = 1, \quad \overline{h} = 2, \quad \text{at} \quad \overline{t} = 0. \tag{2.63}$$

In this manner, the model of Roisman (2022) enables the description of the impact of particles exhibiting a plastic flow behaviour upon impact. A discussion regarding the validity of this model and the corresponding assumptions for the impact of a partly frozen drop originating from nucleation shortly before impact is found in Section 4.3.

The scientific work on the impact of supercooled drops conducted so far has shown that the moment of nucleation is crucial for the developing flow on the surface and the geometry of the eventually frozen drop. Whereas some insight into the physics of the fluid flow and the solidification is gained for well-known conditions of the impact or involved surfaces, its applicability for more complex flow or freezing conditions is still unclear. However, these conditions especially arise, if occurring dynamics of the gaseous phase introduce non-negligible forces which are disregarded in the findings introduced so far.

Impact in a Surrounding Air Flow

Especially regarding the ice accretion of aircraft, the prevailing aerodynamic forces represent a significant factor to the impact of supercooled drops. Similar to the nucleation, the influence of the air flow can take effect at different times of the impact. A sessile liquid drop exposed to an air flow will stick to the surface until a critical velocity is reached leading to locomotion of the drop on the surface (Roisman et al., 2015a; Seiler et al., 2019). Simultaneous freezing of the drop possibly leads to fixation of current deformation arising due to the aerodynamic forces as demonstrated by Jung et al. (2012). Additionally, they could show that the drop possibly rolls off the surface after solidification for sufficiently high air flow velocities. Moreover, they pointed out the effect of evaporative cooling of the drop which increases the nucleation probability. Before the incipient motion of

the drop, the aerodynamic forces are balanced by the adhesion force of the liquid to the surface. The latter depends on the liquids wettability of the surface and may cause the drop to elongate instead of moving forward. Hence, a subsequent freezing entails a higher surface area covered in ice, as shown by Moghtadernejad et al. (2015).

An earlier interaction between air flow and a supercooled drop during the impact would presumably exhibit most characteristics of a liquid drop not prone to solidification. As discussed in the beginning of this section, the short timescales of impact in comparison to those of freezing and an additional freezing delay often make an influence of the freezing front negligible. However, the knowledge about the influence of an air flow superimposed on the drop impact hydrodynamics is generally scarce, and even more so for the impact of supercooled drops. A study dealing with the latter was conducted by Mohammadi et al. (2017), who investigated the impact of supercooled drops in a stagnation flow on a surface. The effect of the air flow is included as an additional downward force, increasing the spreading of a drop on a superhydrophobic surface. Another fundamental difference attributed to the air flow mentioned by Mohammadi et al. (2017) is the increased impact velocity, which entails a transgression of splashing thresholds. An acceleration in the air flow parallel to the drop trajectory can result in velocities exceeding the terminal velocity of the drop, leading to impact scenarios with higher Weber and Reynolds numbers. In experiments, high velocities are achieved in wind tunnels which provide enough distance to accelerate the drop without drag related breakup of the drop (Opfer et al., 2014). This approach is as expensive as complex and, therefore, available work on this topic is rare. C. Zhang and H. Liu (2016) represents one of the few available studies in which they injected mono dispersed droplets into an icing wind tunnel. They were able to observe different impact outcomes for varying drop temperature, diameter and impact velocity (up to 46m/s). However, the air flow around the impact position is not considered in their discussion. The inadequacy of control over the impact position of single drops and the restricted visibility at high impact velocities aggravate a detailed analysis which represents a common problem in such wind tunnel investigations.

For this reason, another approach often utilized to investigate this kind of impact is an acceleration of the surface rather than the drop (Faßmann et al., 2013; Mehdizadeh et al., 2004; Burzynski and Bansmer, 2019). However, this method also lacks visibility of the whole impact process, since the surface leaves the field of view during the impact when observed with a high-speed camera. Considering the comparably slow freezing of a drop, this impedes the ability to observe the freezing process. A study using this approach for supercooled drops was conducted by (Li et al., 2015), although the analysis of their findings did not consider the air flow on the surface. Moreover, literature on this topic is as rare as the studies dedicated to the impact of supercooled drops in wind tunnels.

A particular interesting quantity of the impact of supercooled drops at high impact velocities is the deposited mass after a single drop develops a splash, since the splash directly determines the amount of ice remaining on the surface. However, the influences on the extent of a splash and the amount of fluid ejected are generally still unclear and hard to quantify. Current models often rely on statistical approaches without considering the involved physics (Moreira et al., 2010). Experimental data for the remaining fluid on the surface was collated in Papadakis et al. (2000) and Papadakis et al. (2004) and based on their data an empiric approach was used in a the numeric simulation of ice accretion of Trontin and Villedieu (2017). A more physical approach is derived in Burzynski et al. (2020) which reveals a correlation of the deposited mass with the splashing parameter β of Riboux and Gordillo (2014) introduced in Sec. 2.1.2. Burzynski et al. (2020) considered different fluids, yet none of them were supercooled. Hence, the influences determining the deposited mass of supercooled drops remain elusive.

2.4 Remaining Questions

The fundamentals illuminated in the first two sections of this chapter and the current state of the art illustrated in the latter section show that the basics of solidification are well known and can be employed in steady conditions. However, the statistical nature of nucleation remains and introduces uncertainty to these predictions. Moreover, as soon as a fluid flow of the supercooled liquid is superimposed on the solidification process, the physical mechanisms governing the interaction between solid and liquid phase are still unclear. Whereas some predictions about a cessation of the flow caused by solidification is possible for slow fluid movements, a description of more dynamic scenarios is hardly available. On the one hand, this is attributed to the lack of knowledge regarding the complex fluid flow, e.g. deposited mass from splashing upon drop impact. On the other hand, it is associated with the unfamiliar properties of the mixed ice/water phase developed by fast propagation of ice dendrites during freezing of supercooled water. The problem is further complicated when considering the influence of an additional air flow surrounding the fluid flow. However, this interaction of four phases represents a vital situation in aircraft icing due to supercooled liquid drops and a reliable description is essential in order to minimize the hazards of ice accretion.

Thus, the current work aims for a better understanding of the highly dynamic fluid flow of a liquid supercooled drop impacting onto a surface under development of a splash. In this connection, interest is directed towards the extent of the splash and the deposited mass of a single drop impact on the surface. Moreover, the effect of a superimposed air flow on the drop before and during such an impact is analysed. Further, the interaction of the fluid flow with the fast solidification shortly after impact is investigated with focus on the shape of the remaining frozen drop. In addition, nucleation of the drop prior to impact on the surface is considered in order

to explore the impact behaviour of a mushy frozen drop and to quantify the elusive properties of the ice/water mixture after finishing the first freezing stage. The required subzero conditions for all experiments are achieved in a newly constructed cold chamber and the high impact velocities are achieved in a custom icing wind tunnel. The setup capabilities, the procedure of the experiments and additional methods used for the investigations are introduced in the following chapter.

3 Materials and Methods[1]

In the course of this dissertation, important characteristics of the impact of supercooled drops are captured, examined and quantified. First and foremost, new knowledge was rendered possible by the development of a new icing wind tunnel for single drop impact on cold surfaces exposed to a cold air flow. Its setup and the operating conditions in a subzero environment are described in this chapter. Moreover, an analysis and validation of the flow profile inside the test section during operation is reported after the general description. Subsequently, additional components necessary for the drop impact investigation in the wind tunnel are introduced. Finally, a description of important steps of the execution of the experiments is given in the last section of this chapter.

3.1 Icing Wind Tunnel for the Investigation of Supercooled Drop Impact

The impact of supercooled large drops onto a small target is examined in a newly developed icing wind tunnel. In order to maintain the required temperatures, the wind tunnel is mounted in a cooling chamber. The investigated drops are injected into the air flow of the tunnel through a shroud pipe which they pass until meeting the wind tunnel flow. After entering the air flow, the drop is accelerated towards the test section in which it impacts a small circular target. The impact is filmed via a high-speed video camera with backlight illumination. A sketch of the setup is depicted in Fig. 3.1 and its capabilities and important components are introduced in the following.

3.1.1 Icing Wind Tunnel Set-up and Capabilities

The cooling chamber within which the entire setup is mounted measures $W_x = 1.8\,\mathrm{m}$ wide, $W_y = 2.2\,\mathrm{m}$ deep and $W_z = 2.4\,\mathrm{m}$ high. It is able to achieve ambient temperatures down to $T_\mathrm{amb} = -20\,°\mathrm{C}$ provided by a cooling unit whose heat exchanger is mounted at the ceiling. The unit supplies a cooling power of at least 2500W over the entire range of considered temperatures in order to cool

---

[1]Parts of this chapter are published in Gloerfeld et al. (2021) and Gloerfeld et al. (2023), used under CC BY 4.0. The original contents have been edited and/or extended for this work.
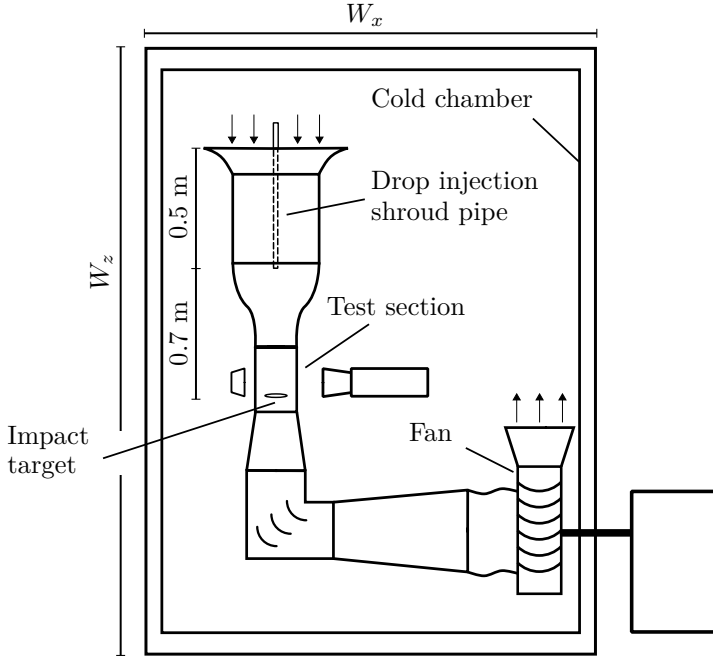
Figure 3.1: Icing Wind Tunnel for the investigation of the impact of supercooled water drops on cold surfaces in a co-flow. Some components in the sketch are not to scale.

it down and compensate the heat brought into the chamber by operation of the wind tunnel and all additional measurement equipment. Once it achieves the desired temperature, the cooling power is regulated by reducing the coolant flow to the heat exchanger with a bypass system. This bypass enables a more dynamic regulation of the temperature. The control of the cooling unit aims at a uniformly distributed temperature in the entire chamber, which thereby determines the temperature of all important components of the experiment. Due to the size of the chamber and the supply of cold air by the unit at the top of the chamber, the temperature varies slightly in different locations. However, local differences are kept to a minimum by the cooling unit regulation. In normal operating conditions between $-20\,^\circ\mathrm{C} < T_{\mathrm{amb}} < 0\,^\circ\mathrm{C}$, a local temperature deviation within $\pm 1.5\,^\circ\mathrm{C}$ of the desired chamber temperature T_{amb} is maintained. Nevertheless, the temperature of the airflow, the drops and the impact target are measured continuously.

The wind tunnel is a vertical open return blower wind tunnel with a square cross section, as depicted in Fig. 3.2. It takes an L shape, where its vertical height is 1.75 m and its horizontal length up to the beginning of the connecting hose
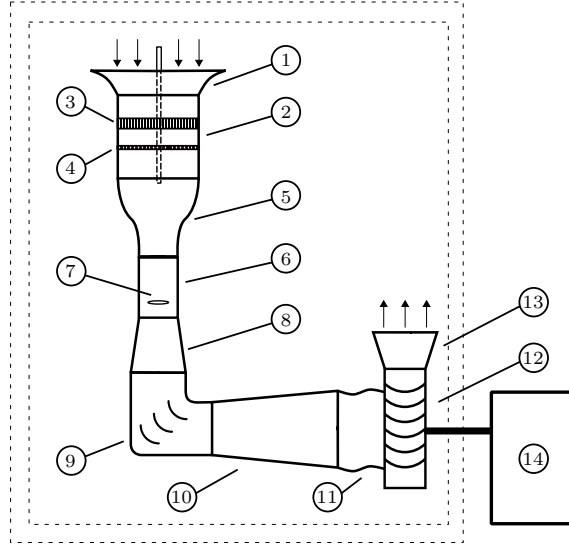
Figure 3.2: Sketch of the icing wind tunnel. The single components are the inlet nozzle (1), settling chamber (2) with flow straighteners (3) and (4), the acceleration nozzle (5), the test section (6) including the impact target (7), a diffusor (8), a turning corner (9), another diffusor (10) and a circular tube (11) which connects the tunnel to the fan (12) and the outlet diffusor (13). The fan is powered by a motor (14) placed outside of the cooling chamber, the walls of which are indicated as dashed lines.

(11) is 0.8 m. The air enters the wind tunnel through an inlet nozzle (1) with 90° opening from the horizontal to the vertical axis. The nozzle converges to a settling chamber (2). Inside this chamber, a honeycomb structure (3) consisting of cells with a diameter of 4 mm and a length of 24 mm eliminates large scale vortices. It is followed by a screen (4) from a mesh of 0.3 mm wires arranged with a grid size of 1.3 mm. The corresponding cell and grid sizes are designed according to Boyle et al. (1999). Both flow straighteners feature a hole (8 mm) in the center through which the injection shroud pipe passes. The side length of the settling chamber is 320 mm and its total length is 415 mm with the honeycomb and the screen placed in the middle with a spacing of 80 mm. After leaving (2), the flow is accelerated in a nozzle (5) which reduces the duct side length. The nozzle contour is based on a fifth degree polynomial with smooth transition to both connecting ducts and this reduction corresponds to a contraction ratio of 5.2 over a length of 320 mm. Hence, the subsequent test section (6) exhibits a side length W_{TS} which also corresponds to its hydraulic diameter $D_{\mathrm{hyd,TS}} = W_{\mathrm{TS}} = 140$ mm. Inside of (6), the drops injected through the shroud pipe impact onto a small circular

target (7). The test section length l_{TS} equals two times the hydraulic diameter of the duct ($l_{\mathrm{TS}} = 2D_{\mathrm{hyd,TS}} = 280\,\mathrm{mm}$). In this manner, remaining disturbances of the flow are given time to settle in the upper part of the test section before the flow approaches the impact target. A detailed description of the test section, installed measurement equipment and a validation of the flow profile are given in Sec. 3.1.2. After leaving the test section, the flow is decelerated in a first diffusor (8) with an opening angle of 5.7° over a length of 300 mm. Note that the opening angle corresponds to two times the angle from the vertical flow axis, since the diffusor is designed symmetric. For further deceleration, the flow requires a redirection due to the limited space in the cooling chamber. For this purpose, it is guided through a 90° corner duct with rounded edges (9). Inside the corner, additional flow control is provided by custom guide vanes designed according to Sahlin and Johansson (1991). After this redirection, the flow cross section is further expanded by another diffusor (10) with a length of 500 mm an opening angle of 7.43°. With a side length of 235 mm, the cross section is now similar to the suction inlet of the fan (12). However, since the opening in the fan is circular, it is connected via an adapter and a circular duct (11). Additionally, the duct is flexible in order to avoid transmission of vibrations from the fan to the rest of the wind tunnel. On the outlet of the fan, an additional diffusor (13) is mounted for flow expansion before releasing the air back into the cold chamber. The majority of wind tunnel ducts and diffusor are manufactured from acrylic glass. This ensures visibility of the impact in the test section (6) as well as possibilities to check for deposited water or ice inside all other parts of the wind tunnel. An exception are the two nozzles (1) and (5) which are 3D-printed with a rapid prototyping machine in order to enable a smooth cross section transition. Moreover, acrylic glass and the polyamide plastic used for the nozzles feature a similar expansion coefficient. Hence, when the tunnel is cooled down the risk of damage caused by tension between connected parts is reduced. The entire setup is mounted in a framework of aluminium profiles which also enables fixation of all other measurement equipment. The fan is mounted on a long shaft connecting it with its electric motor (14) which drives the fan at the required rotation. The engine is mounted outside of the chamber in order to reduce the heat brought into the chamber.

The fan and motor need to provide a suitable volume flow $\dot{V}$ at the corresponding pressure difference ΔP_{tot} which arises from the pressure losses in the wind tunnel. The tunnel is designed to achieve velocities of up to $40\,\mathrm{m/s}$ inside its test section and ΔP_{tot} is estimated from the pressure loss in the single components of the wind tunnel. The pressure loss ΔP_{loc} due to characteristics of a single component is usually combined into a total pressure loss coefficient K_{ls}. It represents the ratio of ΔP_{loc} to the dynamic pressure of the flow as

$$K_{\mathrm{ls}} = \frac{\Delta P_{\mathrm{loc}}}{\frac{1}{2}\rho_{\mathrm{air}}U_{\mathrm{air,loc}}}, \tag{3.1}$$

where $U_{\mathrm{air,loc}}$ is the local velocity in the tunnel component and ρ_{air} is the air density. The corresponding correlations for the estimation of pressure loss in different single tunnel elements are found in Boyle et al. (1999). Summing up all pressure differences corresponding to the velocity in test section $U_{\mathrm{air,TS}}$ yields the characteristic curve of the tunnel as shown in Fig. 3.3 for $T_{\mathrm{air}} = -20\,^{\circ}\mathrm{C}$.
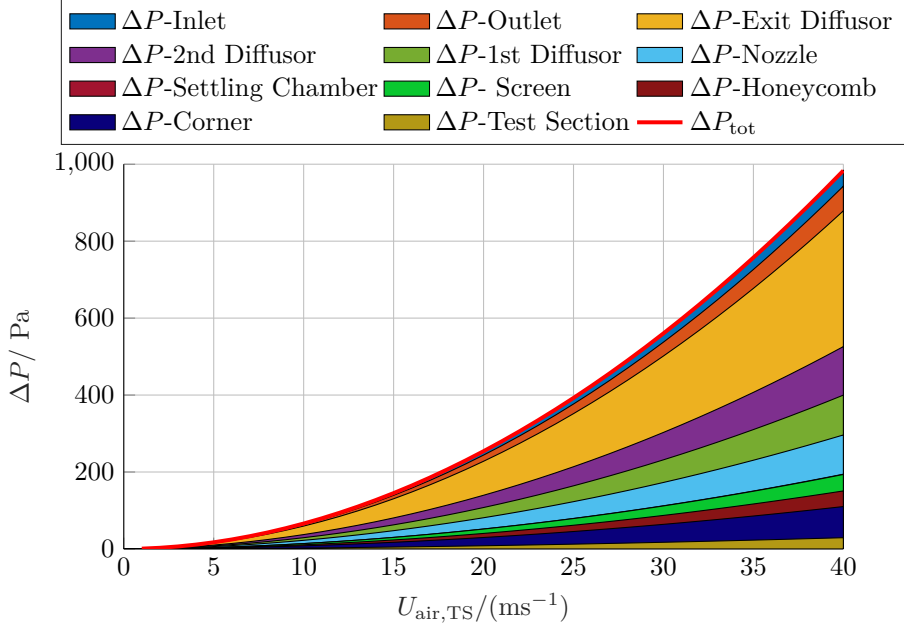
Figure 3.3: Estimated pressure losses ΔP_{loc} in the wind tunnel for various air velocities in the test section $U_{\mathrm{air,TS}}$. The contributions of single components are indicated by the coloured areas under the line of total pressure loss ΔP_{tot} represented by the red line.

Each coloured area in this figure represents contribution of one tunnel element to the total pressure loss, which is indicated by the red solid line. It is visible that the largest losses are expected in the exit diffusor (13) which is connected directly to the fan, followed by the pressure loss in the long diffusor (10). Whereas (10) is necessary in order to expand the flow to the dimensions of the fan inlet, the exit diffusor (13) merely decelerates the flow before it is blown back into the chamber under the development of a Carnot loss. Considering that the pressure loss of a Carnot expansion is $\propto \Delta U_{\mathrm{air}}^2$, a deceleration of the flow beforehand is beneficial, although the corresponding pressure loss exceeds all other contributions. In fact, the pressure loss from the Carnot expansion at the outlet is reduced significantly as seen in Fig. 3.3 (ΔP-Outlet) and the combined losses of outlet and diffusor are less than

the Carnot loss without prior deceleration. As seen from the characteristic curve, the pressure difference to maintain a velocity of $U_{\mathrm{air,TS}} = 40\,\mathrm{m/s}$ is $\Delta P_{\mathrm{tot}} \approx 980\,\mathrm{Pa}$. A suitable fan-motor combination has to overcome this pressure difference at the corresponding volume flow of this velocity $\dot{V} \approx 0.78\,\mathrm{m^3/s}$. Thus, the wind tunnel is operated with a low pressure radial fan (*Elektror - D09* (50 Hz)) which is capable of providing the required $\dot{V}$ and ΔP_{tot} at approximately half of its maximum power.

The pressure loss inside the wind tunnel arises from the energy dissipation due to wall friction, expansion of the flow, etc. in the single components. Hence, a heat flux $\dot{Q}_{\mathrm{diss}}$ is brought into the chamber by dissipation during operation of the wind tunnel. It is related to the loss coefficients K_{ls} (Boyle et al., 1999) according to

$$\dot{Q}_{\mathrm{diss}} = K_{\mathrm{ls}} \frac{1}{2} \rho_{\mathrm{air}} \dot{V} U_{\mathrm{air}}^2. \tag{3.2}$$

Next to the heat dissipation in the single components, the kinetic energy of the air flowing through the tunnel is a major heat input. The entire kinetic energy $\dot{Q}_{\mathrm{kin}} = 1/2 \rho_{\mathrm{air}} \dot{V} U_{\mathrm{air}}^2$ of the air flow is dissipated into the surroundings, since the air flow is blown into the chamber bulk where the air comes to rest. Additionally,
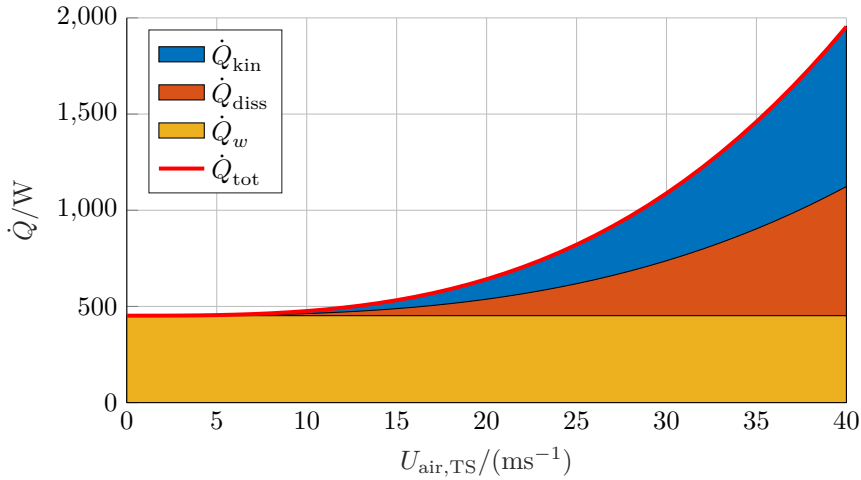
Figure 3.4: Estimated heat input into the cold chamber during wind tunnel operation

the heat brought into the system through the insulation of the chamber walls $\dot{Q}_w$ is estimated from the temperature difference to the surroundings and natural convection at the walls. Note that inside the chamber forced convection also arises which originates from operation of the wind tunnel. However, the unpredictable fluid movements within the chamber walls are impossible to quantify and the influence of the forced convection is neglected in this estimation. The total heat

input for an air temperature of $T_{air} = -20\,°C$ is plotted in Fig. 3.4 according to the velocity achieved in the test section $U_{air,TS}$.

It is visible that the heat input attributed to the wind tunnel operation is negligibly small for low air flow velocities in the test section. The major part of heat is brought into the chamber through the walls which is assumed constant in this estimation. However, the heat dissipated in the tunnel and the kinetic energy are in the same order of magnitude as $\dot{Q}_w$ for higher air flow velocities. Therefore, an amount of $\dot{Q}_{tot} \approx 2000\,W$ needs to be removed from the chamber during operation of the wind tunnel with $U_{air,TS} = 40\,m/s$. This estimation illustrates the basic considerations for the layout of the cooling unit power of at least $2500\,W$ at $T_{air} = -20\,°C$, which also allows for some increase due to smaller measurement equipment and the neglected forced convection on the inside chamber walls. Thus, the combination of wind tunnel, including fan and motor, with the cooling chamber enables investigations with velocities up to $40\,m/s$ at a temperature down to $-20\,°C$. For these investigations, it is also crucial that the air flow in the test section is well defined, since it directly affects the flow arising on the impact target.

3.1.2 Test Section and Validation of Flow Profile

The test section is essentially a square duct mounted between the nozzle and the first diffusor. Like the other sections of the wind tunnel it is manufactured from acrylic glass, yet it exhibits some additional features as shown in Fig. 3.5. The left and right walls are left blank in order to enable an unobstructed view to the impact target with the high-speed camera, and a proper illumination from the other side. The backside wall features a hole for the installation of a pitot tube which is used to measure the test section velocity. It is connected to a differential pressure sensor (*Setra-ASL1*, $0 - 25\,mbar$). The sensor enables precise measurements with $\pm 0.07\%$ of its final value. In order to determine the air density in the chamber, the absolute pressure in the cold chamber is measured with an absolute pressure sensor (*Kobold-SEN 9900*, $0 - 1.6\,bar$, $\pm 0.25\%$ full scale). Moreover, the temperature of the air flow is measured with a thermocouple ($\pm 0.3\,K$) protruding into the section from the rear wall at its lower end. All together enable a velocity measurement with an uncertainty of maximum $0.13\,m/s$. Additionally, the rear wall contains a number of pressure taps aligned in the flow direction. With these taps, the flow can be monitored for blockage, for the case that large impact targets are placed in the wind tunnel. However, in the present work all impact targets cover a maximum 10% of the tunnel cross section, in order to avoid a velocity increase due to significant reduction of the cross-sectional area. The front wall of the test section is interchangeable in order to enable an adaption to requirements of different target mountings and measurement tasks. In the standard configuration, the front wall exhibits a large opening which can be closed tight with a cover plate. The lower end features openings for the target holder as shown in Fig. 3.5. The large opening offers the possibility of installing, cleaning and maintaining the
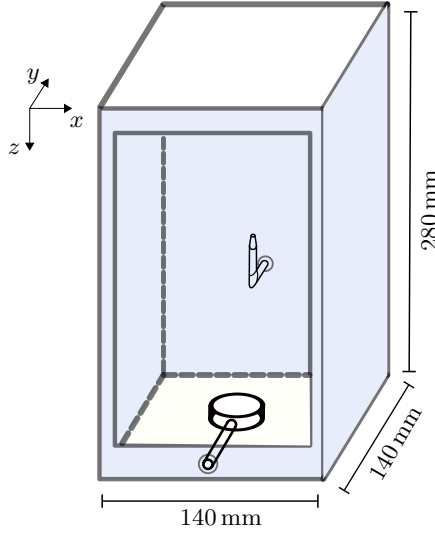
Figure 3.5: Sketch of the wind tunnel section in the configuration for drop impact experiments with access to the impact target through the front wall and the pitot tube installed in the rear wall. The impact target is installed in a mounting which is not illustrated in this sketch.

impact target between experiments. A different front wall is, for instance, installed when measuring the velocity profile across the test section.

The measurement of the velocity profile across the test section is obtained using hot wire anemometry. Several measurements with various velocities at three cross sections downstream of the test section are conducted. In order to precisely control the measurement position of the hot wire probe and automate the measurement, the probe is positioned by a traversing system. The front window is switched for a window with a narrow slot in the corresponding height of the measured cross section and the uncovered area of the slot is covered by a slider system. In this manner, the hot wire probe is moved freely in the horizontal plane of the cross section with minimum leakage of the tunnel flow. The traversing system and the slider enable a fully automated measurement of a single cross section, which takes about one hour. During a measurement of the velocity profile, the fan rotation frequency is held constant in order to obtain a steady flow in the wind tunnel for the time of measurement.

Measurements at three cross sections at $z = 1.32D_{\mathrm{hyd}}, 1.5D_{\mathrm{hyd}}, 1.96D_{\mathrm{hyd}}$ were conducted. At every cross section, the flow was measured for five different velocities $U_{\mathrm{air}} \approx 5, 10, 22, 30, 40\,\mathrm{m/s}$. The hot wire probe is operated in the constant temperature mode and the calibration function connecting the measured

voltage to a certain velocity is assumed to correspond to King's Law (Nitsche and Brunn, 2006). Accordingly, the hot wire probes are calibrated at the beginning of every measurement day, including a temperature compensation.

A measurement of a single cross section covers the full length in the y direction. In the x direction, a measurement closer than 4.5 mm to the wall was not possible using the slot in the front window in combination with the probe width. Within the accessible region, the velocity profile is resolved with a spacing of $\Delta x = \Delta y = 5$ mm. At the rear wall, additional points in the y direction are recorded with a reduced spacing in order to resolve the boundary layer of the flow. At every measurement position, the hot wire probe records data with a frequency of 100 kHz for $t = 2$s and the obtained data is averaged to a single velocity value. A typical velocity profile across the cross section is shown in Fig. 3.6. The illustrated velocity profile
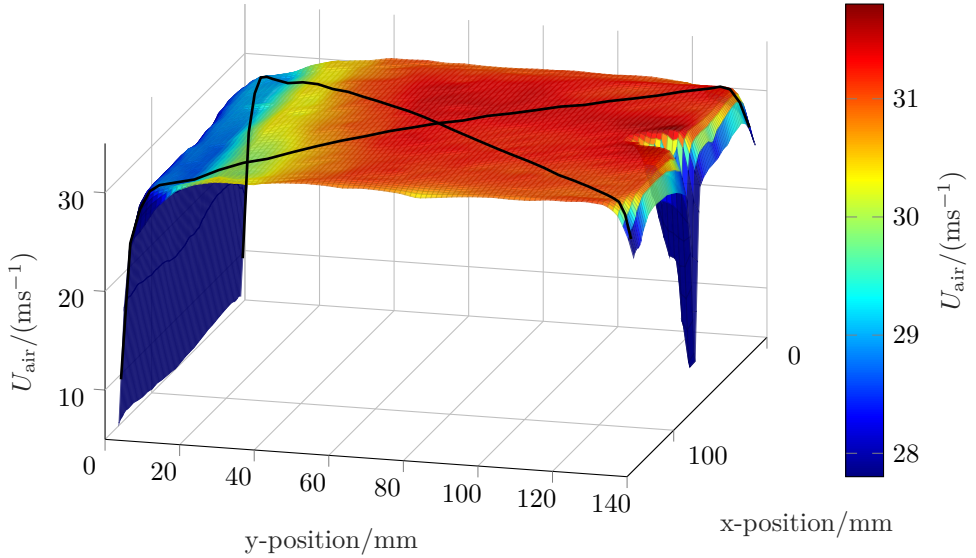
Figure 3.6: Interpolation of the velocity profile measured with hot wire anemometry, plotted over the cross section coordinates. The air flow velocity is additionally rendered in color for highlighting local differences. The measured cross section is located at $z = 1.32 D_{\text{hyd}}$ downstream of the test section and the bulk velocity is $U_{\text{bulk}} = 30.32$ m/s.

reveals a uniform velocity distribution over a wide range of the test section area. The impact target is placed in the cross section center and a homogeneously approaching flow impinging on the surface requires a uniform flow profile over the entire target area. Considering the size of the cylindrical targets including their mounting ($D_{\text{trg,tot}} \approx 40$ mm), the uniform flow needs to span over a region ± 20 mm in all directions from the test section center ($x = y = 70$ mm). As seen

in Fig. 3.6, the flow profile is uniform for even greater distances from the center which verifies a homogeneous flow impinging on the target. Nevertheless, some local divergence from the average velocity throughout the entire cross section is visible. The noticeable velocity reduction at $x = 70\,\mathrm{mm}, y = 140\,\mathrm{mm}$ is a result of the wake of the Pitot tube installed at the back wall. However, its spatial influence is restricted to an area far from the central region and can be neglected. Another deviation is a decreasing velocity between $y = 0 - 40\,\mathrm{mm}$ over the entire width of the test section. Although it is not directly affecting the impact target region, it could possibly cause problems in some target configurations. However, it is most likely caused by leakage through the slider system, which could not be completely sealed in order to allow traversing of the hot-wire probe. It is assumed to vanish for normal operating conditions of the wind tunnel, and a side-wall boundary layer corresponding to the one at the rear wall of the test section ($y = 140\,\mathrm{mm}$) without the wake of the Pitot tube is expected. The boundary layer near the wall is expressed by a decrease of the measured velocity which is visible from $y = 135\,\mathrm{mm}$. With a maximum thickness of $\approx 5\,\mathrm{mm}$, an influence of the boundary layer on the central region flow can be neglected.

In order to compare the velocity distribution for different airflow velocities, normalized profiles along the black diagonal lines corresponding to a coordinate s_{diag} shown in Fig. 3.6 are examined. The origin of the diagonal is always placed at the front wall of the test section ($y = 0\,\mathrm{mm}$) and positive values run along the diagonal to the opposing corner of the test section. For comparison of different velocity profiles, the measured velocities along the diagonal $U_{\mathrm{air,diag}}$ is related to the bulk velocity of the corresponding measurement $U_{\mathrm{air,bulk}}$. The measurements exhibit excellent agreement among the profiles obtained at $z = 1.32 D_{\mathrm{hyd}}$ for different velocities, as illustrated in Fig. 3.7a. It is visible that $U_{\mathrm{air,diag}}/U_{\mathrm{air,bulk}} \approx 1$ over a large portion of the diagonal in the central region, suggesting a uniform velocity, as seen in Fig. 3.6. At the end of the diagonal ($s_{\mathrm{diag}} \to 198$), the effect of corner vortices is visible, which are characteristic for rectangular wind tunnel ducts (Güttler, 2015). The effects are the strongest for lower velocities, as seen in all cross sections in Fig. 3.7. However, in all cases, their influence on the velocity is spatially limited to $s_{\mathrm{diag}} \approx 180\,\mathrm{mm}$ which corresponds to a distance of approximately $12\,\mathrm{mm}$ from the wall. Hence, any influence on the central region can be neglected. Furthermore, these secondary motions are restricted to the corners of the duct. Along the walls, the development of a thinner boundary layer similar to the one visible in Fig. 3.6 is expected. Moreover, the effect on the velocity seems to decrease along the test section length, as seen for $z = 1.96 D_{\mathrm{hyd}}$, which is closest to the impact target position (Fig. 3.7c). At the front corners of the test section (($s_{\mathrm{diag}} \to 0$)), the corner vortices additionally interfere with the flow disturbances attributed to leakage in the probe inlet. The agreement of measured velocity profiles is equally excellent for different velocities and for different cross
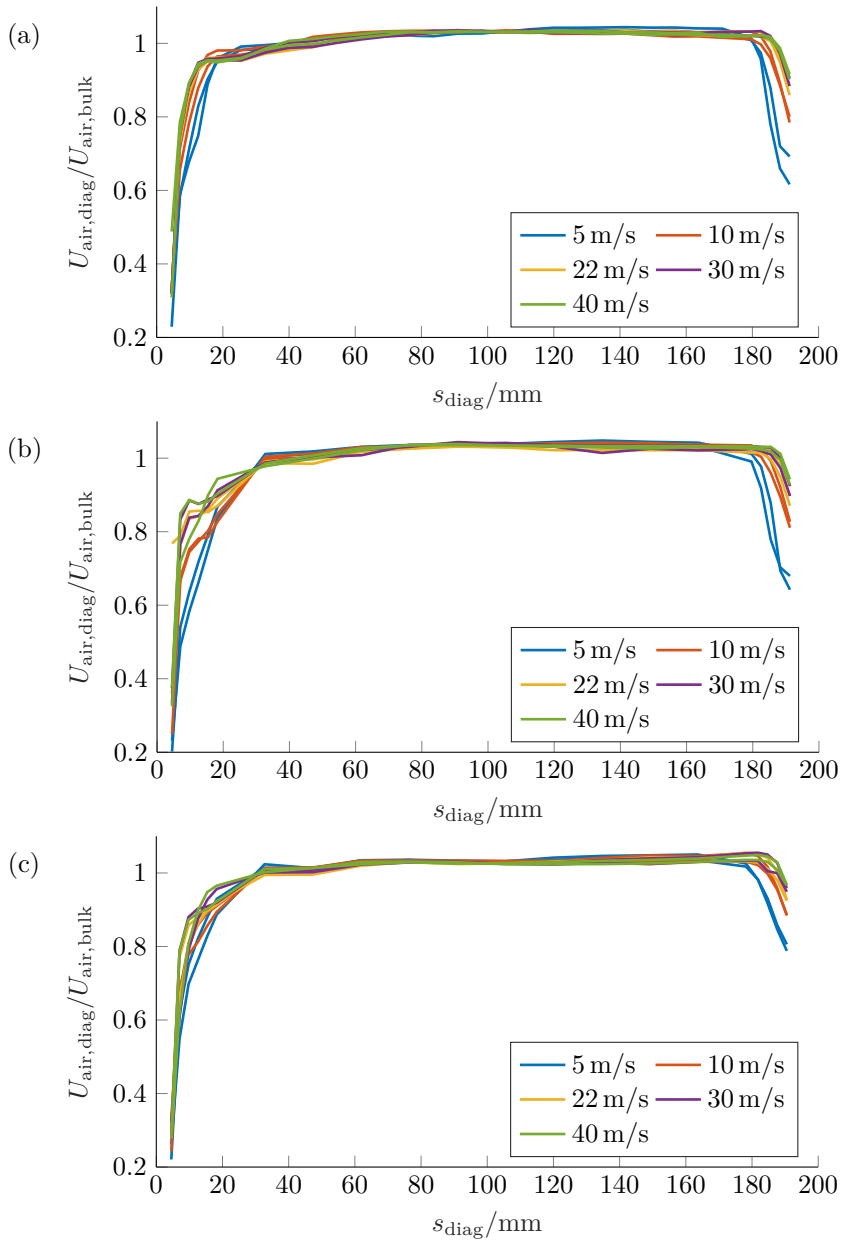
Figure 3.7: Velocity measurements along the diagonal lines of the velocity profile as shown in Fig. 3.6. Velocities are obtained at cross sections (a) $z = 1.32 D_{\text{hyd}}$, (b) $z = 1.5 D_{\text{hyd}}$ and (c) $z = 1.96 D_{\text{hyd}}$.

sections below $z = 1.32D_{\text{hyd}}$. Thus, a uniformly approaching flow on the impact target is ensured for $z > 1.32D_{\text{hyd}}$ in the velocity range of $U_{\text{air,bulk}} = 5 - 40\,\text{m/s}$.

For these velocities, the prevailing flow experiences Reynolds numbers $\text{Re}_{\text{TS}} = U_{\text{air,bulk}}D_{\text{hyd,TS}}/\nu_{\text{air}}$ in a range of $4.5 \cdot 10^4 < \text{Re}_{\text{TS}} < 3.7 \cdot 10^5$. Hence, the flow inside the test section experiences turbulence, which is often quantified in terms of a turbulence intensity $\text{Tu} = \sqrt{(1/3)(u_1'^2 + u_2'^2 + u_3'^2)}/U_{\text{air,bulk}}$, where u_i' denotes a velocity fluctuation in one spatial direction (Nitsche and Brunn, 2006). The hot wire anemometry allows for an estimation of Tu which is usually achieved with probes containing one wire for each direction. However, the measurements regarding the velocity profile in the test section were conducted with a single wire probe which do not distinguish between fluctuations in different directions. Nevertheless, this measurement method also allows for an estimation of the turbulence intensity. Assuming isotropic turbulence, $\text{Tu} = \sqrt{u'^2}/U_{\text{air,bulk}}$ is approximated from the fluctuations in the measurement signal obtained for the velocity measurement. The turbulence intensity profile corresponding to the measurement in Fig. 3.6 is shown in Fig. 3.8. Similar to the velocity, Tu exhibits a uniform distribution in the central
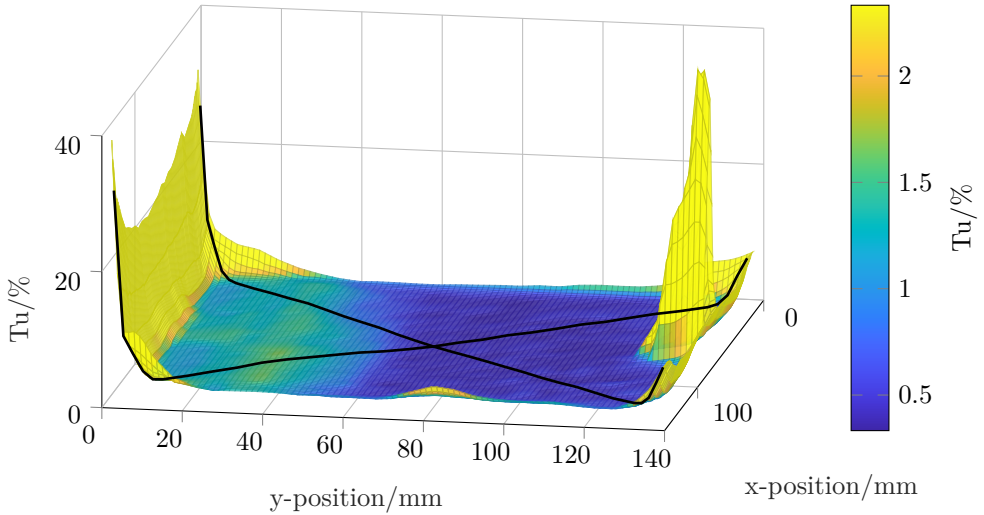
Figure 3.8: Interpolation of the turbulence intensity (Tu) profile estimated from the hot wire anemometry plotted over the cross section coordinates. The magnitude of Tu is additionally rendered in color to highlight local differences. The measured cross section is located at $z = 1.32D_{\text{hyd}}$ downstream of the test section and the bulk velocity is $U_{\text{bulk}} = 30.32\,\text{m/s}$.

region. Local increases arise in regions where the velocity field experiences a strong deviation from the bulk velocity, as seen in Fig. 3.6. Hence, they are also attributed

to the wake of the pitot tube, the corner vortices, the boundary layer and leakage in the cover of the wire probe inlet. This congruence supports the assumption that all velocity decreases are attributed to vorticity in the corresponding region. The effect of the leakage at the front wall is the strongest with a slight increase of Tu up to approximately $y = 50\,\mathrm{mm}$. However, as explained for the velocity, this effect is expected to vanish during operation with a sealed front window. Thus, the air flow in the central region is assumed to exhibit a turbulence intensity of Tu $\approx 0.5\%$ as in the main region of the test section for $y > 60\,\mathrm{mm}$.

Similar to the velocity field comparison, Tu is examined along the displayed diagonals in Fig. 3.8 for different velocities and cross sections. The corresponding curves are shown in Fig. 3.9. The turbulence intensity for all velocities $U_{\mathrm{air,bulk}} > 10\,\mathrm{m/s}$ show excellent agreement in all cross sections. Hence, Tu $\approx 0.5\%$ applies in the test section for $z > 1.32 D_{\mathrm{hyd}}$. The turbulence intensity of $U_{\mathrm{bulk}} = 5\,\mathrm{m/s}$ is slightly higher with Tu $\approx 2\%$. However, this increase in intensity is presumably a consequence of the limited precision of the hot wire measurement. A turbulent fluctuation of 0.5% for $U_{\mathrm{air,bulk}} = 5\,\mathrm{m/s}$ equals a fluctuation of $u' = 0.025\,\mathrm{m/s}$. Such a fluctuation lies in the order of minimum precision of the hot-wire setup, so the measurement is presumably superimposed by measurement noise. Moreover, an increased turbulence intensity only for the lowest velocity is unlikely; hence, the turbulence intensity is assumed to correspond to the quantities measured for higher velocities.

The uniform velocity profiles and the turbulence intensity of the flow were measured without the shroud pipe installed in the upper part, at room temperature and without the cooling unit in operation. In order to rule out effects of these additional components, further measurements were conducted to analyze the effect of the pipe and the flow of air exhibiting $T_{\mathrm{air}} = 0\,°C$ in the wind tunnel. However, no significant effect of any of these modifications was noticeable. Measurements at subzero measurement were not possible, since the traversing system was not designed for such conditions. Moreover, the influence of an installed impact target was examined with respect to its repercussion to the flow. The flow impingement on the target develops a stagnation point flow according to the approaching bulk air flow. A quantification of this flow in the vicinity of the surface was not feasible, since the wake of the probe interacts with the prevailing flow. However, a cross section measurement at $z \approx D_{\mathrm{hyd}}$ revealed that the installation of an impact target introduced no noticeable perturbations at this height. Considering the positioning of the pitot tube shortly upstream of $z \approx D_{\mathrm{hyd}}$, it is ensured that the corresponding measurement still quantifies the free stream velocity despite the installation of an impact target. Thus, the wind tunnel enables examination of supercooled drops impacting on a dry solid surface on which a stagnation point flow develops from uniform free stream velocities between $U_{\mathrm{air,TS}} = 5 - 40\,\mathrm{m/s}$ with Tu $\approx 0.5\%$.
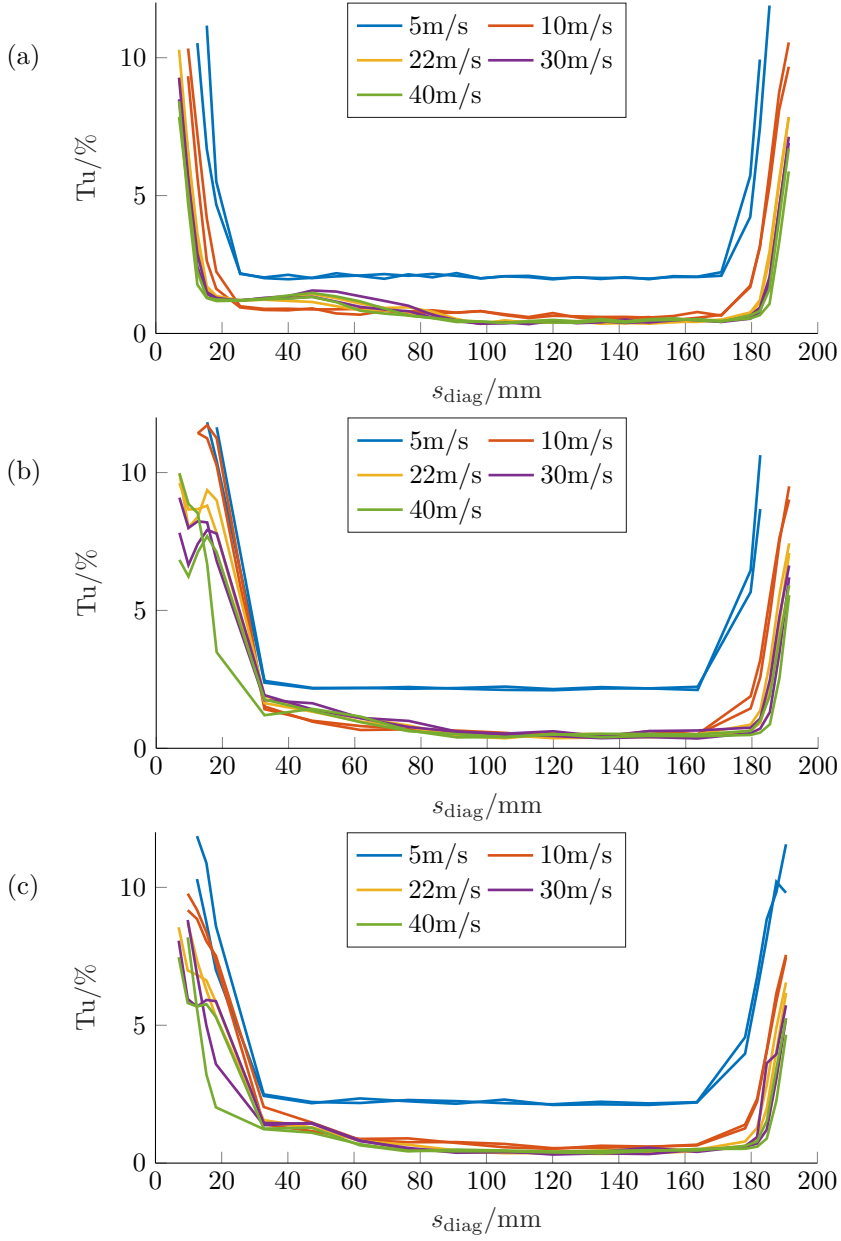
Figure 3.9: Turbulence intensity along the diagonal lines of the cross section, as shown in Fig. 3.8. Intensities are obtained in cross sections at (a) $z = 1.32D_{\mathrm{hyd}}$, (b) $z = 1.5D_{\mathrm{hyd}}$ and (c) $z = 1.96D_{\mathrm{hyd}}$.
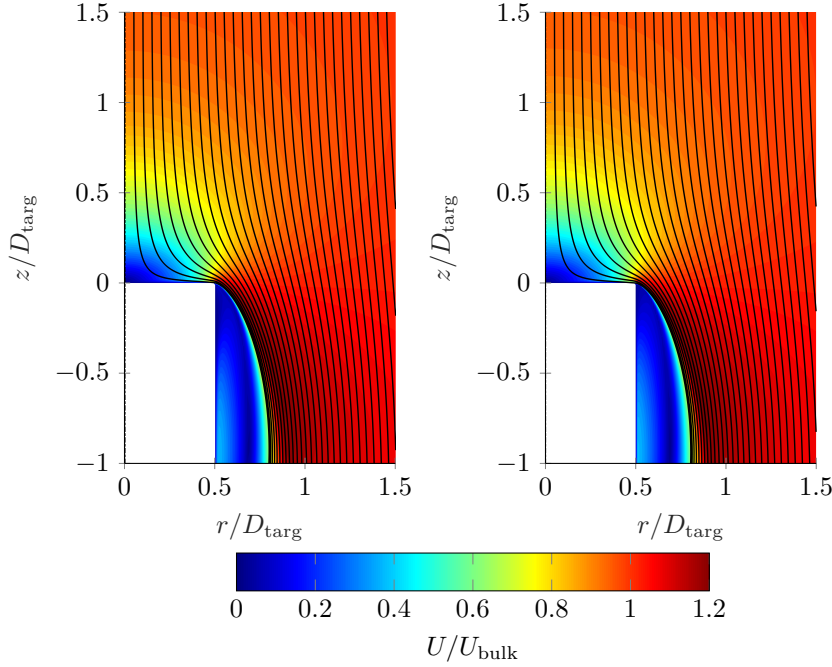
Figure 3.10: Velocity magnitude obtained from numerical simulation of a cylindrical impact target (white rectangle) in a free stream corresponding to an air flow velocity of $5\,\mathrm{m/s}$ (left) and $25\,\mathrm{m/s}$ (right) at the inlet. The black lines indicate the stream lines of the flow which follows them in downward direction.

Target Flow Simulation

In order to estimate the flow developing on an impact target exposed to the wind tunnel flow, a numerical simulation was conducted. All impact targets take a cylindrical shape, where the flat end is facing towards the incoming air flow. Hence, the flow is computed in a two-dimensional, axially symmetric simulation as shown in Fig. 3.10. The computation is based on a finite volume simulation carried out with the code *OpenFOAM*. The pressure/velocity coupling is done with the *SIMPLE* algorithm and the convective terms are discretised with a second order upwind method. The mesh is generated with *blockMesh* which is integrated into *OpenFOAM* and provides a block structured hexahedral mesh. The cell closest the wall is positioned within the viscous sub layer, i.e. $y^+ < 1$. The occurring turbulence is modelled with the common $k-\omega-\mathrm{SST}$ model. The simulation was conducted for five different air flow velocities of $U_\mathrm{air} = 5, 10, 15, 20$ and $25\,\mathrm{m/s}$ at the inlet of the considered volume at the top. Furthermore, the mesh independence was checked

for each configuration. The air properties were held constant corresponding to air with $T_{\mathrm{air}} = -10\,^{\circ}\mathrm{C}$. The obtained flow is illustrated in Fig. 3.10 for $U_{\mathrm{air}} = 5\,\mathrm{m/s}$ (left) and $25\,\mathrm{m/s}$ (right). The dimensionless velocity magnitude of the flow entering at the top is rendered in color. It is evident that it is generally small in the vicinity of the surface over the majority of surface radius r in the central region. Close to the surface edge $r/D_{\mathrm{trg}} \rightarrow 1$ it increases rapidly to the free stream velocity. Moreover, the flow deceleration begins at approximately one target diameter above the surface ($z/D_{\mathrm{trg}} \approx 1$) close to the surface center. The streamlines indicated by the black lines show the convergence of the flow diverted by the target in the wake of the upper surface. Their path and the velocity magnitude illustrate that the recirculation area next to the surface ($z/D_{\mathrm{trg}} < 0$) is separated from the flow on the surface. Thus, its influence on the flow interfering with the drop impact is negligible.

Next to the velocity magnitude, the simulation provides spatially resolved data for the prevailing pressure field and the velocity components above the surface. The flow field is similar for all computed velocities, which suggest analogue flows for arbitrary velocities in the range of $U_{\mathrm{air}} = 5 - 25\,\mathrm{m/s}$ for the investigations conducted with a cylindrical impact target. Next to the air flow in the tunnel, some additional components are necessary for the controlled and repeatable conduction of experiments in the wind tunnel. These installations are introduced in the following.

3.1.3 Further Components Regarding the Investigation of Supercooled Drop Impact in the Icing Wind Tunnel

With the wind tunnel providing the required air flow, two additional components are essential for the investigation of supercooled drop impact in the wind tunnel. A mechanism enabling the controlled and repeatable generation of supercooled drops and the impact target that is mounted in the test section. Both components exhibit additional features ensuring accurate and efficient execution of the experiments.

The supercooled drops are formed from purified de-ionized water (*Millipore, Milli-Q®*). They drip from a syringe needle at the height of the settling chamber. This method enables generation of drops with reproducible size, where the drop volume is determined by the syringe diameter (Tropea et al., 2007). In the scope of this work, two different syringe needles were used with $0.6\,\mathrm{mm}$ and $0.4\,\mathrm{mm}$ diameters, enabling the formation of drops with diameters of approximately $D_0 = 3\,\mathrm{mm}$ and $D_0 = 2.6\,\mathrm{mm}$, respectively. To prevent uncontrolled interaction of the drop with the surrounding air flow and, hence, improve repeatability of their shape and size, the drops were protected from the air flow during their formation by a shroud pipe, as sketched in Fig. 3.11. The pipe is manufactured from $1\,\mathrm{mm}$ glass and exhibits an outer diameter of $8\,\mathrm{mm}$. The syringe inside is attached to a supply tube that leads out of the cold chamber through the ceiling. It is connected to a water tank which is mounted on the cold chamber wall. A micropump
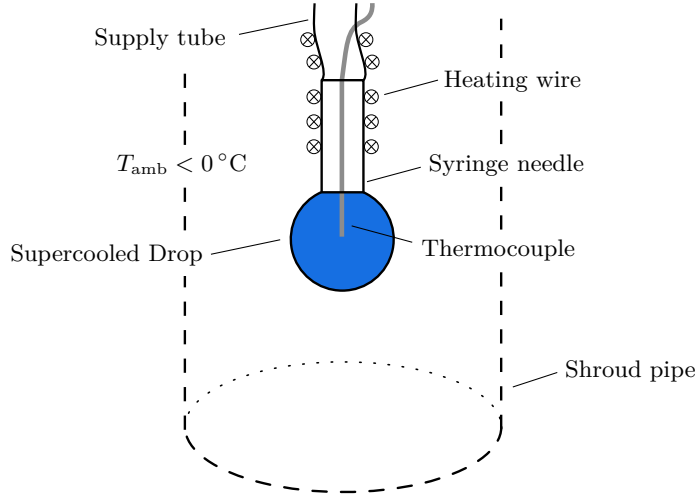
Figure 3.11: Mechanism for the generation of supercooled drops inside of the shroud pipe installed in the wind tunnel

(*Bartels mp-6*) in-between tank and syringe provides low volume flow rates down to 8 μl/min for slow generation of the drops. This way, the drops supercool during their formation due to the prevailing temperatures in the cold chamber. Since the syringe and the tube are also exposed to the subzero temperatures the water inside is also supercooled during the experiments. Depending on the duration of time the water remains inside the supply tube at these temperatures, it possibly freezes and blocks the supply system. For this case, a heating wire is wrapped around the syringe and the tube exposed to the chamber. Thus, ice inside of the supply can be melted without removing the syringe from the pipe. Additionally, the heating power is adjustable in order to maintain temperatures above the chamber temperature in-between experiments, which reduces the risk of solidification. During an experiment, the supercooling of the drops needs to be quantified. Hence, the temperature is continuously measured by a thermocouple. It has a diameter of 0.25 mm and is threaded through the syringe needle, as introduced by Schremb et al., 2017d. This method allows for measurement of the drop temperature up to the moment of dripping. After detaching from the syringe, the drops accelerate solely due to gravity until reaching the end of the shroud pipe, from where they are further accelerated by the flow.

When reaching the test section, the drops impact onto a flat target which is placed in the wind tunnel. In most of the experiments the impact surface is the polished flat end of an aluminium cylinder with a diameter $D_{\mathrm{trg}} = 30\,\mathrm{mm}$. A characterisation with an atomic force microscope determined the statistical mean

roughness of such a target as approximately 5 nm. All aluminium targets used are manufactured in the same manner and polished with a specific machine. Hence, the roughness of all targets is assumed to be in the same order of magnitude. Additionally, the aluminium targets contain an inlet for a thermocouple in order to constantly monitor the target temperature. The choice of targets is variable as long as their diameter does not exceed $D_{\mathrm{trg}} = 30\,\mathrm{mm}$. Aluminium was chosen due to its technical relevance, but experiments were also conducted using a custom ice surface, the manufacture of which is described in Sec. 3.2. The targets are placed inside a mounting that includes some additional features as shown in Fig. 3.12. The mounting is installed in the test section with a rod passed through an inlet in
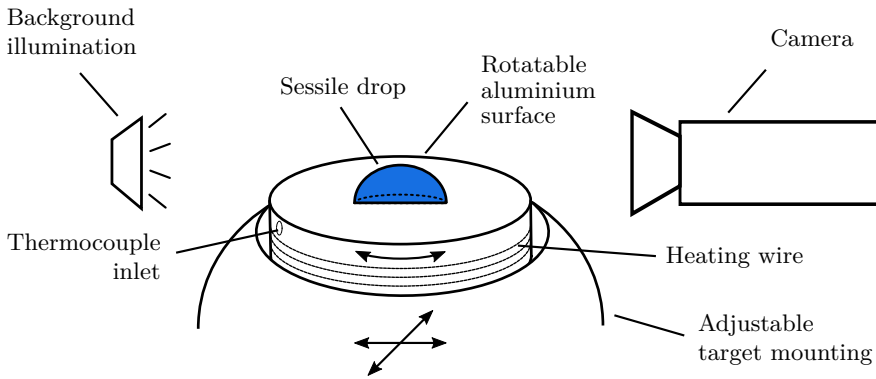
Figure 3.12: Sketch of the impact target in the mounting which is installed in the wind tunnel test section. Camera and illumination are placed opposite to one another outside of the wind tunnel test section.

the front wall as depicted in Fig. 3.5. The mounting is covered by a 3D-printed shell with rounded edges to avoid detachment of the flow on any sharp edges. The target positions inside the test section can be adjusted along the rod axis and perpendicular to it. This way, the impact position of the drops on the target is matched, since their trajectory slightly changes during their descent for certain air flow velocities. Whereas the variability in the x-direction (cf. Fig. 3.5) is limited in range and precision, the rod fixation on the outside of the test section provides a wider range. It is mounted on a precision translation stage which enables adjustment by $\pm 12.5\,\mathrm{mm}$. Moreover, a heating wire is installed around the curved surface of the target. It allows for frozen drops on the surface to melt and remove them or examine the fluid volume on the surface after the impact. For the latter, the mounting also contains a stepper motor which allows for rotation of the target surface in order to achieve multiple viewing angles of the sessile drop. In order to

analyse the impact, shadowgraphy recordings are captured by a high-speed camera with backlight illumination. Both components are placed outside the test section.

As shown in this section, the combination of icing wind tunnel, drop generation mechanism and impact surface enables the investigation of supercooled drops impacting on a solid surface with different drop sizes, varying temperatures and different impact velocities obtained from corresponding air flow velocities. However, some experiments and analysis also require the use of smaller additional setups which are introduced in the following.

3.2 Additional Installations for the Investigation of Supercooled Drops

The impact velocity of the drop and the air flow velocity are always interconnected due to the drop acceleration in the air flow. Moreover, the air flow on the surface interacts with the drop on the surface at any time throughout the impact. In order to achieve higher impact velocities without a superimposed air flow and achieve slightly higher impact velocities, a drop accelerator was developed. Furthermore, some important characteristics of the impact outcome could not be quantified from the recordings obtained in the wind tunnel. In particular, this concerned drops frozen in a thin splat on the surface. Hence, a precision scanning device was set up to resolve the height profile of these splats. They mainly occurred for the impact onto an ice target which were manufactured in a custom mold. In the following, the installations regarding the drop accelerator, the scanning device and the manufacture of ice targets are introduced.

3.2.1 Accelerator for the Impact of Supercooled Drops with High Velocities

Acceleration of the drops in the icing wind tunnel with high air flow velocities possibly causes a drop break-up due to unrestricted deformation of the drop induced by aerodynamic forces. The maximum impact velocity is limited by the relative velocity a drop can endure without disintegrating. Hence, for acceleration to impact velocities exceeding the terminal velocity of the drop, the relative velocity U_{rel} must not lead to aerodynamic Weber number exceeding $\mathrm{We}_{\mathrm{air}} = \rho_{\mathrm{air}} U_{\mathrm{rel}}^2 D_0 / \sigma \approx 10$, where ρ_{air} denotes the air density (Opfer et al., 2014). Keeping U_{rel} small enough during drop acceleration usually requires long distances and a successive increase in air flow velocity. However, inside the cooling chamber where the necessary temperatures for supercooling of the drop are achieved available space is limited. For higher drop acceleration over a shorter distance, a containment of the drop deformation which potentially leads to break-up during the process is vital. Hence,
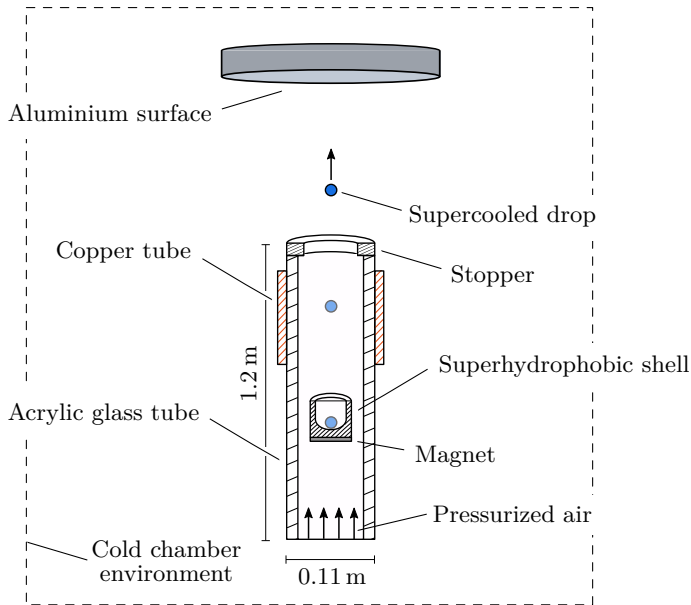
Figure 3.13: Setup for the acceleration of supercooled drops placed inside the cold chamber.

the drops are accelerated inside a 3D printed shell as depicted in Fig. 3.13. The shell bottom is curved allowing for some extension of the drop, yet limiting deformation which would lead to separation of the liquid. Since the drop needs to eventually separate from the accelerator shell without adhering to it, the shells inside is treated with a superhydrophobic coating. The acceleration is obtained by feeding pressurized air into an acrylics glass tube which propels the shell upwards. At the top of the tube, a stopper is installed which abruptly arrests the shell at the end. This stopper features a hole in the center through which the drop leaves the accelerator tube and travels further upwards. When the shell strikes the stopper, the drop possibly deforms significantly or nucleation is triggered. Hence, the drop needs to detach from the shell before it is stopped at the top. For this purpose, the shell is equipped with a magnet at the bottom. The upper third of the accelerator tube is encased within a copper tube. This way, the magnet induces an eddy current in the copper which in turn induces a magnetic field. Since this field acts opposing to the magnet, the shell is slowed down while travelling through the copper covered part of the tube. Meanwhile, the drop maintains its inertia and detaches from the shell favored by the weak adhesion to the superhydrophobic coating. Hence, the drop leaves the shell before the latter hits the stopper. Since the eddy current depends on the magnet velocity inside the tube, this braking system adjusts passively to any acceleration in the tube.

The pressurized air required for acceleration is fed into the tube at the bottom by a magnetic valve which also connects the tube to a pressure tank. Hence, the acceleration is determined by the opening time of the valve and the pressure inside the tank. The latter is adjusted with a pressure gauge. The pressure inside the tank is varied between 1 and 3.6 bar above the ambient pressure, resulting in drop velocities up to 20 m/s. Slightly above the air inlet, the tube has an aperture where the shell including the drop is introduced into the accelerator. During the acceleration process this opening is sealed to maintain the pressure inside the tube. The entire accelerator has a height of 1.2 m and points towards a surface which is installed at a distance of approximately 0.15 m from the stopper. Hence, the drop impacts onto a flat surface after acceleration. The impact targets are the same aluminium surfaces as installed in the wind tunnel. Similar to these experiments, the impact is recorded with a high-speed camera using backlight illumination. However, the analysis of the impact experiments with the accelerator is still limited to the observations from the high-speed recordings. If the drop freezes on the surface, its geometry might not be ascertainable from these images. Thus, a device enabling the additional examination of the impact outcome in three dimensions from a high precision scan is developed and introduced in the following subsection.

3.2.2 Scanner for Reconstruction of Frozen Splats Geometry on a Flat Surface
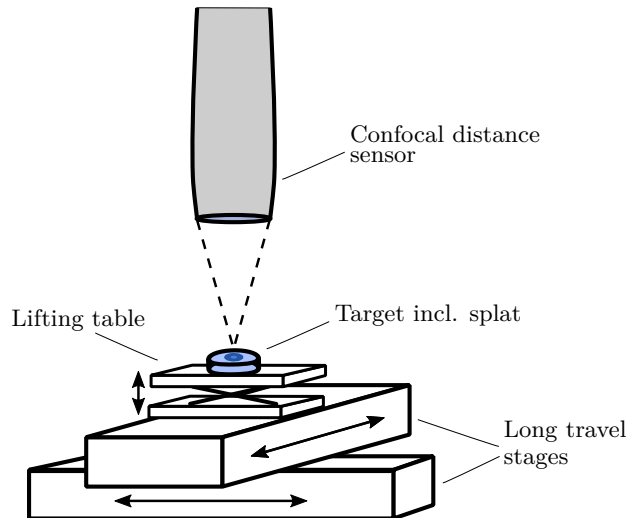
Figure 3.14: Setup for scanning surfaces and supercooled drops frozen into a splat.

When the supercooled drop freezes on the surface during impact, the formation of a thin splat on the surface is likely as shown in Sec. 4.2. The quantification of the splat geometry from the high-speed recordings is limited. The investigated drops typically spread over a length of $\mathcal{O}(10\,\mathrm{mm})$ and the lamella exhibits a thickness in the order of $\mathcal{O}(100\,\mathrm{\mu m})$. Thus, capturing the entire drop during impact entails a resolution which is not suitable for quantification of all splat dimensions. Additionally, the lamella in the middle of the splat is mostly obscured in a side view by the solidified rim. Hence, a scanning device was developed for the investigation of such thin splats.

The splat geometry is determined by measurements of a confocal distance sensor (*Micro-Epsilon IFS2405-1*). It is capable of measuring distances with a precision of $\pm 0.25\,\mathrm{\mu m}$ and is mounted facing downwards as shown in Fig. 3.14. Beneath the sensor, the surface containing the splat is placed on a precision lifting table. The latter is used to manually move the surface into the measurement range of the sensor (only $1\,\mathrm{mm}$) located approximately $10\,\mathrm{mm}$ above the surface. In order to quantify the height profile of the frozen splat, the surface, including the lifting table is moved by a system of linear stages. It consists of two positioning stages mounted orthogonal to one other. Thus, a complete scanning of the surface is possible by moving the surface and the obtained distance measurements can be composed to a spatially resolved height profile. During the scan, lateral movement of the surface is prevented by an adapter plate on top of the lifting table. Note that this plate is not illustrated in Fig. 3.14. The traversing system and the sensor are controlled remotely and the scan of one surface is fully automated, which is particularly important for the measurement of frozen splats on ice surfaces. In this case, the entire scanner needs to be placed in the cooling chamber in order to avoid melting during the scanning process. These ice surfaces are manufactured in a specific mold which is introduced in the next section.

3.2.3 Mold for Flat Ice Surfaces

The most important characteristic of the ice surfaces involved in the experiments in the wind tunnel is a planar impact surface which is free from any defects. Whereas the planarity of the surface is mostly determined from the geometry of the container in which the water freezes, smaller defects may arise from impurities in the water. Hence, the surfaces are manufactured from distilled water. However, defects also possibly arise due to gas dissolved in the water. Since ice is unable to solubilise air, the gas emanates from the solidifying water into the liquid phase as indicated in Fig. 3.15. If the freezing process is sufficiently rapid, the gas bubbles have no time to rise to a free surface and they become trapped in the ice. Additionally, if the solidification starts from several directions, the liquid phase gets trapped and arising gas bubbles form holes in the ice phase upon final solidification. Thus, a freezing process avoiding gas bubble defects requires slow and directional propagation of the freezing front. For this purpose, a mold for the
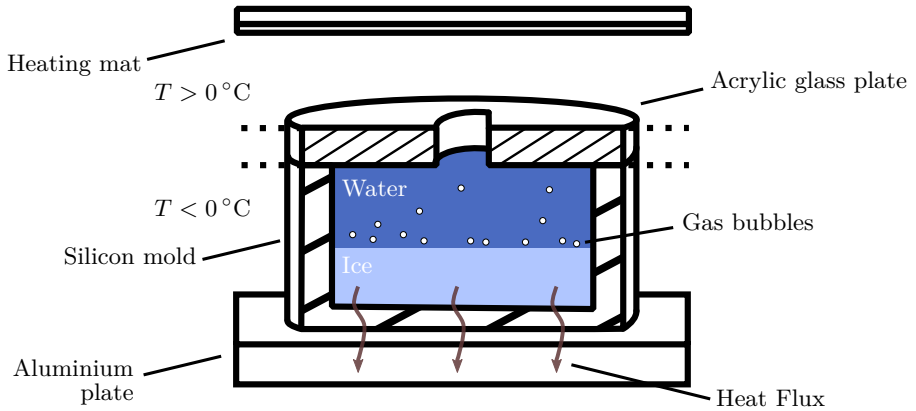
Figure 3.15: Single cell of the freezing mold used for the manufacture of ice impact targets

manufacture of ice surfaces from liquid water was developed. The entire mold is placed inside a freezer, which provides temperatures of approximately $-20\,°C$, causing the water to freeze. A single cell of this mold is shown in Fig. 3.15. The shape of the ice target is determined by a silicon mold with cylindrical cavities. Its flexibility and low adhesion to ice enable a gentle removing of the targets after freezing. The top of the cavities in the form is covered by an acrylic glass plate which features a hole in center of each freezing cell. It exhibits the shape of a truncated circle in order to form a pin on the solidified target. The pin is used for fixation and positioning of the target in the wind tunnel target holder and the scanning device. In order to enable the ascent of arising gas bubbles to the top of the mold, a freezing from bottom to top inside of the mold is ensured. This directional freezing is accomplished by establishing a comprehensive downward heat flux in the cell. For this purpose, the mold is placed on an aluminium plate and isolated from the sides in order to favour heat conduction through the bottom area of the mold. Note that the insulation is not depicted in Fig. 3.15. Additionally, the air temperature above the acrylic glass plate is kept constant just above $0\,°C$ with a regulated heating mat. Thus, the temperature gradient in the vertical direction ensures a directed heat flux. The areas with different temperatures are separated by the acrylic glass plate and the insulation next to the single cells of the mold. Once the solidification front reaches the top of the mold, gas bubbles may be enclosed, since not all of them are able to leave through the pin hole in the top plate. However, these defects are far away from the bottom and do not affect the integrity of the bottom ice layer which then serves as an impact surface in the experiments.

The setups introduced in the past sections enable the execution of drop impact experiments involving supercoooled water on different surfaces exposed to a cold air flow. High-speed recordings of the impact provide insight into the characteristics of the impact and their quantification. Moreover, the drops can be examined after their impact in order to determine parameters which elude the high-speed video recordings. The corresponding methods to obtain these parameters are introduced in the following section.

3.3 Execution of Experiments and Methods Involving Impact of Supercooled drops

Investigating a drop impact in the icing wind tunnel involves multiple steps which enable a controlled, unobstructed and repeatable execution of the experiments. In this chapter, the execution of experiments in the wind tunnel and the determination of important parameters is introduced. At first, steps necessary to prepare an experiment in the icing wind tunnel are described using the example of a single impact of a liquid drop onto an aluminium surface. Subsequently, a short outline of relevant quantities obtained from the high-speed recordings is depicted. Next, an approach to quantify the residual volume of the drop after splashing on the surface is introduced. Furthermore, additional steps for the investigation of a drop impact onto an ice surface and the following analysis of the frozen drop are described. Finally, a method is presented that enables the repeatable generation of drops having completed their first freezing stage before impact.

3.3.1 Conduction of a Drop Impact Experiment in the Icing Wind Tunnel

During the experiments, all involved materials related to the impact experiment and also the required measurement equipment are exposed to the preset temperature in the chamber. Although sensitive components are protected in custom protection boxes, for instance the high-speed camera and other electronic components, the cold chamber is not operated continuously over several days. It is cooled down anew on every measurement day which also enables easy maintenance of the drop generation mechanism (cf. Sec. 3.1.3). In a longer idle state, air is possibly drawn into its tubes which increases the risk of solidification inside the parts exposed to sub-freezing conditions and may cause air bubbles in the dripping drops. Hence, the air is removed by continuously pumping water through the water supply tubes every time before cooling down the chamber. Moreover, several components of the wind tunnel and the measurement equipment are sensitive to the cold temperatures during their operation. In particular, the pressure sensor used for velocity measurement exhibits a signal drift that varies as long as the sensor is not allowed to acclimatise to the current conditions. Hence, $20-30\,\mathrm{min}$ after a desired temperature in the

chamber is reached, the pressure sensor offset is corrected by a new calibration. The waiting period is also advantageous for all involved components of the wind tunnel in order to reach a temperature distribution as uniform as possible.

Once the temperature in the chamber is steady and all equipment adapted to it, the execution of experiments is started. The temperature of the pending drop, the air in the test section and the surface are controlled by the temperature in the chamber. Although a homogeneous temperature of all involved components is desired, local differences possibly cause differences of drop, air and surface temperature up to $\pm 1.5\,°C$. Hence, they are measured continuously throughout an experiment. Another monitored quantity is the air velocity in the test section, which is held approximately constant by setting the fan motor frequency to a corresponding constant value. In this configuration, the velocity typically fluctuates by $0.1\,m/s$. In order to start an experiment, the light is turned on, the high-speed camera is set to capture mode and the pump is activated, which leads to formation of a drop on the syringe needle. After dripping off, the drop travels through the wind tunnel until impacting onto the surface. At this point, the camera is triggered and the current temperature values are saved. Since it is not possible to determine the exact moment of drop detachment, the temperatures refer to the moment of impact. Clearly, at this moment the drop has already left the syringe so the measured value refers to the water remaining at the tip of the needle. In order to check if this temperature represents the temperature of the drop upon impact, two main effects were investigated.

First, the temperature measured after the impact must not vary significantly from the temperature the drop exhibits during its growth. An effect possibly causing a difference of these two measurements is evaporation of the drop (Stull, 2011). However, the air inside the chamber is inherently saturated, due to the newly initiated cooling on the start of every measurement day. Additionally, the drop is protected by the shroud pipe to avoid convective effects from the tunnel flow. Hence, the micro climate around the drop during growth is fully saturated and evaporating effects can be neglected. This assumption is also confirmed by temperature measurements recorded during detachment of several drops, which is shown in Fig. 3.16. During the time of this measurement, five drops drip from the needle. However, the temperature exhibits no visible alteration connected to the drop leaving the needle. The small overall temperature increase is attributed to the cold chamber feedback control. Hence, the temperature measured shortly after detachment (ca. $1\,s$) represents the temperature of the detached drop. Second, in the time between detachment from the needle and its impact onto the surface, the drop exchanges heat with the surrounding air flow. However, an estimation of the heat flux released to the slightly colder air flow revealed a change in temperature in the order of $\mathcal{O}(0.01\,°C)$ for a liquid drop, which is negligibly small.
In-between experiments, also the heating of the drop generation is active (cf. Sec. 3.1.3) in order to avoid nucleation of the water in the supply tubes. Since
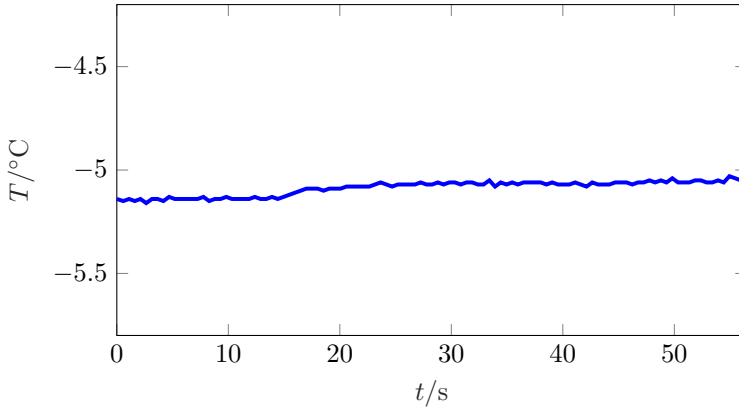
Figure 3.16: Temperature measurement of the thermocouple protruding from the syringe needle during detachment of five drops.

the water in the tubes close to the syringe is also supercooled, the probability of freezing increases with lower temperatures. Additionally, this risk continues to increase with the time the water is exposed to these temperatures. Hence, the supply is held at approximately $-8\,°C$, at which nucleation seldom occurs. Note that this temperature refers to the drop temperature measured by the corresponding thermocouple inserted in the syringe, since there are no additional sensors on the supply tubes. For experiments with lower drop temperatures the heating is turned off before the experiment and reactivated afterwards in order to keep the exposure short. The heating power can be adjusted remotely which enables adaption to different temperatures. Moreover, the power can be raised to a level sufficient to melt ice inside the tubes in case the water in the supply system froze during an experiment.

Shortly after impact, the light and the wind tunnel are turned off in order to minimize alteration of the sessile drop by thermal radiation and aerodynamic effects in case any further analysis is performed. Afterwards, the drop is removed from the surface with pressurized nitrogen in order to prepare the surface for the next experiment. However, in the time between impact and cleaning a solidification of the sessile drop is very likely. Additionally, the movement of the fluid on the surface induced by the nitrogen flow possibly cause nucleation of the drop. Hence, the heating wire around the surface (cf. Sec. 3.1.3) is used to achieve a surface temperature slightly above $0\,°C$ before the drop is removed. Thus, the drop adopts the surface temperature and frozen drops are melted. Moreover, solidification of liquid drops is avoided during removal, since they are no longer supercooled. Prior to the next experiment, the heating is turned off and the target cools down to the

ambient temperature in the chamber. Including the time for the target to reach the chamber temperature again, the execution of one experiment takes about 20 min.

3.3.2 Post-processing of High-speed Recordings

(a)

(b)
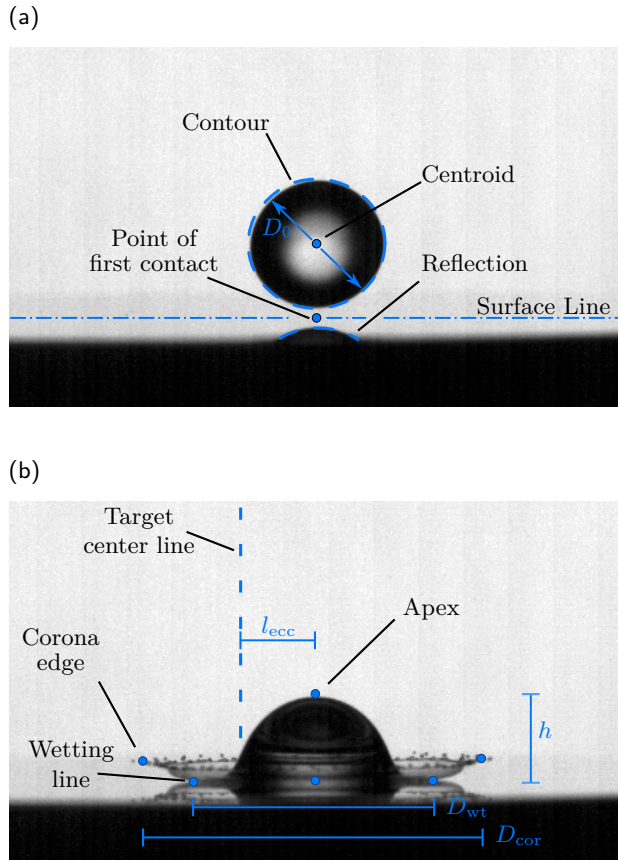
Figure 3.17: Characteristic points and dimensions obtained from the image processing algorithm during flight (a) and impact (b).

The recorded high-speed videos show a single experiment from a side view as seen in Fig. 3.17. They are analysed frame by frame with a custom image processing algorithm. This algorithm provides quantification of important characteristics of the drop movement during its approach towards the surface and the subsequent impact. Prior to the first contact, the centroid of the drop is determined and

tracked in multiple frames. An exemplary frame is depicted in Fig. 3.17a. A combination with the frame rate of the recording and the resolution of the images yields the impact velocity U_0. Additionally, the contour of the drop is determined in order to calculate the average drop diameter D_0, to estimate the volume of the drop, and to quantify possible drop deformations before impact. As the drop approaches the surface, its reflection becomes visible, which is used to determine the point of first contact and the surface contour in the slightly downwards viewing angle. The last frame before impact is also used to calculate the moment of first contact ($t = 0$) of the drop with the surface. This instant usually occurs in-between recorded frames and the last image recorded beforehand depends on the recording rate and the timing of the drop dripping off the needle. In order to determine the corresponding time of the following impact images, $t = 0$ is obtained from a linear extrapolation of the drop leading edge based on the impact velocity.

In the subsequent fluid movement during the impact, several other quantities are determined as shown in Fig. 3.17b. The liquid supercooled drops develop a corona splash upon impact. The emerging liquid film lifting from the surface is tracked by its outer edges. A combination of the points on the left and right side of the lifted film also yields the dimensions of the corona D_{cor}. Moreover, the three-phase contact line of the drop is tracked with the characteristic points at the junction of the drop and its reflection. Similar to the lifting film, the left and right points are combined to obtain the wetted diameter D_{wt}. The vertical movement of the drop is resolved by tracking the drop apex and relating it to the impact point in order to obtain the instantaneous height h. When the air flow is activated a stagnation flow develops at the center point of the surface and then the relative position of the drop to the stagnation point is important. Hence, the eccentricity of the drop l_{ecc} is determined from the distance of impact point and target center. Some important features of the impact are not available from the videos due to the limited resolution of the recordings or the imaging from a single single view. Hence, additional methods are required, for instance to determine the amount of fluid remaining on the surface after drop splashing.

3.3.3 Measurement of the Deposited Fluid after Splashing

In order to estimate the deposited volume (liquid or ice) remaining on the surface, the target is first heated to melt frozen drops which formed during or after the splash. When melted, the liquid recedes into a sessile drop, whose geometry is determined by the volume of the liquid and the substrate wettability. Several images of this sessile drop are then captured from different viewing angles by rotating the target (cf. Sec. 3.1.3). In this manner, any deviations from axial symmetry or off-centering are accounted for, increasing the precision of the determined volume in comparison to a single side view. These images are used for a three-dimensional reconstruction of the drop shape.

(a)
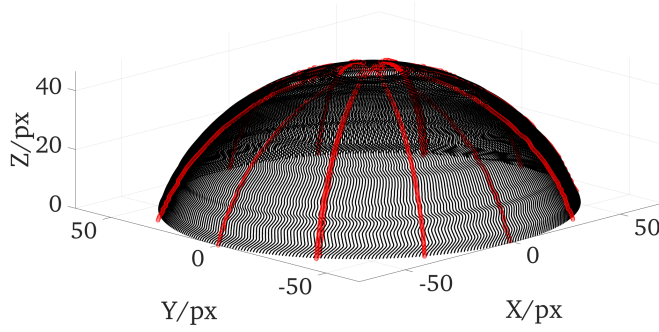
(b)
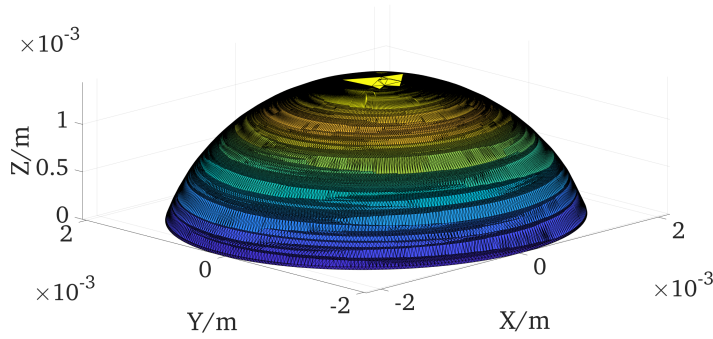
Figure 3.18: Reconstruction of the sessile drop from images with multiple viewing angles. a) Red dots of the point cloud represent data obtained from the images, black dots are obtained from a fit to a connecting curve. b) Triangulation of the point cloud.

The drop apex is used as a fix point to align the various contours obtained from each image. After arranging and scaling the contours into a single bulk object, they are used to create a point cloud of the drop as shown in Fig. 3.18 a). For this purpose, an elliptical curve is fitted to horizontal slices of the constructed object. Thus, the curvature of the drop surface is included in the reconstruction. Any deviation from an elliptic surface would occur most likely immediately adjacent to the surface, caused by pinning of the contact line. However, the undisturbed receding of the drop further reduces the probability of strong deviations of a non-elliptic shape. From the dot cloud, a triangulation of the enclosed volume is

performed, as illustrated in Fig. 3.18 b). The method is calibrated using metal spheres exhibiting a precision better than 10 μm in diameter. In order to estimate their volume, images between 0° and 180° are captured with an angular increment of 30°. During this calibration, a reconstruction of the sphere volume with a maximum deviation of 0.2 μl is achieved. Thus, the method enables a reconstruction of drop volumes with an uncertainty of ±0.2 μl. A discussion of findings obtained with this method from experiments with drops developing a corona splash is found in Sec. 4.1. However, the drop volume is only quantifiable with this method for molten drops and provides no information about the geometry in case of freezing after the impact. Hence, for an investigation of frozen splats, a different method is developed which is particularly helpful for the investigation of supercooled drops impacting onto ice. The method involves the scanning device and ice surfaces from the mold introduced in Sec. 3.2 and is introduced in the following.

3.3.4 Measurement of Frozen Drops on Ice Surfaces

Before investigating the frozen splats on the ice surfaces manufactured with the mold (cf. Fig. 3.15), the drop has to impact onto the surface in an experiment. For the most part, the execution is the same as for the impact on an aluminium surface as described above. However, since the drop always freezes solid on an ice surface it is inseparably connected with the surface afterwards. Hence, every target can only be used for one experiment. The target with the drop is removed and replaced with a new one which also enables further analysis of the surface. Additionally, it can be replaced by a dummy target which is an aluminium cylinder with the same dimensions. The alternative target is used to adjust the impact position of the drop at different air velocities with the movable mounting introduced in Sec. 3.1.3. Further analysis of the surface with a frozen splat is conducted with the scanning system introduced in Sec. 3.2. The target is placed on the scanner and a three-dimensional scan is obtained with the position data of the traversing stages and the height measurements of the confocal sensor. A full scan of a surface ($D_{\text{trg}} = 28 \, \text{mm}$) takes about 70 min, since the step size needs to be sufficiently small to resolve the frozen drop geometries. Such a long scanning time is inefficient since it takes three times longer than a single experiment. Hence, a cycle including the scan of four lines through the drop center with an angle variation of 45° is implemented which reduces the time to a few minutes. In order to move through the drop center, its coordinates are estimated prior to removing the surface from the wind tunnel. Sitting in the target mounting, the middle of the frozen splat is determined from two orthogonal viewing angles achieved by rotating the target with the stepper motor (cf. Sec. 3.1.3). The same orientation of the target during the experiment and the scan is ensured by the notch of the pin at the bottom of the surface (see Fig. 3.15). With a partial scan, the drop contour is not fully resolved, but values concerning the frozen rim and lamella are obtained. This way, the dimensions of drops freezing shortly after impact on ice surfaces in various

conditions are quantified. The discussion of these findings is found in Sec. 4.2.
In another investigation, the freezing of drops even occurs before the impact, which
leads to the impact of partly frozen drops. In the scope of this dissertation, a
method enabling the investigation of these kind of (mushy) drops is developed
which is introduced in the next section.
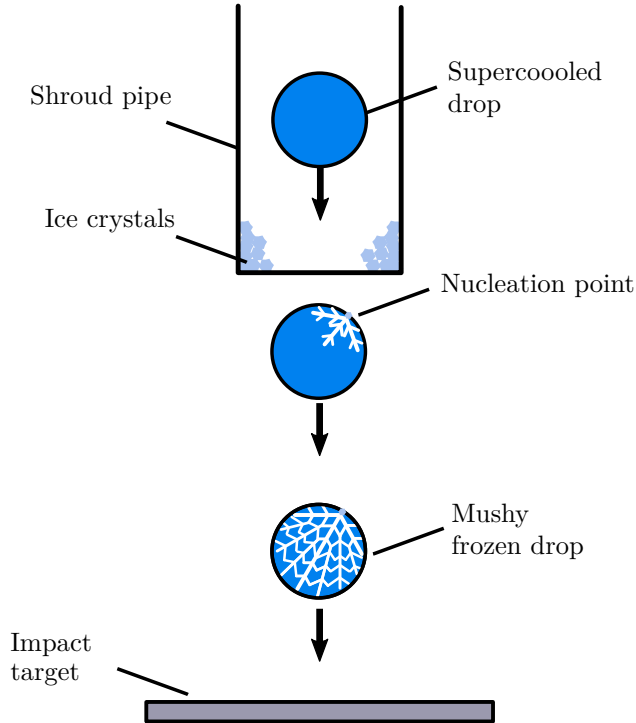
Figure 3.19: Forced nucleation procedure for the reproducible generation of mushy
frozen drops (Gloerfeld et al., 2023).

3.3.5 Forced Nucleation of Supercooled Drops Prior to Impact

Mushy frozen drops are generated similar to the method used for the impact of
a liquid supercooled drop dripping from the syringe needle in the wind tunnel.
However, upon impact, the drops also contain dendrites (mushy phase) which form
during the first freezing stage. In order to obtain this mushy phase inside a free
falling drop, the dendritic freezing has to start and finish during the drop descent
towards the impact target. For this purpose, several small ice crystals are pinned to
the end of the shroud pipe as depicted in Fig. 3.19. In this manner, the drop makes
contact with some of the ice crystals when leaving the pipe, which immediately

results in dendritic freezing of the supercooled drop. This method ensures nucleation of the supercooled drop and also provides enough time for the drop to finish the dendritic freezing stage before impact. The typical time for dendritic freezing of the drop is estimated with the propagation velocity of dendrites in supercooled water (Shibkov et al., 2003). For the investigated drop dimensions and temperatures in this study, the mushy freezing of a drop is estimated to finish within $\mathcal{O}(10\,\mathrm{ms})$. This process is significantly faster than the time it takes the drop to reach the impact target after nucleation, $\mathcal{O}(100\,\mathrm{ms})$. Hence, all drops in the present study have finished the first phase of supercooled solidification upon impact.

The drops generated with the current method vary in initial temperature (controlling its final frozen fraction) as well as in impact speed. While the temperature is indirectly controlled through the cold chamber conditions, the impact speed U_0 is varied through a varying airflow velocity. Upon impact, the mushy drop has always acquired a temperature of $0\,^{\circ}\mathrm{C}$, since the first phase of solidification of a supercooled drop results in a mixture of ice and remaining liquid being in thermal equilibrium at the melting temperature. The initial supercooling ΔT is governed by the ambient conditions inside the chamber and the micro-climate around the suspended drop in the shroud pipe.

The supercooling ΔT also determines the amount of ice formed during the dendritic freezing stage of the drop. During formation of dendrites, the supercooled fluid releases its latent heat of solidification into the surrounding water. When reaching the melting temperature in the remaining water, the development of dendrites ceases, leaving the ice-water mixture in thermal equilibrium as described in Sec. 2.2.3. In this state, the fraction of ice contained in the drop can be obtained by Eq. (2.33).

The entire process from nucleation to completion of the first stage is completed during the fall of the drop. Therefore, the heat exchange with the surrounding air is the only effect possibly causing a deviation from the estimated ice fraction. Since the mushy phase in the drop always remains at the melting temperature, the colder air absorbs energy from the drop, entailing a continuing growth of a uniform ice layer. The heat released to the surrounding air flow is mainly dependent on the drop size, air temperature and air flow velocity. Hence, the highest amount of additional mass would develop for the lowest temperature and highest air flow velocities. In a conservative estimate, a completely mushy frozen drop travelling from the point of nucleation to the impact target with the maximum relative velocity occurring in the wind tunnel experiments is considered. A computation of heat transferred to the air flow in this scenario revealed that the additional ice developed due to the heat flux would increase the amount of ice attributed to dendritic freezing by a maximum of $3\,\%$ for the conditions prevailing in the experiments of this dissertation. Note that the drop in the experiment will accelerate during its descent, which leads to even less time for the heat exchange than assumed in the above estimation. Hence, the actual amount of additional ice

is even lower than the estimate. For this reason, the ice development due to heat exchange with the air flow is neglected in the calculation of the mushy phase ice fraction ξ_{ice}.

All off the methods introduced above aid in the investigations of drop experiments conducted in the icing wind tunnel which provides a broad parameter range. However, the impact velocity is always connected to the air flow velocity achieved in the tunnel and it is also interesting to investigate high impact velocities without a constant air flow. Moreover, the impact velocity in the wind tunnel is limited since drop break-up needs to be avoided. Higher impact velocities without a superimposing air flow are accomplished in the drop accelerator introduced in Sec. 3.2 and the procedure for a corresponding experiment is briefly outlined in the following.

3.3.6 Impact Experiments with the Drop Accelerator

Similar to the generation of drops in the wind tunnel, the drops investigated with the accelerator form on a syringe needle supplied with water by a tube system and a micro-pump. However, the temperature is not measured during formation on the needle, since the water in this supply system is not supercooled. Hence, the drops are placed in the accelerator shell inside of the cold chamber and cool down subsequently. In order to monitor the temperature of the drop, a thin thermocouple (0.25 mm diameter) is immersed into the drop. Once the drop reaches the cold chamber temperature, the thermocouple is pulled out and the shell is moved into the accelerator tube with a slider system. This system ensures quick and smooth insertion of the shell to the tube, which keeps the time between the temperature measurement and the impact small ($\approx 5s$). Similar to the experiments in the wind tunnel, the saturated environment in the chamber prohibits significant evaporation effects and a possible corresponding temperature change. After the shell is placed in the accelerator, the magnetic valve is triggered and pressurized air accelerates the drop as described in Sec. 3.2. Eventually, the drop impacts onto a surface mounted upside down and the drop impact is recorded with a high-speed camera and backlight illumination. The post-processing provides the same quantities as outlined in Sec. 3.3.2.

The installations and methods introduced in this chapter enable controlled, reproducible experiments over a wide parameter range. The investigation of drops exhibiting solidification at different times of the impact and a superimposing air flow provide new insight into the physics involved in the impact of supercooled drops onto cold surfaces. The findings obtained from the corresponding observations and their interpretation is discussed in the following chapter.

4 Results

Within the scope of this dissertation experiments regarding liquid drops impacting a surface and experiencing different moments of nucleation are investigated. The findings of these investigations are presented in the current chapter. First, the outcome of a liquid drop on an aluminum surface is analysed. Exhibiting a significant freezing delay, the drops develop a corona splash and interest is drawn towards the development of the fluid flow and the ejection of mass in Sec. 4.1. Moreover, the influence of drop deformation caused by the surrounding air flow is analysed with respect to the early spreading dynamics and the maximum spreading. In the following Sec. 4.2, the impact of supercooled drops on a planar ice surface is examined. Since the solidification of the drop is initiated upon first contact with the ice, the dendritic freezing interferes with the spreading dynamics of the drop, which is the focus of this investigation. In the last section (Sec. 4.3), the impact of a drop which already experienced the first freezing stage is examined. Emphasis is placed on the impact behaviour of such a drop, since to the author's knowledge such an impact has never been investigated before. Moreover, from the impact, conclusions are drawn regarding the rheological properties of the ice-water mixture with respect to its frozen fraction.

4.1 Supercooled Drops Impacting onto a Surface Free of Ice in a Superimposing Air Flow[1]

The very beginning of ice accretion caused by supercooled drops on technical surfaces often involves liquid drops impacting onto cold metallic surfaces. The statistical nature of nucleation entails a freezing delay of these drops, which renders various fluid movements possible before solidification occurs. A simultaneous movement of the affected surface additionally leads to an airflow being superimposed on the impact hydrodynamics. However, the fluid behaviour during the first moments of impact greatly determines the shape and amount of fluid involved upon freezing, hence also the dynamics of ice accretion. In order to gain insight into the characteristics of this liquid impact, investigations of drops impacting onto an aluminium surface with and without a co-flow were conducted. The most important findings and their influences are discussed in this section. In an order

---

[1]Parts of this chapter are published in Gloerfeld et al. (2021), used under CC BY 4.0. The contents of the article have been edited and/or extended for this dissertation.

following the temporal sequence of the impact, the deformation of drops prior to impact caused by the superimposed air flow is discussed first. Second, the extent of the developed splash upon impact is examined, followed by findings regarding the deposited mass remaining on the surface after splashing. Finally, the maximum spreading of the drop with regard to its initial deformation is reviewed.

4.1.1 Drop Deformation Prior to Impact

In some cases, the drops investigated in this dissertation impact at high velocities, having been accelerated by high air flow velocities. The presence of the air flow leads to significant deformation of the drop prior to impact. The consequences of this deformation on the impact hydrodynamics is significant and discussed in the following section.

(a)   (b)

$t = $ -0.05 ms   Air Vel. $= 0$ m/s $t = $ -0.05 ms   Air Vel. $= 25$ m/s

3 mm   3 mm
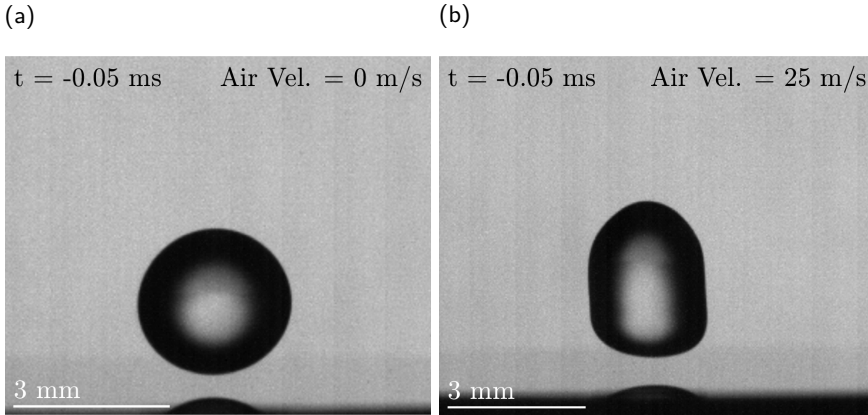
Figure 4.1: Drop deformation before impact due to acceleration in the surrounding air flow. Without a co-flow the drop impacts with a spherical shape (a) and in an air flow with $U_{air} = 25$ m/s the drop exhibits deformation (b). Both drops are of similar volume ($V_0 \approx 14.1$ µl).

To illustrate the drop deformation, two drops immediately prior to impact are visualized in Fig. 4.1. The drop in the left photograph of this figure impacts approximately with its terminal velocity, i.e. without an airflow present before and during the impact. The drop in the right photograph is additionally accelerated in a co-flow with $U_{air} = 25$ m/s. Four features are immediately apparent. The drop is strongly deformed, exhibiting a flattening of the lower surface, a stronger curvature on the upper surface, an elongation normal to the surface and a slight asymmetry. These features become even more apparent in the picture sequences

presented in Fig. 4.2, showing a drop with an impact velocity of $U_0 \approx 9.5$ m/s in an air flow with $U_{\mathrm{air}} = 25$ m/s. Here, it is assumed that the aerodynamic drag
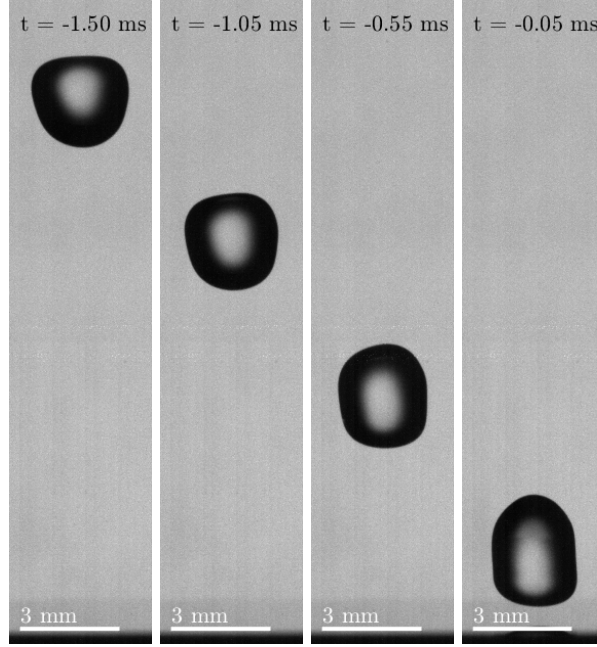
Figure 4.2: Image sequence of a drop approaching the impact surface with $U_0 \approx 9.5$ m/s in an air flow with $U_{\mathrm{air}} = 25$ m/s.

changes from a vertically downward force acting on the drop far from the wall to a vertically upward directed force as the drop is decelerated in proximity to the wall. Correspondingly, the stagnation end of the drop is flattened and the wake end exhibits suction and a bulging, the stagnation and wake ends changing as the drop approaches the substrate.

The role of aerodynamic forces in drop deformation is evident from two of the drop shape alterations. First, the elongation of the drop along its vertical axis changes as the drop approaches the surface, since the direction of the aerodynamic forces changes. In order to quantify the increase in length, the drop shape in the high-speed recordings is tracked before the impact (cf. Fig. 3.17). Together with the frame rate of the recording, the elongation speed U_{el} in the vertical direction is averaged from first to last image of the captured drop descent. The elongation velocities exhibit values in the order of $3 - 5\%$ of the general drop velocity U_0, obtained from the tracking of the centroid. The velocity U_0 exhibits no significant change as the drop approaches the surface. Hence, the elongation

effect on the general impact speed is negligible, although the change in drop shape represents new conditions for the fluid flow developing upon impact. Considering the elongation as characteristic for a flow inside the drop acting against the surface tension, the elongation velocity is used to calculate a Weber number of elongation $We_{el} = \rho U_{el}^2 D_0/\sigma$. The aerodynamic effects inducing this flow inside the drop need to overcome the surface tension and the relation of these forces is represented by an aerodynamic Weber number $We_{air} = \rho_{air} U_{rel}^2 D_0/\sigma$, where $U_{rel} = U_{air} - U_0$ is the difference between maximum velocity of the undisturbed air flow U_{air} and the impact velocity. The drop deformation is investigated for drops impacting at different temperatures and impact velocities achieved in corresponding air flow conditions. The paramter range covered in this study is summarized in Tab. 4.1.

Table 4.1: Test matrix of parameter range covered in studies regarding impact of supercooled drops on an aluminium surface in the icing wind tunnel.

ΔT /K	U_0 /(m s^{-1})	U_{air} /(m s^{-1})	D_0 /mm
3.3 to 13.8	4.1 to 9.5	0 to 25	2.6 and 3

In Fig. 4.3a the correlation between these two Weber number is shown for all conducted experiments. It is visible that the We_{el} and We_{air} exhibit a similar order of magnitude, which suggests that the basic acting forces are accounted for. Moreover, an increase in We_{el} for increasing We_{air} indicates that the elongation velocity depends on the relative velocity of the drop and the airflow during its approach towards the surface. However, the increasing scatter for higher We_{air} implies significant uncertainty in a direct correlation of both parameters. Further, it is not clear whether the elongation of the drop is induced by shear forces of the air flow or local pressure differences of the arising air flow around the drop. Additionally, the vertical elongation is often accompanied by a light vertical asymmetry (cf. Fig. 4.1b) which is neglected when calculating U_{el}. It can be attributed to the fact that the drop does not always impact exactly at the stagnation point of the gas co-flow on the target surface. Falling a distance of approx. 70 cm from entering the air flow to impact and no adjustment of the target, the impact position varied between $\pm$ 0.5 cm from the target center. Considering the flow field on the target (cf. Fig. 3.10), an asymmetric aerodynamic force on the drop acting away from the surface seems plausible.

Second, the deformation of the drop front is characteristic for drops impacting in a co-flow with high velocities. It is quantified for the last image before the drop impacts the surface in terms of a drop front curvature κ. For this purpose, the radius distribution of the deformed drop is determined and the curvature is

(a)

(b)
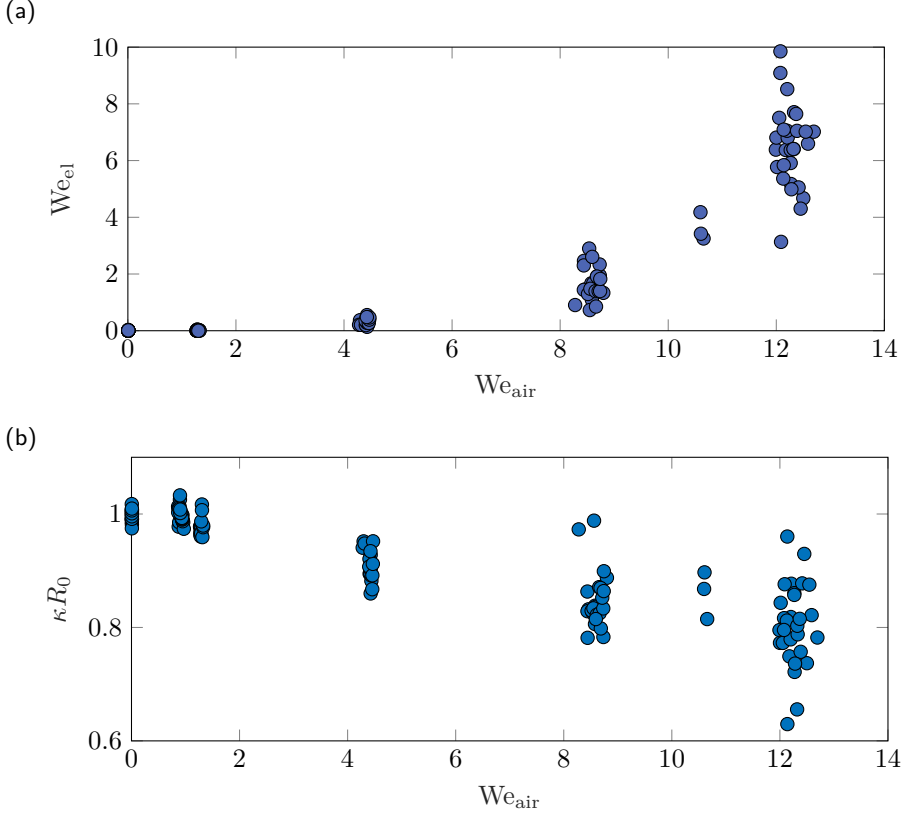
Figure 4.3: Deformation of the drop with respect to the aerodynamic Weber number We_{air}. Vertical elongation velocity of the drop is considered in terms of We_{el} (a) and dimensionless curvature of the drop front as κR_0 (b).

averaged from the derivative of this distribution for an angle of $\pm 75°$ around its vertical axis. As seen in Fig. 4.3b the dimensionless curvature κR_0 decreases with increasing We_{air}, suggesting that a higher relative velocity promotes a flattening of the drop at its front. The flattening is most likely attributed to an increased pressure at the drop front caused by the pressure field of the air flow above the surface and the stagnation pressure of the air flow around the drop. However, similar to the deformation velocity, the scatter of curvature values increases for high We_{air}. Thus, a direct prediction of the front curvature is not possible with the present data. The scatter possibly arises due to the characteristic air flow in the drop vicinity which is unknown for the present study. Hence, the aerodynamic forces affecting the drop shape are not completely clear from the general flow field.

In order to analyse the drop deformation in detail a quantification of the combined flow, for instance in a numerical simulation, may provide more insight. Moreover, general uncertainties may arise from the two-dimensional image of the drop, which does not capture three-dimensional effects. Especially in an off centered impact of the drop in the axisymmetric air flow, these effects might entail deformations of the drop obstructed by its maximum dimensions in the obtained images.

Regardless of the cause of the drop deformation, especially the lower flattened drop front represents a vital change in boundary conditions of the flow emerging shortly after first contact with the surface. This shape change presumably affects the development of the expanding liquid lamella ejected from the drop impact. In order to quantify the effect of drop deformation before impact on this expanding liquid lamella, the radius of the drop as it spreads on the surface (wetted area) is evaluated.

Starting with the case of an impacting spherical drop as a reference, the radius of the wetted area during the initial kinematic stage of impact is given as $r \propto \sqrt{t}$ (Yarin, 2006) as introduced in Sec. 2.1.1. It is obtained simply by truncating a sphere at a radius decreasing linearly with time and examining the radius of the cut cross-section (assuming constant drop velocity upon impact). This leads to the dimensionless relation

$$\bar{r}(\bar{t}) = b\sqrt{\bar{t}_R} \tag{4.1}$$

whereby $\bar{r} = r/R_0$ is the dimensionless radius, $\bar{t}_R = tU_0/R_0$ the dimensionless time and b a dimensionless proportionality constant. R_0 is the radius of the spherical drop. Considering now the impact of a deformed drop, its wetted radius upon impact can be estimated using Eq. (4.1) with b being of the order $\mathcal{O}(2)$ (Rioboo et al., 2002). If now the radius of the lower drop surface differs significantly from the spherical value R_0, then the value of b will also differ. By applying a least square fit to the wetting radius growth with time obtained from the evaluation of the high-speed recordings, b can be determined for every impacting drop event. This experimental result is shown in Fig. 4.4, indicating that b decreases for increasing values of the dimensionless curvature κR_0; i.e. when the drop lower surface flattens before impact, the spreading of the drop on the surface after impact increases in velocity.

A first order model for the quantity b is proposed as

$$b = \frac{b_0}{\sqrt{\kappa R_0}}. \tag{4.2}$$

where b_0 corresponds to the proportionality constant of a spherical drop marked with a vertical dashed line in Fig. 4.4. A least square fit of Eq. (4.2) providing $b_0 = 2.05$ is plotted in Fig. 4.4 as a straight, solid line. The value for b_0 agrees very well with Rioboo et al. (2002), who also suggests a value of $b_0 = 2.05$ for spherical drops (at $\kappa R_0 = 1$). Note that the original value given in their work is obtained
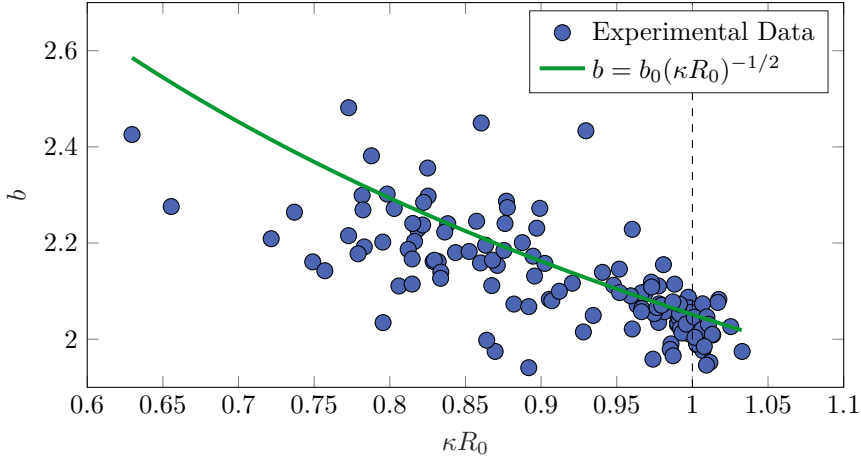
Figure 4.4: Proportionality constant b as a function of the dimensionless curvature κR_0 of the impacting drops lower surface.

with a different scaling, which requires a conversion of the value with the factor $1/\sqrt{2}$ in order to compare it to the findings of the present study.

Finally, inserting Eq. (4.2) into Eq. (4.1) leads to a relation for the wetted area $r(t)$ no longer dependent on R_0 but on κ:

$$r(t) = b_0 \sqrt{\frac{tU_0}{\kappa}};$$ (4.3)

thus, supporting the hypothesis that the initial flow on the surface is governed by the curvature of the lower drop surface instead of the radius representative of its volume, R_0. Note, that the $\sqrt{\kappa R_0}$ dependence of the model shown as a green line in 4.4 does not represent the best fit to the data, but is considered as a self-evident solution leading to Eq. (4.2) with b_0 as the only fitting parameter. Hence, a drop with a flattened front exhibits a faster spreading on the surface during the kinematic phase; a finding that coincides with a recent study of Q. Liu et al. (2021). The scatter of the data in Fig. 4.4 is likely influenced by the fact that the experimental values were obtained from a single projected side view of the impacting drop from the high-speed recordings. An observation of the spreading from the top or bottom perspective would presumably provide more consistent data of the average spreading velocity. However, Fig. 4.4 clearly reveals a dependency of b and the local drop curvature κ agreeing with Eq. 4.2.

An accurate evaluation of the kinematics of spreading, accounting for the local drop curvature is also necessary for an improved description of the conditions for the corona development and splash, and thus the fluid volume remaining on the surface. The splashing behaviour and important parameters determining its development are analysed in the following section.

4.1.2 Splashing Behaviour of Supercooled Drops Impacting on a Dry Solid Surface

The supercooled water drops examined in this study exhibit a corona splash upon impact, which is not immediately self-evident. At temperatures around $20\,^\circ$C a drop impacting with comparable size and impact velocity would exhibit a prompt splash or deposition (Palacios et al., 2012). The change into the corona splash regime is attributed to the low temperature of the water drops. When water is supercooled, its viscosity increases significantly, as described in Sec. 2.2.1. According to Roisman
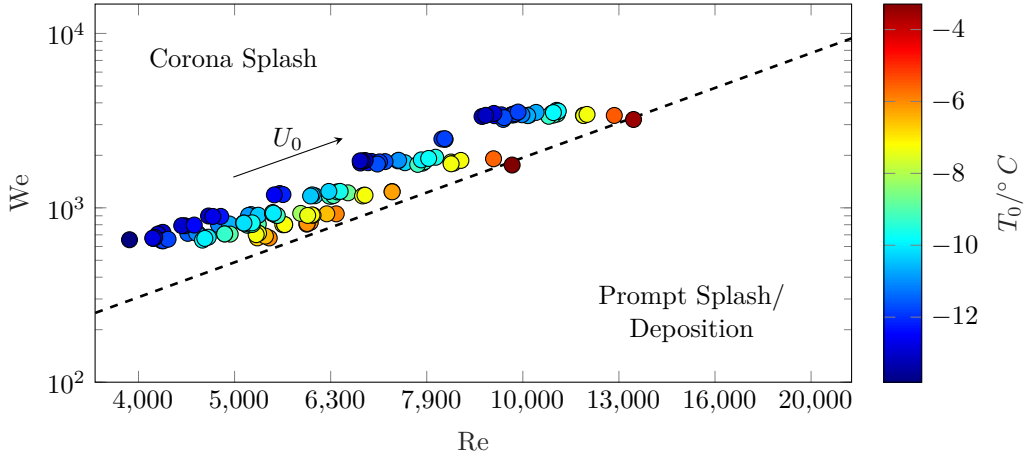
Figure 4.5: We and Re of all investigated drop impacts. The marker color indicates the drop temperature which is also accounted for in the properties used to calculate the dimensionless numbers. The dashed line marks the critical Ohnesorge number $\mathrm{Oh_{cr}} = 0.0044$.

et al., 2015b, the threshold parameters for the prompt/corona splash regimes is well-defined using a critical Ohnesorge number $\mathrm{Oh_{cr}} = \eta/\sqrt{\rho D_0 \sigma} = 0.0044$ (cf. Sec. 2.1.2). A corona splash is predicted for values larger than $\mathrm{Oh_{cr}}$. Considering the change in fluid properties due to supercooling, this condition is fulfilled for all drops investigated in this study, as illustrated in Fig. 4.5. This figure shows the Weber number $\mathrm{We} = \rho U_0^2 D_0/\sigma$ of all examined drop impacts plotted over the corresponding impact Reynolds number $\mathrm{Re} = \rho D_0 U_0/\eta$, where U_0 is the impact

velocity of the drop normal to the target. The critical Ohnesorge number is shown in this figure as a dashed line. The variation of impact parameters is the same as listed in Tab. 4.1.

The drop temperature, represented in Fig. 4.5 by the symbol color, indicates that a change in temperature results in a significant change of the Reynolds number Re; however, the Weber number We is hardly affected, since the fluid properties contained in We (ρ, σ) only change slightly. Since the Ohnesorge number is independent of the impact velocity, the transition to the corona splash regime is merely caused by the fluid properties and the drop diameter. As indicated by the arrow in Fig. 4.5, an increasing impact velocity entails a transition to higher We and Re, yet no transition to the other splashing regime occurs. Considering a change of Oh due to drop size, a prompt splash/deposition of a supercooled drop $(T_{\mathrm{drop}} < 0°\mathrm{C})$ is only possible for large droplets. In fact, according to this threshold, supercooled drops smaller than $D_0 = 2.2\,\mathrm{mm}$ will always exhibit a corona splash on a smooth surface. Moreover, larger droplets will also develop a corona splash for a relatively small increase in supercooling.

Observations of the Splashing Phenomenon of Supercooled Drops

(a) $U_0 \approx 4.2\mathrm{m/s}$, $T_0 \approx -5°\mathrm{C}$

(b) $U_0 \approx 4.2\mathrm{m/s}$, $T_0 \approx -13°\mathrm{C}$

(c) $U_0 \approx 10.5\mathrm{m/s}$, $T_0 \approx -5°\mathrm{C}$

(d) $U_0 \approx 10.5\mathrm{m/s}$, $T_0 \approx -13°\mathrm{C}$
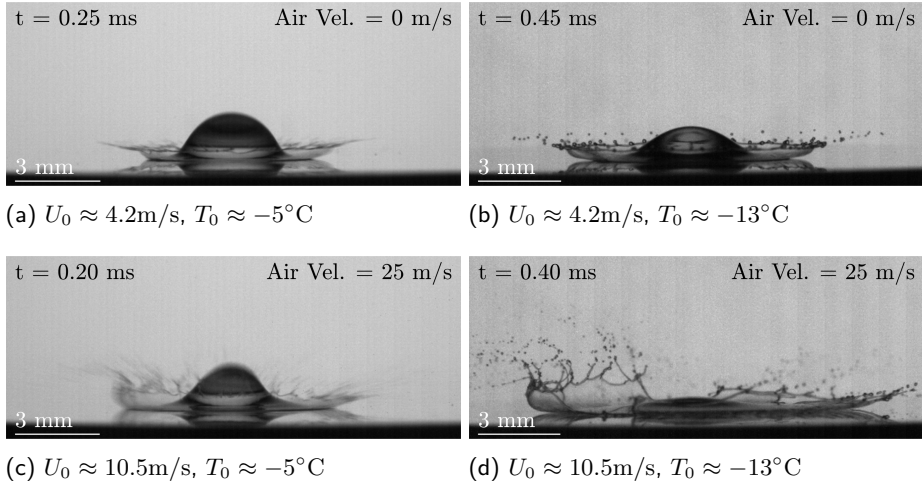
Figure 4.6: Comparison of the splashing extent at the instant before breakup among four drops $(D_0 = 3\,\mathrm{mm})$ with different drop temperatures and impact velocities.

Although all drops observed in the present study impact with a corona splash, the extent of the splash differs with temperature and air flow velocity, i.e. impact velocity. This change is observable qualitatively in Fig. 4.6, which shows the instant before the thin film of the corona breaks up for the highest and lowest

temperatures and impact velocities, respectively. Comparing Fig. 4.6a and 4.6b, a slight influence of the temperature on the splash is noticeable. The crown of the corona of the colder drop extends farther away from the impact position just before breakup. We assume, that the increased time until breakup and the ensuing increased extent of the splash originate from a more stable film during crown formation; the stabilization presumably being a consequence of the increased viscosity at lower temperatures.

A higher impact velocity will increase the extent of the corona distinctly. When comparing Fig. 4.6(c) and (d), a change due to an increased impact velocity is observable. For the higher velocity, the film of the corona spreads faster. An additional increase of supercooling enhances the spreading of the corona even more. Again, the uprising film is stable for a longer period of time, providing more time for its expansion. The asymmetries observed in the photographs of Fig. 4.6(c) and (d) can be attributed to a corresponding drop deformation before impact and the wall tangential flow superimposed on the splashed drop. This asymmetry in the corona development hinders a detailed analysis of the corona extend up to its breakup. Hence, an additional measurement series is conducted with the drop accelerator described in Sec. 3.2 in order to reduce the influences on the impact process.

Lifted Sheet Development Until Break-up of a Corona Splash

(a) $U_0 \approx 9.1\,\mathrm{m/s}$, $T_0 \approx -5°\mathrm{C}$ (b) $U_0 \approx 9.3\,\mathrm{m/s}$, $T_0 \approx -11°\mathrm{C}$
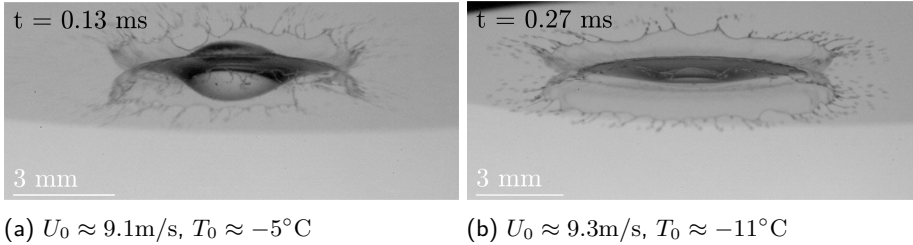
Figure 4.7: Comparison of corona extend shortly before the moment of liquid sheet break-up of two drops ($D_0 = 2.3\,\mathrm{mm}$) impacting without a co-flow. The drops are accelerated upwards towards the impact surface with a drop accelerator.

The liquid film of the corona splash exhibits a large area prone to drag or high pressure areas paired with low inertia. The arising airflow and its fluctuations in the tunnel represents a crucial disturbance to the symmetry of the corona shape. Moreover, an asymmetric drop deformation during its descent towards the surface caused by the air flow might influence the perfectly symmetric development of the

liquid film due to an erratic flow in the lamella. In contrast, the uprising liquid sheet (corona) exhibits a more symmetric form when accelerated upwards towards a target as shown in Fig. 4.7. In comparison to Fig. 4.6 (c) and (d), this already underlines the influence of the air flow on the asymmetric splash.

The experiments with the drop accelerator involved drops impacting with parameters according to the test matrix in Tab. 4.2. With the more symmetric

Table 4.2: Test matrix of parameter range covered in studies regarding impact of supercooled drops on an aluminium surface with the drop accelerator.

ΔT /K	U_0 /(m s^{-1})	D_0 /mm
5 to 13	5.6 to 18	2.3

corona development, the viscosity influence on the splashing extend conditioned by the different temperature is more evident, as seen from the examples in Fig. 4.7. In order to combine multiple influences in a physical model, the corona extent is investigated with regard to the splashing parameter of Riboux and Gordillo (2014) introduced in Sec. 2.1.2.

According to their theory, the corona propagation during drop impact onto a dry smooth substrate is governed mainly by the inertia of the flow in the lamella, surface tension and aerodynamic effects acting on the propagation of the contact line. This propagation is described using the dimensionless parameter β, defined in their work as the ratio of the aerodynamic lift force acting on the spreading lamella to the surface tension force. A critical value $\beta^\star \simeq 0.14$ is given as the splashing threshold. Hence, a splash occurs, if the impact parameters satisfy the condition $\beta > \beta^\star$. It should be noted that the impact parameters in this study also satisfy this condition of the corona generation on a solid substrate, caused by the aerodynamic stresses in the fast propagating contact line. Assume now that any deformation of the drop prior to impact also causes a change in wetting radius propagation and therefore in the spreading velocity of the lamella. Hence, the expression for the tangential velocity of the lifting sheet U_e must be adjusted with the correction term from Eq. (4.2), i.e. $U_{e,\kappa} = U_e/\sqrt{\kappa R_0}$. Additionally, the radius R_0 is replaced by the inverse of the curvature κ in Re_R, Oh_R yielding $\mathrm{Re}_\kappa = \rho U_0/(\eta\kappa)$, $\mathrm{Oh}_\kappa = \eta\sqrt{\kappa/(\rho\sigma)}$ and in the term for the sheet thickness H_e i.e. $H_{e,\kappa} = H_e/(\kappa R_0)$. Note that all β values considered in this section are calculated using this correction according to the determined front curvature of the drops.

Since β includes the major influences responsible for the occurrence of a splash, it possibly also combines crucial factors for the development of the uplifting sheet. This hypothesis is reviewed considering the sheet geometry in the moment t_{BU} in which instabilities in the film lead to cavities and subsequent break-up. The

corresponding values of t_{BU} are obtained from the high-speed recordings. Note that the values from the image recognition refer to the last captured frame of the video (record rate 43000 fps) in which no cavities in the sheet are visible. Fig. 4.8 shows
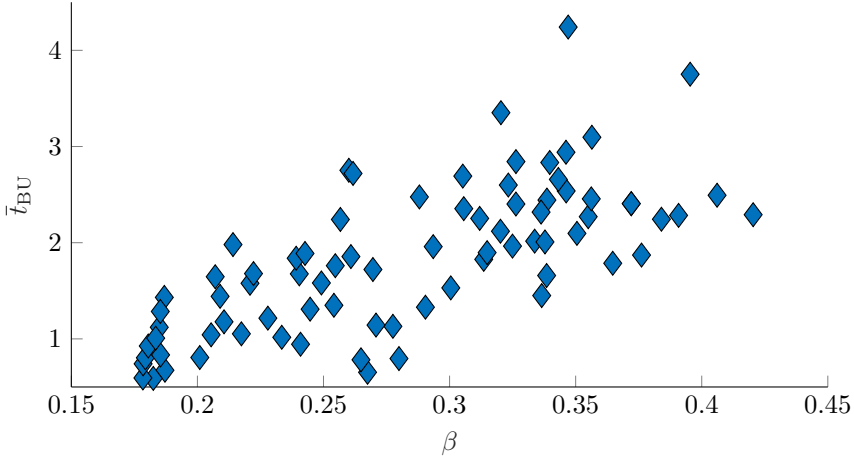
Figure 4.8: Moment of breakup $\bar{t}_{BU}$ obtained from the high-speed recordings plotted against β

the dimensionless time from impact to sheet breakup $\bar{t}_{BU} = t_{BU} U_0 / D_0$ plotted over the splashing parameters β. It is visible that for increasing β the breakup process emerges at later times, suggesting a more stable film and possibly more fluid being involved in its development. Thus, considering that β monotonically increases with the impact velocity U_0, the drop diameter D_0 and the fluid viscosity η, an increase in each of these quantities will lead to a more stable uplifting film. Here, the influence of U_0 is the strongest factor with $\beta \propto U_0^2$ in the range of the present values. These findings conform with the qualitative interpretation of the wind tunnel experiments shown in Fig. 4.6 even though they are obtained with a superimposed air flow. Despite the clear trend towards longer times, the determined values exhibit significant scatter, which may be attributed to either the method or the physics of the breakup process. First, the moment of breakup is determined manually in the videos based on the occurrence of cavities in the film. However, the liquid film in the back is often partly obscured by the impacting drop in the middle (cf. Fig. 4.7a). Cavities occurring in the concealed area may not be detected until they reach the visible region. Second, the breakup process is initiated by instabilities arising randomly in the film, which leads to a stochastic breakup behaviour. Third, the drops are not perfectly spherical before impact due to the acceleration process. Especially for higher velocities, the drop exhibits a flattened profile upon impact. While the general deformation is considered by the curvature correction of β, the acceleration process possibly also induces local

asymmetries in the drop shape, which lead to uneven fluid distribution on the surface and in the sheet; ultimately influencing the breakup process.

The increased time the film stays intact suggests that more fluid is able to enter
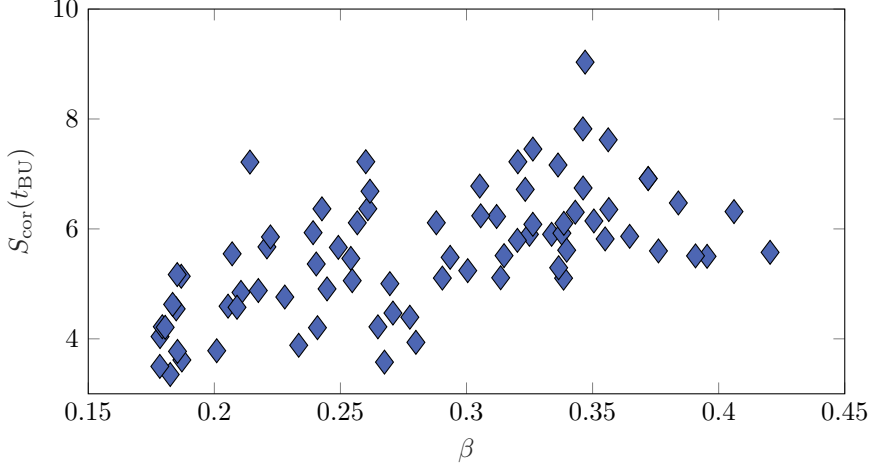
(a) Maximum dimensionless extent $S_{\mathrm{cor}}(t_{\mathrm{BU}})$ of the uplifting corona sheet of the splash in the moment breakup starts.
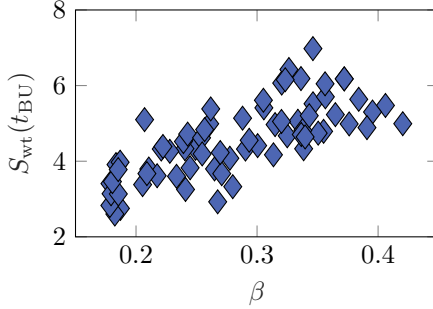
(b) Dimensionless diameter of the wetted area on the surface $S_{\mathrm{wt}}(t_{\mathrm{BU}})$ in the moment of breakup of the uplifting liquid sheet.
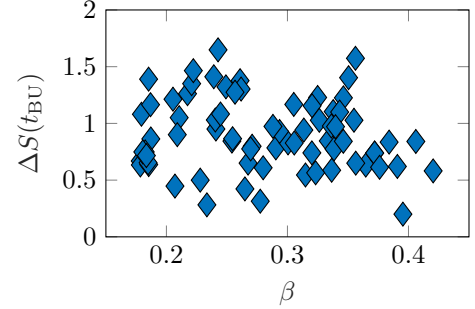
(c) Difference between maximum extent of the liquid sheet and the wetted area diameter $\Delta S(t_{\mathrm{BU}}) = S_{\mathrm{cor}}(t_{\mathrm{BU}}) - S_{\mathrm{wt}}(t_{\mathrm{BU}})$.

Figure 4.9: Dimensions of the uplifting sheet in the moment before its disintegration in relation to the splashing parameter β derived after Riboux and Gordillo (2014).

the film while it propagates away from the impact point. In order to quantify this effect, the maximum extent of the corona close to t_{BU} is determined from the high-speed recordings as illustrated in Fig. 3.17. The obtained values in terms of

the dimensionless extent $S_{\mathrm{cor}}(t_{\mathrm{BU}}) = D_{\mathrm{cor}}(t_{\mathrm{BU}})/D_0$ are plotted in Fig. 4.9a with respect to the β-values calculated from the impact parameters.

It is evident that the diameter of the uplifting sheet increases with increasing β, similar to the breakup time. Hence, in regard to the correlations with β, an increase in U_0, D_0 and η lead to a wider spreading of the liquid film before it breaks up. However, while the outer edge of the liquid sheet propagates, its lower end is also pushed away from the impact point by liquid spreading on the surface. Hence, $S_{\mathrm{cor}}(t_{\mathrm{BU}})$ includes not only the width of the uplifted corona but also the wetted area on the surface. In order to isolate the width of the corona, the spreading diameter $S_{\mathrm{wt}}(t_{\mathrm{BU}}) = D_{\mathrm{wt}}/D_0$ is tracked separately in the high-speed videos as illustrated in Fig. 3.17. The values of $S_{\mathrm{wt}}(t_{\mathrm{BU}})$ plotted over the corresponding splashing parameters of the experiments are shown in Fig. 4.9b. Since the moment of breakup $\bar{t}_{\mathrm{BU}}$ increases with β, an increase of $S_{\mathrm{wt}}(t_{\mathrm{BU}})$ for increasing β is only consequential. However, it shows a similar increase with β as the corona extent $S_{\mathrm{cor}}(t_{\mathrm{BU}})$, which suggests that the increase in corona extent is mainly attributed to a surface contact point at a greater radius. In fact, the difference between the sheet diameter and the spreading diameter $\Delta S(t_{\mathrm{BU}}) = S_{\mathrm{cor}}(t_{\mathrm{BU}}) - S_{\mathrm{wt}}(t_{\mathrm{BU}})$ shows no correlation with β, as seen in Fig. 4.9c. The large scatter in values for $\Delta S(t_{\mathrm{BU}})$ presumably originates from similar effects as discussed for t_{BU}. Thus, the elevated length of the corona does not change significantly with β yet its inner radius represented by $S_{\mathrm{wt}}(t_{\mathrm{BU}})$ increases. Consequentially, the volume of fluid incorporated in the uplifted sheet before breakup presumably increases due to its greater inner radius. In a following disintegration of the corona, more fluid possibly leaves the drop in form of secondary drops. Note that the fluid from the lifted sheet may also recede back to the spreading lamella on the surface upon breakup; hence, the ejected volume does not equal the sheet volume at $t = t_{\mathrm{BU}}$. Moreover, the lateral expansion of the corona eludes further dimensions which may affect the fluid volume in the lamella. First, the height of the corona which was not quantified from the videos due to the slightly tilted viewing angle. However, the obtained recordings do not suggest a significant increase in corona height h_{cor}, especially in comparison to its increased inner radius $(S(t_{\mathrm{BU}}) \gg h_{cor})$. Second, it is not possible to estimate the sheet thickness in the moment of breakup from the high-speed recordings which would affect the amount of fluid bound in the sheet vitally. Nevertheless, the increase in corona expansion already suggests a correlation of the volume of fluid involved in the breakup process with β. In order to quantify this relationship, the residual volume on the surface after the splash is examined. The corresponding experiments were conducted in the wind tunnel, since the downwards faced impact surface is not compatible with the measurement method used to determine the residual volume.
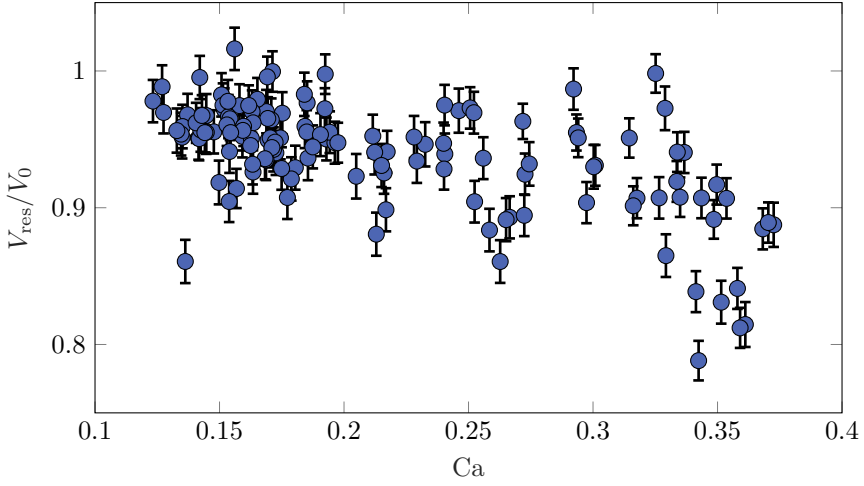
Figure 4.10: Residual volume fraction of supercooled drops in relation to Ca.

Correlation for the Residual Drop Volume

As suggested in the last section, the mass ejected from the drop during a corona splash is strongly connected to the development of the liquid sheet lifting from the surface. The extent and shape of this sheet until it collapses varies with impact velocity as well as with liquid viscosity. Whereas an increase in viscosity is expected to result in a more stable film, an increasing impact velocity presumably lifts the sheet earlier. Both effects provide more time for fluid to enter the liquid sheet before emerging instabilities lead to its breakup. The residual volume on the surface is determined with a three-dimensional reconstruction of the drop as described in Sec. 3.3.3. The corresponding measurement series is conducted in the wind tunnel and covered the same temperatures and velocities as the experiments regarding the drop deformation before impact (cf. Tab. 4.1).

In order to illustrate the residual volume on the surface as a function on impact velocity and liquid viscosity, the Capillary number $\mathrm{Ca} = \eta U_0/\sigma$ is used. Fig. 4.10 shows the residual volume fraction V_res/V_0 plotted in relation to Ca. It is apparent that for higher Ca lower residual volumes occur. However, the large scatter for higher Ca leaves great uncertainty in a clear decreasing trend. Considering the exclusion of drop size and shape in this empirical view, a more physical approach is thought to be more elucidating, which leads to the above-mentioned model from Riboux and Gordillo (2014) and their splashing parameter β.

The characteristics affecting the residual volume are combined in the parameter $\beta > \beta^\star$, as successfully used in Burzynski et al. (2020). Moreover, in contrast to the approach using Ca, the model provides the possibility to include changes conditional on the drop shape, as introduced earlier. In the present study, this

hypothesis is followed by examining the measured residual volume as a function of β (Fig. 4.11) for Ohnesorge numbers $Oh > 0.055$, corresponding to a well-developed corona, far from the threshold for prompt splash. The data for V_{res}/V_0 correlates well with the values of the β parameter, supporting the model of Riboux and Gordillo (2014). The data is supplemented with values obtained by Burzynski et al., 2020, which agree well with the decreasing trend of the residual volume for increasing β. However, the scatter in the data from this study and data of
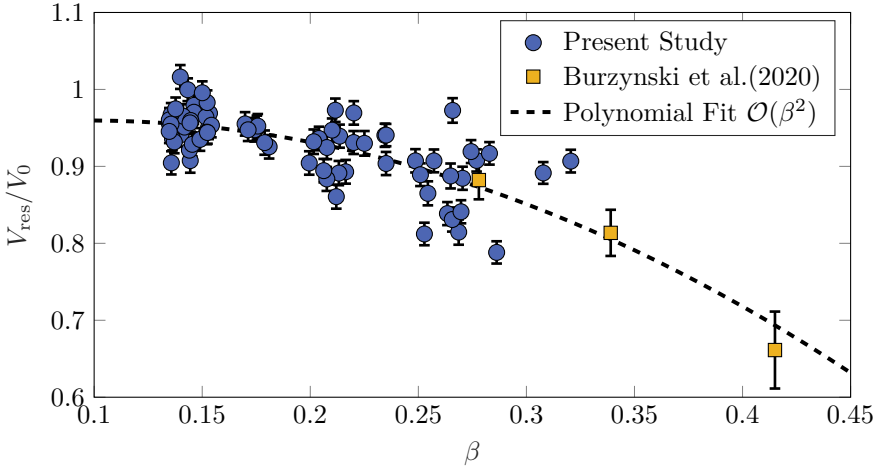
Figure 4.11: Residual volume fraction of supercooled drops with $Oh > 0.055$ in relation to splashing parameter β.

Burzynski et al. (2020) represented in Fig. 4.11 by the error bars, indicate that some influencing parameters are still unaccounted for. The parameter β only characterises the impact during the very first stages of splashing (prompt splash). One can expect that at later stages of the lamella spreading further factors enter the problem, for instance the presence of Rayleigh-Taylor instabilities (Burzynski et al., 2020). Moreover, the air flow in the present experiments will also have an influence, which can only be quantified by performing additional experiments in which the air flow imposes a more unidirectional aerodynamic force as on a long symmetrical impact surface. Nevertheless, the results presented in Fig. 4.11, revealing a strong correlation between the factor β and the residual volume on the surface, are a valuable outcome, for which there are very few alternatives presently available in the literature.

Moreover, the applicable range of parameters for this correlation is most presumably limited. Following the trend of the data indicated by the polynomial fit in Fig. 4.11, an impact with a value of $\beta = 0.7$ would lead to total disintegration

and ejection of the full drop volume. Such a value is achieved, for instance, for a spherical drop with $D_0 = 3\,\mathrm{mm}, T_0 = -10\,^\circ\mathrm{C}$ and $U_0 = 43\,\mathrm{m/s}$, which significantly exceeds the values investigated in our study and the available data in literature (Burzynski et al., 2020). In terms of dimensionless numbers this would correspond to $\mathrm{Re} \approx 50000$ and $\mathrm{We} \approx 70000$. In comparison, complete atomization for a smaller drop ($D_0 = 0.5\,\mathrm{mm}, T_0 = -10\,^\circ\mathrm{C}$) would be predicted for $U_0 \approx 95\,\mathrm{m/s}$ which represents a realistic icing scenario for aircraft.

However, a complete disintegration of the drop seems unlikely, given what is known about icing scenarios of aircraft. If a drop would completely atomize upon impact, all the ice agglomerating on the surface would originate from secondary drops re-impacting on the surface. Given the apparent airflow around the airfoil, the secondary drops will likely travel further downstream on the wing before impacting again, if not carried away completely by the air flow. The highest amount of ice would then be located downstream of the wind tip. However, in general aircraft icing scenarios the tip is affected the most by accumulated ice, which suggests fluid wetting the surface at the tip before freezing (Trontin and Villedieu, 2017). Thus, it seems likely that the correlation in its current form is not applicable up to these high velocities and further experiments are required in order to adapt the model or specify a certain threshold value and its governing influences. However, a drop impact experiment with comparable impact conditions was not possible in the icing wind tunnel setup and is generally hard to achieve. This concerns not only the measurements of the residual mass of such an impact, but its general phenomenological observations. It is still unclear what happens to the drop fluid during such a high-speed drop impact, making it an interesting topic to further investigations. Nonetheless, the correlation with β already suggests influences which might hold even for higher impact velocities.

Generally, the functional dependence of parameter β on material properties and impact parameters is complex which is clear from Eqs. (2.21) to (2.24). Therefore, in an attempt to illuminate to a greater degree the dependence of residual volume on impact parameters, the correlation between residual volume and the parameter β evident in Fig. 4.11 has been used to compute various dimensioned relations. To do this, first a polynomial fit to the data in Fig. 4.11 was determined which is shown in the figure as a dashed line. This fit was then used to compute the residual mass, given changes in various parameters entering the quantity β. The results of this computation are shown in Fig. 4.12 for variations of the impact velocity, impact drop diameter and dynamic viscosity of the drop liquid. In all cases, an increase of these quantities leads to less residual volume. Note that a larger value of drop diameter as well as an increase in impact velocity has the same effect as a lower curvature of the impacting surface of the drop which combines both effects. Thus, a more flattened drop upon impact will result in a lower value of residual volume as seen in Fig. 4.12.

After breakup of the liquid sheet and ejection of the fluid, the drop continues to spread on the surface until viscosity and surface tension cause the fluid flow to
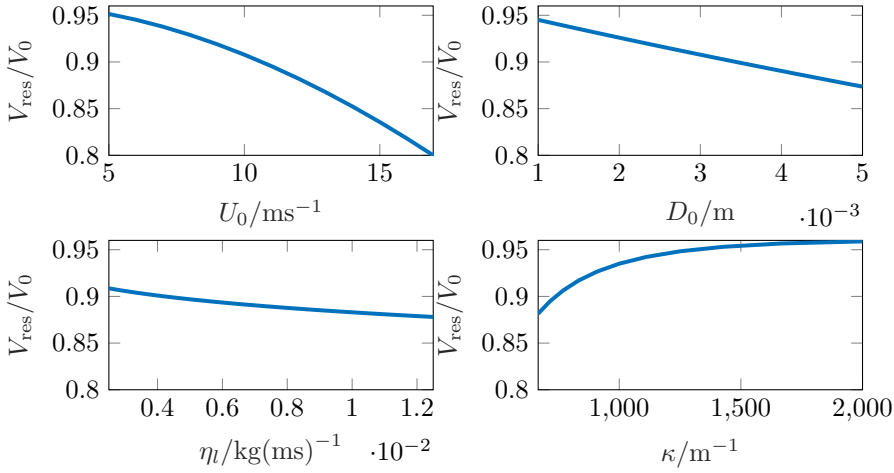
Figure 4.12: Residual volume change according to variation of a single parameter based on the polynomial fit in Fig. 4.11. Computations performed for $U_0 = 10\,\mathrm{ms}^{-1}$, $D_0 = 3$ mm and $\eta_l = 0.0026\,\mathrm{kg(ms)}^{-1}$ $(T_0 = -10°\mathrm{C})$.

cease. Up to this moment, nucleation of the supercooled liquid can occur randomly in the wetted area of the initially dry surface. However, the maximum area of a frozen drop is characterized by the maximum wetted area occurring from the fluid flow on the surface. While the maximum spreading radius for a drop impact on a dry surface is already broadly investigated, it is not clear which effects a superimposing co-flow has on this characteristic value. Hence, the maximum area of the supercooled drops impacting with a co-flow is investigated in the following.

4.1.3 Maximum Spreading of Supercooled Drops Deformed Prior to Impact

The maximum spreading area of a single drop impact onto a dry surface is an important quantity in different physical processes occurring during the impact. On the one hand, it correlates with the heat flux exchanged with the wetted surface, which dictates the fluid temperature in an non-isothermal case (Schremb et al., 2017a). On the other hand, an increase of the wetted area leads to a higher probability of nucleation, as described in Sec. 2.3. Multiple approaches to model the maximum spreading diameter of a drop impacting a dry surface exist (cf. Sec. 2.1.1), yet most of these approaches consider spherical drops in a calm environment where the entire fluid deposits on the surface. However, the drops investigated in the course of this dissertation impact on a surface which exhibits a stagnation point air flow and the drops develop a corona splash upon contact.

In order to investigate the effect these conditions have on the maximum wetted area, the experimentally obtained values are compared to the semi-empiric model of Roisman (2009a).

For this purpose, the drops investigated regarding their deformation before impact and their deposited mass are considered of which the impact conditions are summarized in Tab. 4.1. Their spreading diameter is tracked in the high-speed recordings (cf. Fig. 3.17), which include the maximum spreading diameter $S_{\mathrm{max,exp}} = D_{\mathrm{max}}/D_0$ achieved between the spreading and the receding phase. The values predicted according to Roisman (2009a) $S_{\mathrm{max,mod}}$ are calculated with Eq. (2.19). These values are compared in Fig. 4.13.
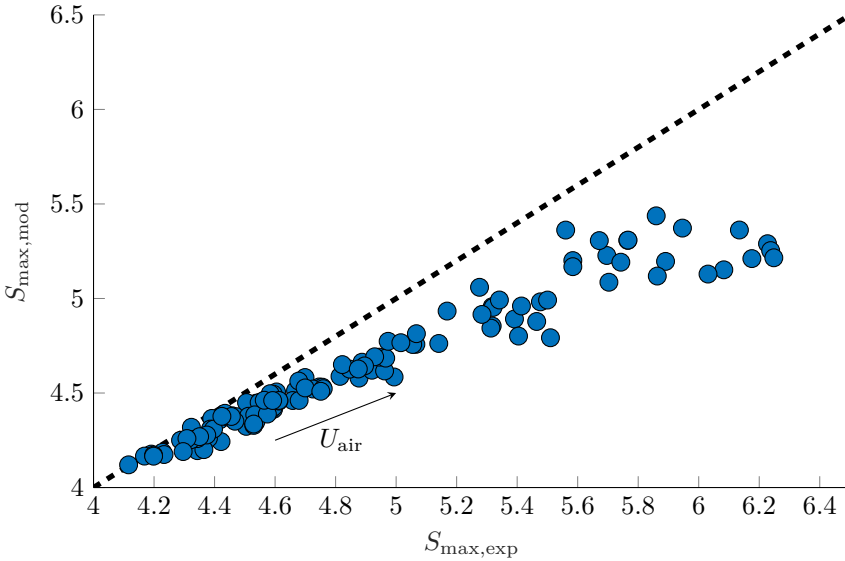
Figure 4.13: Comparison of maximum spreading diameter obtained from the experiments ($S_{\mathrm{max,exp}}$) and predicted according to Roisman (2009a) ($S_{\mathrm{max,mod}}$). The dashed line represents perfect agreement.

Low values of $S_{\mathrm{max,exp}}$ in the experiments are achieved for the lowest impact velocities with no co-flow and their values agree with the predicted values $S_{\mathrm{max,mod}}$. The agreement is regardless of their initial temperature, suggesting that the effect of the changes in liquid properties are included in the model in terms of Re and We. Note that the property most affected by temperature is the viscosity (cf. Sec. 2.2.1) and the lowest values for $S_{\mathrm{max,exp}}$ occur for the lowest temperatures and lowest impact velocity which is properly reproduced by the model. The generally high viscosity of the supercooled drops is also responsible for the development

of a corona splash upon impact, as discussed in Sec. 4.1.2, even for the lowest impact velocities. However, the agreement of the model with the occurring splash suggests that the lifting of the lamella and the subsequent ejection of mass have no significant effect on the maximum spreading diameter in the low velocity range. Nevertheless, when introducing a co-flow to the drop impact, the experimental values deviate considerably from the predicted values obtained with Eq. (2.19), as shown in Fig. 4.13. The difference between the model and the experiments increases with increasing air flow velocity U_{air} which always entails an increase in drop impact velocity U_0 in the experiments. The effect of higher impact velocities is incorporated in the model in terms of Re and We; hence, the deviation is assumed to arise due to aerodynamic forces. Along with the arising air flow, a vital differences to an impact without a co-flow is the drop deformation. The drops accelerated in the air flow deform prior to impact as shown in Fig. 4.1 and the non-spherical shape leads to a change in starting conditions for the fluid distribution. Thus, the model of Roisman (2009a) is adapted with regard to the deformation.

In the present deformation case, the drop exhibits an elongation, i.e. an increase of the vertical diameter D_v, accompanied by a decrease of the horizontal diameter D_h. Both deformations affect the development of the lamella flow described in Sec. 2.1.1 based on the model of Roisman (2009a). It is assumed that the basic physical processes remain the same as for a spherical drop. However, the deformed drop represents a more complex problem with a different supply of fluid entering the lamella over time. Thus, in a first approach, the deformation is considered in form of a correction factor which is expressed as D_v/D_h. Note that the drop deformation of the drop front curvature, which is crucial for the development of a splash as discussed in Sec. 4.1.1, is neglected. While the splashing originates only from the initial fluid movements on the surface, the maximum spreading diameter is a consequence of the flow involving the entire drop fluid. Thus, the overall drop shape needs to be taken into account.

In order to incorporate the corrective term into the original model, the adapted Reynolds and Weber numbers are defined as

$$\mathrm{Re}_{\mathrm{def}} = \frac{\rho U_0 D_0}{\eta}\frac{D_v}{D_h} = \mathrm{Re}\frac{D_v}{D_h} \text{ and } \mathrm{We}_{\mathrm{def}} = \frac{\rho U_0^2 D_0}{\sigma}\frac{D_v}{D_h} = \mathrm{We}\frac{D_v}{D_h}. \qquad (4.4)$$

Considering the characteristic deformation of the drops in the wind tunnel experiments ($D_v > D_h$) the elongation of the drops leads to an increase in Weber and Reynolds numbers ($\mathrm{Re}_{\mathrm{def}} > \mathrm{Re}$ and $\mathrm{We}_{\mathrm{def}} > \mathrm{We}$). In view of the first approximation of an upper bound of the maximum spreading $D_{\mathrm{max,upper}}$ with the shape of a thin disc (see Eq. 2.17), an increased Re would lead to an increase of maximum spreading since the residual lamella is thinner (Eq. 2.16). However, according to Roisman (2009a), this approximation needs to be corrected by the amount of fluid involved in the formation of the rim (Eq. (2.18)). In fact, the

length scale of the rim also increases for higher Re and We yet in a lesser extent $(D_{\mathrm{max,upper}}/L_{\mathrm{rim}} \propto \mathrm{Re}^{-1/5}\mathrm{We}^{1/2})$. Hence, an increase in Re and We due to the enlarged length scale suggests an increased maximum spreading with a smaller portion of the fluid involved in the rim formation. Thus, the maximum spreading of a deformed drop is obtained as $S_{\mathrm{max,mod,def}} = S_{\mathrm{max,mod,def}}(\mathrm{Re}_{\mathrm{def}}, \mathrm{We}_{\mathrm{def}})$ according to Eq. 2.19. In the wind tunnel experiments the drop geometry (D_v, D_h) is obtained from the high-speed recordings in the last frame before the drop impacts the surface. The calculated values are compared to the maximum spreading values $S_{\mathrm{max,exp}}$ in Fig. 4.14.
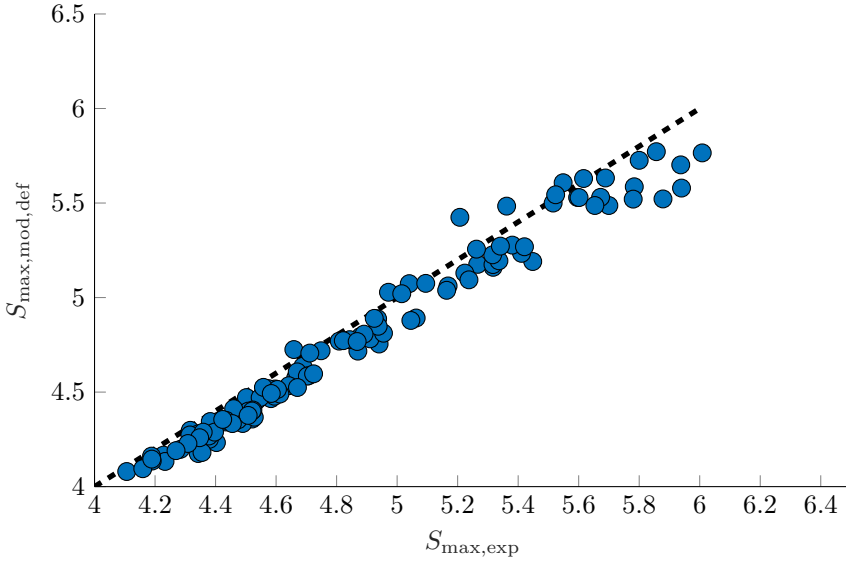
Figure 4.14: Comparison of maximum spreading diameter obtained from the experiments ($S_{\mathrm{max,exp}}$) and predicted after the model with an adaption for drop deformation ($S_{\mathrm{max,mod,def}}$). The dotted line represents perfect agreement.

As seen in this graph, the agreement between the adapted model and the experimental values is distinctly improved. The increasing underestimation of values for higher air flow velocities is drastically decreased, although a remaining dependence might be concealed by the larger scatter for higher spreading values. This uncertainty possibly also originates from a non-negligible effect of the mass loss or general influence of the occurring corona splash. The drops with the highest spreading values correspond to the impacts with the highest parameter β in Fig. 4.11 which also exhibit the highest scatter in measured values. Nevertheless, these findings support the hypothesis that the drop deformation before impact is

crucial for the maximum spreading radius. However, the experimental values still slightly exceed the values of $S_{\mathrm{max,mod,def}}$. Thus, an additional influence seems likely, which could be attributed to the wettability of the surface for the experiments at hand.

In the current model the surface tension σ is considered as the force acting towards
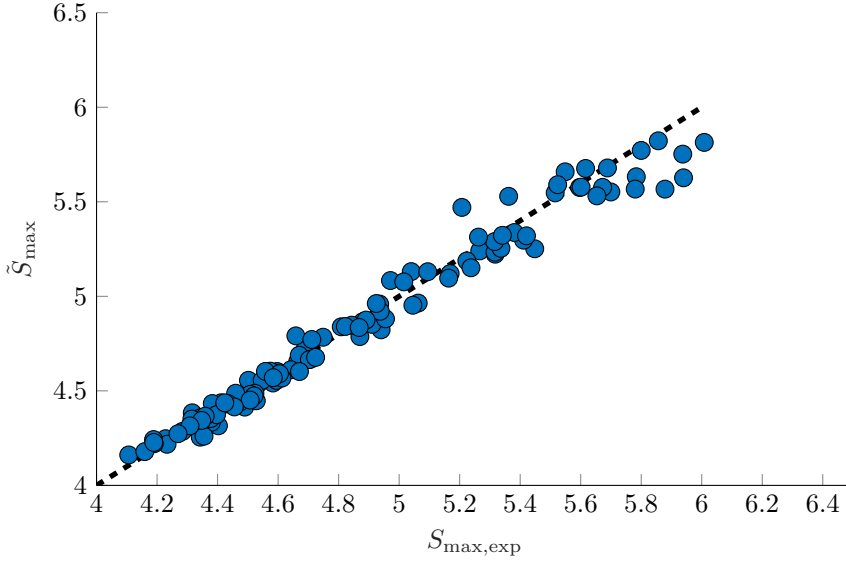
Figure 4.15: Comparison of maximum spreading diameter obtained from the experiments ($S_{\mathrm{max,exp}}$) and predicted after the model with an adaption for drop deformation and wetting properties ($\tilde{S}_{\mathrm{max}}$). The dotted line represents perfect agreement.

the drop center against the spreading connected to its inertia. However, another opposing force to the drop advancing on the surface is the horizontal force arising due to the limited wettability of the surface ($F_{\mathrm{h}} = -\sigma \cos\theta$), where θ is the contact angle of the three phase contact line. Thus, the Weber number is additionally adjusted to

$$\mathrm{We}_{\mathrm{def},\theta} = \frac{\rho U_0^2 D_0}{\sigma(1 - \cos\theta)} \frac{D_v}{D_h}. \tag{4.5}$$

In the current study, the contact angle θ is approximated by the static contact angle of water and aluminium $\theta \approx 70°$. The adjusted values obtained with

$$\tilde{S}_{\mathrm{max}} \approx 0.87\mathrm{Re}_{\mathrm{def}}^{1/5} - 0.4\mathrm{Re}_{\mathrm{def}}^{2/5}\mathrm{We}_{\mathrm{def},\theta}^{-1/2} \tag{4.6}$$

are compared to the experimental values in Fig. 4.15.

The comparison now shows excellent agreement between the model and the experiments for the lower range of spreading parameters. In the upper range, the values are still scattered with a small tendency to an underestimation of the calculated spreading value. Whereas the scatter might arise due to unaccounted effects of the more extensive splashing, the underestimation possibly also originates from drop deformations not expressed in D_v/D_h. Moreover, the adaption with the contact angle θ, requires further investigations regarding its validity for different surfaces. Since in the current study the drops are always exposed to polished aluminum surfaces, it is unclear whether the adaption applies for other materials. However, the current empirical adaption of the model of Roisman (2009a) seems to include the effect of drop deformation prior to impact and the wettability of the target surface.

4.1.4 Summary

The findings in this section illustrate the impact behaviour of liquid supercooled drops on a dry aluminium surface which is characterized by the development of a corona splash. The experiments are conducted in an icing wind tunnel, where the impacting drop experiences a superimposed stagnation point flow developed on the surface by the impinging cold air flow. For the majority of drops, no solidification of the supercooled fluid during formation of the liquid sheet and the subsequent spreading is observed due to a long freezing delay. However, the fluid flow and disintegration of the sheet with subsequent ejection of secondary drops represents a crucial change in the amount of fluid possibly involved in a subsequent freezing and its distribution. A variation of impact velocity and fluid viscosity due to varying drop temperatures is revealed as a significant factor for the splash development. Moreover, a deformation of the drop prior to impact introduces a decisive change in spreading behaviour and the associated corona development. Such a deformation has been shown as characteristic for the impact of drops in the stagnation point flow. All these influences are combined in the splashing parameter β, derived according to the model of Riboux and Gordillo (2014) which correlates with the time of corona breakup and the dimensions achieved up to this moment. Furthermore, a correlation of β and the deposited fluid volume after the splash is quantified. For this purpose, a newly developed measurement method for high precision measurement of the deposited drop volume is used. Moreover, the influence of drop deformation induced by the air flow onto the maximum spreading radius is shown and implemented into an adapted model. Additionally, the model accounts for the wetting characteristics of the surface in terms of the static contact angle. These findings can be used to improve codes predicting the amount of ice originating from drops impacting on a dry surface; thus, considering the first moments of ice accretion due to supercooled drops where a freezing delay is

characteristic. In a subsequent stage of the ice accretion the solidification possibly occurs without delay, for instance, when ice has already formed on the surface. This phenomenon is the topic of the investigation presented in the next section.

4.2 Impact of supercooled drops on an ice surface

The late stages of ice accretion from supercooled drops are characterized by the interaction of impacting drops with ice from previously frozen water on the surface. The presence of ice formations on the surface introduces new conditions to the impact of a single supercooled drop in multiple ways. First, the emerging ice layer represents a morphological complex impact surface to the impacting drops which depends on the surrounding conditions the surface is exposed to. In current research, special interest is directed towards the characterization of roughness of the ice and its effect on the ice layer growth (Anderson et al., 1997; Steiner and Bansmer, 2016; McClain et al., 2017). Second, the impact on ice exhibits no freezing delay of the impacting drops (cf. Sec. 2.3). While this delay enables flow of the drop fluid long after the impact caused by the fluid dynamics, surface movement or a surrounding air flow, a prompt start of the solidification prevents several of these flow developments. Since ice starts to emerge from every contact point of supercooled fluid with the frozen surface, dendrites spread into the bulk from all over the contact area. Hence, during an impact onto an ice surface, the solidification not only starts in the moment of first contact of the drop but also spreads along the contact area as fast as the fluid covers it. The complex interaction of the dynamic fluid flow and the fast propagation of dendrites is still not fully understood and uncertainties in its description affect large scale approaches predicting the ice layer growth.

The fast solidification upon contact with ice on the surface was observed for impact on single frozen drops (James et al., 2021) and analysed for the impact on a small ice target (Schremb et al., 2017c). However, a description of the spreading of supercooled drops after impacting a planar ice surface is still missing. Related approaches mostly involve drops at room temperature impacting an ice surface (Jin et al., 2017b; Thiévenaz et al., 2020), albeit the prior required cooling of the drop fluid entails a significant freezing delay to the impact. If the impacting drops are supercooled this delay is eliminated and a dynamic interaction of fluid flow and solidification emerges. The investigation introduced in the following is dedicated to this phenomenon.

For the corresponding investigations, custom ice targets with a planar surface are manufactured in a mold as described in Sec. 3.2. For the impact experiments, an unused target is placed in the wind tunnel test section and a drop experiment is conducted as described in Sec. 3.3. After each experiment, the geometry of the frozen splat on the surface is quantified with the scanning device introduced in Sec. 3.2. A new target is used for every experiment, since the splat and the ice target are merged after impact. Moreover, the flatness of the surfaces needs to be ensured, which is verified with the scanner. Since full measurements of such an impact surface are time consuming, not every target can be scanned before an experiment. Hence, three surfaces are measured as being representative for

the target manufactured in the ice target mold. The height of the targets varied with a standard deviation of $30\,\mu m$, which mainly occurred over long distances on the surface. Hence, it does not represent a roughness of the surface but rather a measure of the targets planarity. A more precise quantification of the roughness is not possible with the scanner, yet it is assumed to be significantly smaller. Thus, it is assumed that the target surface geometry does not influence the general impact behaviour apart from its material properties. Throughout the test campaign, the drop temperature, air flow velocity and corresponding impact velocity are varied according to the test matrix displayed in Tab. 4.3
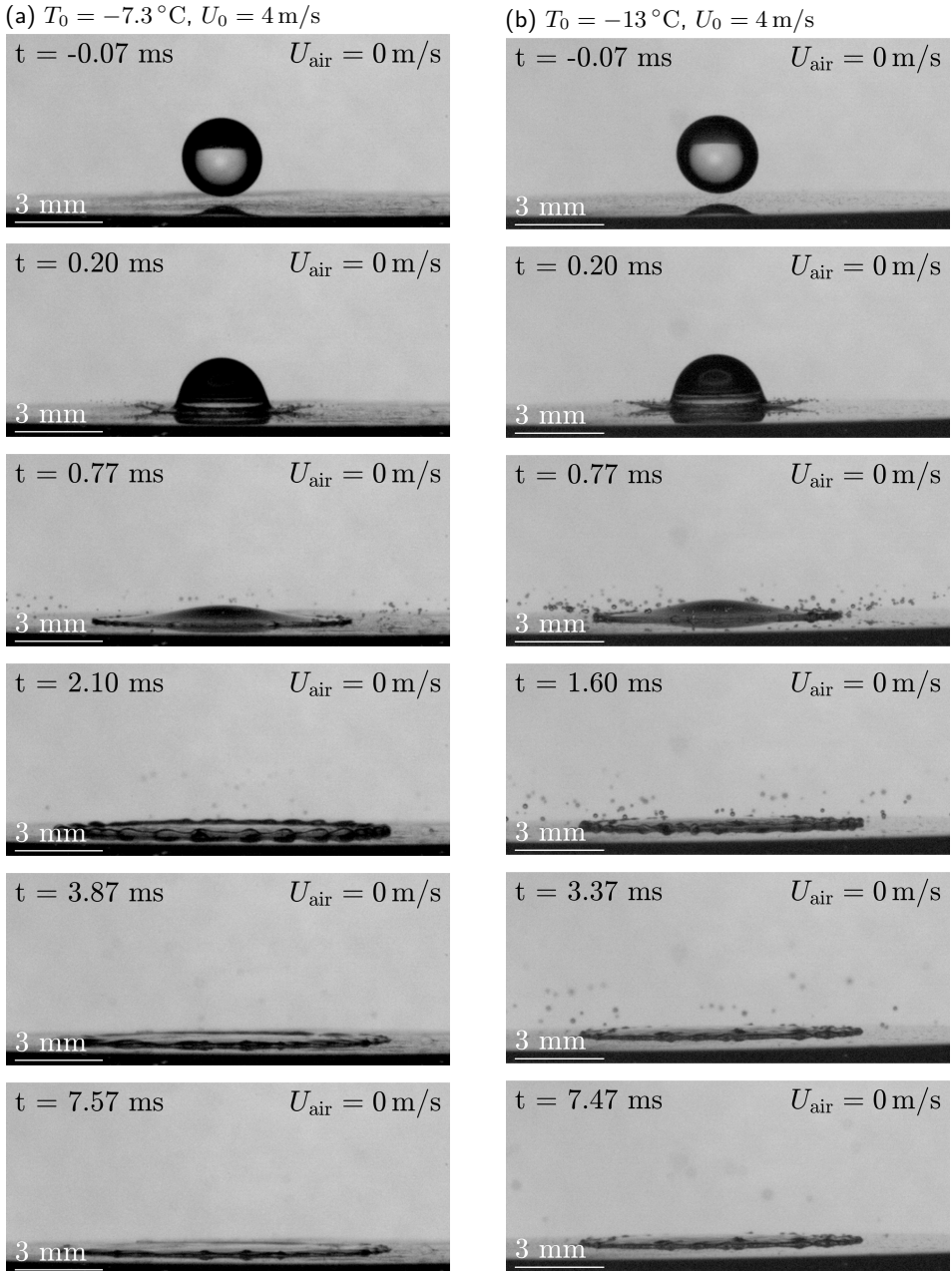
Table 4.3: Test matrix of parameter range covered in studies regarding impact of supercooled drops on an ice surface in the icing wind tunnel.

ΔT /K	U_0 /(m s^{-1})	U_{air} /(m s^{-1})	D_0 /mm
7.3 to 14	3.9 to 7.5	0 to 22.5	2.7

4.2.1 Observations of Supercooled Drops Impacting an Ice Surface

The impact behaviour of supercooled drops onto an ice surface initially resembles the behaviour of drops impacting on a dry metal surface. Image sequences of drops ($D_0 = 2.7\,\mathrm{mm}$) impacting with $U_0 \approx 4\,\mathrm{m/s}$ are shown in Fig. 4.16. Upon impact, the drops develop a corona splash during which secondary drops are emitted from the surface. However, the uplifting film generally extends less than on a metal surface for similar conditions (cf. Fig. 4.6). The smaller dimensions of the liquid sheet possibly originate from the hydrophilic wetting characteristic of ice ($\theta_{\mathrm{ice}} \approx 12°$ (Thiévenaz et al., 2020)). Despite the different wetting attributes, the subsequent spreading on the surface proceeds under the well-known formation of a rim and a thin lamella in the center. However, as the spreading continues, the fluid flow is interfered by the solidification which leads to cessation of the flow and a thin frozen splat on the surface as seen in the last images of Fig. 4.16. Thus, the receding phase of the drop is omitted. This behaviour is observed for all considered temperatures, yet the extent of the frozen splat changes with initial supercooling of the drop. The warmer drop ($T_0 = -7.3\,°\mathrm{C}$) continues its spreading until undulations in the rim indicate the approaching of the maximum spreading radius (see. Fig. 4.16a, $t = 0.21\,\mathrm{ms}$). Subsequently, the solidification fixes the fluid in the vicinity of the surface and some remaining liquid above recedes towards the center. On the contrary, the colder drop ($T_0 = -13\,°\mathrm{C}$) already freezes before the rim undulations occur and the remaining splat exhibits a smaller diameter as seen from the images in Fig. 4.16 at $t \approx 7.5\,\mathrm{ms}$. A smaller maximum spreading diameter

(a) $T_0 = -7.3\,°C$, $U_0 = 4\,m/s$

t = -0.07 ms $U_{air} = 0\,m/s$

3 mm

t = 0.20 ms $U_{air} = 0\,m/s$

3 mm

t = 0.77 ms $U_{air} = 0\,m/s$

3 mm

t = 2.10 ms $U_{air} = 0\,m/s$

3 mm

t = 3.87 ms $U_{air} = 0\,m/s$

3 mm

t = 7.57 ms $U_{air} = 0\,m/s$

3 mm

(b) $T_0 = -13\,°C$, $U_0 = 4\,m/s$

t = -0.07 ms $U_{air} = 0\,m/s$

3 mm

t = 0.20 ms $U_{air} = 0\,m/s$

3 mm

t = 0.77 ms $U_{air} = 0\,m/s$

3 mm

t = 1.60 ms $U_{air} = 0\,m/s$

3 mm

t = 3.37 ms $U_{air} = 0\,m/s$

3 mm

t = 7.47 ms $U_{air} = 0\,m/s$

3 mm

Figure 4.16: Image sequence of drops ($D_0 = 2.7\,mm$) impacting onto an ice surface.

is exptected due to the change in properties for lower water temperatures, i.e. mainly a higher viscosity η (cf. Fig. 2.10). However, the difference in maximum spreading distinctly exceeds the property related reduction predicted by the semi-empiric model of Roisman (2009a) (Eq. (2.19)). Thus, it is assumed that the earlier solidification of the colder drop is attributed to the faster propagation velocity of dendrites v_f (see. Fig. 2.15). Since ice grows into the bulk from every contact point on the surface, the dendrite front propagates almost horizontally into the lamella and the rim (as illustrated in Fig. 2.19). Hence, for lower temperatures, a faster extending front reaches the upper surface of the lamella at a greater thickness and suppresses the ongoing fluid flow.

Moreover, as pointed out in Sec. 2.1.1, the thinning of the lamella increases for higher impact velocities (cf. Eq. 2.10). Assuming the temperature is constant, a faster thinning of the lamella entails shorter lengths for the dendrites to pass in order to stop the fluid low. However, if the lamella thins out quicker, the drop also spreads faster along the surface and will freeze in a more expanded splat. This effect is observed in the experiments with higher impact velocities as shown in Fig. 4.17. It is visible that the drop impacting with a higher velocity

| $t = -0.03$ ms | $U_{\mathrm{air}} = 25\,\mathrm{m/s}$ | $t = 0.17$ ms | $U_{\mathrm{air}} = 25\,\mathrm{m/s}$ |
| 3 mm | | 3 mm | |

| $t = 0.43$ ms | $U_{\mathrm{air}} = 25\,\mathrm{m/s}$ | $t = 1.07$ ms | $U_{\mathrm{air}} = 25\,\mathrm{m/s}$ |
| 3 mm | | 3 mm | |

| $t = 2.40$ ms | $U_{\mathrm{air}} = 25\,\mathrm{m/s}$ | $t = 8.37$ ms | $U_{\mathrm{air}} = 25\,\mathrm{m/s}$ |
| 3 mm | | 3 mm | |
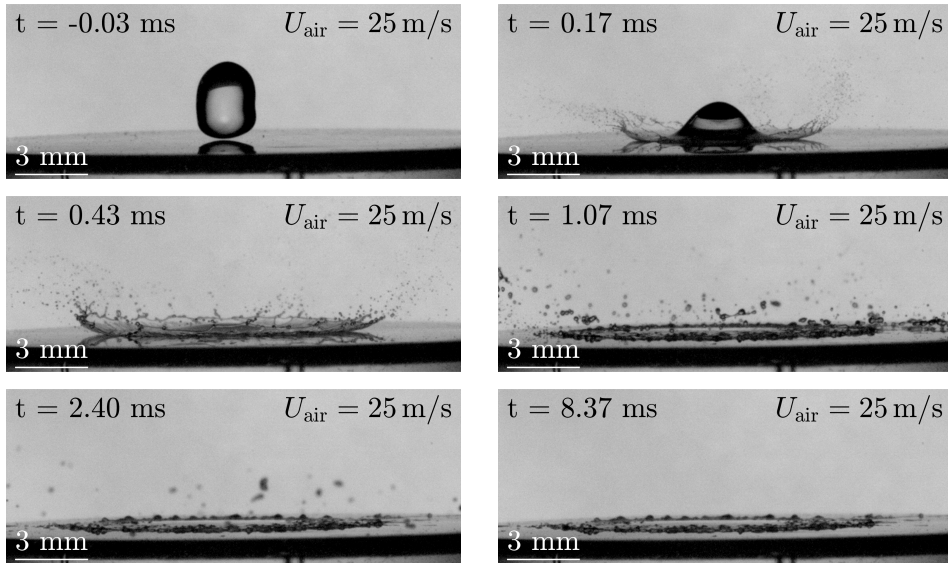
Figure 4.17: Image sequence of a drop ($D_0 = 2.7\,\mathrm{mm}$) impacting onto an ice surface with $T_0 = -12.3\,°\mathrm{C}$, $U_0 = 8.8\,\mathrm{m/s}$.

also exhibits a corona splash. The higher extent of the liquid film and the light asymmetry due to the drop shape is expected, as discussed in Sec. 4.1. The increased diameter is also noticeable suggesting a thinner frozen lamella. Moreover, the outer edge of the frozen splat appears rougher, which suggests that the fluid in

the rim froze before it had time to distribute over already frozen parts after the spreading ceased. In order to quantify the geometry of the splat with focus on its spreading diameter and the remaining thickness of the lamella in the center, the splat is scanned after the impact. Three full scans of these splats obtained with a spatial resolution of $\Delta x = \Delta y = 200\,\mu$m are compared in Fig. 4.18. The scans represent the outcome of impacts with different velocities (Fig. 4.18a & Fig. 4.18b) and different supercoolings (Fig. 4.18b & Fig. 4.18c). Note that the scan measurement always captures the fully frozen geometry of the splat, since the time it takes to remove the ice surface from the wind tunnel target mounting to place it in the scanner is sufficient for both solidification stages to finish.

The splat originating from the smallest supercooling and lowest impact velocity (Fig. 4.18a) reinforces the observations from the high-speed video with similar conditions (Fig. 4.16a). The smooth surface of the splat suggests that the fluid was given enough time to flow back to the central region and settle before being stopped by the expansion of dendrites. In the subsequent solidification phase, the freezing front is presumably guided by the shape predetermined by the dendritic freezing and the expansion of the emerging ice leads to the formation of a tip similar to the solidification of a sessile drop (cf. Fig. 2.18). On the outer edge of the splat, the receding rim is still noticeable but the thickness of rim and fluid in the central region is comparable. However, the height distribution of the splat changes significantly if it results from a drop impact with an increased impact velocity as depicted in Fig. 4.17. The splat of such an impact is pictured in Fig. 4.18b. The thinner lamella during spreading is still visible since it is pervaded by dendrites before the fluid is given time to recede towards the center. The fluid in the rim is separated from the central region by the thin frozen lamella and a distinct circular ring remains on the edge of the splat. The fixation of the rim in its form is presumably also favored by its reduced dimensions during spreading attributed to the higher impact velocity which entails a smaller characteristic rim length ($L_{\mathrm{rim}} \propto U_0^{-3/5}$, cf. Eq. (2.18)). As a consequence of the separation of the rim and the lamella, the tip in the central region is almost not perceptible. An increase in thickness in the center is visible, but it is not clear to what extent this elevation originates from the generally increased thickness of the central lamella or the expansion during the second freezing stage. Also, several smaller peaks suggest local inequalities in the propagation of the solidification front in the lamella. Moreover, the increased impact velocity leads to an increased spreading diameter in comparison to Fig. 4.18a.

However, an additional increase in supercooling of the impacting drop entails a reduction of the spreading diameter as seen in Fig. 4.18c. The decreased expansion of the splat suggests that the dendritic freezing stage stopped the fluid flow distinctly before the maximum spreading is achieved. As mentioned earlier, a reduced maximum spreading diameter would possibly also result from the increased viscosity of the colder water. Nonetheless, if this was the only influence, the

(a) $T_0 = -7.7\,°\text{C}$, $U_0 = 3.9\,\text{m/s}$
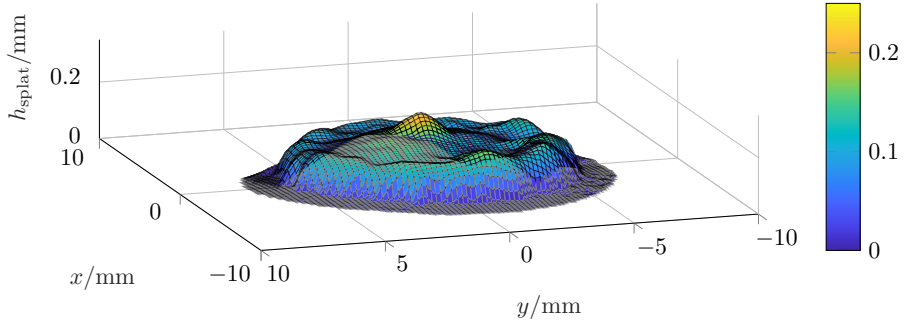
(b) $T_0 = -8.1\,°\text{C}$, $U_0 = 7.4\,\text{m/s}$
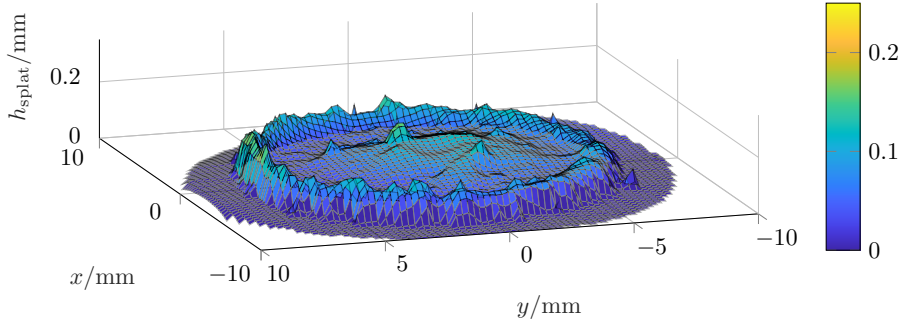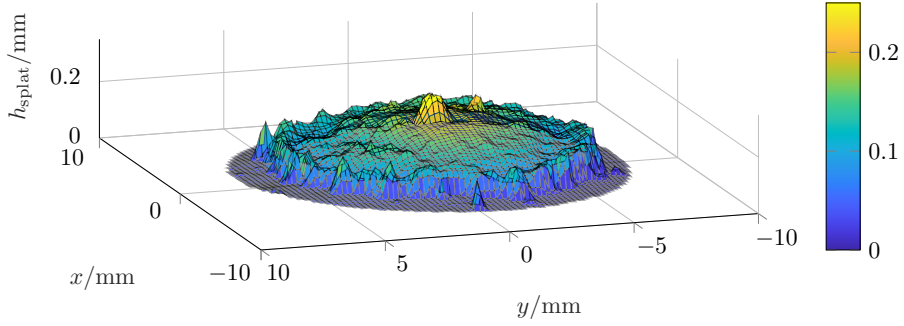

(c) $T_0 = -11.6\,°\text{C}$, $U_0 = 7.4\,\text{m/s}$

Figure 4.18: Scans of fully frozen splats of drops ($D_0 = 2.7\,\text{mm}$) which impacted with different temperatures and velocities on an ice surface. The z-values of the splats are additionally illustrated in color according to the displayed color bars.

splat would exhibit a shape similar to Fig. 4.18b. In Fig. 4.18c, the frozen rim is noticeable on the outer edge, yet the lamella is not visible any more. When the spreading on the surface is prohibited by pinning of the rim, the liquid flowing outwards on top of the dendritic freezing front is redirected towards the center. Eventually, the flow ceases when all liquid is pervaded by the dendritic freezing front and the expansion during the second freezing stage leads to an elevated tip in the center.

In order to analyse the influence of different impact parameters on the splat geometry, every drop is scanned after it froze on the ice surface. However, full scans as seen in Fig. 4.18 take approximately 80 min to finish which is unsuitable for an extensive measurement series. Therefore, the splats are scanned along four radiating diagonals going through the splat center oriented in a 45° angle in order to quantify representative dimensions of the splat. The findings regarding the height in the central region of the drop and its spreading diameter on the surface are discussed in the following.

4.2.2 Maximum Spreading and Residual Height of Supercooled Drops Impacting an Ice Surface

The observations from the high-speed videos and the full scans of the drop splats suggest an influence of a change in freezing dynamics originating from different initial supercooling of the drop. However, the spreading is also influenced by the liquid properties (affected by T_0), impact velocity, drop shape and surface properties as discussed in Sec. 4.1.3. In order to check whether the influence in freezing dynamics is relevant in comparison to the other influences, the experimental values are compared to the values obtained from the adapted model of Roisman (2009a) according to Eq. (4.6). For the corresponding calculation, the steady contact angle of water on ice is assumed as $\theta_{ice} = 12°$ (Thiévenaz et al., 2020). The comparison is shown in Fig. 4.19.

It is visible that only some of the experimental values $S_{frz,exp}$ are close to the modelled values $\tilde{S}_{max}$ while the other values are overestimated in different degrees. Considering that the drops investigated in this study all exhibit the same diameter $D_0 = 2.6\,\mathrm{mm}$ and the influence of U_0 and ν are included in $\tilde{S}_{max}$, only effects connected to the supercooling ΔT are left unaccounted for. In fact, the deviation from the model correlates with ΔT as indicated by the arrow in Fig. 4.19. Regarding the physical mechanisms governing the maximum spreading, Eq. (4.6) accounts for a change in viscous forces and surface tension but does not include any effect of freezing. Thus, it seems likely that a deviation from the model is induced by the solidification dynamics. In a first approach, it is assumed that the freezing dynamics are represented by the dendrite front velocity v_f which depends on ΔT of the drop (Schremb and Tropea, 2016). In order to see whether the decrease in residual spreading correlates with v_f, the marker in Fig. 4.19 are rendered coloured according to the relation of timescales of the lamella flow and
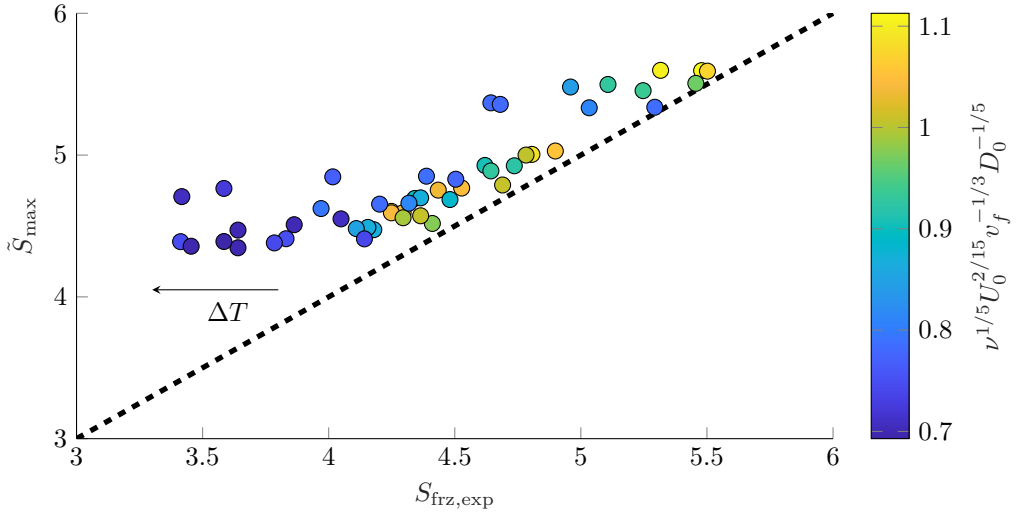
Figure 4.19: Comparison of spreading diameter of the frozen splats $S_{\mathrm{frz,exp}}$ with the values $\tilde{S}_{\max}$ obtained with the adapted model of Roisman (2009a) according to Eq. (4.6). The dotted line represents perfect agreement.

dendritic freezing $t_{\mathrm{frz,sprd}}/t_{\mathrm{sprd}} = \nu^{1/5}U_0^{2/15}v_f^{-1/3}D_0^{-1/5}$ (Eq. (2.42)). The values of v_f for a certain supercooling are determined with a fit to the experimental data of Schremb and Tropea (2016) (cf. Fig. 2.15).

As seen in Fig. 4.19, the maximum spreading on the surface is only slightly overestimated for $t_{\mathrm{frz,sprd}}/t_{\mathrm{sprd}} > 1$. Freezing of the fluid still leads to a flat frozen splat, yet the maximum expansion is close to the maximum spreading on a dry metal surface. Hence, the freezing front is not fast enough to pervade the lamella before the flow is suppressed by viscous forces. However, for $t_{\mathrm{frz,sprd}}/t_{\mathrm{sprd}} < 1$, the dendrite front traverses the lamella before the residual thickness dictated solely by viscous forces is achieved. Thus, the flow cessation in the lamella is favored by the propagating freezing front. Moreover, it is visible that the deviation from the model increases, if the freezing timescale $t_{\mathrm{frz,sprd}}$ increases in comparison to the one of spreading t_{sprd}. The deviation from the model correlating with $t_{\mathrm{frz,sprd}}/t_{\mathrm{sprd}}$ for values < 1 suggests that the cessation of the flow first starts in the lamella where the drop exhibits the smallest dimensions orthogonal to the surface. This assumption leads to a physical model for the residual dimensions of the drop, incorporating the dendrite front velocity v_f as an essential parameter.

Assuming a similar scenario as in Schremb et al. (2017c) (cf. Fig. 2.19), the dendrite front moving upwards in the lamella enhances the deceleration of the flow by additionally moving the base of the viscous boundary layer towards the

upper surface. In this case, the remaining height h_{res} depends on a parameter $Z = 0.39 D_0^3 v_f^5 / (\nu^3 U_0^2)$. Schremb et al. (2017c) also provided an empirical correlation for this, which was introduced in Sec. 2.3 as Eq. (2.46). The residual height h_{res} of the splats in the current study is obtained from the scans conducted after each experiment. In order to compare the obtained values and the empiric model, both are plotted against Z in Fig. 4.20. First, the plot reveals a correlation of the
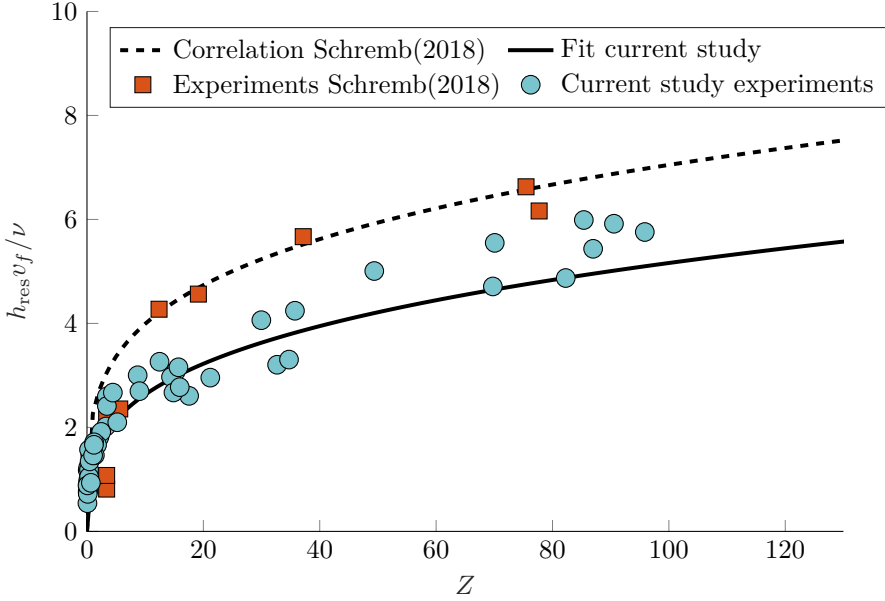

Figure 4.20: Experimental data for dimensionless residual height $h_{res} v_f / \nu$ compared to experimental data of Schremb et al. (2017c). The solid lines represent a power law fit to the corresponding data sets of the current study and Schremb et al. (2017c), respectively.

thickness values h_{res} obtained in this study with the parameter Z. This dependency suggests that the flow following the impact in fact ceases due to a combination of dendritic freezing and viscous flow deceleration in the lamella. Second, like the estimation of the upper bound for h_{res} and the experimental values from Schremb et al. (2017c), the current values follow a power law correlation

$$h_{res} v_f / \nu = A Z^B, \tag{4.7}$$

where A and B are fitting coefficients. However, in contrast to the experimental data of Schremb et al. (2017c), the residual lamella thickness of the frozen splats is slightly smaller. Hence, their correlation (Eq. (2.46)) predicts greater values in the range of Z covered in this study. The current values correspond to Eq. (4.7) with

$A = 1.34$ and $B = 0.29$. It is unclear why the current values are generally smaller. A difference caused by the different experimental approaches is conceivable, though a reason for a thicker residual lamella thickness resulting from the impact on a small target remains unknown. A measurement error may also arise from small random undulations in the ice target beneath the frozen splat. However, a general underestimation of thicknesses caused by these surface imperfections seems unlikely. The smaller values of the current study are surprising in particular, because the residual lamella thickness in the moment the flow ceases is almost certainly even thinner than the obtained values. On the one hand, the water solidifying in the second freezing stage expands the volume of the splat which possibly leads to an unknown increase in thickness at least close to the tip in the center. On the other hand, all fluid redirected by a frozen rim will accumulate on the settled lamella after the flow is stopped. The resulting shape is seen for instance in Fig. 4.18c. Since the amount of fluid accumulating in the center is unknown, it is unclear how severe the increase of thickness caused by this effect is. Nevertheless, the clear correlation with Z in a similar power law to Eq. (2.46) indicates that the effect leading to a stoppage of the flow and subsequent freezing in form of a splat is the dendritic freezing front propagating in the lamella.

If the thickness h_{res} of the lamella in the approximate moment the flow ceases is known, the spreading of the drop can be estimated similar to the model of Roisman (2009a) by an estimation of a thin disc with a rim at the outer edge. For this purpose, Eq. (2.16) is substituted into Eq. (2.19) to obtain a function $\tilde{S}_{\text{frz}} = \tilde{S}_{\text{frz}}(h_{\text{res}}, \text{We})$. Considering also the deformation of the drop prior to impact and the wetting properties incorporated in the adapted Weber number (Eq. (4.5)) yields

$$\tilde{S}_{\text{frz}} \approx 0.77 \sqrt{\frac{D_0}{h_{\text{res}}}} - 0.32 \frac{D_0}{h_{\text{res}}} \text{We}_{\text{def},\theta}^{-1/2}. \tag{4.8}$$

Together with Eq. (4.7) and the coefficients obtained from the current experiments the spreading of the frozen splat can be estimated. The calculated values are again compared to the experimentally obtained values from the scans as shown in Fig. 4.21. It is seen that the calculated values generally follow the line of perfect agreement, although they are still underestimated. Considering the mentioned increase in thickness of the splat due to redirected fluid and expansion during complete solidification, this is expected. An improved thickness estimation for h_{res} would presumably lead to smaller values of h_{res}; hence, to higher values of $\tilde{S}_{\text{frz}}$ since it is $\propto 1/h_{\text{res}}$. Nevertheless, the current estimation already reproduces the right trend for the frozen splat diameter. Moreover, the deviation of the calculated and experimentally obtained values no longer exhibit a dependency relation of timescales $t_{\text{frz,sprd}}/t_{\text{sprd}}$, i.e. initial supercooling ΔT, as in Fig. 4.19, as indicated by the marker colour. The smallest residual splat diameters are now predicted for the highest supercooling as observed in the experiments. Thus, the current approach enables an estimation of the residual splat diameter on the basis of a
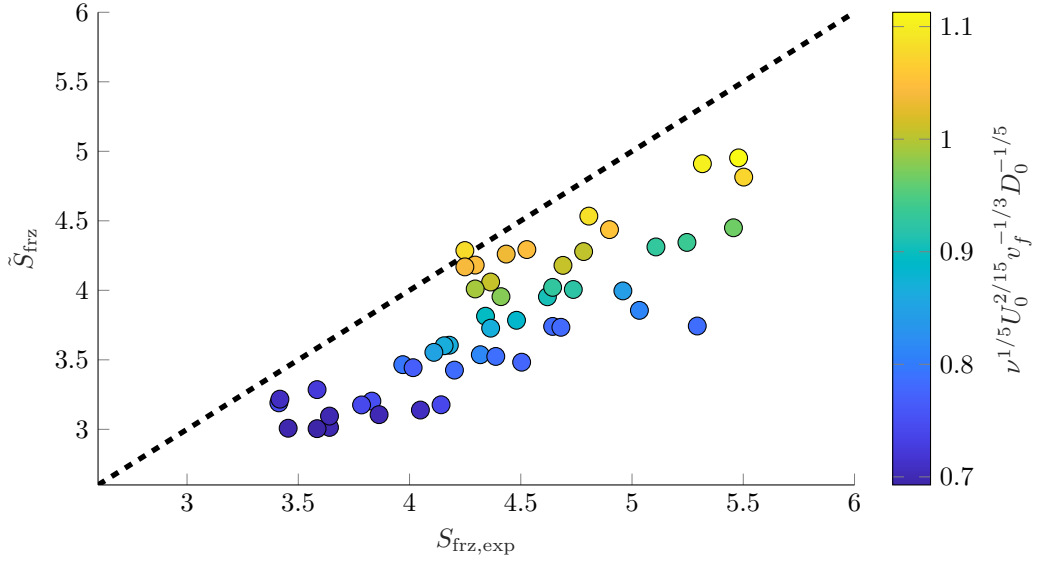
Figure 4.21: Comparison of experimentally obtained diameters of frozen splats $S_{\mathrm{frz,exp}}$ and the values estimated from Eq. (4.8) $\tilde{S}_{\mathrm{frz}}$. The dotted line represents perfect agreement.

combination of lamella flow and dendritic freezing by considering the essential physical dynamics. For a precise prediction of the residual splat diameter, an improved quantification of the thickness in the moment of cessation of the lamella flow is still required. In order to avoid, the effects of the second freezing stage, a determination of the lamella height during the impact would be advantageous. Since the lamella is usually obscured by the rim, an in-situ measurement with a clear view on the frozen lamella in a high-speed recording would be required. Such an experiment could be possible for the impact on an spherical ice target similar to the measurements of Bakshi et al. (2007). However, this kind of experiment is left for future work.

4.2.3 Summary

This section is devoted to the impact of supercooled drops on an ice surface where no freezing delay occurs. The experiments covered a range of different impact velocities as well as different initial supercooling of the impacting drops. The impact is captured in high-speed recordings and the residual frozen splats are scanned with a high precision scanning system. The experiments revealed a significant influence of the freezing dynamics on the spreading diameter and the height in the

central area of the frozen splat. While drops with small supercooling temperatures reach values close to their maximum spreading without solidification, the effect is more profound for large supercooling. In this case, the solidification stops the spreading of the drop leading to pinning of the three phase contact line and a residual diameter distinctly smaller than in a scenario without freezing. Moreover, fluid flowing on top of the frozen lamella is redirected by the frozen rim towards the center of the spreading drop. This phenomenon is observed in high-speed recordings and its aftermath is visible in scans of the frozen splats on the surface. It is assumed that the first significant effect of freezing is noticeable in the flow of the lamella. Hence, an approach based on the interaction of the propagating dendrite front and the lamella flow derived by Schremb et al. (2017c) is used to estimate the diameter of the frozen splat. A comparison with the experimental values indicate that the basic physical processes governing the interaction of freezing and the lamella flow are included in the model. An estimation of the residual height based on the experimental values shows qualitative agreement with the theory, yet presumably overestimate the thickness in the moment of freezing. Nevertheless, the residual height estimation is used for a prediction of the splat diameter based on the work of Roisman (2009a). It incorporates a change in the freezing dynamics by means of the front velocity of the emerging dendrites. The predicted values still underestimate the actual spreading diameter of the frozen splats, which is most likely attributed to uncertainty in the height measurements. However, the outcomes suggest that the influence of a change in dendrite velocity is accounted for. Thus, the findings presented in this section have the potential to improve numerical codes considering the impact of supercooled drops on ice substrates. This scenario represents a crucial phenomenon of ice accretion on technical surfaces since the missing freezing delay upon impact represents the earliest possible interaction of solidification and fluid flow after impact.

However, it is also possible that the incoming drops already nucleate before the first contact with the surface. In this case, a partly frozen drop impacts the surface which entails a crucial change in flow development. The impact of such partly frozen drops is the topic of the next section.

4.3 Impact of Mushy Frozen Drops[2]

The freezing of supercooled drops possibly even occurs prior to impact; particularly in the atmosphere, where contaminants in the form of particles are present. It is therefore possible that supercooled drops impacting onto surfaces are not pure liquid, but exhibit a dendritic frozen state referred to as mushy (cf. Sec. 2.2.3). Clearly, these drops will exhibit a different impact behaviour than pure liquid drops, which is the subject of the present study.

To the authors' knowledge there has been no work devoted to investigating the impact of mushy drops originating from supercooled water, although the interest in the impact of two-phase drops in general has grown in the recent past. Studies of compound drop impact focus on the cases where two liquid phases are involved (Blanken et al., 2021) or deal with suspension drops (Ueda et al., 2010; Marston et al., 2013; Bertola and Haw, 2015; Grishaev et al., 2017). In a more recent study (Kant et al., 2020b), the impact of a partially frozen binary drop consisting of hexadecane and diethyl ether has been examined. However, these drops solidify evenly from the outside to the centre during their descent. Hence, the impacting drops are surrounded by a uniform shell rather than being pervaded with a solid phase like a mushy particle.

In the present study, interest is directed towards the remaining shape after mushy drop impact, as this is considered to be instrumental in determining dynamic properties of the mushy phase. The characteristics of the mushy phase significantly influence ice accretion rates, a particular important quantity in predicting icing related safety factors in the aircraft industry. For this reason, an experiment has been designed in which the amount of ice inside the drop and the velocity of impacting drops onto cold surfaces can be well controlled and systematically varied as described in Sec. 3.3.5. The goal is to first make observations about the outcome of such impacts using a high-speed video camera. From the video data, the evolution of the spreading diameter and of the drop height in time is measured. The characteristics of a single mushy frozen drop impact are elucidated with regard to a variation of impact parameters. The deformation of the mushy drop during its impact on the wall is described theoretically assuming plastic flow in the drop. The development of the flow is determined by the inertial terms and by the plastic stresses characterized by the rate dependent yield strength. The yield strength of the mushy drops is estimated based on a comparison of the theoretically predicted (Roisman, 2022) and measured values of the residual drop height. In this scope, the theoretical model of Roisman (2022) (cf. Sec. 2.3) for a wall impact of a plastic particle and its validity for such an impact is reviewed. Finally, a correlation of the yield strength with the degree of supercooling, i.e. the amount of ice in the mushy phase, is determined.

---

[2]Parts of this chapter are adapted from Gloerfeld et al. (2023). The contents of the article have been edited and/or extended for this dissertation.
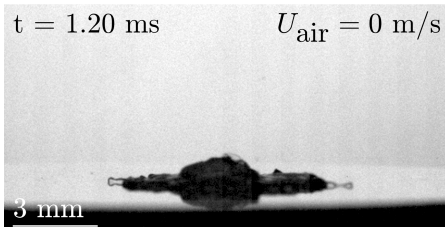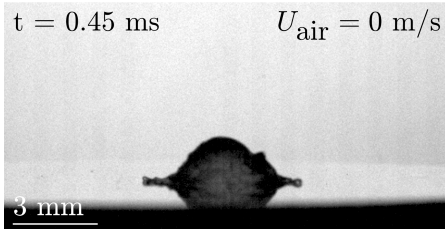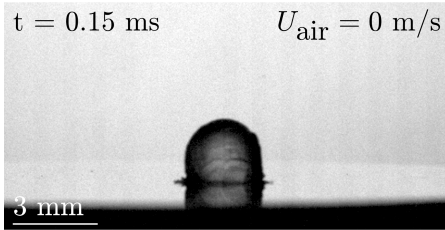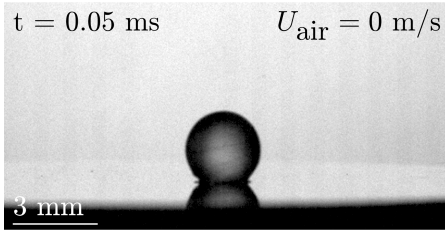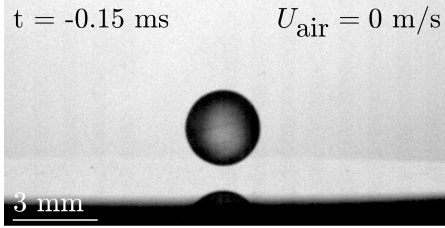
4.3.1 Impact Behaviour of Mushy Frozen Drops

As is well known, the impact of a pure liquid drop is governed by the development of a viscous flow, leading to the spreading of a thin lamella on the surface (Yarin, 2006). However, in a mushy frozen drop, the existence of ice dendrites changes the fluid properties significantly. As a consequence, the arising flow during impact corresponds more to a plastic behaviour. For low ice fractions of the mushy phase, the impact results in a nearly cone shaped ice agglomeration near the impact axis, as seen in Fig. 4.22a. The mushy frozen state of the drops is already recognizable from their appearance prior to the impact in the first images of Fig. 4.22. A pure liquid drop exhibits a bright spot in the middle of the drop, resulting from first-order refracted light passing through the drop in the forward scatter direction. However, in the mushy particle, the dendrites cause diffuse light scattering within the drop, prohibiting the undisturbed light passage through the drop. Thus, an evenly distributed grey level in the image is an indicator for a fully developed dendrite structure inside the mushy particle.
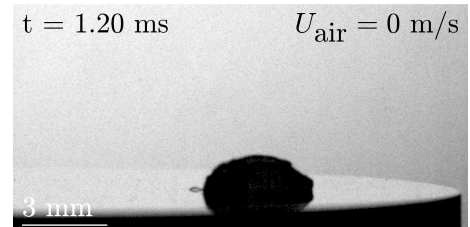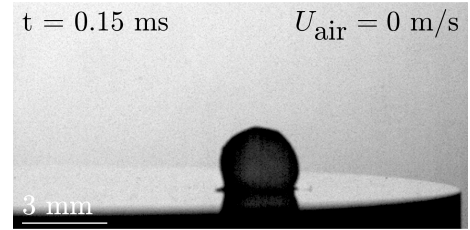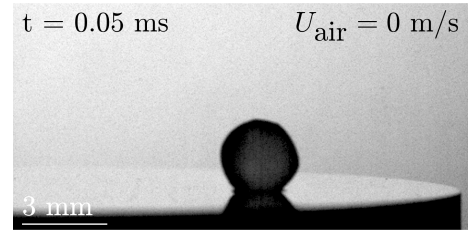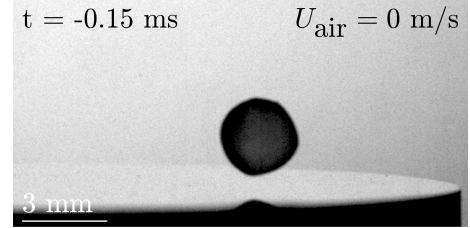
During the first moments of impact, the mushy drops behave similar to an impacting liquid drop in its kinematic stage. The drop will spread on the surface, yet not under the development of a thin lamella or a distinct rim at its edge. The remaining ice-water mixture in the drop is decelerated during spreading, causing the characteristic cone shape, which is incidentally also observed for the impact of wet granular drops (Marston et al., 2013). The granular character of the phase also prohibits any receding caused by surface tension of the contained water. Hence, the drop remains on the surface in this cone shape and the remaining water freezes solid. From the images in Fig. 4.22, it is also apparent that the spreading of the drop is not axisymmetric, but exhibits some fluctuation in spreading as well as in the height distribution. Note that especially at the edge of the spreading mixture, this effect can be intensified by water separating and leaving the mushy phase during impact (see Fig. 4.22a, $t = 1.20\,\text{ms}$).

After separation, this water possibly freezes even outside of the mushy splat. However, this phenomenon only occurs locally and the general dynamics of the impact are unaffected by any water separation. The plastic flow characteristic of the mushy drop impact becomes even more evident with an increased ice fraction ξ_{ice}. The impact of a drop originating from a supercooled drop with $T_0 = -13.8\,^\circ\text{C}$, i.e. $\xi_{\text{ice}} = 17.8\,\%_{\text{vol}}$ is pictured in Fig. 4.22b, where the increased ice fraction is already visible before impact. Whereas some light is able to pass through the drop with $\xi_{\text{ice}} = 10.7\,\%_{\text{vol}}$, here, the passage of light is completely inhibited. During the impact, the deceleration of the flow inside the drop is drastically increased. As a consequence, the spreading of a drop decreases whilst the remaining height after impact increases for increasing ice fractions. For the shown case with $\xi_{\text{ice}} = 17.8\,\%_{\text{vol}}$, the mushy drop forms a spherical cap in which the remaining liquid will eventually solidify. The increased deceleration is also visible from the height evolution. The height of the drops during impact is obtained

(a) $D_0 = 2.7\,\text{mm}$, $\xi_{\text{ice}} = 10.7\,\%_{\text{vol}}$,
$\quad U_0 = 3.18\,\text{m/s}$

(b) $D_0 = 2.77\,\text{mm}$, $\xi_{\text{ice}} = 17.8\,\%_{\text{vol}}$,
$\quad U_0 = 3.12\,\text{m/s}$

t = -0.15 ms $\qquad U_{\text{air}} = 0$ m/s

3 mm

t = -0.15 ms $\qquad U_{\text{air}} = 0$ m/s

3 mm

t = 0.05 ms $\qquad U_{\text{air}} = 0$ m/s

3 mm

t = 0.05 ms $\qquad U_{\text{air}} = 0$ m/s

3 mm

t = 0.15 ms $\qquad U_{\text{air}} = 0$ m/s

3 mm

t = 0.15 ms $\qquad U_{\text{air}} = 0$ m/s

3 mm

t = 0.45 ms $\qquad U_{\text{air}} = 0$ m/s

3 mm

t = 0.45 ms $\qquad U_{\text{air}} = 0$ m/s

3 mm

t = 1.20 ms $\qquad U_{\text{air}} = 0$ m/s

3 mm

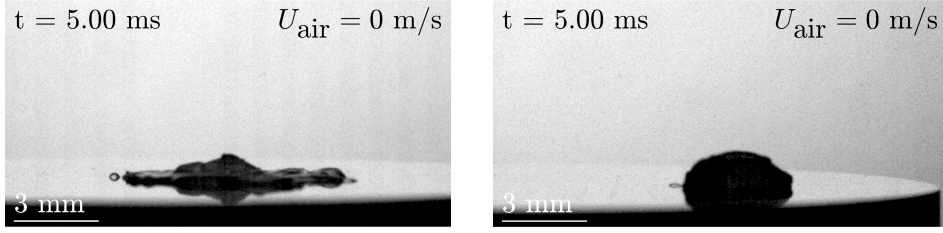t = 1.20 ms $\qquad U_{\text{air}} = 0$ m/s

3 mm

Figure 4.22: Image sequence of an impacting mushy frozen drop with different amounts of ice ξ_{ice} originating from varied initial supercooling ΔT.

from the high-speed recordings and its dimensionless value (related to the average drop radius R_0) is monitored over the dimensionless time $\bar{t}_R = tU_0/R_0$ of the impact. Note that the moment of first contact of the mushy drop with the surface mostly occurs in-between recorded frames ($\Delta t_R = 0.05\,\mathrm{ms}$). In order to determine the corresponding time of the impact images, $\bar{t}_R = 0$ is obtained from a linear extrapolation of the drop leading edge based on the impact velocity emanating from the last image before contact. On this basis, the corresponding times of each image are calculated and the evolution of height is obtained as plotted in Fig. 4.23.
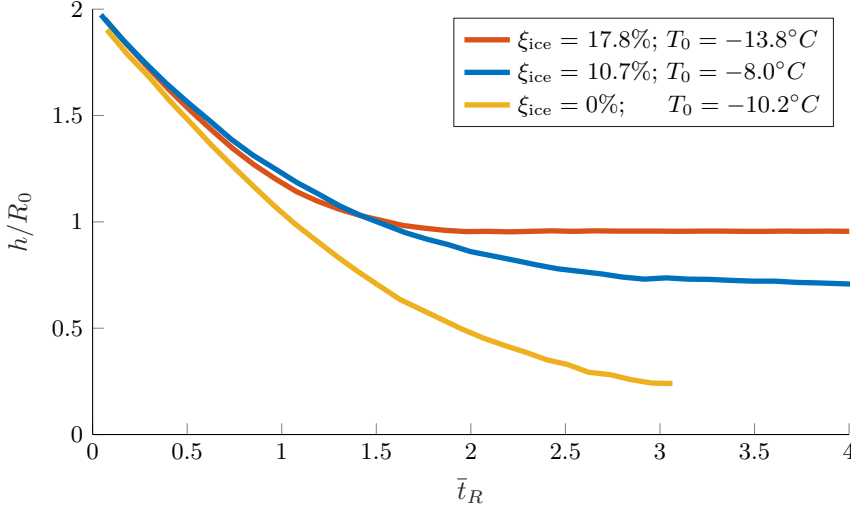

Figure 4.23: Comparison of height evolution of an impact of two mushy frozen drops with varying ice fractions and a supercooled liquid drop during their impact onto a solid substrate. Apart from a varying drop composition, the impact conditions are similar with $U_0 \approx 3.1\,\mathrm{m/s}$ and $D_0 \approx 2.8\,\mathrm{mm}$.

It is apparent that both mushy frozen drops evolve in height similarly until $\bar{t}_R \approx 1$. Afterwards, the drop with the higher ice load (red curve) decelerates until it comes to rest significantly earlier than the drop with the low ice fraction (blue curve). The faster deceleration suggests that the kinetic energy of the impacting drop is redirected towards breaking, collision and potential jamming of ice dendrites in the moving mushy phase. As a consequence, the drop containing more ice exhibits a greater residual height after the impact. This observation is supported by a comparison to a supercooled but purely liquid drop (yellow curve). Both mushy drops show significantly increased deceleration of the rear tip, evident even for lower ice fractions. Note that for the liquid drop, fewer data of the impact is plotted, since the thin lamella is obscured by the rim, prohibiting a height measurement of the thin film at later times. Additionally, three-dimensional perspective effects falsify the measurements for smaller heights of the liquid drop, which are therefore excluded from the graph.
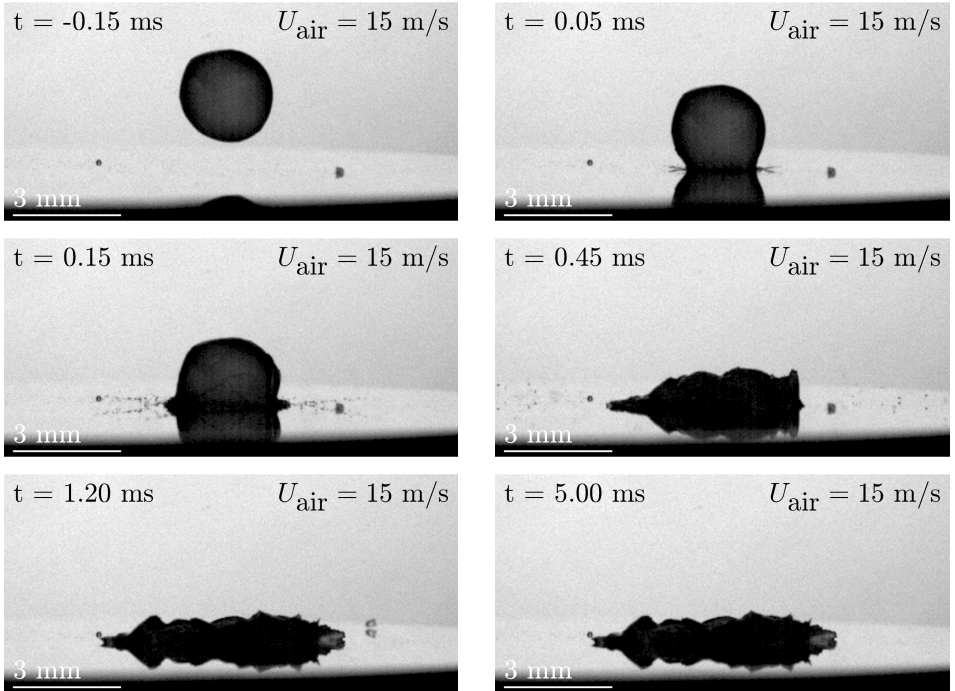

Figure 4.24: Image sequence of a mushy frozen drop with $D_0 = 2.7\,\mathrm{mm}$, $\xi_\mathrm{ice} = 17.9\,\%$ impacting the surface with $U_0 = 5\,\mathrm{m/s}$.

Next to the portion of ice in the mushy frozen drop, the impact velocity U_0 has a significant effect on the final shape of the drop after impact. As seen in Fig. 4.24, a drop with a high fraction of ice ($\xi_{ice} = 17.9\,\%_{vol}$) will exhibit increased spreading for an increased impact velocity ($U_0 = 5\,\mathrm{m/s}$). Consequently, the height of the residual splat decreases and a flatter height profile is established. However, compared to the splat of a low ice fraction drop, the surface shows more local ice accumulation, i.e. a rougher surface. Additionally, the higher impact energy causes small fragments being ejected from the drop shortly after impact ($t = 0.15\,\mathrm{ms}$), similar to a prompt splash of a liquid drop. However, the size and the absence of glare points on the ejected particles suggest a composition of water and ice, i.e. broken dendrites from the mushy phase. Subsequently, the fragments leave the drop without re-impacting on the surface. Note that the highest impact velocities in this study are obtained by increasing the air velocity inside the wind tunnel. Hence, a stagnation point flow develops on the circular impact surface superimposing with the impacting drop. However, the ballistic fragment trajectories and the comparable impact behaviour at low and high impact velocities suggest a minor influence of the air flow. Thus, in the analysis of the impacts in the present study any influence of the aerodynamic forces is neglected. The parameter range covered in the experiments is given in Tab. 4.4. The significant influence of the impact velocity U_0 and ice fraction ξ_{ice} is

Table 4.4: Test matrix of parameter range covered in study regarding the impact of mushy frozen drops.

ΔT /K	ξ_{ice} /$\%_{vol}$	U_0 /(m s^{-1})	D_0 /mm
7 to 14.5	9.3 to 18.6	2.8 to 7.2	2.6 and 3

also visible from the spreading radius D_{res} of the splat remaining on the surface after the impact. The observations of Fig. 4.22 and Fig. 4.24 suggest that D_{res} increases with increasing U_0 and decreases with increasing ξ_{ice}. In a first approach, the effect of velocity is attributed to the inertial forces while the influence of ξ_{ice} is associated with the yield strength of the ice $Y_{0,ice}$ contained in the mushy drop. Combining both effects, a dimensionless yield strength of ice is taken into account as $\overline{Y}_{ice} = Y_{0,ice}/(\rho U_0^2)$. In order to attribute this value to a given portion of ice, an empirical analysis suggested a scaling according to ξ_{ice}, yielding $1/(\overline{Y}_{ice}^{1/2}\xi_{ice})$. In order to account for the asymmetric spreading of a mushy frozen drop, a mean splat diameter $D_{res,mn}$ is determined. For this purpose, the surface is mounted rotatable. After the impact, the splat is captured from several viewing angles by rotation of the target. In all images of a single splat the spreading diameter is determined and averaged as a mean spreading diameter $D_{res,mn}$. The mean splat diameter of all examined mushy drops, made dimensionless using the initial drop diameter D_0, is plotted against $1/(\overline{Y}_{ice}^{1/2}\xi_{ice})$ in Fig. 4.25 whereas the static yield
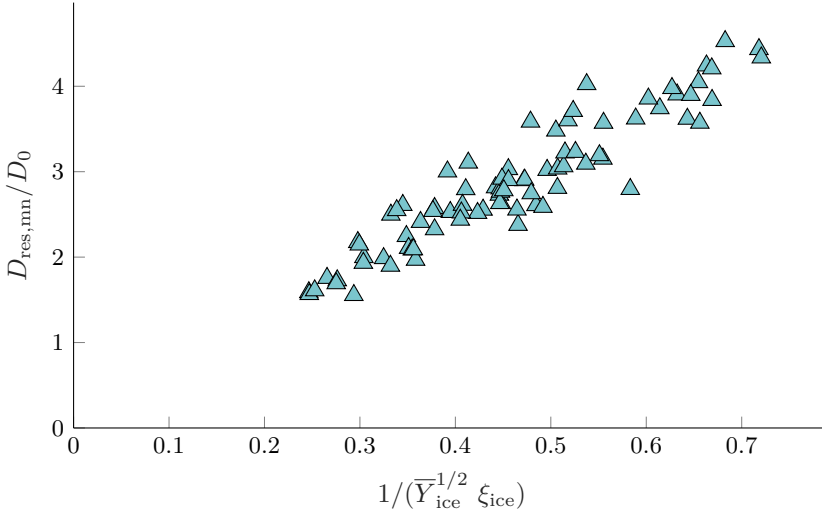
Figure 4.25: Residual splat diameter of all investigated mushy frozen drops plotted against the inverse of the proportionate dimensionless yield strength of ice $(Y_{0,\text{ice}} \approx 5\,\text{MPa})$ as $1/(\overline{Y}_{\text{ice}}^{1/2}\xi_{\text{ice}})$.

strength of ice is estimated with $Y_{0,\text{ice}} \approx 5\,\text{MPa}$ (Petrovic, 2003). The clear linear increase confirms that $D_{\text{res}} \propto 1/(\overline{Y}_{\text{ice}}^{1/2}\xi_{\text{ice}})$, i.e. $D_{\text{res}} \propto U_0/\xi_{\text{ice}}$, which supports the observations from the high-speed recordings and also indicates that the influence of both scaling parameters is of the same order of magnitude.

4.3.2 Refined Modelling of the Impact of a Mushy Frozen Drop

The impact of a mushy frozen drop is a highly complex phenomenon since the fluid inside the drop interacts with the solid ice dendrites, the nature of which depends on the initial supercooling of the drop. Furthermore, the continual disintegration of the dendrites during the impact results in changes of bulk properties, which are difficult to predict. An impacting mushy drop exhibits both characteristics of a liquid drop impact as well as those of a rigid, perfectly plastic flow, as seen in the experiments. Hence, approaches to modelling the impact dynamics of a mushy drop must reflect both states.

The spreading of a mushy drop resembles to some extent the spreading of a liquid drop. Therefore, the evolution of the spreading radius follows the widely known approach of Rioboo et al. (2002), who suggest $\overline{r} = r/R_0 = 2.05\sqrt{t_R}$ for the initial moments of impact. This approach introduced in Sec. 2.1.1 and adapted for deformed drops in Sec. 4.1 agrees well for a liquid drop. However, attributed to plastic stresses involved in the flow of the mushy mixture a deceleration sets in

shortly after first contact. This deceleration is incorporated in the dimensionless particle dislodging ζ whose propagation is derived from Eq. (2.62). Thus, the spreading of a mushy drop is estimated by $\bar{r} = 2.05\sqrt{\zeta}$ in a first approach. A comparison between the experiment and the adapted model reveals good agreement in the initial moments of impact, as seen in Fig. 4.26.

At the beginning of the impact, the spreading diameter in the experiment and the
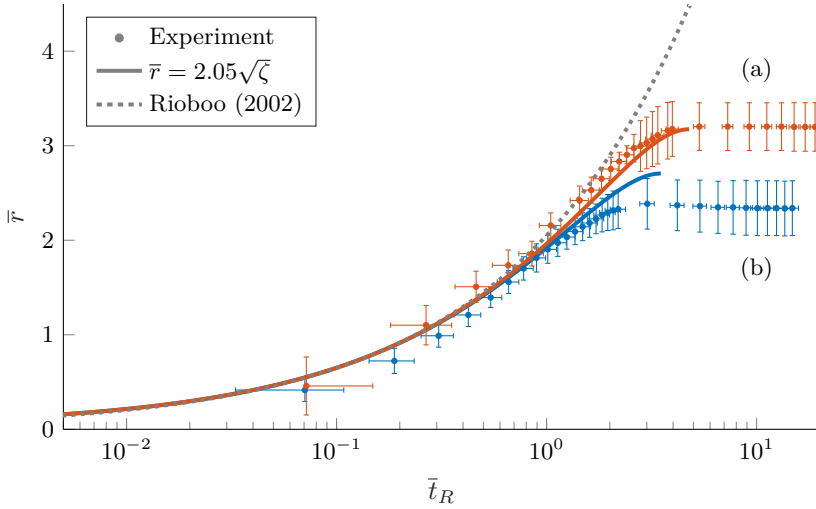

Figure 4.26: Time resolved evolution of the splat diameter $\bar{r}$ of mushy frozen drops impacting with similar conditions. Experimental values are obtained from three repetitions with average conditions of (a) $D_0 = 2.8 \pm 0.1\,\mathrm{mm}$, $\xi_{\mathrm{ice}} = 14.4 \pm 0.2\,\%$, $U_0 = 5.5 \pm 0.1\,\mathrm{m/s}$ and (b) $D_0 = 2.6 \pm 0.26\,\mathrm{mm}$, $\xi_{\mathrm{ice}} = 12.7 \pm 0.3\,\%$, $U_0 = 3.1 \pm 0.1\,\mathrm{m/s}$ in comparison to the modelled evolution assuming $\bar{r} = 2.05\sqrt{\zeta}$ with the average impact parameters.

model evolve according to the hypothesis of Rioboo et al. (2002), which is shown as a grey dotted line in Fig. 4.26. However, from $\bar{t}_R \approx 1$ onward the spreading of the mushy drops diverges from this behaviour and eventually exhibits a constant spreading diameter $\bar{r}_{\mathrm{res}}$. It is also visible that the mushy drop with the higher value of $1/(\overline{Y}_{\mathrm{ice}}^{1/2}\xi_{\mathrm{ice}})$ (a) follows the approach of Rioboo et al. (2002) for a longer period before coming to rest; hence, supporting the hypothesis introduced in connection with Fig. 4.25. The spreading diameter evolution derived from the model, shown with a solid line, agrees with the experimental values up until $\bar{t}_R \approx 1$. Subsequently, a deceleration of the spreading is observed, yet the final values of the spreading diameter $\bar{r}_{\mathrm{res}}$ obtained from the experiment vary significantly although the impact conditions are comparable. The spreading data predicted by the model show qualitatively good agreement. However, despite the large

error in $\overline{r}_{\mathrm{res}}$, the spreading values at later stages possibly differ from the range suggested by the experimental data (see model values for (b)). Hence, in order to quantitatively predict the residual spreading diameter for times $\overline{t}_R > 1$, the current approach is yet to be improved. Note that the last value of the modelled spreading $\overline{r}$ represents $\overline{r}_{\mathrm{res}}$ which refers to the instant where the flow velocity $\overline{U}$ reaches zero. Hence, this value is taken as the final, constant value of the modelled spreading. Moreover, not all experimental data obtained at later spreading stages is displayed in Fig. 4.26 for the sake of clarity.

The discrepancy in $\overline{r}_{\mathrm{res}}$ between the model and the experiments is most likely attributed to the fact that the model of Rioboo et al. (2002) is only valid for the first moments of impact. One reason for this restriction is a missing deceleration of the flow, which also arises in a liquid drop impact when surface tension begins to govern the flow. However, a consideration of ζ instead of $\overline{t}_R$ accounts for a flow deceleration according to Eq. (2.62), which results in the qualitative agreement with the experiment. Further factors causing the observed discrepancy might partly be caused by the asymmetry of the flow as well as it may be attributed to more specific model deficiencies. On the one hand, the time resolved data from the experiment is obtained from a single side view recording of the experiment. The spreading of the mushy drop on the surface is noticeably asymmetric, whereas the spreading after Rioboo et al. (2002) uses an axisymmetric approach. Hence, a determination of an averaged spreading diameter as a function of time might improve the agreement between the model and the experimental data. However, this would entail an additional camera angle or a top view recording of the impact, which was not available in the present study. On the other hand, a more precise model presumably has to account for asymmetry, arising due to various factors, such as local agglomeration of the mushy phase. Consideration of such disturbances in the flow model requires detailed knowledge about the crystalline structure of the dendrites in the mushy drop and characteristics of their disintegration. The detailed description of such an impact is a highly complex problem to which the combination of the models of Roisman (2022) and Rioboo et al. (2002) nonetheless represent a promising first approach.

Regarding the observed deviation between spreading values of the model and the experiment, a legitimate question is how significant this error is to the development of the flow according to Eq. (2.62)? Although this equation is only valid near the impact axis, the force transmission area $\overline{a}(\zeta)$ is a vital quantity in order to model the flow development. Since the correlation for the growth of $\overline{a}$ and $\overline{r}$ are based on the same assumption, an error in spreading possibly indicates an error in assuming that $\overline{a} = \sqrt{2\zeta}$. In order to rule out such an error, the force transmitted to the surface by the particle is considered. In the model, this force is equally distributed over the entire surface characterized by $\overline{a}$, which enables a computation of the force at every moment of the impact. According to Roisman (2022), the total force

produced by the impacting mushy drop is obtained by

$$F_z(\zeta) \approx -\pi a^2 \sigma_{zz} = \bar{a}^2 \pi \rho R_0^2 U_0^2 \left(\mathcal{B}\overline{U}^2 + \frac{\mathcal{C}K\overline{Y}}{K + \bar{a}^2 \mathcal{A}} \right). \tag{4.9}$$

For the impact parameters considered in Fig. 4.26 this force is calculated and plotted in Fig. 4.27.

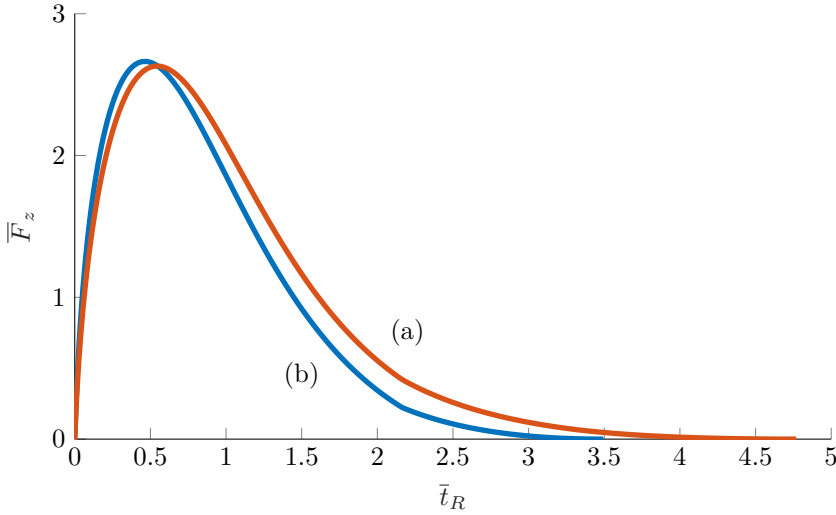It is clear that the qualitative evolution of the force is similar for both experiments.

Figure 4.27: Time dependent evolution of the dimensionless impact force $\overline{F}_z = F_z/(\rho U_0^2 R_0^2)$ of the average conditions considered in Fig. 4.26 according to Eq. (4.9).

In fact, it develops similarly for all conducted experiments. The force increases rapidly until reaching its maximum value at $\bar{t}_R \approx 0.5$ and subsequently decreases slightly slower. It eventually reaches zero when the drop comes to rest. Thus, most of the impact energy is transmitted during the first moments of impact and the larger part of impact energy is transmitted before $\bar{t}_R \approx 2$. Regarding the contact area $\bar{r}$ and the impression radius $\bar{a}$, this is the time span in which the model and the experiments agree well (see Fig. 4.26). Hence, the error caused by the deviation in the last moments before coming to rest is negligible for a consideration of the flow parameters in the vertical direction near the impact axis (cf. Eq. 2.62). Moreover, in the original formulation by Roisman (2022), the validity of $\bar{a} = \sqrt{2\zeta}$ is restricted to $\bar{t}_R < 2$. However, the portion of energy transmitted afterwards suggests that using the model for times $\bar{t}_R > 2$ causes no significant error with respect to the flow development until the flow comes to rest.

The absolute amount of momentum transferred to the surface is linked to the impact parameters; hence, all crucial quantities have to be considered in the model. Whereas the impact velocity, average density and drop radius are directly linked to the input conditions of the model, the ice fraction is included in the consideration of the plastic deformation force. More precisely, it is assumed that the effects of the portion of solid ice, the dendrite structure inside and the force required to break single dendrites can be incorporated into a characteristic yield strength Y. In order to determine the equivalent yield strength of the mushy phase, the differential equation system of Eq. (2.62) is solved for multiple values of Y_0. This way, a look-up table is generated for each variation of impact conditions. As already illustrated in Fig. 4.23, a variation of ξ_{ice} results in a different residual height $\overline{h}_{\text{res}}$ of the mushy drop on the surface. Hence, by comparing all values for the remaining height in the look-up table to $\overline{h}_{\text{res}}$ obtained from the corresponding experiment, an appropriate yield strength is determined.

In a first approach with a constant yield strength $Y = Y_0$, a trend towards higher values of Y_0 for higher impact velocities emerged. A similar behaviour is reported for solid ice particles (Tippmann et al., 2013) and granular ice layers (Schremb et al., 2019), where the computed yield strength increases for higher shear rates $\dot{\gamma} \propto U_0/D_0$. Hence, in this study, the yield strength is scaled with a dimensionless function as $Y = Y_0 y(\dot{\gamma})$ (Eq. (2.55)). However, to the authors' knowledge, there is no available data regarding the shear rate dependence of a mushy fluid originating from supercooled liquid. Hence, as a first approach it is estimated from the values obtained for a constant yield strength. In this manner, the dimensionless function $y(\dot{\gamma})$ is obtained by a fit to the increase of Y with U_0/D_0, which represents the involved shear rate.

In the moment of first contact of the mushy drop with the surface, the shear rate tends to infinity. In order to avoid an overestimation of the mushy phase yield strength for $t \to 0$, the function $y(\dot{\gamma})$ is approximated similar to the suggestion of Roisman (2022) for ice particles, yielding

$$y(\dot{\gamma}) = 1 + \chi - \chi e^{-\varepsilon \dot{\gamma}}, \qquad (4.10)$$

where χ and ε are constants. The function corresponds to $y(\dot{\gamma} = 0) = 1$ and $y(\dot{\gamma} \to \infty) = 1 + \chi$; thus, limiting the acting yield strength for both high and low shear rates. The parameters χ and ε are determined from the data for $Y = Y_0$ and are computed from a fit to distinct independent data sets for an approximately constant ice fraction ξ_{ice}. The obtained values are $\chi = 1.85$ and $\varepsilon = 1.96 \cdot 10^{-4}\,\text{s}$, which limits the yield strength to the highest determined yield strength $Y_{0,\text{max}}$ of this study for $\dot{\gamma} \to \infty$. The substitution of Eq. (4.10) into Eq. (2.55) reveals a weaker dependency of the determined yield strength values for increasing impact velocities, although the influence is not completely eliminated. However, this first approach provides satisfactory results especially with regards to the modeling of the height evolution of the drop near the impact axis.

Considering the height of the impacting mushy drop during and after the impact, the deceleration of the flow is evident. As visible from the qualitative analysis, the remaining shape of the drop depends on the impact velocity U_0 as well as the portion of ice ξ_{ice} in the mushy drop . Hence, comparison of the height evolution during impact to the values predicted by the adapted model offers a possibility for model verification. In Fig. 4.28 the evolution of the dimensionless drop height $\bar{h}$ is shown
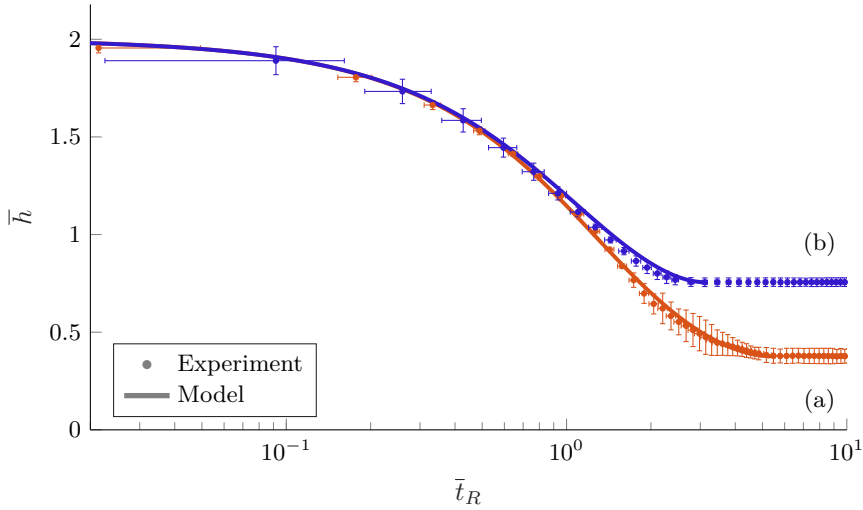
Figure 4.28: Time dependent evolution of the dimensionless height of the mushy drop during impact. Comparison between model (solid line) and experiment (circular markers) for drops impacting with (a) $D_0 = 2.9 \pm 0.08\,\mathrm{mm}$, $\xi_{\mathrm{ice}} = 9.6 \pm 0.3\,\%$, $U_0 = 4.4 \pm 0.1\,\mathrm{m/s}$ and (b) $D_0 = 2.6 \pm 0.02\,\mathrm{mm}$, $\xi_{\mathrm{ice}} = 17.5 \pm 0.4\,\%$, $U_0 = 4.4 \pm 0.02\,\mathrm{m/s}$. The yield strength values determined from the experiments are (a) $Y = 3.3 \pm 0.3\,\mathrm{kPa}$ (b) $Y = 6.3 \pm 0.3\,\mathrm{kPa}$. The model values are obtained with the average values.

for two sets of impact conditions. The general evolution was already discussed in the context of Fig. 4.23; however, note the logarithmic scaling of $\bar{t}_R$ which also entails the apparent reduction of error in time values. The values obtained from the experiments are depicted with error bars representing one standard deviation, since each set is averaged from three repetitions. The corresponding height evolution obtained from the averaged values with the adapted model is plotted in solid lines. Only the value of the residual height h_{res} was used to determine the yield strength and the resulting height evolution exhibits good agreement with the experiments. A noticeable variation in experimental values for (a) is evident especially in the deceleration of the flow at $t \approx 2$. However, the model agrees well within the range of the experimental values. The variation in the values of (b) is generally lower

and the agreement with the model is similarly good. Only an underestimation of the deceleration between $1 < \bar{t}_R < 4$ results in a slightly delayed attainment of $\bar{h}_{\text{res}}$. A similar error possibly arises in (a), which may be obscured by the larger variation in experimental values. In general, the region of deceleration exhibits the largest variation in experimental values and deviation from the model shortly before coming to rest. This may be attributed to the fact that the embedded dendrites in the mushy phase accumulate at the bottom of the drop at this time, intensifying the interactions between fluid and solid and leading to more statistical behaviour. The underestimation of the deceleration in this phase for the values obtained from the model occurred especially for higher impact velocities i.e. higher shear rates. This correlation suggests that the approach for the dimensionless function $y(\dot{\gamma})$ has potential for improvement, which however would necessitate further experimental data. Nevertheless, the generally good agreement between the model predictions and the experimental data reveals the current modelling approach to be an important step towards modelling the complex dynamics of a mushy frozen fluid and associated icing phenomena.

4.3.3 Yield Strength of the Mushy Phase

The complexity of the mushy frozen phase arising from the dendritic crystalline structure and the interaction between solid and liquid significantly impedes the quantification of mushy phase parameters. Additionally, this is further complicated by the dependence of shape and number of dendrites from the initial supercooling of the fluid (Schremb and Tropea, 2016). Together with the short timescales involved, the experimental determination of bulk properties is a very challenging task. However, to tackle highly dynamic processes like aircraft icing, such information and characterisation is necessary.

The introduced experimental procedure and the theoretical model of Roisman (2022) provide a first approach to quantifying parameters capturing the plastic effects of the mushy phase in an equivalent static yield strength Y_0. As outlined above, the residual height h_{res} from the experiment can be used to determine an equivalent Y_0. In combination with a shear rate dependent element in the model (Eq. (2.55) & Eq. (4.10)), a connection between Y_0 and the portion of ice in the mushy phase ξ_{ice} (Eq. (2.33)) is derived.

The derived yield strength values are of the order of $\mathcal{O}(5\,\text{kPa})$ and are plotted in Fig. 4.29. They reveal a clear trend of increasing Y_0 for an increased portion of ice in the mushy phase. Thus, a mushy frozen fluid originating from a higher supercooling exhibits a stiffer flow behaviour. The increase in yield strength for higher ice fractions is attributed to both, the increased amount of solid and a more even distribution of the dendrites in the bulk phase. Significant scatter in the determined yield strength is still visible in this data. One possible reason for this scatter is a remaining dependence of yield strength on the shear rate $\dot{\gamma}$. The arising shear rates can be estimated as $\dot{\gamma} \propto U_0/D_0$ and the corresponding values of the
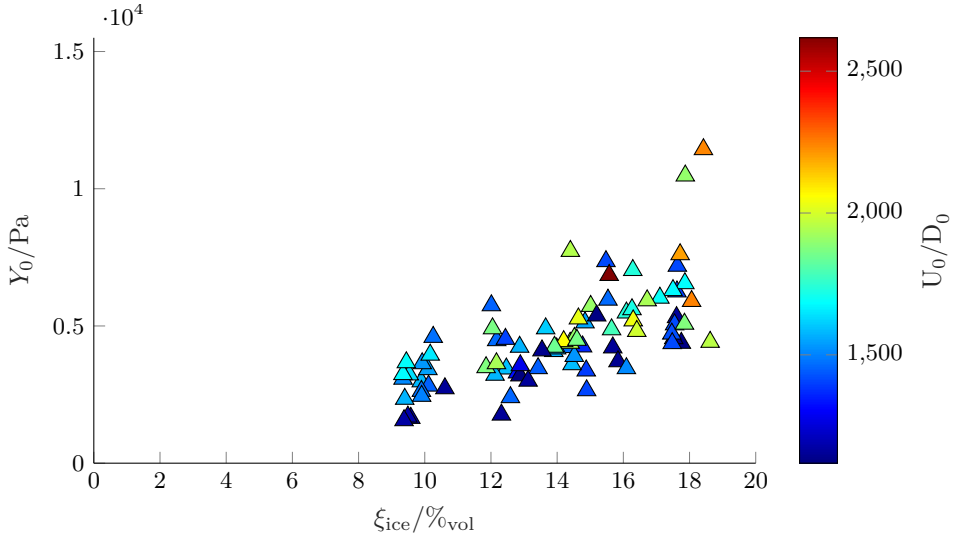
Figure 4.29: Static yield strength Y_0 determined with the model of Roisman (2022) and the residual height of the mushy drop plotted against the fraction of ice in the mushy phase ξ_{ice}. The marker color indicates a measure for the involved shear rates $(\dot{\gamma} \propto U_0/D_0)$ acting during the impact.

experiments are rendered in marker color in Fig. 4.29. It is noticeable that the yield strengths obtained from impacts which involve higher $\dot{\gamma}$ generally provide slightly higher values. Hence, the shear rate dependence contemplated in Eq. (4.10) possibly does not capture the shear rate effect in its entirety. Considering the limitation to the highest and lowest values obtained from a constant yield strength approach with Eq. (4.10), an underestimation of the shear rate dependence seems plausible and would explain the remaining shear rate effect. Moreover, the unsteady nature of the complex flow which exhibits coincidental cohesion of ice particles might affect the symmetry of the flow developing upon impact. Another reason associated with the latter may be the crystalline structure including the orientation of dendrites in the mushy phase which is not quantifiable in the scope of this study. However, the general correlation between yield strength Y_0 and the amount of ice in the mushy phase of the drops is distinctive. Thus, the determination of an equivalent static yield strength in this study represents a first step towards modelling and predicting the dynamics of a mushy phase in an icing scenario involving supercooled drops.

4.3.4 Summary

The study presented in this section is focused on the impact and propagation of initially supercooled water drops on a solid, dry wall, whereby the drops completed the first dendritic phase of freezing prior to impact - these drops are termed mushy frozen drops. A reproducible method for the experimental investigation of the drop impact in their mushy state is developed. The material properties of such drops are complex and unknown, leading to the modelling assumption of a plastic flow behaviour of the impacting mixture. An existing model from Roisman (2022) is invoked and further extended to account especially for the mixed behaviour as a liquid and as partially frozen during the spreading phase. This model development is accompanied and validated by systematic experiments, yielding detailed information about the dimensions of the drops during and after impact.

The predictive capabilities of the refined model are excellent, capturing the influence of the degree of supercooling (fraction of ice in the mushy phase) on the time evolution and final value of the residual height of the drop. Being an analytic model, further information, not available directly from the experiment, is available; in particular the time dependent impact force on the target surface and the nominal yield strength of the mushy drop upon impact. The latter is derived directly by fitting the model predictions to the observed residual height of the drop rear tip; revealing a correlation between this yield strength and the amount of solid in the mushy phase.

The derived yield strengths of ice water suspensions of varying composition may help to improve the description of rheological properties of ice water mixtures upon impact and subsequent movements with relevance to modeling aircraft icing. Eventually, the present experimental observations, in combination with the predictive model and the quantified properties, can be considered as an important complementary element to existing icing codes, enabling them to be extended to the impact and accretion of supercooled drops.

5 Summary and Outlook

This work is motivated by the demand for more insight into the physical mechanisms of icing of surfaces resulting from impacting supercooled water drops, a process crucial for ice accretion. However, a detailed description of the interaction of the fluid flow with the dynamic solidification is fragmentary, especially for impact velocities above the terminal velocity, which occur, for instance, when the impact is coupled with a surrounding air flow. Uncertainties in describing the basic phenomenon propagate to numerical codes aiming for a prediction of the onset and accretion of ice on a larger scale in scenarios regarding, for instance, aircraft icing or icing of wind turbines. Inaccuracies in simulations are partly related to a lack of knowledge about the deposited fluid mass and its distribution after a drop impact with development of a splash. Moreover, a description of the dynamic interaction of the dendritic freezing with the well-known fluid movement of a drop impact and its consequences for the remaining frozen shape is incomplete. Furthermore, the behaviour of the dendritic frozen phase, which possibly persists for a significant time before the mixture entirely solidifies, is extremely elusive which is also attributed to their unknown properties.

In order to contribute to a deeper understanding of these problems and enable an improvement of existing codes, this dissertation is devoted to the investigation of single supercooled drops impacting on solid surfaces inside of a superimposing air flow. The corresponding experiments are conducted in a custom icing wind tunnel placed in a cold chamber which was designed, built and commissioned within the scope of this work. It enables experiments with a highly reproducible air flow at the temperatures required for a significant supercooling of the impacting water drops. The drops are accelerated in the air flow prior to impact, realizing impact velocities well above the terminal velocity of the examined supercooled drops. The impact is captured in high-speed recordings in order to analyse the drop shape, velocity and the impact dynamics. Additional small components and methods are developed which enable retroactive measurement of the deposited fluid volume and the dimensions of frozen drops. Focusing on conditions in which the nucleation of the drop occurs at different times of the impact, new insight into different outcomes of a single impact is gained.

Regarding the impact of a liquid supercooled drop onto a smooth solid dry surface superimposed by a stagnation point air flow, a deformation of the drop prior to impact is observed. It is shown in Sec. 4.1.1 that the drops deform as they

approach the surface in the stagnation point flow. Similar situations are likely to occur for instance at the front of an airfoil where severe ice accretion often arises. The importance of taking this deformation into account is revealed by a vital influence on the maximum spreading radius (cf Sec. 4.1.3) of the drop. Moreover, a significant change of initial spreading velocity is identified in Sec. 4.1.1, which is linked to the front curvature of the drop.

Drops from supercooled pure water are likely to experience a long freezing delay upon impact on smooth surfaces. Hence, the developing fluid flow is crucial for the fluid distribution once the nucleation sets in or external forces from incoming drops or air flow arise. The fluid flow from a single impact with high Reynolds and Weber numbers usually involves the development of a corona splash. The thin liquid sheet lifting from the surface and breaking up into secondary drops ejected away from the fluid on the surface introduces a scatter of fluid well exceeding the maximum spreading diameter of the drop. In Sec. 4.1.2, it is shown that the extent of the splash up to the moment of break-up correlates with the splashing parameter β of Riboux and Gordillo (2014). The dimensions of the corona are possibly vital when the drop is exposed to significant aerodynamic forces, since the liquid sheet provides a distinct enlarged fluid area orthogonal to the surface in comparison to a spreading drop. An indication of the aerodynamic influence on the liquid sheet is already visible in the experiments in the wind tunnel. However, the rather slow air flow velocities in the central region of the stagnation point flow and the complex overlap of the air flow with peripheral drop impact prohibited a robust investigation of this topic. Nevertheless, the fluid not leaving the surface is measured, which revealed a correlation with the parameter β. The amount of fluid remaining on the surface after a splash (often also referred to as sticking efficiency) is a crucial quantity in large scale icing codes. The findings in this work can directly help in improving existing codes since experimental data on this matter is rare. It directly connects to the amount of ice arising as long as the fluid is not further distributed by external effects. One scenario in which external influences are most likely less critical is when the solidification of fluid arises without a delay after the first surface contact.

An immediate start of solidification occurs when the supercooled drops make contact to ice. In the scope of this work, this kind of freezing onset is achieved in experiments of drops impacting onto a planar ice surface as described in Sec. 4.2. The impact results in a thin frozen splat on the surface whose geometry varies with impact velocity as well as supercooling temperature. It is assumed that first of all the flow in the lamella is affected by the expanding dendrite front which leads to cessation of the flow and subsequent freezing of the resting ice-water mixture. This assumption is supported by the qualitative agreement with the model of Schremb et al. (2017c) which is extended to an approach to predict the residual spreading diameter of the splat. Although the calculated values agree qualitatively with the experiments, an error in absolute value of the spreading remains. Nevertheless, the qualitative agreement and the prediction of the maximum spreading already

provide useful approaches to improve icing codes considering the late stages of ice accretion. Once the whole surface is covered in ice, every other drop will freeze without a delay into a thin splat adapted to the shape of the ice surface. In this fast comprehensive growth of ice, the extent of a single impact can then be estimated similar to the presented approach.

Although the impact on ice represents the earliest onset of solidification after impact, it is shown in Sec. 4.3 that supercooled drops are able to freeze prior to first contact and impact as a partly frozen drop which is termed a mushy frozen drop. The impact behaviour of such a drop has never been investigated before and a substantial difference from the impact characteristics of a liquid drop is observed. Assuming that the flow corresponds to a rigid plastic flow behaviour, a model of Roisman (2022) originally developed for the impact of an ice crystal is adapted. The agreement of the temporal evolution of height near the impact axis of the model and the experiment is excellent. Furthermore, the approach enabled the estimation of an equivalent static yield strength Y_0. A variation of the amount of ice in the drop which is associated with the initial supercooling of drops reveals a correlation with Y_0. It is not clear how likely the impact of such a mushy drop in a natural icing scenario is, yet the turbulent air flow and possible dispersed contamination in the surroundings of an aircraft suggest a reasonable likelihood. However, apart from the description of the impact of a mushy drop, the presented method of creation in combination with the model enabled the quantification of a rheological property of the extremely elusive mixture of ice and water arising upon dendritic freezing. Although the last stage of freezing always supersedes the ice/water mixture, the significantly faster spreading of this first stage provides enough time to interact as a mixture. Especially in highly dynamic icing scenarios like aircraft icing, the movement of this mushy phase can have a vital effect on distribution of adhered matter; hence, on the ice layer growth.

The findings presented in this work contribute to a deeper understanding of the solidification taking place at different times of the impact of supercooled drops and help describing the interplay of fluid flow and dynamic freezing in various conditions. However, the identified influences and derived correlations are obtained from a limited parameter range. Especially considering a highly dynamic scenario like aircraft icing, it is necessary to investigate whether these relations apply for such a scenario. In aircraft icing, drops are usually smaller and impact velocities higher which results in comparable Reynolds numbers of the problem, yet the corresponding Weber numbers considerably exceed the range covered in this work. Under these circumstances, some of the correlations might have to be adapted to the parameter range as for instance discussed for the deposited amount of fluid in Sec. 4.1.2. Moreover, influences that are neglected in the correlations of this work might become significant in an aircraft icing scenario. For instance, the influence of the surrounding air flow is reduced to effects of the occurring drop deformation in the current work. Aerodynamic forces during the impact are not

considered due to the low air flow velocities in the central region of the stagnation point flow. However, the generally increasing scatter in the quantified results of liquid drop impacts for high air flow velocities might be attributed to aerodynamic forces as already suspected for the asymmetric development of the lifted sheet in Sec. 4.1.2. For an air flow with significantly higher velocities near the surface, the aerodynamic forces will affect the spreading and receding of the drop on the surface. This behaviour could already be observed for drops impacting close to the impact surface edge, yet the stagnation point flow developing in the current setup is not ideal for a controlled investigation of this phenomenon.

Regarding the impact on an ice surface with fast solidification of the fluid, the approach considering a residual spreading extent introduced in Sec. 4.2 reveals a remaining error in the quantitative predictions. It most likely derives from an overestimation of the residual lamella thickness from the scans of frozen splats. Their geometry is affected by additional fluid movements and the subsequent complete solidification, although it is the dendritic freezing in the lamella that traps the fluid and entails the cessation of its flow. Moreover it is not clear, whether or to what extent the mushy phase originating from this first freezing stage remains rigid in the presence of considerable aerodynamic forces. The findings regarding the impact behaviour and yield strength of this mushy phase represent a first approach to predict its dynamics. However, the general flow behaviour of this mixture is highly complex and not fully understood as already indicated by the spreading behaviour which is also influenced by local adhesion and rolling of agglomerations of this mixture. The discussed remaining gaps in understanding of such highly complex icing scenarios require a verification of the presented findings and correlations for an extended parameter range. An investigation of further influences in these might be solved in further studies addressing particular aspects.

Outlook

Despite the knowledge successfully gained in the scope of this dissertation, a universal understanding of the complex physics of the solidification and fluid flow occurring on impact onto a supercooled surface is still far from reached. The remaining obscurity regarding highly dynamic freezing and complex fluid flows discussed above might be illuminated by investigations tying in with the presented results.

First, the parameter range of the icing wind tunnel built throughout this work is not used to full capacity. As shown in Sec. 3.1, uniform flow profiles are achieved up to $U_{\text{air}} = 40\,\text{m/s}$. However, in the current work velocities of $U_{\text{air}} = 25\,\text{m/s}$ are not exceeded in order to avoid a break-up of the drop before impact. An acceleration prior to entrance into the wind tunnel flow would enable measurements at higher velocities. Moreover, a reduction of drop size may be possible to reduce the risk of break-up, albeit the current method of measuring the drop temperature is not applicable for generation of smaller drops. Next to higher air flow velocities,

an unidirectional flow on the surface possibly enables easier conclusion on the aerodynamic effects. Such a flow would for instance develop on a rectangle plate with large aspect ratio or an inclined plane placed inside the test section. The latter is also an interesting topic in order to investigate the locomotion of liquid drops after impact due to aerodynamic forces up to the moment of freezing. Regarding the solidification during spreading, the height estimation of frozen splats in the moment of flow cessation might be improved by its quantification from high-speed recordings. For this purpose, the surface shape would need to enable visibility of the lamella while providing enough area for the spreading, like for instance a truncated ice sphere. However, for an unobstructed view on the lamella, the drop also needs to impact on the apex of the sphere and guaranteeing such a precise impact position after acceleration in the air flow is a challenging task. A precise control of impact position would also enable the investigation of multiple consecutive drop impacts in an approach to study the ice layer growth of supercooled drop impacts. When the time span between impacts is short, the importance of the mushy phase originating from solidification of deposited drops might become clearer. However, a prediction of this movements most likely necessitates further investigation of the rheological properties. The study in Sec. 4.3 already suggested a correlation of yield strength with the occurring shear rate in a mushy phase flow. However, the rough approach to quantify this dependency would benefit from an investigation of the mushy phase behaviour in a less dynamic behaviour. Moreover, some experiments with velocities exceeding the one of the presented work were already conducted which indicate a noticeable separation of water spreading on the surface and ice remaining in agglomerations or leaving the surface. However, these experiments were only achieved in the drop accelerator with a less controlled method of nucleation which requires improvement for reproducible experiments.

Apart from further investigations, the findings of the current dissertation already provide the possibility to improve numeric codes aiming for a prediction of ice accretion. The correlations between influential parameters and the outcome of the impact along with the adapted models can be implemented in large scale simulation; thus, improve their accuracy and help to reduce the risks of icing due to supercooled drops in various scenarios.

Bibliography

[1] D. Anderson, D. Hentschel, and G. Ruff. "Measurement and correlation of ice accretion roughness". In: *36th AIAA Aerospace Sciences Meeting and Exhibit* (1997). DOI: 10.2514/6.1998-486.

[2] S. Bakshi, I. V. Roisman, and C. Tropea. "Investigations on the impact of a drop onto a small spherical target". In: *Physics of Fluids* 19.3 (2007), p. 032102. ISSN: 0022-1120. DOI: 10.1063/1.2716065.

[3] G. K. Batchelor. *An Introduction to Fluid Dynamics*. Cambridge: Cambridge University Press, 1967.

[4] A. Baumert, S. E. Bansmer, P. Trontin, and P. Villedieu. "Experimental and numerical investigations on aircraft icing at mixed phase conditions". In: *International Journal of Heat and Mass Transfer* 123.5 (2018), pp. 957–978. ISSN: 00179310. DOI: 10.1016/j.ijheatmasstransfer.2018.02.008.

[5] E. Berberović, M. Schremb, Ž. Tuković, S. Jakirlić, and C. Tropea. "Computational modeling of freezing of supercooled water using phase-field front propagation with immersed points". In: *International Journal of Multiphase Flow* 99 (2018), pp. 329–346. ISSN: 03019322. DOI: 10.1016/j.ijmultiphaseflow.2017.11.005.

[6] V. Bertola and M. D. Haw. "Impact of concentrated colloidal suspension drops on solid surfaces". In: *Powder Technology* 270.50–20 (2015), pp. 412–417. ISSN: 00325910. DOI: 10.1016/j.powtec.2014.02.017.

[7] N. Blanken, M. S. Saleem, M.-J. Thoraval, and C. Antonini. "Impact of compound drops: a perspective". In: *Current Opinion in Colloid & Interface Science* 51 (2021), p. 101389. ISSN: 13590294. DOI: 10.1016/j.cocis.2020.09.002.

[8] F. Boulogne and A. Salonen. "Drop freezing: Fine detection of contaminants by measuring the tip angle". In: *Applied Physics Letters* 116.10 (2020), p. 103701. ISSN: 0003-6951. DOI: 10.1063/1.5144071.

[9] M. T. Boyle, W. H. Rae, and A. Pope. *Low-speed Wind Tunnel Testing*. New York: John Wiley & Sons, Inc., 1999. DOI: 10.1109/SEMTHE.1988.10594.

[10] T. W. Brakel, J. Charpin, and T. G. Myers. "One-dimensional ice growth due to incoming supercooled droplets impacting on a thin conducting substrate". In: *International Journal of Heat and Mass Transfer* 50.9-10 (2007), pp. 1694–1705. ISSN: 00179310. DOI: 10.1016/j.ijheatmasstransfer.2006.10.014.

[11] J. Breitenbach, I. V. Roisman, and C. Tropea. "From drop impact physics to spray cooling models: a critical review". In: *Experiments in Fluids* 59.3 (2018), p. 418. ISSN: 0723-4864. DOI: 10.1007/s00348-018-2514-3.

[12] D. A. Burzynski and S. E. Bansmer. "Role of surrounding gas in the outcome of droplet splashing". In: *Physical Review Fluids* 4.7 (2019), p. 073601. DOI: 10.1103/PhysRevFluids.4.073601.

[13] D. A. Burzynski, I. V. Roisman, and S. E. Bansmer. "On the splashing of high-speed drops impacting a dry surface". In: *Journal of Fluid Mechanics* 892 (2020), A2. ISSN: 0022-1120. DOI: 10.1017/jfm.2020.168.

[14] H.-J. Butt, I. V. Roisman, M. Brinkmann, P. Papadopoulos, D. Vollmer, and C. Semprebon. "Characterization of super liquid-repellent surfaces". In: *Current Opinion in Colloid & Interface Science* 19.4 (2014), pp. 343–354. ISSN: 13590294. DOI: 10.1016/j.cocis.2014.04.009.

[15] Y. Cao, C. Ma, Q. Zhang, and J. Sheridan. "Numerical simulation of ice accretions on an aircraft wing". In: *Aerospace Science and Technology* 23.1 (2012), pp. 296–304. ISSN: 12709638. DOI: 10.1016/j.ast.2011.08.004.

[16] Y. Cao, W. Tan, and Z. Wu. "Aircraft icing: An ongoing threat to aviation safety". In: *Aerospace Science and Technology* 75.5 (2018), pp. 353–385. ISSN: 12709638. DOI: 10.1016/j.ast.2017.12.028.

[17] Y. Cao and M. Xin. "Numerical Simulation of Supercooled Large Droplet Icing Phenomenon: A Review". In: *Archives of Computational Methods in Engineering* 27.4 (2020), pp. 1231–1265. ISSN: 1134-3060. DOI: 10.1007/s11831-019-09349-5.

[18] T. Cebeci and F. Kafyeke. "Aircraft Icing". In: *Annual Review of Fluid Mechanics* 35.1 (2003), pp. 11–21. ISSN: 0066-4189. DOI: 10.1146/annurev.fluid.35.101101.161217.

[19] C. Clanet, C. Béguin, D. Richard, and D. Quéré. "Maximal deformation of an impacting drop". In: *Journal of Fluid Mechanics* 517 (2004), pp. 199–208. ISSN: 0022-1120. DOI: 10.1017/S0022112004000904.

[20] L. Courbin, J. C. Bird, M. Reyssat, and H. A. Stone. "Dynamics of wetting: from inertial spreading to viscous imbibition". In: *Journal of Physics: Condensed Matter* 21.46 (2009), p. 464127. DOI: 10.1088/0953-8984/21/46/464127.

[21] A. Criscione, I. V. Roisman, S. Jakirlić, and C. Tropea. "Towards modelling of initial and final stages of supercooled water solidification". In: *International Journal of Thermal Sciences* 92 (2015), pp. 150–161. ISSN: 12900729. DOI: 10.1016/j.ijthermalsci.2015.01.021.

[22] N. Dalili, A. Edrisy, and R. Carriveau. "A review of surface engineering issues critical to wind turbine performance". In: *Renewable and Sustainable Energy Reviews* 13.2 (2009), pp. 428–438. ISSN: 13640321. DOI: 10.1016/j.rser.2007.11.009.

[23] S. H. Davies. *Theory of Solidification*. Cambridge: Cambridge University Press, 2001. ISBN: 978-0-521-65080-9.

[24] P. G. Debendetti. "Supercooled and glassy water". In: *Journal of Physics: Condensed Matter* 15.45 (2003), R1669–R1726.

[25] A. R. Dehghani-Sanij, S. R. Dehghani, G. F. Naterer, and Y. S. Muzychka. "Sea spray icing phenomena on marine vessels and offshore structures: Review and formulation". In: *Ocean Engineering* 132.5 (2017), pp. 25–39. ISSN: 00298018. DOI: 10.1016/j.oceaneng.2017.01.016.

[26] P. Eberle, M. K. Tiwari, T. Maitra, and D. Poulikakos. "Rational nanostructuring of surfaces for extraordinary icephobicity". In: *Nanoscale* 6.9 (2014), pp. 4874–4881. DOI: 10.1039/c3nr06644d.

[27] B. J. K. Engdahl, B. E. K. Nygaard, V. Losnedal, G. Thompson, and L. Bengtsson. "Effects of the ICE-T microphysics scheme in HARMONIE-AROME on estimated ice loads on transmission lines". In: *Cold Regions Science and Technology* 179.12 (2020), p. 103139. DOI: 10.1016/j.coldregions.2020.103139.

[28] B. W. Faßmann, S. E. Bansmer, T. J. Möller, R. Radespiel, and M. Hartmann. "High velocity impingement of single droplets on a dry smooth surface". In: *Experiments in Fluids* 54.5 (2013), p. 2194. ISSN: 0723-4864. DOI: 10.1007/s00348-013-1516-4.

[29] F. Franks, ed. *Water and Aqueous Solutions at Subzero Temperatures*. Vol. 7. Water - A comprehensive treatise. New York: Springer, 1982. DOI: 10.1007/978-1-4757-6952-4.

[30] M. Gloerfeld, M. Schremb, I. V. Roisman, J. Hussong, and C. Tropea. "Wall impact of mushy frozen water drops". In: *Cold Regions Science and Technology* 206 (2023), p. 103732. DOI: 10.1016/j.coldregions.2022.103732.

[31] M. Gloerfeld, I. V. Roisman, J. Hussong, and C. Tropea. "Measurements and modelling of the residual mass upon impact of supercooled liquid drops". In: *Experiments in Fluids* 62.10 (2021), p. 4520. ISSN: 0723-4864. DOI: 10.1007/s00348-021-03292-7.

[32] L. Greer. "A cloak of liquidity". In: *Nature* 464 (2010), pp. 1137–1138. DOI: 10.1038/4641137a.

[33] V. Grishaev, C. S. Iorio, F. Dubois, and A. Amirfazli. "Impact of particle-laden drops: Particle distribution on the substrate". In: *Journal of Colloid and Interface Science* 490 (2017), pp. 108–118. DOI: 10.1016/j.jcis.2016.11.038.

[34] M. Grizen, T. Maitra, J. P. Bradley, and M. K. Tiwari. "Nanotextured Aluminum-Based Surfaces with Icephobic Properties". In: *Heat Transfer Engineering* 41.19-20 (2020), pp. 1663–1672. ISSN: 0145-7632. DOI: 10.1080/01457632.2019.1640461.

[35] A. Güttler. "High accuracy determination of skin friction differences in an air channel flow based on pressure drop measurements". PhD thesis. Karslruhe: Karlsruhe Institut für Technologie, 2015.

[36] R. Herbaut, P. Brunet, L. Limat, and L. Royon. "Liquid spreading on cold surfaces: Solidification-induced stick-slip dynamics". In: *Physical Review Fluids* 4.3 (2019). DOI: 10.1103/PhysRevFluids.4.033603.

[37] R. Herbaut, J. Dervaux, P. Brunet, L. Royon, and L. Limat. "A criterion for the pinning and depinning of an advancing contact line on a cold substrate". In: *The European Physical Journal Special Topics* 229.10 (2020), pp. 1867–1880. ISSN: 1951-6355. DOI: 10.1140/epjst/e2020-900261-5.

[38] V. Holten, C. E. Bertrand, M. A. Anisimov, and J. V. Sengers. "Thermodynamics of supercooled water". In: *The Journal of Chemical Physics* 136.9 (2012), p. 094507. DOI: 10.1063/1.3690497.

[39] R. L. James, V. T. J. Phillips, and P. J. Connolly. "Secondary ice production during the break-up of freezing water drops on impact with ice particles". In: *Atmospheric Chemistry and Physics* 21.24 (2021), pp. 18519–18530. DOI: 10.5194/acp-21-18519-2021.

[40] W. J. Jasinski, S. C. Noe, M. S. Selig, and M. B. Bragg. "Wind turbine performance under icing conditions". In: *Journal of Solar Energy Engineering* 120 (1998), pp. 60–65. DOI: 10.1115/1.2888048.

[41] Z. Jin, X. Cheng, and Z. Yang. "Experimental investigation of the successive freezing processes of water droplets on an ice surface". In: *International Journal of Heat and Mass Transfer* 107.69 (2017), pp. 906–915. ISSN: 00179310. DOI: 10.1016/j.ijheatmasstransfer.2016.11.001.

[42] Z. Jin, D. Sui, and Z. Yang. "The impact, freezing, and melting processes of a water droplet on an inclined cold surface". In: *International Journal of Heat and Mass Transfer* 90 (2015), pp. 439–453. ISSN: 00179310. DOI: 10.1016/j.ijheatmasstransfer.2015.06.086.

[43] Z. Jin, H. Zhang, and Z. Yang. "Experimental investigation of the impact and freezing processes of a water droplet on an ice surface". In: *International Journal of Heat and Mass Transfer* 109 (2017), pp. 716–724. ISSN: 00179310. DOI: 10.1016/j.ijheatmasstransfer.2017.02.055.

[44] C. Josserand and S. T. Thoroddsen. "Drop Impact on a Solid Surface". In: *Annual Review of Fluid Mechanics* 48.1 (2016), pp. 365–391. ISSN: 0066-4189. DOI: 10.1146/annurev-fluid-122414-034401.

[45] S. Jung, M. K. Tiwari, N. V. Doan, and D. Poulikakos. "Mechanism of supercooled droplet freezing on surfaces". In: *Nature Communications* 3 (2012), p. 615. DOI: 10.1038/ncomms1630.

[46] P. Kant, R. B. J. Koldeweij, K. Harth, M. A. J. van Limbeek, and D. Lohse. "Fast-freezing kinetics inside a droplet impacting on a cold surface". In: *Proceedings of the National Academy of Sciences of the United States of America* 117.6 (2020), pp. 2788–2794. DOI: 10.1073/pnas.1912406117.

[47] P. Kant, H. Müller-Groeling, and D. Lohse. "Pattern Formation during the Impact of a Partially Frozen Binary Droplet on a Cold Surface". In: *Physical Review Letters* 125.18 (2020), p. 184501. DOI: 10.1103/PhysRevLett.125.184501.

[48] L. Karlsson, H. Lycksam, A.-L. Ljung, P. Gren, and T. S. Lundström. "Experimental study of the internal flow in freezing water droplets on a cold surface". In: *Experiments in Fluids* 60.12 (2019), p. 329. ISSN: 0723-4864. DOI: 10.1007/s00348-019-2823-1.

[49] W. Kong and H. Liu. "A theory on the icing evolution of supercooled water near solid substrate". In: *International Journal of Heat and Mass Transfer* 91.1 (2015), pp. 1217–1236. ISSN: 00179310. DOI: 10.1016/j.ijheatmasstransfer.2015.08.005.

[50] W. Kong and H. Liu. "Unified icing theory based on phase transition of supercooled water on a substrate". In: *International Journal of Heat and Mass Transfer* 123.1776 (2018), pp. 896–910. ISSN: 00179310. DOI: 10.1016/j.ijheatmasstransfer.2018.03.028.

[51] J. L. Laforte, M. A. Allaire, and J. Laflamme. "State-of-the-art on power line de-icing". In: *Atmospheric Research* 46 (1998), pp. 143–158. DOI: 10.1016/S0169-8095(97)00057-4.

[52] J. S. Langer and H. Müller-Krumbhaar. "Theory of dendritic growth - I. Elements of a stability analysis". In: *Acta Metallurgica* 26 (1978), pp. 1681–1687. DOI: 10.1016/0001-6160(78)90078-0.

[53] H. Li, I. V. Roisman, and C. Tropea. "Influence of solidification on the impact of supercooled water drops onto cold surfaces". In: *Experiments in Fluids* 56.6 (2015), p. 3180. ISSN: 0723-4864. DOI: 10.1007/s00348-015-1999-2.

[54] K. G. Libbrecht. "Physical Dynamics of Ice Crystal Growth". In: *Annual Review of Materials Research* 47.1 (2017), pp. 271–295. ISSN: 1531-7331. DOI: 10.1146/annurev-matsci-070616-124135.

[55]   Q. Liu, J. H. Y. Lo, Y. Li, Y. Liu, J. Zhao, and L. Xu. "The role of drop shape in impact and splash". In: *Nature Communications* 12.1 (2021), p. 3068. DOI: `10.1038/s41467-021-23138-4`.

[56]   J.-M. Löwe, V. Hinrichsen, M. Schremb, and C. Tropea. "Ice nucleation forced by transient electric fields". In: *Physical Review E* 104.6-1 (2021), p. 064801. DOI: `10.1103/PhysRevE.104.064801`.

[57]   T. Maitra, C. Antonini, M. K. Tiwari, A. Mularczyk, Z. Imeri, P. Schoch, and D. Poulikakos. "Supercooled water drops impacting superhydrophobic textures". In: *Langmuir* 30.36 (2014), pp. 10855–10861. DOI: `10.1021/la502675a`.

[58]   L. Makkonen. "Modeling power line icing in freezing precipitation". In: *Atmospheric Research* 46 (1998), pp. 131–142. DOI: `10.1016/S0169-8095(97)00056-2`.

[59]   L. Makkonen. "Salinity and growth rate of ice formed by sea spray". In: *Cold Regions Science and Technology* 14 (1987), pp. 163–171. DOI: `10.1016/0165-232X(87)90032-2`.

[60]   L. Makkonen. "Solid fraction in dendritic solidification of a liquid". In: *Applied Physics Letters* 96.9 (2010), p. 091910. ISSN: 0003-6951. DOI: `10.1063/1.3306728`.

[61]   A. G. Marín, O. R. Enríquez, P. Brunet, P. Colinet, and J. H. Snoeijer. "Universality of tip singularity formation in freezing water drops". In: *Physical Review Letters* 113.5 (2014), p. 054301. DOI: `10.1103/PhysRevLett.113.054301`.

[62]   J. O. Marston, M. M. Mansoor, and S. T. Thoroddsen. "Impact of granular drops". In: *Physical Review E* 88.1 (2013), p. 010201. DOI: `10.1103/PhysRevE.88.010201`.

[63]   S. T. McClain, M. Vargas, Tsao Jen-Ching, A. P. Broeren, and S. Lee. "Ice Accretion Roughness Measurements and Modeling". In: *7TH European Conference For Aeronautics And Space Sciences (EUCASS)* (2017).

[64]   N. Z. Mehdizadeh, S. Chandra, and J. Mostaghimi. "Formation of fingers around the edges of a drop hitting a metal plate with high velocity". In: *Journal of Fluid Mechanics* 510 (2004), pp. 353–373. ISSN: 0022-1120. DOI: `10.1017/S0022112004009310`.

[65]   S. Moghtadernejad, M. Jadidi, M. Tembely, N. Esmail, and A. Dolatabadi. "Concurrent Droplet Coalescence and Solidification on Surfaces With Various Wettabilities". In: *Journal of Fluids Engineering* 137 (2015). DOI: `10.1115/1.4029672`.

[66] M. Mohammadi, M. Tembely, and A. Dolatabadi. "Predictive Model of Supercooled Water Droplet Pinning/Repulsion Impacting a Superhydrophobic Surface: The Role of the Gas-Liquid Interface Temperature". In: *Langmuir* 33.8 (2017), pp. 1816–1825. DOI: 10.1021/acs.langmuir.6b04394.

[67] A. Moreira, A. S. Moita, and M. R. Panão. "Advances and challenges in explaining fuel spray impingement: How much of single droplet impact research is useful?" In: *Progress in Energy and Combustion Science* 36.5 (2010), pp. 554–580. ISSN: 03601285. DOI: 10.1016/j.pecs.2010.01.002.

[68] C. Mundo, M. Sommerfeld, and C. Tropea. "Droplet-Wall Collisions: Experimental studies of the deformation and breakup process". In: *International Journal of Multiphase Flow* 21 (1995), pp. 151–173. ISSN: 03019322.

[69] W. Nitsche and A. Brunn. *Strömungsmesstechnik*. 2., aktualisierte und bearbeitete Auflage. VDI-Buch. Berlin, Heidelberg: Springer-Verlag Berlin Heidelberg, 2006. ISBN: 9783540209904. DOI: 10.1007/3-540-32487-9.

[70] L. Opfer, I. V. Roisman, J. Venzmer, M. Klostermann, and C. Tropea. "Droplet-air collision dynamics: evolution of the film thickness". In: *Physical Review E* 89.1 (2014), p. 013023. DOI: 10.1103/PhysRevE.89.013023.

[71] D. W. Oxotoby. "Homogeneous nucleation: theory and experiment". In: *Journal of Physics: Condensed Matter* 4 (1992), pp. 7627–7650.

[72] J. Palacios, J. Hernández, P. Gómez, C. Zanzi, and J. López. "Experimental study of splashing patterns and the splashing/deposition threshold in drop impacts onto dry smooth solid surfaces". In: *Experimental Thermal and Fluid Science* 44.056316 (2012), pp. 571–582. ISSN: 08941777. DOI: 10.1016/j.expthermflusci.2012.08.020.

[73] M. Papadakis, K. Hung, H.-W. Yeong, C. Bidwell, and M. Breer. "Experimental investigation of water impingement on single and multi-element airfoils". In: *38th Aerospace Sciences Meeting and Exhibit*. Reston, Virigina: American Institute of Aeronautics and Astronautics, 2000, p. 3587. DOI: 10.2514/6.2000-100.

[74] M. Papadakis, A. Rachman, S.-C. Wong, H.-W. Yeong, K. Hung, and C. Bidwell. "Water Impingement Experiments on a NACA 23012 Airfoil with Simulated Glaze Ice Shapes". In: *42nd AIAA Aerospace Sciences Meeting and Exhibit*. Reston, Virigina: American Institute of Aeronautics and Astronautics, 2004, p. 289. ISBN: 978-1-62410-078-9. DOI: 10.2514/6.2004-565.

[75] O. Parent and A. Ilinca. "Anti-icing and de-icing techniques for wind turbines: Critical review". In: *Cold Regions Science and Technology* 65.1 (2011), pp. 88–96. DOI: 10.1016/j.coldregions.2010.01.005.

[76] J. Pasieka, R. Nanua, S. Coulombe, and P. Servio. "The crystallization of sub-cooled water: Measuring the front velocity and mushy zone composition via thermal imaging". In: *International Journal of Heat and Mass Transfer* 77.3 (2014), pp. 940–945. ISSN: 00179310. DOI: 10.1016/j.ijheatmasstransfer.2014.06.009.

[77] J. J. Petrovic. "Review - Mechanical properties of ice and snow". In: *Journal of Material Science* 38 (2003), pp. 1–6. DOI: 10.1023/A:1021134128038.

[78] M. K. Politovich. "Aircraft Icing". In: *Encyclopedia of Athmospheric Sciences (Second Edition)*. Ed. by G. R. North, J. Pyle, and F. Zhang. Academic Press, 2015, pp. 160–165. ISBN: 9780123822253. DOI: 10.1016/B978-0-12-382225-3.00055-4.

[79] D. A. Porter, K. E. Easterling, and M. Y. Sherif. *Phase Transformations in Metals and Alloys*. 3rd ed. Boca Ranton: Taylor & Francis Group, 2009. ISBN: 978-1-4200-6210-6.

[80] H. R. Pruppacher and J. D. Klett. *Microphysics of Clouds and Precipitation*. 1st ed. Vol. 18. Springer eBook Collection Earth and Environmental Science. Dordrecht: Springer Netherlands, 2010. ISBN: 9780306481000. DOI: 10.1007/978-0-306-48100-0.

[81] T. Rashid, H. A. Khawaja, and K. Edvardsen. "Review of marine icing and anti-/de-icing systems". In: *Journal of Marine Engineering & Technology* 15.2 (2016), pp. 79–87. ISSN: 2046-4177. DOI: 10.1080/20464177.2016.1216734.

[82] M. Rein and J.-P. Delplanque. "The role of air entrainment on the outcome of drop impact on a solid surface". In: *Acta Mechanica* 201.1-4 (2008), pp. 105–118. ISSN: 0001-5970. DOI: 10.1007/s00707-008-0076-9.

[83] L. M. Reitter, H. Lohmann, M. Schremb, I. V. Roisman, J. Hussong, and C. Tropea. "Impact of an ice particle onto a dry rigid substrate: Dynamic sintering of a residual ice cone". In: *Cold Regions Science and Technology* 194 (2022), p. 103416. DOI: 10.1016/j.coldregions.2021.103416.

[84] G. Riboux and J. M. Gordillo. "Experiments of drops impacting a smooth solid surface: a model of the critical impact speed for drop splashing". In: *Physical Review Letters* 113.2 (2014), p. 024507. DOI: 10.1103/PhysRevLett.113.024507.

[85] R. Rioboo, M. Marengo, and C. Tropea. "Time evolution of liquid drop impact onto solid, dry surfaces". In: *Experiments in Fluids* 33.1 (2002), pp. 112–124. ISSN: 0723-4864. DOI: 10.1007/s00348-002-0431-x.

[86] I. V. Roisman. "Inertia dominated drop collisions. II. An analytical solution of the Navier–Stokes equations for a spreading viscous film". In: *Physics of Fluids* 21.5 (2009), p. 052104. ISSN: 0022-1120. DOI: 10.1063/1.3129283.

[87] I. V. Roisman, E. Berberović, and C. Tropea. "Inertia dominated drop collisions. I. On the universal flow in the lamella". In: *Physics of Fluids* 21.5 (2009), p. 052103. ISSN: 0022-1120. DOI: 10.1063/1.3129282.

[88] I. V. Roisman. "Hydrodynamic model of a collision of a spherical plastic ice particle with a perfectly rigid substrate". In: *International Journal of Impact Engineering* 133.4 (2022), p. 104019. ISSN: 0734743X. DOI: 10.1016/j.ijimpeng.2021.104019.

[89] I. V. Roisman, A. Criscione, C. Tropea, D. K. Mandal, and A. Amirfazli. "Dislodging a sessile drop by a high-Reynolds-number shear flow at sub-freezing temperatures". In: *Physical Review E* 92.2 (2015), p. 023007. DOI: 10.1103/PhysRevE.92.023007.

[90] I. V. Roisman, T. Gambaryan-Roisman, O. Kyriopoulos, P. Stephan, and C. Tropea. "Breakup and atomization of a stretching crown". In: *Physical Review E* 76.2 Pt 2 (2007), p. 026302. DOI: 10.1103/PhysRevE.76.026302.

[91] I. V. Roisman, A. Lembach, and C. Tropea. "Drop splashing induced by target roughness and porosity: The size plays no role". In: *Advances in Colloid and Interface Science* 222 (2015), pp. 615–621. DOI: 10.1016/j.cis.2015.02.004.

[92] I. V. Roisman, R. Rioboo, and C. Tropea. "Normal impact of a liquid drop on a dry surface: model for spreading and receding". In: *Proceedings of the Royal Society of London. Series A: Mathematical, Physical and Engineering Sciences* 458.2022 (2002), pp. 1411–1430. ISSN: 1364-5021. DOI: 10.1098/rspa.2001.0923.

[93] I. V. Roisman and C. Tropea. "Wetting and icing of surfaces". In: *Current Opinion in Colloid & Interface Science* 53 (2021), p. 101400. ISSN: 13590294. DOI: 10.1016/j.cocis.2020.101400.

[94] A. Sahlin and A. V. Johansson. "Design of guide vanes for minimizing the pressure loss in sharp bends". In: *Physics of Fluids A: Fluid Dynamics* 3.8 (1991), pp. 1934–1940. ISSN: 0899-8213. DOI: 10.1063/1.857923.

[95] E. M. Samuelsen. "Ship-icing prediction methods applied in operational weather forecasting". In: *Quarterly Journal of the Royal Meteorological Society* 144.710 (2018), pp. 13–33. ISSN: 00359009. DOI: 10.1002/qj.3174.

[96] B. L. Scheller and D. W. Bousfield. "Newtonian drop impact with a solid surface". In: *American Institute of Chemical Engineers* 41 (1995), pp. 1357–1367. DOI: 10.1002/aic.690410602.

[97] A. Schetnikov, V. Matiunin, and V. Chernov. "Conical shape of frozen water droplets". In: *American Journal of Physics* 83.1 (2015), pp. 36–38. ISSN: 0002-9505. DOI: 10.1119/1.4897499.

[98]   P. F. Scholander, W. Flagg, R. J. Hock, and L. Irving. "Studies on the physiology of frozen plants and animals in the arctic". In: *Journal of Cellular and Comparative Physiology* 42 (1953), pp. 1–56. DOI: 10.1002/jcp.1030420403.

[99]   M. Schremb, S. Borchert, E. Berberovic, S. Jakirlic, I. V. Roisman, and C. Tropea. "Computational modelling of flow and conjugate heat transfer of a drop impacting onto a cold wall". In: *International Journal of Heat and Mass Transfer* 109 (2017), pp. 971–980. ISSN: 00179310. DOI: 10.1016/j.ijheatmasstransfer.2017.02.073.

[100] M. Schremb, J. M. Campbell, H. K. Christenson, and C. Tropea. "Ice Layer Spreading along a Solid Substrate during Solidification of Supercooled Water: Experiments and Modeling". In: *Langmuir* 33.19 (2017), pp. 4870–4877. DOI: 10.1021/acs.langmuir.7b00930.

[101] M. Schremb, I. V. Roisman, and C. Tropea. "Normal impact of supercooled water drops onto a smooth ice surface: experiments and modelling". In: *Journal of Fluid Mechanics* 835 (2017), pp. 1087–1107. ISSN: 0022-1120. DOI: 10.1017/jfm.2017.797.

[102] M. Schremb, I. V. Roisman, and C. Tropea. "Transient effects in ice nucleation of a water drop impacting onto a cold substrate". In: *Physical Review E* 95.2-1 (2017), p. 022805. DOI: 10.1103/PhysRevE.95.022805.

[103] M. Schremb and C. Tropea. "Solidification of supercooled water in the vicinity of a solid wall". In: *Physical Review E* 94.5-1 (2016), p. 052804. DOI: 10.1103/PhysRevE.94.052804.

[104] M. Schremb. "Hydrodynamics and Thermodynamics of Ice Accretion through Impact of Supercooled Large Droplets: Experiments, Simulations and Theory". PhD thesis. Darmstadt: Technische Universität Darmstadt, 2018.

[105] M. Schremb, K. Malicevic, L. Reitter, I. Roisman, and C. Tropea. "Material Properties of Granular Ice Layers Characterized Using a Rigid-Body-Penetration Method: Experiments and Modeling". In: *SAE Technical Paper 2019-01-2034* (2019). DOI: 10.4271/2019-01-2034.

[106] M. Schwarzer, T. Otto, M. Schremb, C. Marschelke, H. T. Tee, F. R. Wurm, I. V. Roisman, C. Tropea, and A. Synytska. "Supercooled Water Drops Do Not Freeze During Impact on Hybrid Janus Particle-Based Surfaces". In: *Chemistry of Materials* 31.1 (2019), pp. 112–123. ISSN: 0897-4756. DOI: 10.1021/acs.chemmater.8b03183.

[107] P. M. Seiler, M. Gloerfeld, I. V. Roisman, and C. Tropea. "Aerodynamically driven motion of a wall-bounded drop on a smooth solid substrate". In: *Physical Review Fluids* 4.2 (2019). DOI: 10.1103/PhysRevFluids.4.024001.

[108] A. A. Shibkov, Y. I. Golovin, M. A. Zheltov, A. A. Korolev, and A. A. Leonov. "Morphology diagram of nonequilibrium patterns of ice crystals growing in supercooled water". In: *Physica A* 319 (2003), pp. 65–79. DOI: 10.1016/S0378-4371(02)01517-0.

[109] A. A. Shibkov, M. A. Zheltov, A. A. Korolev, A. A. Kazakov, and A. A. Leonov. "Crossover from diffusion-limited to kinetics-limited growth of ice crystals". In: *Journal of Crystal Growth* 285.1-2 (2005), pp. 215–227. DOI: 10.1016/j.jcrysgro.2005.08.007.

[110] J. H. Snoeijer and P. Brunet. "Pointy ice-drops: How water freezes into a singular shape". In: *American Journal of Physics* 80.9 (2012), pp. 764–771. ISSN: 0002-9505. DOI: 10.1119/1.4726201.

[111] J. Steiner and S. E. Bansmer. "Ice Roughness and its Impact on the Ice Accretion Process". In: *8th AIAA Atmospheric and Space Environments Conference* 06132016 (2016). DOI: 10.2514/6.2016-3591.

[112] C. S. Stevens, A. Latka, and S. R. Nagel. "Comparison of splashing in high- and low-viscosity liquids". In: *Physical Review E* 89.6 (2014), p. 063006. DOI: 10.1103/PhysRevE.89.063006.

[113] C. D. Stow and M. G. Hadfield. "An experimental investigation of fluid flow resulting from the impact of a water drop with an unyielding dry surface". In: *Proceedings of the Royal Society of London. A. Mathematical and Physical Sciences* 373.1755 (1981), pp. 419–441. ISSN: 0080-4630. DOI: 10.1098/rspa.1981.0002.

[114] R. Stull. "Wet-Bulb Temperature from Relative Humidity and Air Temperature". In: *Journal of Applied Meteorology and Climatology* 50.11 (2011), pp. 2267–2269. ISSN: 1558-8424. DOI: 10.1175/JAMC-D-11-0143.1.

[115] K. Szilder, E. P. Lozowski, and G. Reuter. "A Study of Ice Accretion Shape on Cables Under Freezing Rain Conditions". In: *Journal of Offshore Mechanics and Arctic Engineering* 124 (2002), pp. 162–168. DOI: 10.1115/1.1488932.

[116] M. Tembely and A. Dolatabadi. "A comprehensive model for predicting droplet freezing features on a cold substrate". In: *Journal of Fluid Mechanics* 859 (2019), pp. 566–585. ISSN: 0022-1120. DOI: 10.1017/jfm.2018.839.

[117] V. Thiévenaz, T. Séon, and C. Josserand. "Solidification dynamics of an impacted drop". In: *Journal of Fluid Mechanics* 874 (2019), pp. 756–773. ISSN: 0022-1120. DOI: 10.1017/jfm.2019.459.

[118] V. Thiévenaz, C. Josserand, and T. Séon. "Retraction and freezing of a water film on ice". In: *Physical Review Fluids* 5.4 (2020), p. 250. DOI: 10.1103/PhysRevFluids.5.041601.

[119] S. T. Thoroddsen, K. Takehara, and T. G. Etoh. "Micro-splashing by drop impacts". In: *Journal of Fluid Mechanics* 706 (2012), pp. 560–570. ISSN: 0022-1120. DOI: 10.1017/jfm.2012.281.

[120] J. D. Tippmann, H. Kim, and J. D. Rhymer. "Experimentally validated strain rate dependent material model for spherical ice impact simulation". In: *International Journal of Impact Engineering* 57.7 (2013), pp. 43–54. ISSN: 0734743X. DOI: 10.1016/j.ijimpeng.2013.01.013.

[121] P. Trontin and P. Villedieu. "Revisited Model for Supercooled Large Droplet Impact onto a Solid Surface". In: *Journal of Aircraft* 54.3 (2017), pp. 1189–1204. ISSN: 0021-8669. DOI: 10.2514/1.C034092.

[122] C. Tropea, J. Foss, and A. L. Yarin. *Handbook of Experimental Fluid Mechanics.* Berlin, Heidelberg: Springer, 2007.

[123] Y. Ueda, S. Yokoyama, M. Nomura, R. Tsujino, and M. Iguchi. "Bouncing behaviors of suspension liquid drops on a superhydrophobic surface". In: *Journal of Visualization* 13.4 (2010), pp. 281–283. DOI: 10.1007/s12650-010-0051-0.

[124] VDI and GVC. *VDI-Wärmeatlas.* Berlin, Heidelberg: Springer, 2006. ISBN: 3-540-25504-4.

[125] E. Villeneuve, E. Karmouch, and X. Boulerice. "Development of a small and transportable de-icing/anti-icing drone-mounted system. Part 1: System design". In: *Drone Systems and Applications* 10.1 (2022), pp. 155–177. ISSN: 2564-4939. DOI: 10.1139/dsa-2021-0036.

[126] V. Vinš, M. Fransen, J. Hykl, and J. Hrubý. "Surface tension of supercooled water determined by using a counterpressure capillary rise method". In: *The Journal of Physical Chemistry B* 119.17 (2015), pp. 5567–5575. DOI: 10.1021/acs.jpcb.5b00545.

[127] T. Wang, L. Ai, Y. Zhou, and M. Chen. "Numerical Simulation of Supercooled Water Droplets Impacting Ice with Rapid Crystal Growth Taken into Consideration". In: *Langmuir* 36.19 (2020), pp. 5466–5473. DOI: 10.1021/acs.langmuir.9b03196.

[128] A. M. Worthington. "On the forms assumed by drops of liquids falling vertically on a horizontal plate". In: *Proceedings of the Royal Society of London* 25 (1876), pp. 261–272. DOI: 10.1098/rspl.1876.0048.

[129] L. Xu, W. W. Zhang, and S. R. Nagel. "Drop splashing on a dry smooth surface". In: *Physical Review Letters* 94.18 (2005), p. 184505. DOI: 10.1103/PhysRevLett.94.184505.

[130] M. Yamazaki, A. Jemcov, and H. Sakaue. "A Review on the Current Status of Icing Physics and Mitigation in Aviation". In: *Aerospace* 8.7 (2021), 188Yama. DOI: 10.3390/aerospace8070188.

[131] F. Yang, O. Cruikshank, W. He, A. Kostinski, and R. A. Shaw. "Nonthermal ice nucleation observed at distorted contact lines of supercooled water drops". In: *Physical Review E* 97.2-1 (2018), p. 023103. DOI: 10.1103/PhysRevE.97.023103.

[132] A. L. Yarin. "Drop Impact Dynamics: Splashing, Spreading, Receding, Bouncing...". In: *Annual Review of Fluid Mechanics* 38.1 (2006), pp. 159–192. ISSN: 0066-4189. DOI: 10.1146/annurev.fluid.38.050304.092144.

[133] A. L. Yarin, C. Tropea, and I. Roisman. *Collision Phenomena in Liquids and Solids.* Cambridge University Press, 2017.

[134] A. L. Yarin and D. A. Weiss. "Impact of drops on solid surfaces: self-similar capillary waves, and splashing as a new type of kinematic discontinuity". In: *Journal of Fluid Mechanics* 283.-1 (1995), p. 141. ISSN: 0022-1120. DOI: 10.1017/S0022112095002266.

[135] C. Zhang and H. Liu. "Effect of drop size on the impact thermodynamics for supercooled large droplet in aircraft icing". In: *Physics of Fluids* 28.6 (2016), p. 062107. ISSN: 0022-1120. DOI: 10.1063/1.4953411.

[136] C. Zhang, H. Liu, F. Wang, and W. Kong. "Supercooled large droplet icing accretion and its unsteady aerodynamic characteristics on high-lift devices". In: *Proceedings of the Institution of Mechanical Engineers, Part G: Journal of Aerospace Engineering* 232.10 (2018), pp. 1985–1997. ISSN: 0954-4100. DOI: 10.1177/0954410017706991.

[137] H. Zhang, Y. Zhao, R. Lv, and C. Yang. "Freezing of sessile water droplet for various contact angles". In: *International Journal of Thermal Sciences* 101 (2016), pp. 59–67. ISSN: 12900729. DOI: 10.1016/j.ijthermalsci.2015.10.027.